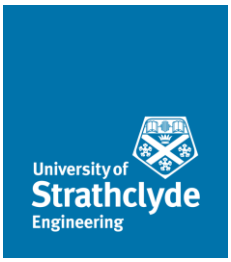

University of Strathclyde

Department of Naval Architecture, Ocean & Marine Engineering

PERIDYNAMICS

AND

ITS APPLICATIONS IN MARINE STRUCTURES

by

Cagan Diyaroglu

A thesis presented in fulfilment of the requirements for the degree of

Doctor of Philosophy

Glasgow, UK

2016

This thesis is the result of the author's original research. It has been composed by the author and has not been previously submitted for examination which has led to the award of a degree.

Signed: Cagan Diyaroglu *Date:* 07 February 2016

Dedicated to

Nagihan
Whose love always makes me strong

Acknowledgements

First of all, I would like to thank Dr. Erkan Oterkus who showed me the way of success.

I am very greatful to my dad, mom and grandma for their strong beliefs on my success.

I would like to thank Prof. Osman Turan for inviting me to Glasgow.

Lastly, I would like to express my gratitude to University of Strathclyde, Lloyd's Register and The Scientific and Technological Research Council of Turkey (TUBITAK) for their sponsorships.

Abstract

Prediction of fracture and failure is a challenging research area. There are various methods available in the literature for this purpose including well-known finite element (FE) method. FE method is a powerful technique for deformation and stress analysis of structures. However, it has various disadvantageous in predicting failure due to its mathematical structure since it is based on classical continuum mechanics (CCM). CCM has governing equations in the form of partial differential equations. These equations are not valid if the displacement field is discontinuous as a result of crack occurance. In order to overcome this problem, a new continuum mechanics formulation was introduced and named as Peridynamics. Peridynamics uses integrals equations as opposed to partial differential equations of CCM. Moreover, it does not contain any spatial derivatives. Hence, its equations are always valid regardless of discontinuities. In this thesis, the applications of Peridynamics for marine structues are demonstrated. Particularly, the Peridynamic equations are rederived for simplified structures commonly used in marine structures including beams and plates. Furthermore, underwater shock response of marine composites is investigated. Finally, the peridynamic formulation for contact analysis which can be used for collision and grounding of ship structures is demonstrated. In order to reduce the computational time, several solution strategies are explained.

Contents

List of Figures

List of Tables

Nomenclature

Acronyms

ADR	Adaptive Dynamic Relaxation
AF	Amplification Factor
ASTM	American Society for Testing and Materials
BM	Base Material
CCM	Classical Continuum Mechanics
CMOD	Crack Mouth Opening Displacement
CPU	Central Processing Unit
CST	Conical Shock Tube
CTE	Coefficient of Thermal Expansion
CTOA	Crack Tip Opening Angle
CTOD	Crack Tip Opening Displacement
CZE	Cohesive Zone Elements
DAA	Doubly Asymptotic Approximation
DCB	Double Cantilever Beam
DR	Dynamic Relaxation
ELS	End Loaded Split
ENF	End Notched Flexure
EOM	Equation of Motion
FCAW	Flux Cored Arc Welding
FE	Finite Element
FEA	Finite Element Analysis
FEM	Finite Element Method
FL	Fusion Line
FSI	Fluid Structure Interaction

GPU	Graphics Processing Unit
HAZ	Heat Affected Zone
HPC	High Performance Computing
IACS	International Association of Classification Societies
JSTRA	Japan Ship Technology Research Association
LEFM	Linear Elastic Fracture Mechanics
LNG	Liquefied Natural Gas
LSP	Laser Shock Processing
MEMS	Micro Electro Mechanical Systems
MIMD	Multiple Instruction Multiple Data
MISD	Multiple Instruction Single Data
MMB	Mixed Mode Bending
NEMS	Nano Electro Mechanical Systems
1D	One Dimensional
PD	Peridynamic
PUF	Polyurethane Foam
RPUF	Reinforced Polyurethane Foam
SAW	Submerged Arc Welding
SIMD	Single Instruction Multiple Data
SS NILT	State Space Numerical Inversion of Laplace Transform
3D	Three Dimensional
2D	Two Dimensional
UNDEX	Underwater Explosion
USLS	Underwater Shock Loading Simulator
WP	Weld Position
XFEM	Extended Finite Element Method

Symbols

A	Cross – sectional area
$\mathbf{a_G}$	Acceleration of a centre of gravity
α	Plane angle of the cone
$\mathbf{B}$	Body load matrix
$\mathbf{b}$	Body load vector
$\hat{b}$	Body load arising from the shear deformation
$\tilde{b}$	Body load arising from the bending deformation
β	Slope of a bond
$\mathbf{C}$	Damping matrix
c	Bond constant
c_d	Damping coefficient
$\mathbf{D}$	Diagonal density matrix
D	Flexural rigidty
δ	Radius of a domain of influence
$\Delta\xi$	Spacing between two consecutive material points
Δt	Time step size
Δx	Distance between material points
E	Young's modulus
E_1	Young's modulus along the fiber direction
E_2	Young's modulus perpendicular to the fiber direction
$\dot{\mathbf{H}}_\mathbf{G}$	The rate of angular momentum
H	Failure parameter
$H_\mathbf{x}$	The domain of influence

$\underline{e}$	Extension scalar state
ε^d	Deviatoric part of strain tensor
$\boldsymbol{\eta}$	Relative displacement vector of two material points
$\mathbf{F}$	Total force acting on a rigid body
F_n	Contact force
$\mathbf{f}$	Pairwise force function
$\hat{f}$	Pairwise force function related with the shear deformation
$\tilde{f}$	Pairwise force function related with the bending deformation
Φ	Local damage
ϕ	Shear rotation of a material point
ϕ_c	Critical shear angle
φ	Orientation of a bond with respect to x axis
G	Energy release rate
G_I	Mode I energy release rate
G_{II}	Mode II energy release rate
G_{III}	Mode III energy release rate
G_c	Critical energy release rate
G_{Ic}	Mode - I critical energy release rate
G_{Ic}	Mode – I critical energy release rate
G_{IIc}	Mode – II critical energy release rate
G_{IIIc}	Mode – III critical energy release rate
Γ	Half wavelength
h	Thickness of the structure

$\mathbf{I}$	Identity matrix
I	Second moment of the cross sectional area
j	Member material point
$\mathbf{K}$	Stiffness matrix
K	Stress intensity factor
$\underline{\mathrm{K}}$	Double state
K_a	Crack arrest toughness
K_c	Crack initiation toughness
K_{Ia}	Crack arrest fracture toughness
K_{Ic}	Mode – I critical energy release rate
K_{IIIc}	Mode – III critical energy release rate
K_n	Contact stiffness
k	Main material point
k^2	Shear correction factor of a plate
κ	Bulk Modulus
κ_c	Critical curvature
$\boldsymbol{\xi}$	Relative position vector of two material points in the reference configuration
ξ	Distance between the material points
L	Lagrangian
λ	Decay constant
$\mathbf{M}$	Diagonal mass matrix
M	Moment loading
$\underline{\mathbf{M}}$	Deformed direction vector state
m	Weighted volume

μ	Shear Modulus
ν	Poisson's ratio
$\mathbf{\Omega}$	Angular velocity of the rotating axes
Ω	Nondimensional wave frequency
$\boldsymbol{\omega}$	Angular velocity of the rigid body
ω	Micropotential of a bond
$\underline{\omega}$	Spherical influence function
P	Pressure
p	Peridynamic pressure
Q	Shear loading
R	Standoff distance
ρ	Density
S	Surface correction
s	Stretch
s_c	Critical stretch
sf	Safety factor
$\boldsymbol{\sigma}$	Stress tensor
$\mathbf{T}$	Traction vector
$\underline{\mathbf{T}}$	Force vector state
T	Kinetic energy
$\mathbf{t}$	Force density vector of material point $\mathbf{x}$
$\mathbf{t}'$	Force density vector of material point $\mathbf{x}'$
$\underline{\mathbf{t}}$	Force density vector state
$\underline{t}$	Force scalar state
$\hat{t}$	Force density arising from the shear deformation

$\tilde{t}$	Force density arising from the shear deformation
t	Time
θ	Dilatation
$\mathbf{U}$	Displacement matrix
$\ddot{\mathbf{U}}$	Acceleration matrix
U	Potential energy
$\mathbf{u}$	Displacement vector
$\dot{\mathbf{u}}$	Velocity vector
$\ddot{\mathbf{u}}$	Acceleration vector
u_n	Penetration distance
V	Volume of a material point
W	Strain energy density function
w	Influence function
$\mathbf{x}$	Position vector of the main material point
$\mathbf{x}'$	Position vector of the member material point
$\underline{x}$	Magnitude of position vector in un - deformed configuration
$\mathbf{y}$	Deformed position vector of a material point
$\mathbf{y}'$	Un-deformed position vector of a material point
$\underline{y}$	Magnitude of position vector in deformed configuration
υ	Phase velocity of the wave
$\boldsymbol{\upsilon}_0$	Initial velcocity
ζ	Nondimensional wave number

Chapter 1

Introduction

1.1 General Perspectives

Peridynamic (PD) theory or Peridynamics (PDs) was first introduced by Dr. S. A. Silling at Sandia National Laboratories, USA. Peridynamics is a state-of the-art technique which is relatively new and promising tool. It is basically re-formulation of continuum mechanics theory introduced by the French mathematician Augustin Louis Cauchy more than 200 years ago and very suitable for failure analysis of structures due to its mathematical structure. It satisfies all the fundamental balance laws of classical (local) continuum mechanics; however, it is different in the sense that it is a nonlocal continuum theory which introduces an internal length parameter into the field equations. This internal length parameter defines the association among the material points within a finite distance through micropotentials. Removal of micropotentials between the material points allows damage initiation and growth through a single critical failure parameter regardless of the mixed-mode loading conditions. The creation of a new (crack) surface is based on a local damage measure. The local damage of a material point is defined as the ratio of the broken interactions to the total number of interactions.

Peridynamic equation of motion has a form of integro-differential equation rather than a partial differential equation as in the classical continuum mechanics (CCM) and so it allows the continuous usage of equations at the discontinuities like cracks. Although relatively new, it is successfully verified and utilized for modelling both metallic and composite structures (Madenci and Oterkus, 2014; Oterkus and Madenci, 2012; Oterkus et al., 2012). Hence, it is an excellent candidate to investigate complex problems in estimation of failure characteristics of materials and structures. As for the modelling of ship structures, PD results particularly advantageous with respect to CCM for the following reasons;

1. The governing equation of PD theory is in integral form and not partial differential equation form. As a consequence, the formulation remains valid everywhere regardless to the presence of discontinuities in the domain (e.g. cracks).
2. The concept of damage is naturally present in Peridynamics formulation. Therefore, there is no need for external crack growth criteria aimed to guide the crack or to specify its propagation behavior.
3. Various studies (Ha and Bobaru, 2010; Kilic, 2008; Madenci and Oterkus, 2014; Oterkus, 2010) have demonstrated that Peridynamics is a powerful tool for predicting complex material failure mechanisms such as crack nucleation, crack propagation, crack branching, coalition of multiple cracks and crack arrest.
4. There is no need computationally expensive re-meshing procedures in order to re-define the crack boundary.
5. In Peridynamic theory, there is no need for external equation aimed to treat the special case of material points located along interfaces.
6. Multiple physical fields can be treated within the same Peridynamic framework.
7. Peridynamics is equipped with a length-scale parameter called horizon, which allows to consider different length scales within the same domain, avoiding the burden of coupling different numerical tools (e.g. Finite Element Method at the macroscopic scale and Molecular Dynamics at the nanoscale). In other words, Peridynamic domain can be divided in regions where different length scales

are used. Hence, it can allow multi-scale analysis which bridges macro, micro, meso or nano scales.

Different versions of Peridynamics are currently available in literature. Bond-based Peridynamic theory (Silling, 2000) is the original version and it is often regarded as straightforward, easy to comprehend/implement. The improved version of the Peridynamic theory is named as ordinary based theory (Silling et al., 2007) and it removes restrictions of the former. As a consequence, bond-based PDs is the special form of ordinary based PD theory. Both theories will be discussed in Section 2.4.

1.2 Challenges

Progressive failure analysis of structures is still a major challenge in the literature. There exist various predictive techniques to tackle this challenge by using both classical (local) and nonlocal theories. Peridynamic (PD) theory (nonlocal) is very suitable for this challenge, but computationally costly with respect to the finite element method (FEM). However, Finite Element Analysis (FEA) with traditional elements suffers from the following shortcomings;

1. The interface between dissimilar materials is assumed to have zero thickness without any specific material properties; however, it presents a weak link and it is usually the location of failure. Therefore, it fails to appropriately model the interface between dissimilar materials.
2. Failure is a dynamic process, and it requires re-meshing. It is computationally costly, and the crack growth is guided based on the linear elastic fracture mechanics (LEFM) concepts. It breaks down when multiple complex crack growth patterns develop.
3. Stress and strain fields are discontinuous, and mesh refinement does not necessarily ensure accurate stress fields near geometric and material discontinuities.
4. Finally, crack initiation is not resolved. The analysis always requires a pre-existing crack.

However, in order to remedy or remove these shortcomings, Cohesive Zone Elements (CZE) and eXtended Finite Elements (XFEM) methods were developed. But, CZE method requires a priori knowledge of the crack path. In a complex analysis, it is not practical and the results are dependent on the mesh (structured or unstructured). Furthermore, the results are sensitive to the strength parameters in the traction-separation law of the cohesive zone model. Determination of these parameters poses additional uncertainties. Although XFEM removed such uncertainties, it still requires an external criteria for crack propagation. Thus, the results depend on the criteria employed in the analysis. It also breaks down when multiple complex crack growth patterns develop.

1.3 Advantages

The PD theory overcomes the weaknesses of the existing methods, and it is capable of identifying all of the failure modes without any additional assumptions. The PD methodology effectively predicts complex failure in complex structures under general loading conditions. Damage is inherently calculated in a PD analysis without special procedures, making progressive failure analysis more practical. An extensive literature survey on PDs is given in a recently published textbook by Madenci and Oterkus (2014). A comparison study between Peridynamics, CZE, and XFEM techniques is given by Agwai et al. (2011). They showed that the crack speeds obtained from all three approaches are on the same order; however, the fracture paths obtained by using Peridynamics are closer to experimental results with respect to other two techniques.

Another advantage of PD is its length-scale parameter, which does not exist in classical continuum mechanics. Such a length-scale parameter gives PD a nonlocal character. Hence, it allows the capture of physical phenomena not only at the macro-scale, but also at various other scales. This characteristic can be established through the PD dispersion relations. The classical theory is only valid for a special case of a long wavelength limit; however, the PD shows dispersion behavior similar to that observed in real materials. Hence, it is proven to be acceptable to perform multi-scale analysis simulations.

Moreover, PD theory does not only deal with mechanical field problems, in fact the equations can also be used to describe other fields such as the thermal diffusion (Bobaru and Duangpanya, 2010; Oterkus et al., 2014), moisture diffusion (Han et al., 2015), electric flow (Gerstle et al., 2008; S. Oterkus et al., 2013), porous flow (Katiyar et al., 2014) and corrosion (Oterkus et al., 2015), etc.

1.4 Objectives

PD theory is an excellent candidate to investigate complex problems such as the failure analysis of ship structures. As in the other theories, computational tools can be very suitable option for Peridynamic theory. However, one of the greatest challenge on implementing Peridynamic equations is the computational cost. Ships are big size structures and implementation of Peridynamics for these structures is not straightforward. In light of these, specific objectives of this study can be listed as;

1. Development of basic Peridynamic codes suitable for the problems of interest.
2. Performing validation studies against benchmark problems.
3. Implementing contact analysis capability within the Peridynamic codes.
4. Simulating ship-oriented problems in Peridynamic theory.
5. Comparisons of the results against available data found in the literature including experimental, analytical and numerical studies.
6. Investigating ways to reduce the computational time by introducing an updated Peridynamic formulations suitable for ship structures.

Overall, current study aims to develop Peridynamic codes suitable for the problems of interest of complex structures like ship structures. In a general sense, it may bring a new dimension contrary to the existing analytical and numerical modelling tools for the analysis of marine structures. The capability of proposed approaches will be demonstrated by considering various problem cases.

1.5 Novelty of the Thesis

This thesis has made novel and significant contributions to the current scientific literature, especially in the area of Peridynamic theory. Peridynamics is a new continuum theory and the number of available publications is rather limited with respect to other similar approaches. Moreover, the method uses non-conventional terminology which is mostly new to the researchers working in the area of structural mechanics. Hence, a new strategy has been followed to explain Peridynamics in simple terms by considering direct and indirect interactions.

There are currently two fundamental formulations of Peridynamics which were developed by Silling (2000); Silling et al. (2007) and Madenci and Oterkus (2014). Although the final outcomes of these two approaches appear to be similar, there are also some important differences in both the derivation of equations and the relationships between important Peridynamic parameters. These differences are relatively unknown to the scientific community and this thesis highlighted them in brief terms.

Although Peridynamics is a powerful technique in failure prediction, it is usually more computationally expensive with respect to some other techniques including finite element method. Therefore, any improvement in computationally efficiency will be very beneficial. In this thesis, a novel and efficient family member search algorithm is proposed.

As explained in Chapter 3 of the thesis, peridynamic theory is very suitable for parallel programming. However, some structures of interest such as ship structures can still be very challenging by using 3-Dimensional discretization strategies. Hence, it is essential to develop formulations for parts of the structure which can be simplified by making beam, plate and shell type idealizations. In this thesis, a novel Peridynamic formulation is developed for both Timoshenko and Mindlin plate formulations which take into account transverse shear deformations (Diyaroglu et al., 2015b; Diyaroglu et al., 2014; E. Oterkus et al., 2013). The approach is based on utilization of Lagrangian formulation and the unknown peridynamic parameters are determined by comparing against equations of classical continuum mechanics for a special case of the length

scale parameter, i.e. horizon, converging to zero. This approach can also be used for other idealized structures.

Since Peridynamic theory is a non-local continuum mechanics formulation, it is capable of capturing non-local effects which cannot be done by using classical formulation. This difference can easily be confirmed by determining wave dispersion characteristics (Oterkus et al., 2015). This information can also be used to determine the value of the length scale parameter. In this thesis, the wave dispersion characteristics of Timoshenko beam and Mindlin plate are derived for the first time in the literature (Diyaroglu et al., 2015b).

In addition to the traditional metallic materials, the usage of composite materials is increasing in many different areas. In order to model composite structures, an extended version of the original Peridynamic formulation is required. This can be achieved by strengthening the fiber direction interactions and introducing an efficient methodology for the interaction of neighbouring plies (Madenci and Oterkus, 2014). In this study, a novel underwater shock analysis of composite marine structures is performed and can be very beneficial to predict the response of various naval vessels including naval ships and submarines subjected to extreme loading conditions (Diyaroglu et al., 2015a; Diyaroglu et al., 2015). The numerical results are verified against experimental findings. Moreover, a novel shock wave Peridynamic formulation is proposed as a first step for a fully-coupled fluid structure analysis.

Finally, various improvements on contact analysis capability of Peridynamics are presented. This is especially important to perform collision and grounding analysis of ship structures. As mentioned earlier, peridynamics is fundamentally different with respect to classical theory which includes well-known finite element method (FEM). However, it is possible to implement Peridynamics within a commercial finite element (FE) software as explained in ref. (Macek and Silling, 2007). In this thesis, this approach is further extended by utilizing the currently existing contact analysis capability of the FE software.

1.6 Thesis Structure

This thesis proposes several ways to implement PD theory for complex structures, e.g. ship type of structures.

In Chapter 3, several solution methods to implement PD theory for complex structures, e.g. ship type of structures are proposed. The computational time can significantly be reduced by using correct method for the intended analysis because PD equations of motion are very suitable for parallel computing either by using a CPU (Central Processing Unit) and/or GPU - based (Graphics Processing Unit) architecture. Alternatively, the capability of already existing FE Software, e.g. ANSYS, can be exploited for modelling and solution purposes in PD theory. Furthermore, Peridynamic codes can be written in a more efficient way to reduce computational time.

However, modelling/analyzing very large and complex structures such as aerospace and marine vehicles can still be computationally demanding. Hence, it is necessary to utilize structural idealizations to make the computations feasible. Peridynamic (PD) theory was originally introduced for the solution of deformation field equations (Silling, 2000) without any structural idealizations. Hence, the existing beam/plate theories should be incorporated in Peridynamic framework in addition to solid type model. Chapter 4 presents PD equations of motions for structural idealizations such as beams and plates, while accounting for transverse shear deformations for them. Such structures can be the part of a ship. In the same chapter, PD dispersion relations, which represent wave propagation characteristics of materials, are presented and compared with classical theory. It is found that PD theory is also capable of capturing very well - known properties of real materials for very small wave lengths. Thus, this property of PDs allows the use of idealized structures in micro or nano scales, such as for nano packaging.

At the end, the last two chapters present PD models for marine structures applications.

Chapter 2

Literature Review

2.1 Introduction

The trend in ship and offshore building industry is to construct ever bigger structures by means of their sizes and as a result of this strength of material must be satisfied under several loading scenarios. Apart from strength, toughness of material has become an important issue for big structures and both must have acceptable limits. Unfortunately, the attainment of both of these properties is not a simple issue and there are several studies on this. Ritchie (2011) indicated strength-toughness relationships for several engineering materials (Figure 2.1) and which for new state-of-art materials, i.e. metallic glasses, metallic-glass composites, as well as future trends of materials (indicated as white arrow in Figure 2.1). In this study, it is concluded that both of these properties is related with several length scales, i.e. nano to macro scale, and one should consider the effect of different length scales on material behavior.

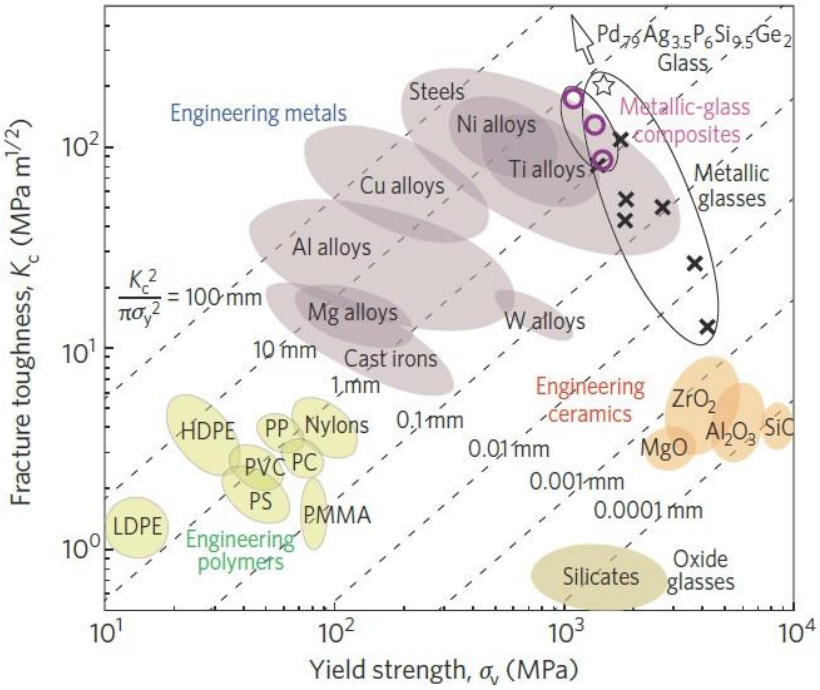

Figure 2.1 Conflicts of strength versus toughness (Ritchie, 2011)

Constructing ever bigger ship structures leads to the application of thicker steel plates in shipbuilding industry. Several attempts has been done in order to gain both strength and toughness of shipbuilding materials especially for thick steel plates. Recently, International Association of Classification Societies (2013) (IACS) has released new rule so-called "Requirement for Use of Extremely Thick Steel Plates" in January 2013. In this documentation, several requirements and recommendations are highlighted for the use of extremely thick steel plates, i.e. between 50mm and 100mm, concerning brittle fracture toughness and brittle crack arrest-ability.

It is also important to express some commonly used phrases of fracture, damage and failure in here. So, one may be aware of the differences between them. As a summary (Ramesh and Chandra, 2012), fracture is a breakage of atomic bonds and formation of internal surfaces in a material, damage can be all irreversible changes within the structure by energy dissipating mechanisms and failure can be regarded as inability of a structure to perform its functionality under several loading and/or environmental conditions. Damage also encompasses fracture but it may not lead to a final failure of a structure. As an example, small cracks need to interact with each other and accumulate to cause a final failure. Analysis of different damage mechanisms and their

interactions with each other, so called damage progressive analysis, play an important role on final failure of a system.

2.2 Fracture Toughness and Crack Growth

There are several parameters describing fracture toughness of materials like energy release rate (G), stress intensity factor (K), J – integral, crack tip opening displacement (CTOD) and crack tip opening angle (CTOA). These parameters are related with material behavior which can be linear elastic, non-linear elastic or elastic-plastic. While measuring and evaluating these parameters, proper test methods must be adopted. A detailed research reviewing these issues from past to state-of-art developments has been done by Zhu and Joyce (2012). Their review is based on American Society for Testing and Materials (ASTM) standards. Usually fracture tests give too conservative results when compared with actual structures. That is why Bayley and Aucoin (2013) examined fracture behavior of welded single edge notched tension specimen using constraints and loading conditions encountered by ship structures in service. They examined large scale samples of hull structural material. They developed crack mouth opening displacement (CMOD) - CTOD transfer function utilizing Finite Element Method (FEM) simulations of these samples and this leads to the determination of fracture toughness values. So, the fracture toughness values of non-standardized tests specimens can also be determined using the same procedure. On the other hand, while measuring fracture toughness values of thick steel plates, large test specimens and so large testing machine with huge expenditures are necessary. This issue addressed by Yajima et al. (2011) and they used small sized center-notched tension test specimen using steel plate thickness as the specimen width. They accomplished to evaluate fracture toughness of 70 mm thick steel plate using this specimen.

The relationship between microstructure of weld joints and fracture toughness was investigated by Leng et al. (2012). They performed several experiments including CTOD test, metallographic analysis and fracture surface analysis on high strength low alloy steel S335G10+N that is suitable for marine structures. Weld joints are subjected to different thermal cycles and experience crystallization and solid transformation

which lead to heterogeneity. So, samples from weld position (WP), fusion line (FL) and fusion line plus 2 mm (FL+2) are used in experiments. In their study, the average grain sizes of samples were measured and compared with the CTOD values that are listed in Table 2.1 and Table 2.2. It was observed that average grain size distribution is in agreement with CTOD values. The larger the CTOD is the smaller the average grain size will be.

Table 2.1 CTOD values (Leng et al., 2012)

Crack position	WP	WP	WP	FL	FL	FL	FL+2	FL+2	FL+2
Specimen	S3553	S3554	S3557	S3556	S35510	S35511	S3551	S3552	S3559
δ_u (mm)	0.583	0.455	0.623	0.596	0.531	-	-	0.837	0.714
δ_m (mm)	-	-	-	-	-	0.889	0.925	-	-
Mean value (mm)		0.554			0.672			0.825	

Table 2.2 Average grain sizes (Leng et al., 2012)

Sample number	S3557B	S3556B	S3559B
Average grain size	9.39	8.40	7.85

In fracture mechanics, crack arrest toughness (K_a) has also become an important parameter and it is to determine failure characteristics of materials along with crack initiation toughness (K_c). After crack initiation takes place, it is important to arrest its propagation in order to prevent failure or fracture of the related structure. In fatigue study field, crack arrest toughness and/or crack retardation effects are also investigated for failure characteristics of structures under several variations of loads, i.e. sea loadings. An et al. (2014) investigated crack arrest fracture toughness (K_{Ia}) characteristics of thick steel base material and its heat-input weld for 50 mm thick high strength shipbuilding steel. They concluded that K_{Ia} is a linear function of temperature. In their experiments, while base material (BM) satisfied IACS (2013) rule, this was not the case for the weld material. In addition, they obtained straight crack propagation path along the fusion line (FL) of weld and that is why some investigation of the material properties of the path, i.e. grain size, hardness, Charpy impact energy, was carried out and it is found that localized degradation of materials' strength and toughness in the impact notch region of the experimental setup can be the cause of it. One can see that it is also important to obtain satisfactory fracture toughness

values for weld joints of ship structures. Moon et al. (2013) carried out several experiments to obtain CTOD values of API 2W Gr.50 steel at welds and its heat affected zone (HAZ) using two types of welding, submerged arc welding (SAW) and flux cored arc welding (FCAW). Apart from a utilization of the crack initiation and arrest toughnesses, the crack tip opening displacement (CTOD) is a commonly used parameter for evaluating fracture toughness of structures in fracture mechanics. It can be related with *J* integral using plastic constraint factor, *m*, as

$$J = m \cdot \sigma_y \cdot \delta \tag{2.1}$$

where δ is CTOD value. From several experiments of two types of welding they concluded that plastic constraint factor based on the American Society for Testing and Materials (ASTM) standard, E1820, does not include the effect of weld process and it is too conservative. They also carried out Charpy impact and hardness tests of SAW and FCAW welding process and compared them with each other. They concluded that CTOD values have similar tendency with impact energy and hardness results.

A comprehensive research has been made by Japan Ship Technology Research Association (JSTRA) to prevent failure in large container ships and the results are published by Sumi et al. (2013). They mainly focused on initiation of brittle crack, fatigue crack growth under several sea loading conditions and investigated crack arrest designs in deck structure of large container ships for thickness range of 50 – 75 mm steel plates. It is emphasized that allowable initial defects in the weld joints can grow in critical sizes and may cause brittle fracture. They also referred to guidelines published by ClassNK on Brittle Crack Arrest Design for countermeasures of brittle crack propagation. It has also shown that the most reliable method to prevent crack propagation along welded joints is a weld line shift shown in Figure 2.2.

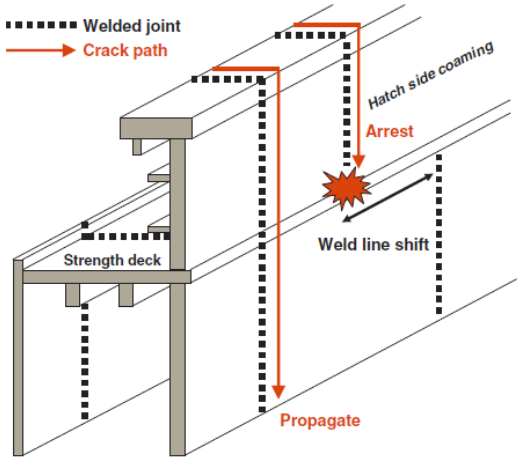

Figure 2.2 Concept of weld line shift (Sumi et al., 2013)

A more detailed research on fatigue crack growth has been done by Sumi (2014a) considering same locations and thickness range of container ships. In this research, the fatigue crack growth is simulated using two models namely the crack growth model based on ΔK_{RP} and the simple crack growth model, i.e. Paris-Elber law, with random sequence of clustered loading, so-called storm model. Fatigue lives of ΔK_{RP} criterion were found 2-3 times longer than the simple method. Because the retardation and acceleration effects cannot be considered with the latter one which does not properly take into account the increase of the plastic wake (Figure 2.3). Crack growth model based on ΔK_{RP} is basically defined by Equation (2.2) and please refer to (Toyosada et al., 2004) for detailed discussion.

$$da / dN = C\left(\Delta K_{RP}\right)^m \tag{2.2}$$

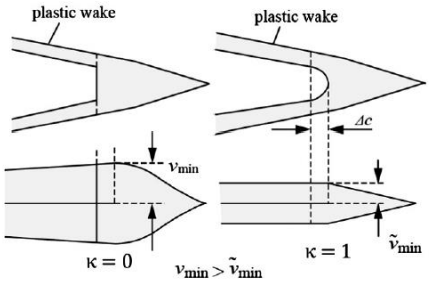

Figure 2.3 Formation of plastic wake during fatigue crack growth (Sumi, 2014b)

In the same paper, the effect of a slam-induced whipping stress on fatigue crack growth is also investigated since the longer marine structures mean more slam-induced vibratory stresses considering its flexible body. It is concluded that M-series specimens may be used in order to estimate fatigue crack propagation life under whipping stress. But still further studies are needed on this area.

Quéméner et al. (2013) made fatigue crack evaluation of stiffened plate longitudinal elements located at bottom and deck regions of ships where critical bending stresses occur. First, critical crack lengths were evaluated for extreme bending moments which represent fracture resistance of members based on actual CTOD values and these critical lengths correspond to end of fatigue life of each component for which fatigue crack propagation becomes unstable. Another fatigue crack evaluation study for longitudinal elements of ship structures has been done by Wengang and Jonas (2013). They considered an effective method for fatigue crack propagation which is based on the narrow band spectral fatigue method and it is validated with full scale measurements of 2800 TEU container ship. In general, ships are subjected to several cyclic loads during the service life and it is hard to expect occurrence frequency of these loads. Additionally, other uncertainties such as residual stresses from manufacturing, corrosion, weld defects etc. can also make difficulties in fatigue analysis. So, it is highly probable that fatigue cracks may occur earlier than the expected. Different approaches are applied for fatigue strength assessment of ship structures. Fricke et al. (2012) performed several tests using two types of structures, i.e. web frame corners and the intersection between longitudinals and transverse web frames, under several loading conditions. All available techniques were applied to these models and they investigated both large and small scale specimens experimentally and numerically. In their analysis, fabrication-related conditions, welding induced pre-deformations and residual stresses were all included. At the end, strength behaviors of chosen complex welded structures were summarized.

Mechanical properties of materials such as fracture toughness, strength and fatigue life can be improved with several techniques. In this respect, Rubio-González et al. (2011) studied duplex stainless steels which are used in different fields including ship industry. These steels have high strength and excellent fracture toughness as well as high corrosion resistance. They investigated relatively new laser shock processing

(LSP) technique and its effects on mechanical properties of these steels. It has already known that LSP technique especially increases fatigue crack initiation life and reduces fatigue growth rate of materials. This work confirmed that application of LSP on 2205 duplex steel improved fatigue properties and no effect has been found on micro-hardness and microstructure of material but improvement of fracture toughness was reported. Kim et al. (2012) studied mechanical properties of adhesive joints which used to join stainless steel sheets. Stainless steel sheets have been used at cryogenic temperature of -150°C for their relatively high mechanical and low coefficient of thermal expansion (CTE) properties in containment system of LNG ships. But adhesives of steel sheets become quite brittle at that temperature and need to be reinforced to improve fracture toughness values. In this study the film-type epoxy adhesive was reinforced with randomly oriented aramid fiber mats. As fracture toughness values are influenced by mechanical properties as well as thermal residual stresses, both properties are investigated. It was found that aramid fibers could reduce the thermal residual stresses between the stainless steel and adhesive layer. Optimum volume fraction of the aramid fiber mats was found as 16.3% from double cantilever beam (DCB) tests of the adhesive joint. It was concluded that the adhesive reinforced with aramid fiber mat has higher load-carrying capacity and fracture toughness at cryogenic temperature of -150°C than those of other choices such as polyester or glass fiber mats. Liquefied natural gas (LNG) ship's containment system is mainly composed of dual barriers and insulation board. The insulation board must be reliable against leakage of LNG and have high thermal insulation performance. The reliability of insulation board considering sufficient fracture toughness at cryogenic temperature of -163°C was studied by Yu et al. (2013). Conventionally, the polyurethane foam (PUF) reinforced with glass fiber (RPUF) is used for insulation board to increase fracture toughness. This implementation not only increases costs but also decreases thermal insulation characteristics. As a result, the volume fraction of a glass fiber is restricted to less than 0.5% and the sufficient fracture toughness is uncertain. This uncertainty can possibly lead to crack propagation in insulation board and induce leakage of LNG. Cracks usually initiate and propagate as a result of local tensile stress concentrations due to the temperature change. In this study, crack resistance of insulation board is increased with reinforcement of glass fiber polymer composite in

selective areas which have high stress concentrations. Mainly glass fiber reinforcement sustains high thermal stresses by high stiffness property. The tensile failure strengths of both conventional RPUF system and glass composite reinforcement were measured and safety factor of the latter one is calculated as 42% higher than the former by

$$\text{Safety factor} = \frac{\text{Failure strength of insulation board}}{\text{Average thermal stress on insulation board}} \tag{2.3}$$

2.3 Marine Composites

Marine structures must be built to have sufficient strength under several loading scenarios and varying environment conditions e.g. moisture, temperature and so. It is also important to minimize weight without any compromise to strength of structure. The optimization procedures for high strength and lightweight structures revealed that composite structures are the best way out. Apart from strength, toughness is also an important quantity for engineering structures and ensures high load bearing capacity for them. So, the future trend is to build both strong and tough structures. Unlike brittle materials, tough materials are high damage tolerable and so catastrophic failure does not occur. Composites are very complex structures because they are composed of combination of several constituent materials while each of which keeping its own property. The behavior of composite structures depends on their constituent materials as well as geometry, loading and environment conditions. So it is possible to build such composite structures both providing high strength and toughness values like metallic-glass composites in ref. (Ritchie, 2011) as well as lightness. Sandwich composite structures may take the stage on this part because they have ability to provide lightness in addition to strength and toughness especially for big structures like ships and aero planes.

2.3.1 Failure modes

In general, engineering structures are exposed to several loadings under different service conditions. So, cracks, which already exist in imperfect materials or emerge spontaneously in macro/micro or nano scales, propagate in the most energy favorable direction. It is generally accepted that there are fundamental loading conditions for an

already existing crack in the material and they are named as mode I-II and III loadings as shown in Figure 2.4. Although they are very fundamental and distinctive, in reality, they appear as combinations of those so called mixed mode loadings. The most common mixed mode loadings are mode I-II and mode I-III.

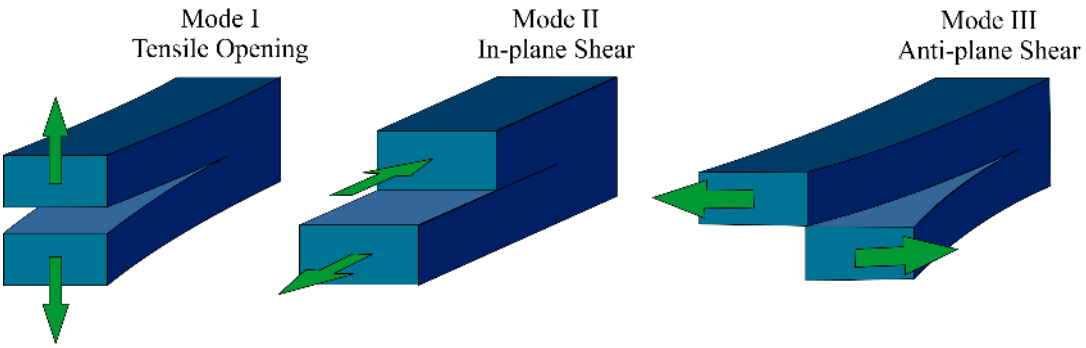

Figure 2.4 Loading types

Many experimental studies have been conducted in order to investigate crack propagation behaviors in isotropic, orthotropic or composite materials (Araki et al., 2005; Benzeggagh and Kenane, 1996; Farshad and Flüeler, 1998; Hashemi et al., 1990). In those, the most common experiments are the mode I double cantilever beam (DCB) test, mode II end loaded split (ELS) test, mode II end notched flexure (ENF) test and mixed mode bending (MMB) test (Figure 2.5).

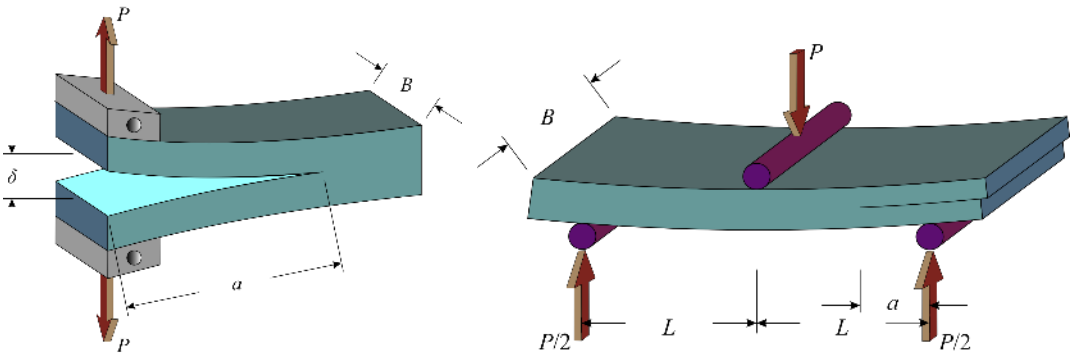

a) DCB test b) ENF test

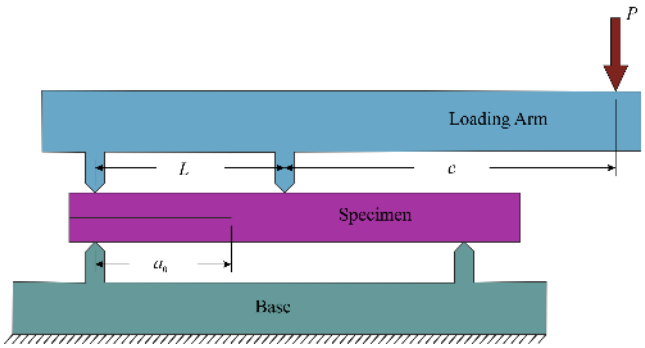

c) MMB test

Figure 2.5 Test methods

As generally excepted, cracks propagate in mode I loading direction for isotropic materials (Griffith, 1921; Melin, 1991; Nuismer, 1975), i.e. Figure 2.6, however, this is not the case for more complex composite structures. Because cracks are usually constrained between plies in resin reach layers and they are forced to propagate through these layers.

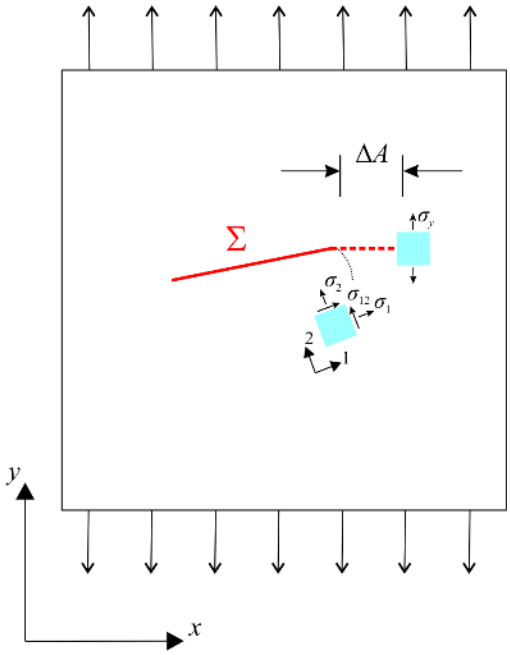

Figure 2.6 Crack propagation direction

Researchers commonly use critical energy release rate (G_c) in order to determine fracture toughness and to investigate crack initiation, propagation characteristics of materials under several loading conditions (Charalambides et al., 1992; LEE, 1997; O'Brein, 1997; Williams, 1988). It is basically the estimation of amount of work that

is available for generating new crack surfaces within the bulk material. Three main loading conditions are related with three components of energy release rate, i.e. G_I; G_{II}; G_{III}, and those can be expressed in terms of stress intensity factors as

$$G_m = \alpha_m K_m^2 \qquad m = I, II, III \tag{2.4}$$

where α_m is a parameter depending on material constants. The Griffith failure criterion states that the fracture occurs when the sum of the energy release rates exceeds critical energy release rate, G_c. So, it is apparent that G_c is the material parameter.

2.3.1.1 Composite failure

In order to decrease the weight of marine structures, there is significant interest in replacing traditional metallic designs with composite materials. By doing so, it must be ensured that composite materials must show high resistance to extreme loading conditions. Failure behavior of composites are quite complex and can occur in different modes including fiber breakage, matrix cracking, fiber/matrix debonding and delamination. These failure modes can also be classified as

I. Interlaminar failure: Progressive disbond of plies within the laminated stack. They are commonly denoted as delamination.
II. Intralaminar failure: Formation of in-plane cracks, parallel to the reinforcement direction. These are often denoted as ply splits.
III. Translaminar cracks: Tensile or compressive failure of the reinforcement fibers.

and they can be seen in Figure 2.7.

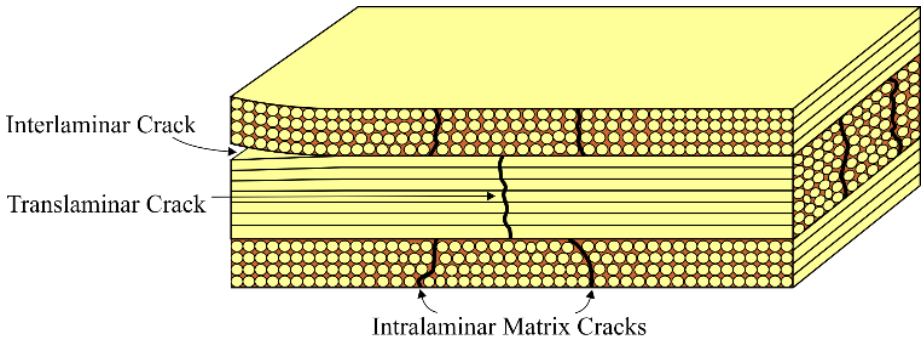

Figure 2.7 Failure modes in composite structures

2.4 Peridynamic Theory

2.4.1 Introduction

Peridynamic (PD) theory was first introduced by Silling (2000) at Sandia National Laboratories and it was structured as an extended version of classical theory. In classical continuum mechanics (CCM) theory, which is introduced by French mathematician Augustin Louis Cauchy, only neighboring interactions of an infinitesimal volume is considered with traction vectors, **T**, and PD theory further incorporates distant interactions, **t** and **t′**, in the most general sense. The length scale, which is termed as horizon, available in the theory designates extent of such interactions and classical theory can be recovered as it approaches to zero. Please see the Figure 2.8 for a comparison purpose.

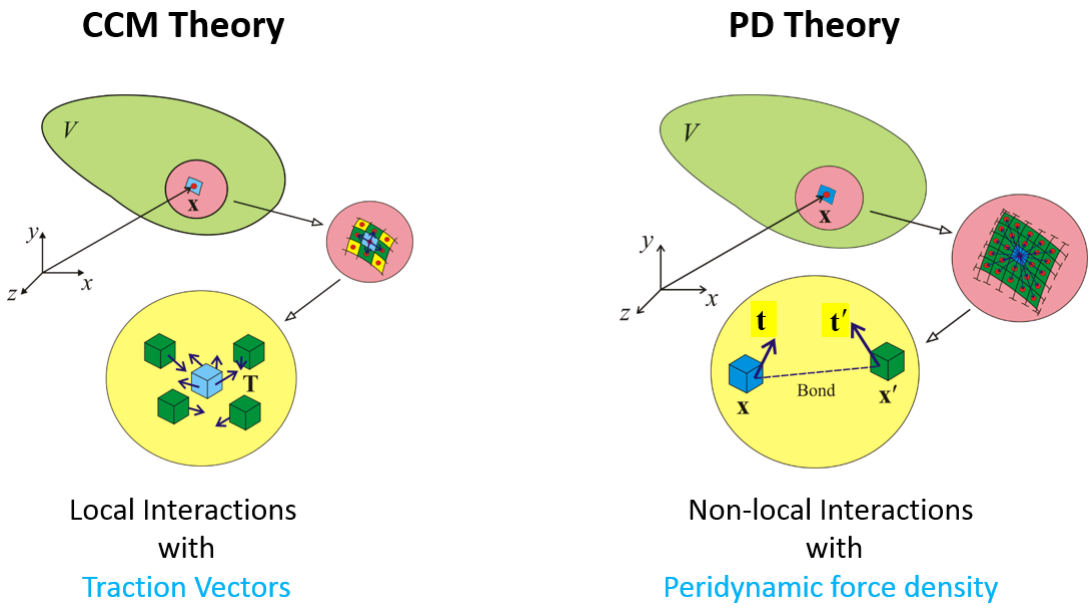

Figure 2.8 Comparison of CCM theory and PD theory

The most remarkable property of PD theory is that the equation of motion (EOM) does not include any spatial derivatives as in CCM theory and in other nonlocal theories such as the Eringen's nonlocal elasticity theory (Eringen, 1972). As a result of this, PD theory has several advantages against local, i.e. CCM, and other nonlocal theories. In fracture mechanics sense, PD theory is especially promising tool for failure analysis of structures because the formulation is valid everywhere regardless of the presence of discontinuities in the domain and it does not need any external crack growth criteria to

predict when and where the crack propagates. As a consequence, Peridynamics is a very powerful tool for predicting complex material failure mechanisms such as crack nucleation, crack propagation, crack branching, coalition of multiple cracks and crack arrest. This capability of Peridynamics has already been demonstrated in refs. (Madenci and Oterkus, 2014; Oterkus and Madenci, 2012; Oterkus et al., 2012) with various benchmark problems both for isotropic and anisotropic materials.

As mentioned above, when PDs was first introduced by Silling (2000), the fundamental idea beneath it was to replace spatial derivatives of stresses from the equation of motion of CCM theory (Equation (2.5)) with an integral term.

$$\rho(\mathbf{x})\ddot{\mathbf{u}}(\mathbf{x},t) = \boldsymbol{\sigma}_{ij,j} + \mathbf{b}(\mathbf{x},t) \qquad i\ \&\ j = 1,2,3 \tag{2.5}$$

in which comma sign represents differentiation in space. So, the new form of equation of motion is given by

$$\rho(\mathbf{x})\ddot{\mathbf{u}}(\mathbf{x},t) = \int_{H_x} \left(\mathbf{t}(\mathbf{x}'-\mathbf{x},\mathbf{u}'-\mathbf{u}) - \mathbf{t}'(\mathbf{x}-\mathbf{x}',\mathbf{u}-\mathbf{u}')\right) dH_x + \mathbf{b}(\mathbf{x},t) \tag{2.6}$$

where ρ and **x** represent the density and position vector of the main material point in the undeformed configuration, respectively and *t* represents the time. By doing so, the solution procedure of discontinuities or cracks as well as representation of interfaces of different materials become no more challenging because they are already included in the nature of PD formulation. As in the CCM theory, the body is partitioned into many infinitesimal volumes and each volume is named as material point in Peridynamics. The main material point, **x**, which is a variable in acceleration term in the left hand side of Equation (2.6), interacts with other material points, **x′**, named as family members of material point **x**, inside its domain of influence. Each interaction is referred as a bond in Peridynamics. The domain of influence, which is called horizon, *H*, is a sphere in three-dimensional body and its radius is denoted by δ. It is assumed that the material point **x** cannot see beyond its horizon (Silling and Askari, 2005).

2.4.2 The most general sense of Peridynamic theory

Equation of motion of one material point can be derived by getting benefit of principle of virtual work as is done by Madenci and Oterkus (2014) in Peridynamic theory. When the body is deformed, each interaction or bond in PDs gains energy, which is called micropotential. Micropotential, ω, of a bond is composed of two components as

$$\omega_{(k)(j)} = \omega_{(k)(j)}(\mathbf{y}_{(1^k)} - \mathbf{y}_{(k)}, \mathbf{y}_{(2^k)} - \mathbf{y}_{(k)}, ...) \tag{2.7}$$

$$\omega_{(j)(k)} = \omega_{(j)(k)}(\mathbf{y}_{(1^j)} - \mathbf{y}_{(j)}, \mathbf{y}_{(2^j)} - \mathbf{y}_{(j)}, ...) \tag{2.8}$$

where **y** denotes the deformed position vector of a material point. $\omega_{(k)(j)}$ originates from every material point that interacts with the material point *k* and $\omega_{(j)(k)}$ originates from every material point that interacts with the material point *j* in a body. These interactions or bonds and micropotentials can be seen from Figure 2.9a. Micropotentials depend on material properties and relative positions of material points after deformation. Micropotential of a bond can be assumed as the average of those

$$\omega = \frac{1}{2}\left(\omega_{(k)(j)} + \omega_{(j)(k)}\right) \tag{2.9}$$

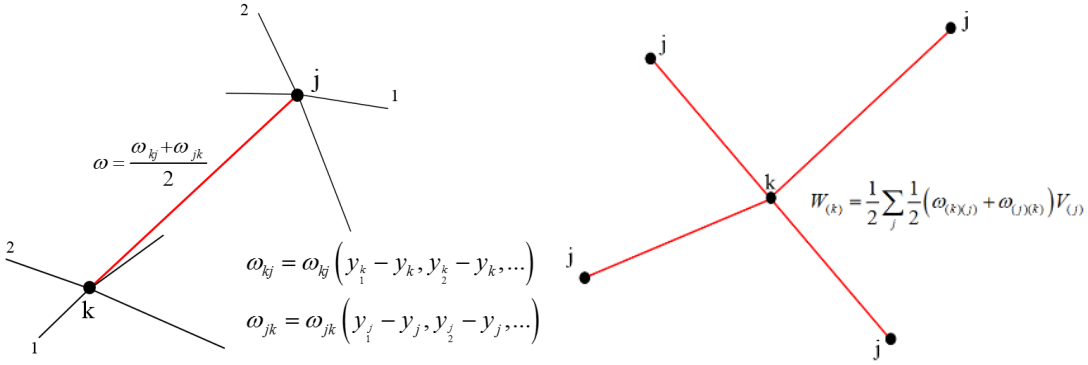

a) Micropotential of a bond

b) Strain energy density from micropotentials

Figure 2.9 Micropotentials

Strain energy density function of a material point *k* is then found by summation of micropotentials of all bonds connected to that point as can be seen in Figure 2.9b and it is expressed as

$$W_{(k)} = \frac{1}{2}\sum_{j}\frac{1}{2}\left(\omega_{(k)(j)} + \omega_{(j)(k)}\right)V_{(j)} \tag{2.10}$$

where $V_{(j)}$ is the volume of each member material point, *j*. Here, it is assumed that the material point *k* owns only half of the energy of bonds. In Peridynamic point of view, the potential energy of a body, which is composed of many material points (Figure 2.10), can be expressed as the summation of strain energies of all material points in a body minus the total energy of external loads

$$U = \sum_{k} W_{(k)}V_{(k)} - \sum_{k}\mathbf{b}_{(k)}.\mathbf{u}_{(k)}V_{(k)} \tag{2.11}$$

where $\mathbf{b}_{(k)}$ denotes the body load on a material point *k* and $\mathbf{u}_{(k)}$ is the displacement vector of a material point *k*. Also, kinetic energy of a body can easily be expressed as

$$T = \sum_{k}\frac{1}{2}\rho_{(k)}\dot{\mathbf{u}}_{(k)}.\dot{\mathbf{u}}_{(k)}V_{(k)} \tag{2.12}$$

in which $\rho_{(k)}$ represents density of the material point *k*.

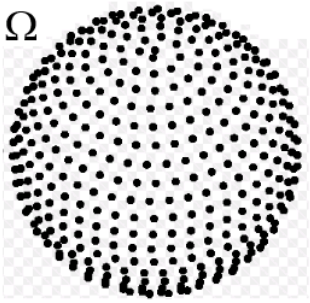

Figure 2.10 Body composed of many material points

After determining the potential and the kinetic energies of a body, the EOM of one material point can be obtained by using principle of virtual work. The principle of virtual work states that the body must have a stationary point in time whenever the variations of Lagrangian (*L*) is equal to zero (Equation (2.13)). Here, the Lagrangian is basically the difference between the kinetic and potential energies, i.e. $L = T - U$.

$$\delta \int_{t_0}^{t_1} L dt = 0 \tag{2.13}$$

Following the calculus of variations, Lagrange's equation of motion is obtained as

$$\frac{d}{dt}\left(\frac{\partial L}{\partial \dot{\mathbf{u}}_{(k)}}\right) - \frac{\partial L}{\partial \mathbf{u}_{(k)}} = 0 \tag{2.14}$$

Substituting Equations (2.11) and (2.12) into Equation (2.14) results in equation of motion of material point *k* in terms of micropotentials (please see the ref. (Madenci and Oterkus, 2014), pg. 24 - 26 for the detailed derivation procedure) as

$$\rho_{(k)}\ddot{\mathbf{u}}_{(k)}V_{(k)} + \frac{1}{2}\sum_j \left\{ \begin{array}{l} \dfrac{\partial \omega_{(k)(j)}\left(\mathbf{y}_{1^k} - \mathbf{y}_k\right)}{\partial(\mathbf{y}_{(i)} - \mathbf{y}_{(k)})} \dfrac{\partial(\mathbf{y}_{(i)} - \mathbf{y}_{(k)})}{\partial \mathbf{u}_k} V_{(j)} + \\ \dfrac{\partial \omega_{(k)(j)}\left(\mathbf{y}_{2^k} - \mathbf{y}_k\right)}{\partial(\mathbf{y}_{(i)} - \mathbf{y}_{(k)})} \dfrac{\partial(\mathbf{y}_{(i)} - \mathbf{y}_{(k)})}{\partial \mathbf{u}_k} V_{(j)} + \dfrac{\partial \omega_{(k)(j)}\left(\mathbf{y}_{3^k} - \mathbf{y}_k\right)}{\partial(\mathbf{y}_{(i)} - \mathbf{y}_{(k)})} \dfrac{\partial(\mathbf{y}_{(i)} - \mathbf{y}_{(k)})}{\partial \mathbf{u}_k} V_{(j)} + \ldots \end{array} \right\} V_{(k)}$$

$$+ \frac{1}{2}\sum_j \left\{ \begin{array}{l} \dfrac{\partial \omega_{(j)(k)}\left(\mathbf{y}_{1^j} - \mathbf{y}_j\right)}{\partial(\mathbf{y}_{(k)} - \mathbf{y}_{(i)})} \dfrac{\partial(\mathbf{y}_{(k)} - \mathbf{y}_{(i)})}{\partial \mathbf{u}_k} V_{(j)} + \\ \dfrac{\partial \omega_{(j)(k)}\left(\mathbf{y}_{2^j} - \mathbf{y}_j\right)}{\partial(\mathbf{y}_{(k)} - \mathbf{y}_{(i)})} \dfrac{\partial(\mathbf{y}_{(k)} - \mathbf{y}_{(i)})}{\partial \mathbf{u}_k} V_{(j)} + \dfrac{\partial \omega_{(j)(k)}\left(\mathbf{y}_{3^j} - \mathbf{y}_j\right)}{\partial(\mathbf{y}_{(k)} - \mathbf{y}_{(i)})} \dfrac{\partial(\mathbf{y}_{(k)} - \mathbf{y}_{(i)})}{\partial \mathbf{u}_k} V_{(j)} + \ldots \end{array} \right\} V_{(k)} - \mathbf{b}_{(k)}V_{(k)} = 0 \tag{2.15}$$

or in a more compact form

$$\begin{aligned} &\rho_{(k)}\ddot{\mathbf{u}}_{(k)}V_{(k)} + \frac{1}{2}\sum_j \sum_i \frac{\partial \omega_{(k)(j)}}{\partial(\mathbf{y}_{(i)} - \mathbf{y}_{(k)})} V_{(j)} \frac{\partial(\mathbf{y}_{(i)} - \mathbf{y}_{(k)})}{\partial \mathbf{u}_k} V_{(k)} + \\ &\frac{1}{2}\sum_j \sum_i \frac{\partial \omega_{(j)(k)}}{\partial(\mathbf{y}_{(k)} - \mathbf{y}_{(i)})} V_{(j)} \frac{\partial(\mathbf{y}_{(k)} - \mathbf{y}_{(i)})}{\partial \mathbf{u}_k} V_{(k)} - \mathbf{b}_{(k)}V_{(k)} = 0 \end{aligned} \tag{2.16}$$

In Equation (2.16), additional summation functions related with the material point *i* comes from the chain rule of differentiation as

$$\frac{\partial \omega_{(k)(j)}}{\partial \mathbf{u}_k} = \sum_i \frac{\partial \omega_{(k)(j)}}{\partial\left(\mathbf{y}_{(i)} - \mathbf{y}_{(k)}\right)} \frac{\partial\left(\mathbf{y}_{(i)} - \mathbf{y}_{(k)}\right)}{\partial \mathbf{u}_k} \tag{2.17}$$

Since $\omega_{(k)(j)}$ is composed of deformations of all bonds that are connected to the material point *k*, i.e. $\left(\mathbf{y}_i - \mathbf{y}_k\right)$, Equation (2.7) can be written in a slightly different form as

$$\omega_{(k)(j)} = \omega_{(k)(j)}(\sum_i \mathbf{y}_{(i)} - \mathbf{y}_{(k)}) \tag{2.18}$$

The same is also true for micropotential $\omega_{(j)(k)}$ as follows

$$\frac{\partial \omega_{(j)(k)}}{\partial \mathbf{u}_k} = \sum_i \frac{\partial \omega_{(j)(k)}}{\partial\left(\mathbf{y}_{(k)} - \mathbf{y}_{(i)}\right)} \frac{\partial\left(\mathbf{y}_{(k)} - \mathbf{y}_{(i)}\right)}{\partial \mathbf{u}_k} \tag{2.19}$$

and from Equation (2.8)

$$\omega_{(j)(k)} = \omega_{(j)(k)}(\sum_i \mathbf{y}_{(i)} - \mathbf{y}_{(j)}) \tag{2.20}$$

Comparing Equations (2.19) and (2.20), an interesting inference can be done which is

$$\omega_{(j)(k)}(\sum_i \mathbf{y}_{(i)} - \mathbf{y}_{(j)}) = \omega_{(j)(k)}(\sum_i \mathbf{y}_{(k)} - \mathbf{y}_{(i)}) \tag{2.21}$$

The similar observation can also be obtained with the following derivations. Let us change the order of summation indices in Equation (2.16)

$$\begin{aligned} &\rho_{(k)}\ddot{\mathbf{u}}_{(k)} + \frac{1}{2}\sum_j \sum_i \frac{\partial \omega_{(k)(i)}}{\partial(\mathbf{y}_{(j)} - \mathbf{y}_{(k)})} V_{(i)} \frac{\partial(\mathbf{y}_{(j)} - \mathbf{y}_{(k)})}{\partial \mathbf{u}_k} \\ &+ \frac{1}{2}\sum_j \sum_i \frac{\partial \omega_{(i)(k)}}{\partial(\mathbf{y}_{(k)} - \mathbf{y}_{(j)})} V_{(i)} \frac{\partial(\mathbf{y}_{(k)} - \mathbf{y}_{(j)})}{\partial \mathbf{u}_k} - \mathbf{b}_{(k)} = 0 \end{aligned} \tag{2.22}$$

and in a more simplified form, it is expressed as

$$\begin{aligned} &\rho_{(k)}\ddot{\mathbf{u}}_{(k)} - \frac{1}{2}\sum_j \sum_i \frac{\partial \omega_{(k)(i)}}{\partial(\mathbf{y}_{(j)} - \mathbf{y}_{(k)})} V_{(i)} \\ &+ \frac{1}{2}\sum_j \sum_i \frac{\partial \omega_{(i)(k)}}{\partial(\mathbf{y}_{(k)} - \mathbf{y}_{(j)})} V_{(i)} - \mathbf{b}_{(k)} = 0 \end{aligned} \tag{2.23}$$

Above equation may also be expressed in a slightly different form with introducing force density vectors, $\mathbf{t}_{(k)(j)}$ and $\mathbf{t}_{(j)(k)}$, as

$$\rho_{(k)}\ddot{\mathbf{u}}_{(k)} = \sum_j (\mathbf{t}_{(k)(j)} - \mathbf{t}_{(j)(k)})V_{(j)} + \mathbf{b}_{(k)} \tag{2.24}$$

This equation is the very well-known Peridynamic equation of motion in the most general sense and it can also be called as non - ordinary state based PD theory. Here, the force densities can be written explicitly as

$$\mathbf{t}_{(k)(j)} = \frac{1}{2}\frac{1}{V_{(j)}}\sum_i \frac{\partial \omega_{(k)(i)}}{\partial(\mathbf{y}_{(j)} - \mathbf{y}_{(k)})}V_{(i)} = \frac{1}{V_{(j)}}\frac{\partial\left(\frac{1}{2}\sum_i \omega_{(k)(i)}V_{(i)}\right)}{\partial(\mathbf{y}_{(j)} - \mathbf{y}_{(k)})} \tag{2.25}$$

and

$$\mathbf{t}_{(j)(k)} = \frac{1}{2}\frac{1}{V_{(j)}}\sum_i \frac{\partial \omega_{(i)(k)}}{\partial(\mathbf{y}_{(k)} - \mathbf{y}_{(j)})}V_{(i)} = \frac{1}{V_{(j)}}\frac{\partial\left(\frac{1}{2}\sum_i \omega_{(i)(k)}V_{(i)}\right)}{\partial(\mathbf{y}_{(k)} - \mathbf{y}_{(j)})} \tag{2.26}$$

As shown in Figure 2.11, it is understood that the force density vectors of a bond, i.e. $\mathbf{t}_{(k)(j)}$ and $\mathbf{t}_{(j)(k)}$, result from summation of all bonds' micropotentials that are connected to the material point *k* and its differentiations with respect to the deformation of a bond which is in question, i.e. bond *k*-*j*. Furthermore, force densities can be in any direction with different magnitudes.

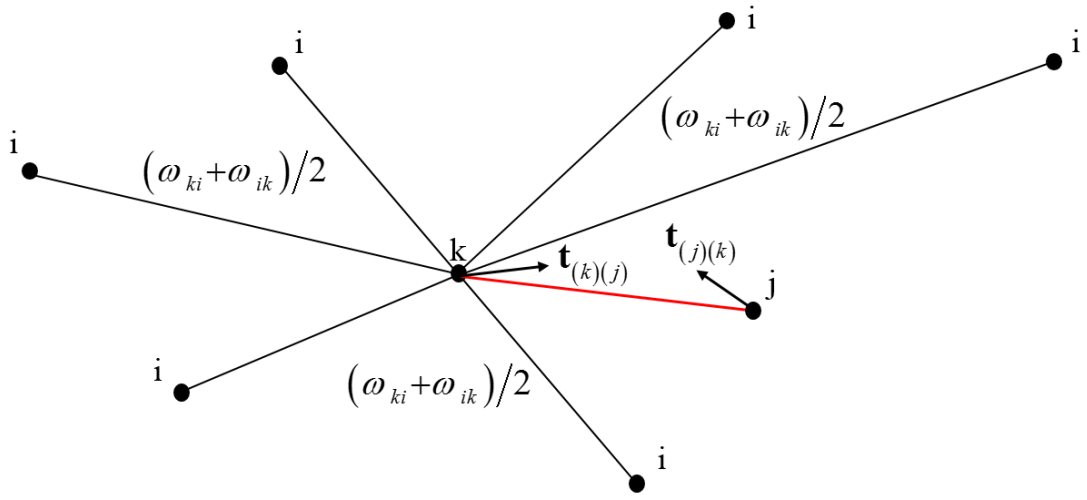

Figure 2.11 Force densities of a bond

Equations (2.25) and (2.26) can also be expressed by means of strain energy densities of material points *k* and *j*, i.e. $W_{(k)}$ and $W_{(j)}$ respectively, as

$$\mathbf{t}_{(k)(j)} = \frac{1}{V_{(j)}} \frac{\partial W_{(k)}}{\partial \left(\mathbf{y}_{(j)} - \mathbf{y}_{(k)} \right)} \quad \text{and} \quad W_{(k)} = \frac{1}{2} \sum_i \omega_{(k)(i)} V_{(i)} \tag{2.27}$$

in which $\mathbf{t}_{(k)(j)}$ is the force density, that material point j exerts on material point k.

$$\mathbf{t}_{(j)(k)} = \frac{1}{V_{(j)}} \frac{\partial W_{(j)}}{\partial \left(\mathbf{y}_{(k)} - \mathbf{y}_{(j)} \right)} \quad \text{and} \quad W_{(j)} = \frac{1}{2} \sum_i \omega_{(i)(k)} V_{(i)} \tag{2.28}$$

in which $\mathbf{t}_{(j)(k)}$ is the force density, that material point k exerts on material point j. Strain energy density at material point j, $W_{(j)}$, can also be expressed in a different form as similar to strain energy density at material point k, $W_{(k)}$, i.e. Equation (2.27), as

$$W_{(j)} = \frac{1}{2} \sum_i \omega_{(j)(i)} V_{(i)} \quad \text{and} \quad \mathbf{t}_{(j)(k)} = \frac{1}{V_{(k)}} \frac{\partial W_{(j)}}{\partial \left(\mathbf{y}_{(k)} - \mathbf{y}_{(j)} \right)} \tag{2.29}$$

Thus, equating Equations (2.28) and (2.29) leads to the important inference that

$$\sum_i \omega_{(i)(k)} V_{(i)} = \sum_i \omega_{(j)(i)} V_{(i)} \tag{2.30}$$

Also be aware of the similarity of Equations (2.21) and (2.30). The inferred Equation (2.30) can have several physical meanings. Firstly, this equality is shown in Figure 2.12 to make the understanding more physical. Here, bond $k - j$, which is in red color, is in question and its force densities depend on many other interactions as well. Now, let us introduce the horizon to a current theory in order to make the PD formulation simpler, cf. Figures 2.11 and 2.12. In Figure 2.12, the horizons of the material points k, j and i are shown and it is already mentioned in Section 2.4.1 that the material points outside the horizon region cannot see each other. However, in a more general sense of PD theory, it can be proved that there are still indirect interactions between the material points even if they are outside of their horizons. Please also note that the horizons are different than the circular form in the deformed state however they are shown as circular form in Figure 2.12 for the simplicity.

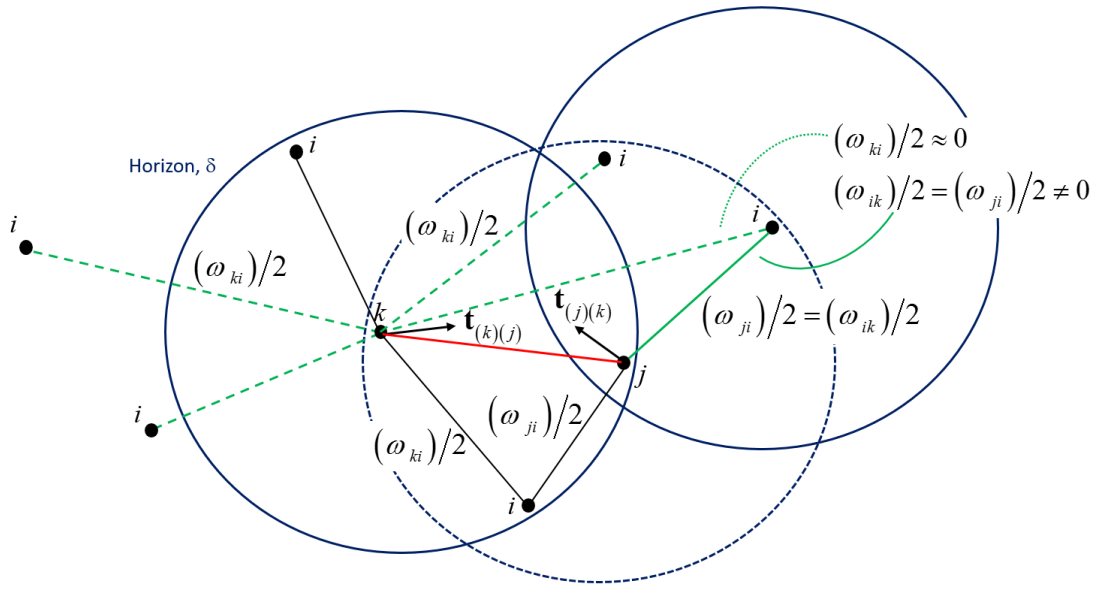

Figure 2.12 Direct and indirect interactions with micropotentials

In Figure 2.12, force densities, $\mathbf{t}_{(k)(j)}$ and $\mathbf{t}_{(j)(k)}$, resulting from the interaction between material points *k* and *j* are shown. The force density, $\mathbf{t}_{(k)(j)}$, has its property, i.e. the magnitude and the direction, from the micropotentials of all bonds which are connected to material point *k*, i.e. $\sum_i \omega_{(k)(i)}$, as in Equation (2.27). Since, the dashed green bonds are outside the horizon of point *k*, their micropotentials may be very small in magnitude and it is assumed that they are equal to zero, i.e. $\omega_{(k)(i)} = 0$. On the other hand, the force density, $\mathbf{t}_{(j)(k)}$, has its property, i.e. the magnitude and the direction, from the micropotentials of all bonds which are connected to material point *k* as well, i.e. $\sum_i \omega_{(i)(k)}$, as in Equation (2.28). Besides, Equation (2.30) tells us the force density $\mathbf{t}_{(j)(k)}$ may also have its property from all bonds which are connected to material point *j*, i.e. $\sum_i \omega_{(j)(i)}$. Thus, micropotentials of dashed green bonds should not vanish because

$$\sum_i \omega_{(i)(k)} V_{(i)} = \sum_i \omega_{(j)(i)} V_{(i)} \neq 0 \tag{2.31}$$

So, it is apparent that the micropotentials of bonds, which are outside the horizon region, can still have an effect on the force density of a bond. Because the material point *j* is actually a common point of the material points *i* and *k* such that its horizon

includes both material points *i* and *k*. So, in the light of these, it can be said that $\omega_{(i)(k)}$ has its property from $\omega_{(j)(i)}$ or micropotential of dashed green bond is influenced by solid green bond's micropotential as shown in Figure 2.12. As a result, even material points *k* and *i* are outside of their horizons, i.e. $\delta < \left| x_{(i)} - x_{(k)} \right| < 2\delta$, energy of the dashed green bond can still contribute to force density $\mathbf{t}_{(j)(k)}$ because of common material point *j* and it causes indirect interaction between *i* and *k*. The similar observation was also made by Silling (2010) with a different form of equation of motion which is in a linearized form. Silling (2010) introduced vector and double states in his work and explained their mathematical operations. Vector state basically involves infinite number of array of vectors and double state is an infinite number of second order tensors. We do not introduce the detailed expressions for states here but still the similarities can be observed between our work and ref. (Silling, 2010). Equation of motion in PD theory is introduced by Silling (2010) in a linearized form as

$$\begin{aligned} \rho_{(k)}\ddot{\mathbf{u}}_{(k,t)} &= \int_{\mathrm{B}}\int_{\mathrm{B}} \underline{\mathrm{K}}[k]\langle j-k, i-k\rangle \left(\mathbf{u}(i,t)-\mathbf{u}(k,t)\right) dV_i dV_j \\ &-\int_{\mathrm{B}}\int_{\mathrm{B}} \underline{\mathrm{K}}[j]\langle k-j, i-j\rangle \left(\mathbf{u}(i,t)-\mathbf{u}(j,t)\right) dV_i dV_j + \mathbf{b}_{(k,t)} \end{aligned} \tag{2.32}$$

where $\underline{\mathrm{K}}[k]\langle j-k, i-k\rangle$ and $\underline{\mathrm{K}}[j]\langle k-j, i-j\rangle$ are the double states or named as the modulus states of material points *k* and *j*, respectively. From the similarity of micropotentials and double states, cf. Equations (2.27) – (2.29) and (2.32), following equities can be established

$$\mathbf{t}_{(k)(j)} = \frac{1}{2}\frac{1}{V_{(j)}}\sum_i \frac{\partial\left(\omega_{(k)(i)}\right)}{\partial\left(\mathbf{y}_{(j)}-\mathbf{y}_{(k)}\right)} V_{(i)} = \int_{\mathrm{B}} \underline{\mathrm{K}}[k]\langle j-k, i-k\rangle \left(\mathbf{u}(i,t)-\mathbf{u}(k,t)\right) dV_i \tag{2.33}$$

and

$$\mathbf{t}_{(j)(k)} = \frac{1}{2}\frac{1}{V_{(j)}}\sum_i \frac{\partial\left(\omega_{(j)(i)}\right)}{\partial\left(\mathbf{y}_{(k)}-\mathbf{y}_{(j)}\right)} V_{(i)} = \int_{\mathrm{B}} \underline{\mathrm{K}}[j]\langle k-j, i-j\rangle \left(\mathbf{u}(i,t)-\mathbf{u}(j,t)\right) dV_i \tag{2.34}$$

As already mentioned before, Equation (2.34) includes indirect interactions between the material points *i* and *k* arising from the equity given in Equation (2.30). So, it can

be deduced that the modulus state $\underline{\mathrm{K}}[j]\langle k-j, i-j\rangle$ has the same type of indirect interactions. This property was also emphasized by Silling (2010) with further modification in Equation (2.32) as

$$\rho_{(k)}\ddot{\mathbf{u}}_{(k,t)} = \int_{\mathrm{B}} C_0(k,i)\mathbf{u}(i,t)\,dV_i - P_0(k)\mathbf{u}(k,t) + \mathbf{b}(k,t) \tag{2.35}$$

where

$$C_0(k,i) = \int_{\mathrm{B}} \left(\underline{\mathrm{K}}[k]\langle j-k, i-k\rangle - \underline{\mathrm{K}}[j]\langle k-j, i-j\rangle + \underline{\mathrm{K}}[i]\langle k-i, j-i\rangle\right) dV_j \tag{2.36}$$

and

$$P_0(k) = \int_{\mathrm{B}}\int_{\mathrm{B}} \underline{\mathrm{K}}[k]\langle j-k, i-k\rangle\, dV_i dV_j \tag{2.37}$$

So, the term $C_0(k,i)$ may be non-zero even if $\delta < \left|x_{(i)} - x_{(k)}\right| < 2\delta$ and this is because of the modulus state $\underline{\mathrm{K}}[j]\langle k-j, i-j\rangle$ appearing in Equation (2.36) which defines the force state of material point *j* (Silling, 2010). It is also mentioned by Silling (2010) that the non-zero modulus state, i.e. $\underline{\mathrm{K}}[j]\langle k-j, i-j\rangle$, results from the horizon of material point *j* and it includes both of the material points *i* and *k*.

2.4.3 Ordinary state based Peridynamics

Indeed, non - ordinary and ordinary state based PDs published by Silling et al. (2007) following the simpler form of PD formulation which is named as bond – based PDs (Silling, 2000). Since the more general form of PDs, which can also be named as non – ordinary state based PDs, was already explained in Section 2.4.2, the following sections are structured so as to follow this towards the simpler form of PD theory. The PD force densities can be derived from micropotentials such that they may have any direction and magnitude in a bond (see the Figure 2.12). In a most general sense of PD theory, i.e. non – ordinary state based PDs, there is no constraint on the force densities. However, one must find the best solution in order to represent the continuum model of a structure considering the micropotentials or the strain energy density function of a material point.

2.4.3.1 The work done by Madenci and Oterkus (2014)

Madenci and Oterkus (2014) proposed strain energy density function based on the idea that PD theory is just the extension of local interactions of CCM theory to a non – local sense. Please see the Chapter 3 of ref. (Madenci and Oterkus, 2014) for the expansion procedure to non – local interactions. This newly proposed strain energy density function (Equation (2.38)) results in ordinary state based PD formulation for continuum domain of solid materials. The difference between ordinary and non – ordinary state based formulations is just the direction of the force densities in a bond. In ordinary state based formulation, the force densities are aligned such that they are in the direction of the deformed position of a bond and they can still possess any magnitude (Silling et al., 2007) as shown in Figure 2.13.

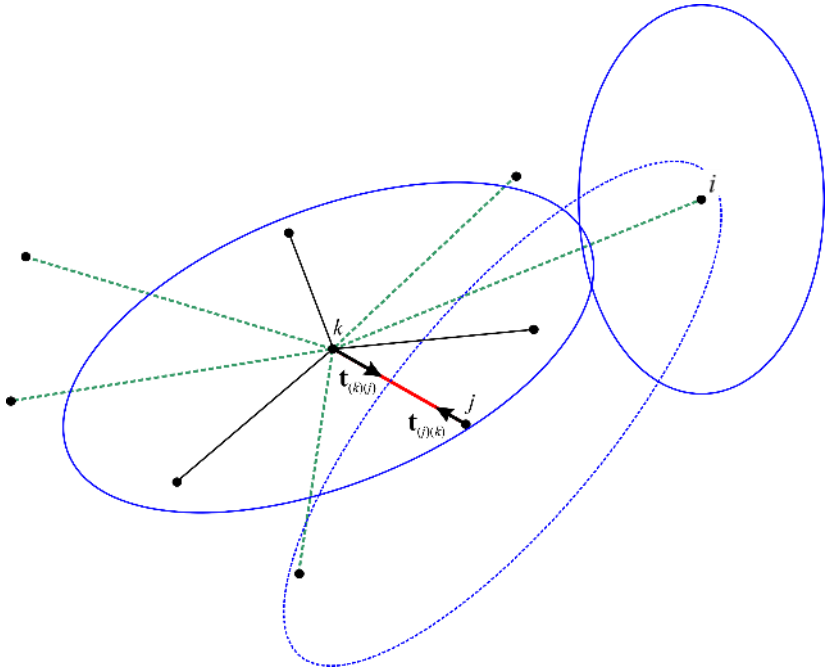

Figure 2.13 Ordinary state based theory with direct and indirect interactions

The proposed strain energy density function of Madenci and Oterkus (2014) is

$$W_{(k)} = a\theta_{(k)}^2 - a_2\theta_{(k)}T_{(k)} + a_3T_{(k)}^2 + b\sum_{j=1}^{N} w_{(k)(j)}\left(\left(\left|\mathbf{y}_{(j)} - \mathbf{y}_{(k)}\right| - \left|\mathbf{x}_{(j)} - \mathbf{x}_{(k)}\right|\right) - \alpha T_{(k)}\left|\mathbf{x}_{(j)} - \mathbf{x}_{(j)}\right|\right)^2 V_{(j)} \tag{2.38}$$

in which $\theta_{(k)}$ is the dilatation term

$$\theta_{(k)} = d\sum_{j=1}^{N} w_{(k)(j)}\left(s_{(k)(j)} - \alpha T_{(k)}\right)\frac{\mathbf{y}_{(j)} - \mathbf{y}_{(k)}}{\left|\mathbf{y}_{(j)} - \mathbf{y}_{(k)}\right|}\left(\mathbf{x}_{(j)} - \mathbf{x}_{(k)}\right)V_{(j)} + 3\alpha T_{(k)} \tag{2.39}$$

where $s_{(k)(j)}$ is the stretch definition of a bond in PD theory and is expressed as

$$s_{(k)(j)} = \frac{\left|\mathbf{y}_{(j)} - \mathbf{y}_{(k)}\right| - \left|\mathbf{x}_{(j)} - \mathbf{x}_{(k)}\right|}{\left|\mathbf{x}_{(j)} - \mathbf{x}_{(k)}\right|} \tag{2.40}$$

In Equation (2.38), $T_{(k)}$ represents temperature change of a material and α is the coefficient of thermal expansion. The terms a, a_2, a_3 and b are the PD material parameters and can be related to engineering constants by equating the strain energy densities of CCM and PD theories for simple loading conditions. As well as d ensures that the dilatation term remains non - dimensional. Following the procedure defined by Madenci and Oterkus (2014) (c.f. Chapter 4), material parameters can be expressed for three – dimensional structures as

$$a = \frac{1}{2}\left(\kappa - \frac{5\mu}{3}\right),\ a_2 = 6\alpha a,\ a_3 = 9\alpha^2 a,\ b = \frac{15\mu}{2\pi\delta^5} \text{ and } d = \frac{9}{4\pi\delta^4} \tag{2.41}$$

Here, κ and μ are the bulk and shear moduli of a structure and they, for three – dimensional body, are $\kappa = \frac{E}{3(1-2\nu)}$, $\mu = \frac{E}{2(1+\nu)}$. Please see Chapter 4 of ref. (Madenci and Oterkus, 2014) for two and one – dimensional structures. Furthermore, $w_{(k)(j)}$ is named as influence or weight function and it adjusts the influence of material points away from the main material point k. It may simply be expressed as

$$w_{(k)(j)} = \frac{\delta}{\left|\mathbf{x}_{(j)} - \mathbf{x}_{(k)}\right|} \tag{2.42}$$

Now, the force densities can be derived from the Lagrange's equation of motion. They already are given by Equations (2.27) and (2.28) in terms of strain energy densities. It can be realized from Equation (2.38) that the strain energy density is composed of scalar distance between the deformed form of material points, i.e. $\left|\mathbf{y}_{(j)} - \mathbf{y}_{(k)}\right|$, and the following equity can be established

$$W_{(k)}\left(\left|\mathbf{y}_{(j)}-\mathbf{y}_{(k)}\right|,\left|\mathbf{x}_{(j)}-\mathbf{x}_{(k)}\right|\right)=W_{(k)}\left(\left(\mathbf{y}_{(j)}-\mathbf{y}_{(k)}\right),\left|\mathbf{x}_{(j)}-\mathbf{x}_{(k)}\right|\right) \tag{2.43}$$

The similar equity is also given by Silling et al. (2007) for ordinary, elastic material. So, this leads to a slightly different form of force density expression

$$\mathbf{t}_{(k)(j)}=\frac{1}{V_{(j)}}\frac{\partial W_{(k)}}{\partial\left(\mathbf{y}_{(j)}-\mathbf{y}_{(k)}\right)}=\frac{1}{V_{(j)}}\frac{\partial W_{(k)}}{\partial\left(\left|\mathbf{y}_{(j)}-\mathbf{y}_{(k)}\right|\right)}\frac{\left(\mathbf{y}_{(j)}-\mathbf{y}_{(k)}\right)}{\left|\mathbf{y}_{(j)}-\mathbf{y}_{(k)}\right|} \tag{2.44}$$

The similar equation can also be written for $\mathbf{t}_{(j)(k)}$ but we do not show this for simplicity and integrity of the section. Please see Chapter 4 of ref. (Madenci and Oterkus, 2014) for details. It is obvious from Equation (2.44) that the force density is oriented in the direction of deformed position of a bond and this is the property of ordinary state based PD theory. It also ensures the balance of angular momentum of a body. Substituting Equation (2.38) into Equation (2.44) leads to a force density expression of the ordinary state based theory as

$$\mathbf{t}_{(k)(j)}=\frac{1}{2}A\frac{\left(\mathbf{y}_{(j)}-\mathbf{y}_{(k)}\right)}{\left|\mathbf{y}_{(j)}-\mathbf{y}_{(k)}\right|} \tag{2.45}$$

with

$$A=4w_{(k)(j)}\left\{\begin{array}{l} d\Lambda_{(k)(j)}\left(a\theta_{(k)}-\frac{1}{2}a_2T_{(k)}\right)+ \\ b\left(\left(\left|\mathbf{y}_{(j)}-\mathbf{y}_{(k)}\right|-\left|\mathbf{x}_{(j)}-\mathbf{x}_{(k)}\right|\right)-\alpha T_{(k)}\left|\mathbf{x}_{(j)}-\mathbf{x}_{(j)}\right|\right) \end{array}\right\} \tag{2.46}$$

where $\Lambda_{(k)(j)}$ is the parameter defined by

$$\Lambda_{(k)(j)}=\frac{\mathbf{y}_{(j)}-\mathbf{y}_{(k)}}{\left|\mathbf{y}_{(j)}-\mathbf{y}_{(k)}\right|}\frac{\mathbf{x}_{(j)}-\mathbf{x}_{(k)}}{\left|\mathbf{x}_{(j)}-\mathbf{x}_{(k)}\right|} \tag{2.47}$$

2.4.3.2 The work done by Silling et al. (2007)

The first ordinary state based PD formulation was proposed by Silling et al. (2007). The vector states and their mathematical operations are proposed in their work. Vector state is composed of infinite number of array of vectors. We do not introduce the

detailed expressions of states here, please refer to ref. (Silling et al., 2007) for more information.

In this work, Silling et al. (2007) firstly proposed extension scalar state of bonds as

$$\underline{e} = \underline{y} - \underline{x} \tag{2.48}$$

in which $\underline{y}$ and $\underline{x}$ are the magnitude of position vectors in the deformed and un – deformed configurations, respectively. Please remember that states include information of all material points in a domain. Then, the dilatation term in PD theory is proposed as

$$\theta = \frac{3}{m}\left(\underline{\omega x}\right) \bullet \underline{e} \tag{2.49}$$

in which *m* is named as the weighted volume and is given by

$$m = \left(\underline{\omega x}\right) \bullet \underline{x} \tag{2.50}$$

where $\underline{\omega}$ is the influence function and the dot "$\bullet$" sign represents the dot product of two states. After defining the dilatation term, it is possible to decompose extension state into two parts as isotropic ($\underline{e}^i$) and deviatoric ($\underline{e}^d$) extension scalar states

$$\underline{e}^i = \frac{\theta \underline{x}}{3} \quad \text{and} \quad \underline{e}^d = \underline{e} - \underline{e}^i \tag{2.51}$$

Then, isotropic ($\underline{t}^i$) and deviatoric ($\underline{t}^d$) parts of force scalar state, $\underline{t}$, are proposed as

$$\underline{t}^i = \frac{-3p}{m}\underline{\omega x} \quad \text{and} \quad \underline{t}^d = \underline{t} - \underline{t}^i \tag{2.52}$$

and *p* is the Peridynamic pressure,

$$p = -\frac{\underline{t} \bullet \underline{x}}{3}. \tag{2.53}$$

Please also note that the relation between the force scalar state, $\underline{t}$ and the force vector state, $\underline{\mathbf{T}}$, which is

$$\underline{\mathbf{T}} = \underline{t}\underline{\mathbf{M}} \tag{2.54}$$

where $\underline{\mathbf{M}}$ is the deformed direction vector state which stores the relative unit vectors of deformed bonds. Silling et al. (2007) also proved the following relations for ordinary, elastic material.

$$p = -\frac{\partial W}{\partial \theta} \quad \text{and} \quad \underline{t}^d = \frac{\partial W}{\partial \underline{e}^d} \tag{2.55}$$

After above derivations, the strain energy density function for ordinary, elastic material is proposed as

$$W\left(\theta, \underline{e}^d\right) = \frac{k\theta^2}{2} + \frac{\alpha}{2}\left(\underline{\omega e}^d\right) \bullet \underline{e}^d \tag{2.56}$$

This expression has the similarity with the classical form of strain energy density function. In light of Equations (2.52), (2.55) and (2.56), one may lead to an open form of force scalar state as

$$\underline{t} = \frac{-3p}{m}\underline{\omega x} + \alpha \underline{\omega e}^d \tag{2.57}$$

where

$$p = -k\theta \tag{2.58}$$

in which k and α are the Peridynamic material constants for linear Peridynamic solid. These constants may be obtained by equating classical and PD strain energy densities while assuming spherical influence function, $\underline{\omega}$, as

$$\alpha = \frac{15\mu}{m} \tag{2.59}$$

and it can be realized that k is simply a bulk modulus. Substituting Equations (2.58) and (2.59) into Equation (2.57) leads to

$$\underline{t} = \frac{3k\theta}{m}\underline{\omega x} + \frac{15\mu}{m}\underline{\omega e}^d \tag{2.60}$$

The similarity between force density function given in Equation (2.60) and the stress tensor of CCM (Equation (2.61)) is now apparent.

$$\boldsymbol{\sigma} = k\theta\mathbf{I} + 2\mu\varepsilon^d \tag{2.61}$$

in which **I** is the identity matrix and ε^d represents deviatoric part of strain tensor. Finally, the equation of motion in PD theory is written by means of states as

$$\rho(\mathbf{x},t)\ddot{\mathbf{u}}(\mathbf{x},t)=\int_{H_x}\left\{\underline{\mathbf{T}}[\mathbf{x},t]\langle\mathbf{x}'-\mathbf{x}\rangle-\underline{\mathbf{T}}[\mathbf{x}',t]\langle\mathbf{x}-\mathbf{x}'\rangle\right\}dV_{x'}+\mathbf{b}(\mathbf{x},t) \tag{2.62}$$

Here, the square brackets represent the force state vectors which are on the material points **x** and $\mathbf{x}'$ as well as the angle brackets are used to indicate the vector on which the force state operates. For example, $\underline{\mathbf{T}}[\mathbf{x},t]\langle\mathbf{x}'-\mathbf{x}\rangle$ is the force vector on a material point **x** which includes the effect of material point $\mathbf{x}'$ on a material point **x**. It is also worth mentioning that the balance of linear and angular momentums are satisfied for ordinary material and objectivity is also proved for ordinary, elastic material.

2.4.3.3 Comparison of the results of refs. (Madenci and Oterkus, 2014) and (Silling et al., 2007)

Mainly, two approaches from refs. (Madenci and Oterkus, 2014) and (Silling et al., 2007) proposed different strain energy densities. Madenci and Oterkus (2014) based their function to CCM which is a non – local extension of local function and they derived PD force densities by exploiting Lagrange's equation of motion. On the other hand, Silling et al. (2007) firstly verified the linear and the angular momentums as well as the objectivity for an ordinary material. Moreover, the PD terms such as dilatation, isotropic and deviatoric parts of extension scalar states, force scalar states and pressure were derived. Thus, the strain energy density function, similar with the classical theory, was proposed in order to derive the explicit form of force scalar state. Both approaches are complete and it has already been proven that they can reach similar results. However, it may be remarkable to point out some differences of both approaches. Before proceeding the following subsections, the person, who is unfamiliar with the bond based PD theory, should take a look at Section 2.4.4.

Influence function

Let us first define the some frequently used PD terms. Relative position of two points in the reference configuration is

$$\boldsymbol{\xi}=\mathbf{x}'-\mathbf{x} \tag{2.63}$$

and their relative displacement is

$$\boldsymbol{\eta} = \mathbf{u}\left(\mathbf{x}', t\right) - \mathbf{u}\left(\mathbf{x}, t\right) \tag{2.64}$$

Then, the deformed form of a bond can relatively be expressed as $\boldsymbol{\xi} + \boldsymbol{\eta}$. Now, Silling et al. (2007)'s equations can be expressed in a more precise form. Extension scalar state of a bond, Equation (2.48), can be rewritten as

$$\underline{e}\langle\boldsymbol{\xi}\rangle = \underline{y}\langle\boldsymbol{\xi}\rangle - \underline{x}\langle\boldsymbol{\xi}\rangle = |\boldsymbol{\xi} + \boldsymbol{\eta}| - |\boldsymbol{\xi}| \tag{2.65}$$

and weighted volume of a point or its horizon, Equation (2.50), is expressed by using the dot product expression for states as

$$m = \int_{\mathrm{H}_x} \underline{\omega}\langle\boldsymbol{\xi}\rangle |\boldsymbol{\xi}|^2 \, dV_{\xi} \tag{2.66}$$

Now, it is easy to rewrite dilatation term of a material point (Equation (2.49)) as

$$\theta = \frac{3}{m} \int_{\mathrm{H}_x} \underline{\omega}\langle\boldsymbol{\xi}\rangle |\boldsymbol{\xi}| \left(|\boldsymbol{\xi} + \boldsymbol{\eta}| - |\boldsymbol{\xi}|\right) dV_{\xi} \tag{2.67}$$

Isotropic ($\underline{e}^i$) and deviatoric ($\underline{e}^d$) parts of the extension scalar state, i.e. Equation (2.51), can also be rewritten as

$$\underline{e}^i\langle\boldsymbol{\xi}\rangle = \frac{\theta|\boldsymbol{\xi}|}{3} \quad \text{and} \quad \underline{e}^d\langle\boldsymbol{\xi}\rangle = \left(|\boldsymbol{\xi} + \boldsymbol{\eta}| - |\boldsymbol{\xi}|\right) - \frac{\theta|\boldsymbol{\xi}|}{3} \tag{2.68}$$

The magnitude of force vector for a bond $\boldsymbol{\xi}$ then becomes

$$\underline{t}\langle\boldsymbol{\xi}\rangle = \frac{3k\theta}{m} \underline{\omega}\langle\boldsymbol{\xi}\rangle |\boldsymbol{\xi}| + \frac{15\mu}{m} \underline{\omega}\langle\boldsymbol{\xi}\rangle \left(\left(|\boldsymbol{\xi} + \boldsymbol{\eta}| - |\boldsymbol{\xi}|\right) - \frac{\theta|\boldsymbol{\xi}|}{3} \right) \tag{2.69}$$

and it can also be rearranged as similar with Equation (2.46),

$$\underline{t}\langle\boldsymbol{\xi}\rangle = \frac{\underline{\omega}\langle\boldsymbol{\xi}\rangle |\boldsymbol{\xi}|}{m} \left(3k - \frac{15\mu}{3} \right) \theta + \frac{15\mu}{m} \underline{\omega}\langle\boldsymbol{\xi}\rangle \left(\left(|\boldsymbol{\xi} + \boldsymbol{\eta}| - |\boldsymbol{\xi}|\right) \right) \tag{2.70}$$

In Equation (2.70), the influence function, $\underline{\omega}\langle\boldsymbol{\xi}\rangle$, is the unknown term and so the term *m*. This term is proposed as $\omega = \delta / |\boldsymbol{\xi}|$ (Equation (2.42)) by Madenci and Oterkus (2014) and this can also be deduced by using the equaity of the ordinary state based

and the bond based theories. Please see Section 2.4.4 for the details of bond based PD theory. In bond based PDs, there is only one material parameter, *c*, which is generally called as bond constant given in Equation (2.122). Rearranging this equation leads to

$$k = \frac{c\pi\delta^4}{18} \tag{2.71}$$

Bulk modulus can also be written in a slightly different form introducing the constraint on a Poisson's ratio, which is 1/4, as

$$k = \frac{E}{3(1-2\nu)} = \frac{2E}{3} \tag{2.72}$$

Then, the shear modulus in the bond based PD theory becomes

$$\mu = \frac{E}{2(1+\nu)} = \frac{3k}{5} \tag{2.73}$$

Substituting Equation (2.73) into Equation (2.70) leads to

$$\underline{t}\langle\boldsymbol{\xi}\rangle = \frac{9k}{m}\underline{\omega}\langle\boldsymbol{\xi}\rangle\left(\left(|\boldsymbol{\xi}+\boldsymbol{\eta}|-|\boldsymbol{\xi}|\right)\right) \tag{2.74}$$

where the dilatation term, θ, cancels out and the ordinary based force density transforms into a bond based force density. Substituting Equation (2.71) into Equation (2.74) results in force density expression in terms of PD bond constant *c* as

$$\underline{t}\langle\boldsymbol{\xi}\rangle = \frac{c\pi\delta^4}{2m}\underline{\omega}\langle\boldsymbol{\xi}\rangle\left(|\boldsymbol{\xi}+\boldsymbol{\eta}|-|\boldsymbol{\xi}|\right) \tag{2.75}$$

The very well – known properties of the bond based force densities are;

1. They are aligned in the direction of the deformed position of a bond as in the ordinary state based theory
2. Their magnitudes are equal to each other in a bond (Silling and Askari, 2005), please see the Figure 2.14.

Thus, it is apparent that the pairwise force function, **f**, in a bond based PD theory is the twice the force density, **t**, so that the following equity holds

$$\underline{\mathbf{t}}\langle\boldsymbol{\xi}\rangle = \frac{1}{2}\mathbf{f} \tag{2.76}$$

Substituting Equations (2.75) and (2.120), which is the pairwise force function in a bond based theory, into Equation (2.76) leads to an influence function term as

$$\frac{c\pi\delta^4}{m}\underline{\omega}\langle\boldsymbol{\xi}\rangle\left(|\boldsymbol{\xi}+\boldsymbol{\eta}|-|\boldsymbol{\xi}|\right)=c\frac{|\boldsymbol{\xi}+\boldsymbol{\eta}|-|\boldsymbol{\xi}|}{|\boldsymbol{\xi}|} \tag{2.77}$$

$$\underline{\omega}\langle\boldsymbol{\xi}\rangle=\frac{m}{\pi\delta^4|\boldsymbol{\xi}|} \tag{2.78}$$

In Equation (2.78), the influence function is expressed in terms of the weighted volume, *m*, and it is noticed that the following equity holds

$$\underline{\omega}\langle\boldsymbol{\xi}\rangle=\underline{\omega}_s\langle|\boldsymbol{\xi}|\rangle \tag{2.79}$$

Here, the subscript *s* denotes the spherical horizon because the influence function can only be spherical if it only depends on the undeformed length of a bond, i.e. $|\boldsymbol{\xi}|$ (Silling et al., 2007). Substituting Equation (2.66) into Equation (2.78) while taking into account the relation given in Equation (2.79) leads to

$$\underline{\omega}_s\langle|\boldsymbol{\xi}|\rangle=\frac{\int_{H_x}\underline{\omega}_s\langle|\boldsymbol{\xi}|\rangle|\boldsymbol{\xi}|^2\,dV_{\xi}}{\pi\delta^4|\boldsymbol{\xi}|} \tag{2.80}$$

and the infinitesimal volume in the integration can be expressed, considering the spherical horizon, as

$$dV_{\xi}=4\pi r^2dr\quad\text{with}\quad r=|\boldsymbol{\xi}| \tag{2.81}$$

Then, the integration becomes

$$\underline{\omega}_s\langle|\boldsymbol{\xi}|\rangle=\frac{4\int_0^{\delta}\underline{\omega}_s\langle r\rangle r^4dr}{\delta^4 r} \tag{2.82}$$

Now, it can be proved that the influence function may take the form of

$$\omega=\frac{\delta}{r} \tag{2.83}$$

as proposed by Madenci and Oterkus (2014). Substituting Equation (2.83) into the right hand side of Equation (2.82) results in

$$\underline{\omega}_s \langle |\xi| \rangle = \frac{4\int_0^{\delta} r^3 dr}{\delta^3 r} = \frac{\delta}{r} \tag{2.84}$$

which is the same result as given by Madenci and Oterkus (2014).

Dilatation

In light of the influence function, ω, and the weighted volume, m, proposed by Silling et al. (2007), the Equation (2.66) can be rewritten as

$$m = 4\pi \int_0^{\delta} \delta r^3 dr \tag{2.85}$$

and integrating this results in

$$m = \pi \delta^5 \tag{2.86}$$

Substituting Equations (2.84) and (2.86) into the dilatation, θ, term, i.e. Equation (2.67), leads to

$$\theta = \frac{3}{\pi \delta^4} \int_{H_x} \left(|\xi + \eta| - |\xi| \right) dV_{\xi} \tag{2.87}$$

and with the following equity,

$$\pi \delta^4 = \int_{H_x} |\xi| \, dV_{\xi} \tag{2.88}$$

the dilatation term can also be expressed as

$$\theta = 3 \frac{\int_{H_x} \left(|\xi + \eta| - |\xi| \right) dV_{\xi}}{\int_{H_x} |\xi| \, dV_{\xi}} \tag{2.89}$$

This is the dilatation of a material point proposed by Silling et al. (2007). It can now be compared to the form proposed by Madenci and Oterkus (2014), i.e. Equation (2.39). However, Equation (2.39) must be converted to a more appropriate form for a comparison purpose. Firstly, let us define the following equity,

$$4\pi\delta^3 = 3\int_{\mathrm{H}_x} dV_\xi \tag{2.90}$$

Then, converting the summation into an integration and considering the material parameter *d*, i.e. Equation (2.41), as well as the influence function ω, i.e. Equation (2.84), lead to a dilatation term as

$$\theta = 3\frac{\int_{H_x}\left(\frac{|\boldsymbol{\xi}+\boldsymbol{\eta}|-|\boldsymbol{\xi}|}{|\boldsymbol{\xi}|}\right)\frac{\boldsymbol{\xi}+\boldsymbol{\eta}}{|\boldsymbol{\xi}+\boldsymbol{\eta}|}\frac{\boldsymbol{\xi}}{|\boldsymbol{\xi}|}dV}{\int_{\mathrm{H}_x} dV_\xi} \tag{2.91}$$

Please also note that the temperature change, $T_{(k)}$, of a material point was ignored. Equation (2.91) can further be simplified considering $\frac{\boldsymbol{\xi}+\boldsymbol{\eta}}{|\boldsymbol{\xi}+\boldsymbol{\eta}|}\frac{\boldsymbol{\xi}}{|\boldsymbol{\xi}|}\approx 1$ for very small deformations as

$$\theta = 3\frac{\int_{H_x}\left(\frac{|\boldsymbol{\xi}+\boldsymbol{\eta}|-|\boldsymbol{\xi}|}{|\boldsymbol{\xi}|}\right)dV_\xi}{\int_{\mathrm{H}_x} dV_\xi} \tag{2.92}$$

This defines the dilatation of a material point proposed by Madenci and Oterkus (2014).

Force function

The derived force function by Silling et al. (2007) can be rewritten by substituting the influence function $\underline{\omega}\langle\boldsymbol{\xi}\rangle$, i.e. Equation (2.84), and the weighted volume *m*, i.e. Equation (2.86), into Equation (2.70) as

$$\underline{t}\langle\boldsymbol{\xi}\rangle = \frac{(3k-5\mu)\theta + 15\mu\frac{|\boldsymbol{\xi}+\boldsymbol{\eta}|-|\boldsymbol{\xi}|}{|\boldsymbol{\xi}|}}{\pi\delta^4} \tag{2.93}$$

and considering Equation (2.88) leads to

$$\underline{t}\langle\boldsymbol{\xi}\rangle = \frac{\left(3k-5\mu\right)\theta + 15\mu\dfrac{|\boldsymbol{\xi}+\boldsymbol{\eta}|-|\boldsymbol{\xi}|}{|\boldsymbol{\xi}|}}{\int\limits_{\mathrm{H}_x}|\boldsymbol{\xi}|\,dV_\xi} \tag{2.94}$$

This is the force function derived by Silling et al. (2007). It can now be compared with the form derived by Madenci and Oterkus (2014), i.e. Equations (2.45) – (2.47). However, it must be converted to a more appropriate form for a comparison purpose. Firstly, the scalar force function is defined as

$$t = \frac{1}{2}A \tag{2.95}$$

where A is the parameter given in Equation (2.46). Then, considering the material parameters a, b and d, i.e. Equation (2.41), as well as the influence function ω, i.e. Equation (2.84), gives the parameter A as

$$A = \frac{\left(3k-5\mu\right)\Lambda\dfrac{\theta}{|\xi|}}{2\pi\delta^3/3} + \frac{30\mu\dfrac{|\xi+\eta|-|\xi|}{|\xi|}}{\pi\delta^4} \tag{2.96}$$

with

$$\Lambda = \frac{\boldsymbol{\xi}+\boldsymbol{\eta}}{|\boldsymbol{\xi}+\boldsymbol{\eta}|}\frac{\boldsymbol{\xi}}{|\boldsymbol{\xi}|} \tag{2.97}$$

Substituting Equation (2.96) into Equation (2.95) and using the equities given in Equations (2.88) and (2.90) result in

$$t = \frac{\left(3k-5\mu\right)\Lambda\dfrac{\theta}{|\xi|}}{\int\limits_{\mathrm{H}_x}dV_\xi} + \frac{15\mu\dfrac{|\xi+\eta|-|\xi|}{|\xi|}}{\int\limits_{\mathrm{H}_x}|\boldsymbol{\xi}|\,dV_\xi} \tag{2.98}$$

Please also note that the temperature change, $T_{(k)}$, of a material point was ignored. Equation (2.98) can further be simplified considering $\Lambda \approx 1$ for very small deformations as

$$t = \frac{\left(3k - 5\mu\right)\dfrac{\theta}{|\xi|}}{\displaystyle\int_{H_x} dV_\xi} + \frac{15\mu\dfrac{|\xi+\eta|-|\xi|}{|\xi|}}{\displaystyle\int_{H_x} |\boldsymbol{\xi}|\, dV_\xi} \tag{2.99}$$

This defines the scalar force function on a material point derived by Madenci and Oterkus (2014).

Strain energy density function

The proposed strain energy density function of Silling et al. (2007) can be rewritten by substituting the influence function $\underline{\omega}\langle\boldsymbol{\xi}\rangle$, i.e. Equation (2.84), the Peridynamic material constant α, i.e. Equation (2.59) and the deviatoric part of extension scalar state $\underline{e}^d$, i.e. Equation (2.68), into Equation (2.56) as well as with the help of Equation (2.86) and by using the dot product expression for the states as

$$W\left(\theta, \underline{e}^d\right) = \frac{k\theta^2}{2} + \frac{15\mu\displaystyle\int_{H_x} \frac{1}{|\boldsymbol{\xi}|}\left(\left(|\boldsymbol{\xi}+\boldsymbol{\eta}|-|\boldsymbol{\xi}|\right) - \frac{\theta|\boldsymbol{\xi}|}{3}\right)^2 dV_\xi}{2\pi\delta^4} \tag{2.100}$$

and with the equity given in Equation (2.88), it can also be expressed as

$$W\left(\theta, \underline{e}^d\right) = \frac{k\theta^2}{2} + \frac{15\mu\displaystyle\int_{H_x} \frac{1}{|\boldsymbol{\xi}|}\left(\left(|\boldsymbol{\xi}+\boldsymbol{\eta}|-|\boldsymbol{\xi}|\right) - \frac{\theta|\boldsymbol{\xi}|}{3}\right)^2 dV_\xi}{2\displaystyle\int_{H_x} |\boldsymbol{\xi}|\, dV_\xi} \tag{2.101}$$

This is the strain energy density function proposed by Silling et al. (2007). It can now be compared with the form proposed by Madenci and Oterkus (2014), i.e. Equation (2.38). However, it must be converted to a more appropriate form for a comparison purpose. Converting summation into an integration and considering the material parameters a and b, i.e. Equation (2.41) as well as the influence function ω, i.e. Equation (2.84), lead to

$$W = \frac{1}{2}\kappa\theta^2 + \frac{15\mu\left(\displaystyle\int_{H_x} \frac{1}{|\boldsymbol{\xi}|}\left(|\boldsymbol{\xi}+\boldsymbol{\eta}|-|\boldsymbol{\xi}|\right)^2 dV_\xi - \frac{\pi\delta^4}{9}\theta^2\right)}{2\pi\delta^4} \tag{2.102}$$

Please also note that the temperature change, $T_{(k)}$, of a material point was ignored. Equation (2.102) can further be simplified with the help of equity given in Equation (2.88) as

$$W = \frac{1}{2}\kappa\theta^2 + \frac{15\mu \int_{H_x} \frac{1}{|\boldsymbol{\xi}|}\left(\left(|\boldsymbol{\xi}+\boldsymbol{\eta}|-|\boldsymbol{\xi}|\right)^2 - \left(\frac{\theta}{3}|\boldsymbol{\xi}|\right)^2\right) dV_\xi}{2\int_{H_x} |\boldsymbol{\xi}|\, dV_\xi} \tag{2.103}$$

This defines the strain energy density function of a material point proposed by Madenci and Oterkus (2014).

As a summary, please see the Table 2.3 for a comparison purpose.

Table 2.3 Comparison of functions of ordinary state based PDs

	The work done by	
	Silling et al. (2007)	**Madenci and Oterkus (2014)**
Assumed Influence Function, $\boldsymbol{\omega}$	$\frac{\delta}{\lvert\boldsymbol{\xi}\rvert}$	$\cdot\frac{\delta}{\lvert\boldsymbol{\xi}\rvert}\cdot$
Dilatation, $\boldsymbol{\theta}$	$3\frac{\int_{H_x}\left(\lvert\boldsymbol{\xi}+\boldsymbol{\eta}\rvert-\lvert\boldsymbol{\xi}\rvert\right)dV_\xi}{\int_{H_x}\lvert\boldsymbol{\xi}\rvert\, dV_\xi}$	$3\frac{\int_{H_x}\left(\frac{\lvert\boldsymbol{\xi}+\boldsymbol{\eta}\rvert-\lvert\boldsymbol{\xi}\rvert}{\lvert\boldsymbol{\xi}\rvert}\right)dV_\xi}{\int_{H_x} dV_\xi}$
Force Function, $\mathbf{t}$	$\frac{(3k-5\mu)\theta+15\mu\frac{\lvert\boldsymbol{\xi}+\boldsymbol{\eta}\rvert-\lvert\boldsymbol{\xi}\rvert}{\lvert\boldsymbol{\xi}\rvert}}{\int_{H_x}\lvert\boldsymbol{\xi}\rvert\, dV_\xi}$	$\frac{(3k-5\mu)\frac{\theta}{\lvert\boldsymbol{\xi}\rvert}}{\int_{H_x} dV_\xi} + \frac{15\mu\frac{\lvert\boldsymbol{\xi}+\boldsymbol{\eta}\rvert-\lvert\boldsymbol{\xi}\rvert}{\lvert\boldsymbol{\xi}\rvert}}{\int_{H_x}\lvert\boldsymbol{\xi}\rvert\, dV_\xi}$
Strain Energy Density Function, $\mathbf{W}$	$\frac{k\theta^2}{2} + \frac{15\mu\int_{H_x}\frac{1}{\lvert\boldsymbol{\xi}\rvert}\left(\left(\lvert\boldsymbol{\xi}+\boldsymbol{\eta}\rvert-\lvert\boldsymbol{\xi}\rvert\right)-\frac{\theta\lvert\boldsymbol{\xi}\rvert}{3}\right)^2 dV_\xi}{2\int_{H_x}\lvert\boldsymbol{\xi}\rvert\, dV_\xi}$	$\frac{1}{2}\kappa\theta_{(k)}^2 + \frac{15\mu\int_{H_x}\frac{1}{\lvert\boldsymbol{\xi}\rvert}\left(\left(\lvert\boldsymbol{\xi}+\boldsymbol{\eta}\rvert-\lvert\boldsymbol{\xi}\rvert\right)^2-\left(\frac{\theta}{3}\lvert\boldsymbol{\xi}\rvert\right)^2\right)dV_\xi}{2\int_{H_x}\lvert\boldsymbol{\xi}\rvert\, dV_\xi}$

2.4.4 Bond based Peridynamics

As mentioned in Section 2.4.3, bond based PDs is the simplest form and the very first PD theory found by Silling (2000). In the bond based theory, force densities, i.e. $\mathbf{t}_{(k)(j)}$ and $\mathbf{t}_{(j)(k)}$, are aligned such that they are in the direction of deformed position of a

bond as in the ordinary state based theory however they are also equal in magnitude, as shown in Figure 2.14.

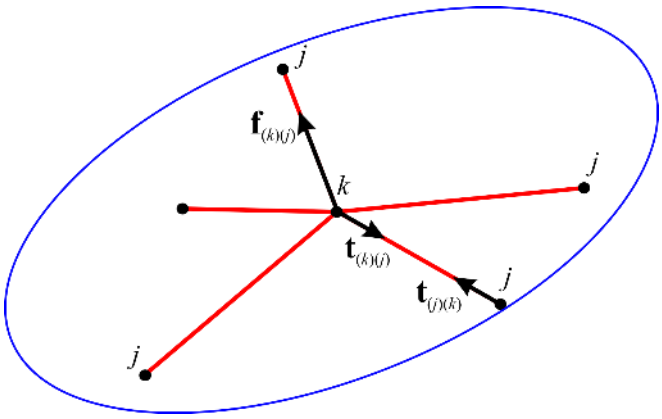

Figure 2.14 Bond based theory

In order to satisfy above mentioned assumptions for the force densities, each bond must be individual which means that their force functions should not be affected from other bonds unlike the non – ordinary and the ordinary state based PD theories. Individual bonds are depicted as red color in Figure 2.14. Thus, micropotentials of a bond only depend on its own material points' deformations given by

$$\omega_{(k)(j)} = \omega_{(k)(j)}(\mathbf{y}_{(j)} - \mathbf{y}_{(k)}) \tag{2.104}$$

$$\omega_{(j)(k)} = \omega_{(j)(k)}(\mathbf{y}_{(k)} - \mathbf{y}_{(j)}) \tag{2.105}$$

Then, the average micropotential of a bond and the strain energy density function of a material point *k* can be expressed using Equations (2.9) and (2.10) while substituting the micropotentials given by Equations (2.104) and (2.105) into these equations. Implementing Lagrange's equation of motion leads to EOM for a material point *k* as

$$\rho_{(k)}\ddot{\mathbf{u}}_{(k)} - \frac{1}{2}\sum_j \frac{\partial \omega_{(k)(j)}}{\partial(\mathbf{y}_{(j)} - \mathbf{y}_{(k)})} V_{(j)} + \frac{1}{2}\sum_j \frac{\partial \omega_{(j)(k)}}{\partial(\mathbf{y}_{(k)} - \mathbf{y}_{(j)})} V_{(j)} - \mathbf{b}_{(k)} = 0 \tag{2.106}$$

Please compare Equations (2.23) and (2.106). It is now apparent from Equation (2.106) that the PD force densities given by Equation (2.107) are equal to and opposite to each other in a bond.

$$\mathbf{t}_{(k)(j)} = \frac{1}{2}\frac{\partial \omega_{(k)(j)}}{\partial(\mathbf{y}_{(j)} - \mathbf{y}_{(k)})} \quad \text{and} \quad \mathbf{t}_{(j)(k)} = \frac{1}{2}\frac{\partial \omega_{(j)(k)}}{\partial(\mathbf{y}_{(k)} - \mathbf{y}_{(j)})} \tag{2.107}$$

So, the following equity can be written.

$$\mathbf{t}_{(k)(j)} = -\mathbf{t}_{(j)(k)} \tag{2.108}$$

Then, the equation of motion given by Equation (2.24) takes the form of

$$\rho_{(k)}\ddot{\mathbf{u}}_{(k)} = \sum_j \mathbf{f}_{(k)(j)} V_{(j)} + \mathbf{b}_{(k)} \tag{2.109}$$

where $\mathbf{f}_{(k)(j)}$ is named as the pairwise force function and is given by

$$\mathbf{f}_{(k)(j)} = 2\mathbf{t}_{(k)(j)} \tag{2.110}$$

Silling (2000) also proved that there also exists scalar valued function such that

$$\omega_{(k)(j)}\left(\left|\mathbf{y}_{(j)} - \mathbf{y}_{(k)}\right|, \xi\right) = \omega_{(k)(j)}\left(\mathbf{y}_{(j)} - \mathbf{y}_{(k)}, \boldsymbol{\xi}\right) \tag{2.111}$$

Thus, according to Equations (2.107), (2.110) and (2.111), the following equity holds.

$$\mathbf{f}_{(k)(j)} = \frac{\partial \omega_{(k)(j)}\left(\left|\mathbf{y}_{(j)} - \mathbf{y}_{(k)}\right|\right)}{\partial\left(\left|\mathbf{y}_{(j)} - \mathbf{y}_{(k)}\right|\right)} \frac{\mathbf{y}_{(j)} - \mathbf{y}_{(k)}}{\left|\mathbf{y}_{(j)} - \mathbf{y}_{(k)}\right|} \tag{2.112}$$

The pairwise force function can now be found by using the equity given in Equation (2.108) as well as with the help of force densities $\mathbf{t}_{(k)(j)}$, given in Equations (2.45) – (2.47), and $\mathbf{t}_{(j)(k)}$. The latter can similarly be defined as

$$\mathbf{t}_{(j)(k)} = -\frac{1}{2} B \frac{\left(\mathbf{y}_{(j)} - \mathbf{y}_{(k)}\right)}{\left|\mathbf{y}_{(j)} - \mathbf{y}_{(k)}\right|} \tag{2.113}$$

with

$$B = 4w_{(j)(k)}\left\{d\Lambda_{(j)(k)}\left(a\theta_{(j)} - \frac{1}{2}a_2 T_{(j)}\right) + b\left(\left(\left|\mathbf{y}_{(k)} - \mathbf{y}_{(j)}\right| - \left|\mathbf{x}_{(k)} - \mathbf{x}_{(j)}\right|\right) - \alpha T_{(j)}\left|\mathbf{x}_{(k)} - \mathbf{x}_{(j)}\right|\right)\right\} \tag{2.114}$$

where $\Lambda_{(j)(k)}$ is

$$\Lambda_{(j)(k)} = \frac{\mathbf{y}_{(k)} - \mathbf{y}_{(j)}}{\left|\mathbf{y}_{(k)} - \mathbf{y}_{(j)}\right|} \frac{\mathbf{x}_{(k)} - \mathbf{x}_{(j)}}{\left|\mathbf{x}_{(k)} - \mathbf{x}_{(j)}\right|} \tag{2.115}$$

So, it is clear that parameters *A* and *B* must be equal to each other therefore the PD material constants must vanish as follows.

$$ad = 0 \tag{2.116}$$

and the pairwise force function takes the form of

$$\mathbf{f}_{(k)(j)} = 4bw_{(k)(j)}\left(\left(\left|\mathbf{y}_{(j)} - \mathbf{y}_{(k)}\right| - \left|\mathbf{x}_{(j)} - \mathbf{x}_{(k)}\right|\right) - \alpha T_{(k)}\left|\mathbf{x}_{(j)} - \mathbf{x}_{(k)}\right|\right)\frac{\left(\mathbf{y}_{(j)} - \mathbf{y}_{(k)}\right)}{\left|\mathbf{y}_{(j)} - \mathbf{y}_{(k)}\right|} \tag{2.117}$$

Substituting the value of the influence function *w*, i.e. Equation (2.84), into Equation (2.117) results in

$$\mathbf{f}_{(k)(j)} = 4b\delta\left(s_{(k)(j)} - \alpha T_{(k)}\right)\frac{\left(\mathbf{y}_{(j)} - \mathbf{y}_{(k)}\right)}{\left|\mathbf{y}_{(j)} - \mathbf{y}_{(k)}\right|} \tag{2.118}$$

where $s_{(k)(j)}$ is the stretch of a bond given by Equation (2.40). Furthermore, mostly used bond based PD parameter in the literature is the bond constant, *c* and it can be defined as

$$c = 4b\delta \tag{2.119}$$

Introducing this into Equation (2.118) results in a most common form of pairwise force function, which is also introduced by Silling and Askari (2005), as

$$\mathbf{f}_{(k)(j)} = c\left(s_{(k)(j)} - \alpha T_{(k)}\right)\frac{\left(\mathbf{y}_{(j)} - \mathbf{y}_{(k)}\right)}{\left|\mathbf{y}_{(j)} - \mathbf{y}_{(k)}\right|} \tag{2.120}$$

It is now clear that there is only one PD material parameter, which is *c*, in the bond based PD theory. In view of Equations (2.41), (2.116) and (2.119), the bond constant *c* can be obtained for three – dimensional structures as

$$c = \frac{30\mu}{\pi\delta^4} \quad \text{with} \quad \nu = \frac{1}{4} \tag{2.121}$$

or

$$c = \frac{18\kappa}{\pi\delta^4} \quad \text{with} \quad \nu = \frac{1}{4} \tag{2.122}$$

It is, for two – dimensional structures, obtained as

$$c = \frac{24\mu}{\pi h \delta^3} \quad \text{with} \quad \nu = \frac{1}{3} \tag{2.123}$$

or

$$c = \frac{12\kappa}{\pi h \delta^3} \quad \text{with} \quad \nu = \frac{1}{3} \tag{2.124}$$

where h represents the thickness of a structure and the bulk modulus for two – dimensional structures is defined as $\kappa = E/2(1-\nu)$. The bond constant given in Equation (2.124) can only be used for plane stress conditions. Gerstle et al. (2005) also derived PD bond constant, c, for plane strain conditions as

$$c = \frac{12E}{(1+\nu)\pi h \delta^3} \quad \text{with} \quad \nu = \frac{1}{4} \tag{2.125}$$

Moreover, one dimensional structures has the bond constant of

$$c = \frac{2E}{A\delta^2} \tag{2.126}$$

in which A is the cross – sectional area of a one – dimensional bar. Please see Chapter 4 of ref. (Madenci and Oterkus, 2014) for more details on derivations of these bond constants.

2.4.5 Damage in Peridynamic theory

In PD theory, damage introduction is a quite straightforward process. The stretch, s, is monitored for each bond during solution procedure and the interaction between material points is terminated whenever it exceeds some critical value, s_c. The force – stretch relationship, which is in the linear form, is shown in Figure 2.15 for a bond based theory.

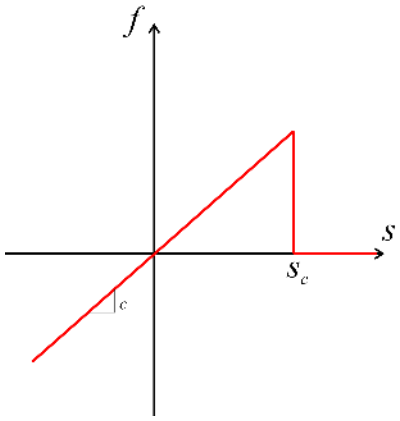

Figure 2.15 Force – stretch relationship

The termination of an interaction between material points is also commonly named as "bond breakage" in PD theory. This is achieved by introducing history dependent failure parameter, $H(x_{(j)}-x_{(k)},t)$, into Peridynamic force function as

$$\mathbf{f}_{(k)(j)}=H(x_{(j)}-x_{(k)},t)c\left(s_{(k)(j)}\right)\frac{\left(\mathbf{y}_{(j)}-\mathbf{y}_{(k)}\right)}{\left|\mathbf{y}_{(j)}-\mathbf{y}_{(k)}\right|} \tag{2.127}$$

with

$$H(x_{(j)}-x_{(k)},t)=\begin{cases}1 & \text{if} \quad s_{(k)(j)}\left(\mathbf{x}_{(j)}-\mathbf{x}_{(k)},t'\right)<s_c \quad \text{for all} \quad 0<t'<t \\ 0 & \text{otherwise}\end{cases} \tag{2.128}$$

This failure parameter is valid for a bond based theory however similar relation can also be defined for an ordinary state based theory but it is not shown here, please refer to Chapter 6 of ref. (Madenci and Oterkus, 2014). After defining the failure parameter in PD theory, the local damage of each material point **x** is introduced in order to indicate crack formation in a body. It is simply the ratio of the amount of broken interactions to the total amount of interactions and can be expressed as

$$\Phi\left(\mathbf{x},t\right)=1-\frac{\int_H \mu(\mathbf{x}'-\mathbf{x},t)dH}{\int_H dH} \tag{2.129}$$

Crack formation with the local damage value can be seen in Figure 2.16. It is now apparent that the damage is treated as part of the constitutive model of PDs through

irreversible breakage of interactions and there is no need any complicated special algorithms.

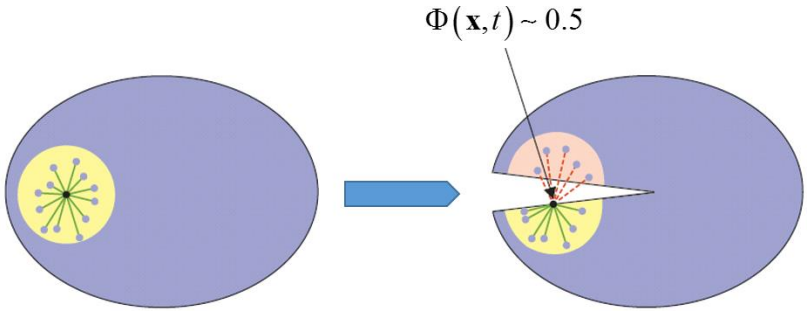

Figure 2.16 Local damage (Madenci and Oterkus, 2014)

Here, it is crucial to define the critical stretch value, s_c and it can be expressed in terms of the critical energy release rate, G_c, of a material. Firstly, the total strain energy required to remove all of the interactions across a newly created crack surface, *A*, is determined. Figure 2.17 shows these interactions and the following equation defines the total strain energy of those.

$$W^c = \sum_{k=1}^{K^+}\sum_{j=1}^{J^-}\frac{1}{2}c\left(s_c\right)^2\left(\left|\mathbf{x}_{(j^-)}-\mathbf{x}_{(k^+)}\right|\right)V_{(k^+)}V_{(j^-)} \tag{2.130}$$

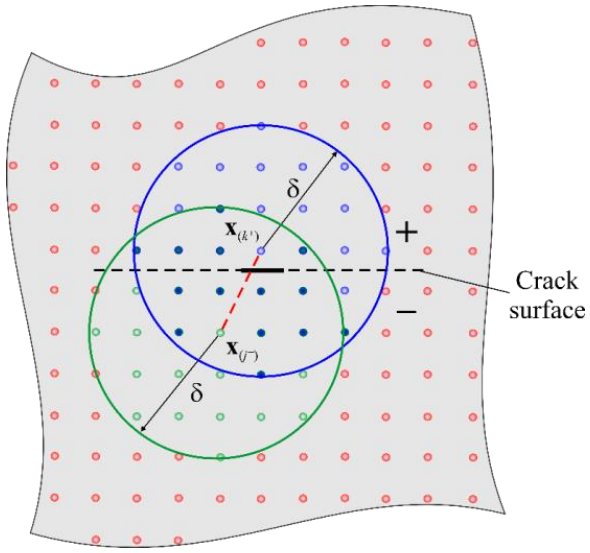

Figure 2.17 Interactions across crack surface (Madenci and Oterkus, 2014)

In order to determine the value of critical stretch, s_c, the total strain energy, W^c, given in Equation (2.130) is equated to corresponding critical energy release rate value, which can be mode - I critical energy release rate (G_{Ic}), as

$$G_{Ic} = \frac{\frac{1}{2} c\left(s_c\right)^2 \sum_{k=1}^{K^+} \sum_{j=1}^{J^-} \left(\left| \mathbf{x}_{(j^-)} - \mathbf{x}_{(k^+)} \right| \right) V_{(k^+)} V_{(j^-)}}{A} \tag{2.131}$$

Based on the expressions derived by Silling and Askari (2005) and Madenci and Oterkus (2014) for the critical energy release rate, it is evident that

$$\frac{\sum_{k=1}^{K^+} \sum_{j=1}^{J^-} \left(\left| \mathbf{x}_{(j^-)} - \mathbf{x}_{(k^+)} \right| \right) V_{(k^+)} V_{(j^-)}}{A} = \begin{cases} \dfrac{\delta^5 \pi}{5} & \text{for 3D} \\ \dfrac{h\delta^4}{2} & \text{for 2D} \end{cases} \tag{2.132}$$

Finally, the critical stretch can be expressed as

$$s_c = \begin{cases} \sqrt{\dfrac{10 G_{Ic}}{c\pi\delta^5}} & \text{for 3D} \\ \sqrt{\dfrac{4 G_{Ic}}{ch\delta^4}} & \text{for 2D} \end{cases} \tag{2.133}$$

2.5 Shortcomings and Concluding Remarks

In this section, the importance of failure prediction in ship structures is introduced and some commonly used terms and methods in crack propagation and prevention processes are mentioned. Then, the interest in marine composites is pointed out. The properties of composite structures are explained (Oterkus et al., 2016). It is evident that their failure prediction procedure is even more complicated than the isotropic structures like steel. Taking into account the complexity of the failure prediction process and the abundance of the crack related terms and formulations in the literature, the necessity for a new simpler theory is obvious and inevitable. In this regard, the new theory, Peridynamics, is introduced in order to make the failure prediction procedure much simpler and to find a remedy for the solution procedure of equation of motion, which has derivatives in the classical sense. This new theory replaced derivatives with

integration and pave the way for handling more complicated structures like composites and even composite sandwiches. The idea beneath the theory and the derivation of its equations including all of its types were explained in detail. As a result, it is apparent that damage prediction is quite a straightforward procedure in PD theory because of the nature of its equations. One of the aim of this thesis is to prove that PD theory has a bright future in the fracture mechanics sense.

Chapter 3

Solution Methods

3.1 Introduction

In Section 2.4, PD theory was explained deterministically including its types and equations of motion. The PD equation of motion can be solved getting the benefit of several solution procedures and numerical methods. In order to obtain accurate results and solve the problem in a more efficient way, one must choose the best solution method. In this section, several ways of solving PD equations of motion as well as how and when to choose the best way are discussed.

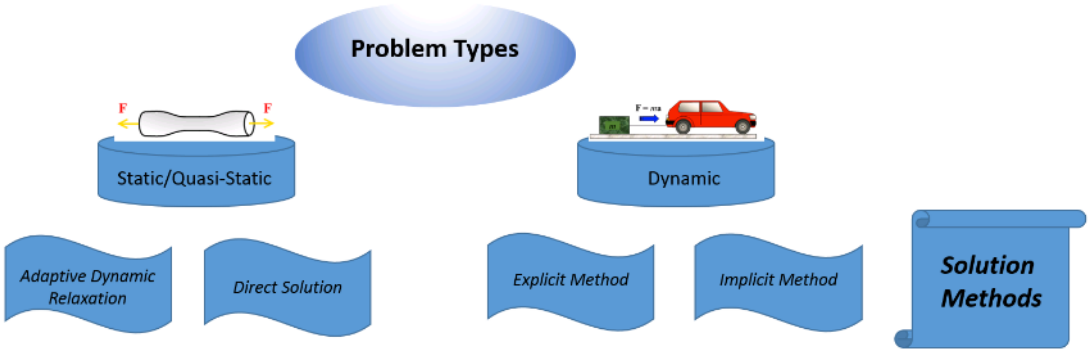

Figure 3.1 Solution methods for different problem types

Firstly, the problem type must be defined as shown in Figure 3.1. It can either be static/quasi – static or dynamic. In static or quasi – static problems, PD equations can be solved directly with matrix equations or Adaptive Dynamic Relaxation (ADR) technique can be benefitted to converge static solution. Besides, if the problem is dynamic, which means that the acceleration and/or inertia effects are important, it can either be solved with explicit or implicit solution methods.

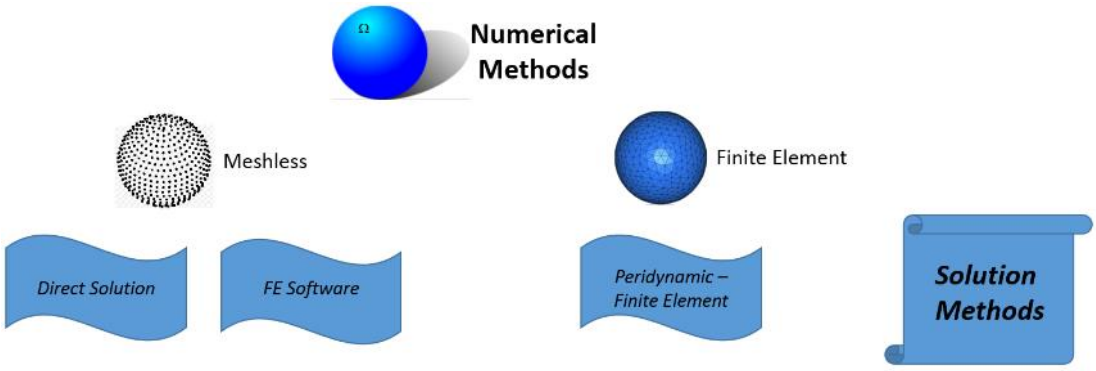

Figure 3.2 Solution methods for a chosen numerical method

On the other hand, the convenient numerical method must be chosen to discretize and solve the PD domain as shown in Figure 3.2. Since the PD equation of motion is in integro – differential form, it is very convenient for meshless discretization methods and most of the researchers choose this way. However, Finite Element (FE) method can also be implemented to some PD problems.

Lastly, it is discussed how the PD codes can be accelerated. They can simply be accelerated by coding them in a more efficient way. In this regard, a very effective procedure for a family member search of a material point is introduced. Furthermore, parallel programming procedures can also be incorporated to PD codes. When solving a PD problem without matrix equations, e.g. solving with ADR, explicit or meshless methods, it is very simple to parallelize the PD code especially in the time integration section. By doing so, PD codes can be made applicable to complex and big problems.

3.2 Different Problem Types

3.2.1 Static or quasi – static problems

PD equation of motion is introduced in a dynamic form in Equation (2.109) however it is also possible to solve static or quasi – static problems in PD theory. In the literature, the most common way of solving these problems is to use Adaptive Dynamic Relaxation (ADR) technique. Apart from that PD matrix equations can also be directly solved using the methods for solving the linear system of equations, explained in Section 3.2.1.2.

3.2.1.1 Adaptive dynamic relaxation technique

In dynamic relaxation (DR) method, artificial mass, **M** and artificial damping, **C**, matrices are introduced to the dynamic equation of motion of the system which is

$$\mathbf{M}\ddot{\mathbf{U}} + \mathbf{C}\dot{\mathbf{U}} + \mathbf{K}\mathbf{U} = \mathbf{F} \tag{3.1}$$

where **K** and **U** are the stiffness matrix and the displacement vector of the system, respectively. In dynamic relaxation technique, the mass and damping matrices are chosen such that the solution of dynamic equation of motion, i.e. Equation (3.1), converges to a steady state part of the transient response which is

$$\mathbf{K}\mathbf{U} = \mathbf{F} \tag{3.2}$$

In dynamic relaxation technique, explicit time integration scheme is used and the unknowns, **U**, of Equation (3.1) become the solution of a static problem (Equation (3.2)) after a certain number of time steps. The convenient choice of time step size is, $\Delta t = 1$.

However, in dynamic relaxation technique, it is tricky to select the fictitious damping matrix which ensures the convergence of Equation (3.1) to Equation (3.2). For that reason, Adaptive Dynamic Relaxation (ADR) technique was introduced by Underwood (1983) in which damping matrix is determined at each time step adaptively. As for making the ADR solution method more clear, Madenci and Oterkus (2014) rearranged Equation (3.1) in a more appropriate form for PD theory as

$$\mathbf{D}\ddot{\mathbf{U}} + c_d\mathbf{D}\dot{\mathbf{U}} = \mathbf{F} \tag{3.3}$$

with

$$\mathbf{F}_{(k)} = \sum_{j} \left(\mathbf{t}_{(k)(j)} - \mathbf{t}_{(j)(k)} \right) V_{(j)} + \mathbf{b}_{(k)} \tag{3.4}$$

where **D** is the fictitious diagonal density matrix and c_d the damping coefficient. The diagonal elements of **D** is chosen based on Greschgorin's theorem. Please refer to Section 7.5 of ref. (Madenci and Oterkus, 2014) for more details on ADR technique.

The advantage of ADR technique is to use the dynamic EOM in order to obtain the static or quasi – static solution for a related PD problem. Since the explicit time integration scheme is used, each bond interaction can be handled independently and thus there is no need for matrix equations to solve a system. On the other hand, the convergence of the static solution can take too many time steps depending on the characteristics of a problem. For some problems, it can be tedious and direct solution of matrix equations can be a better solution option, especially for the problems including bending deformations.

3.2.1.2 Direct solution

Static and quasi - static problems in physics mean that they do not include any acceleration and/or inertia terms. However, in reality, very small acceleration and/or inertia effects always exist, while applying the intended load to a structure. When acceleration and inertia terms have no significant effect on the results, they can be ignored in the physical representation of a problem. Hence, in order to solve static or quasi – static problems in PD theory the acceleration term, $\ddot{\mathbf{u}}$, can be omitted from the equation of motion, i.e. Equation (2.109), which can be rewritten as

$$\sum_{j} \mathbf{f}_{(k)(j)} V_{(j)} + \mathbf{b}_{(k)} = 0 \tag{3.5}$$

Equation (3.5) can be named as local static PD equation since it only shows the static equation of one main material point, which interacts with other member material points in its horizon, δ, as shown in Figure 3.3.

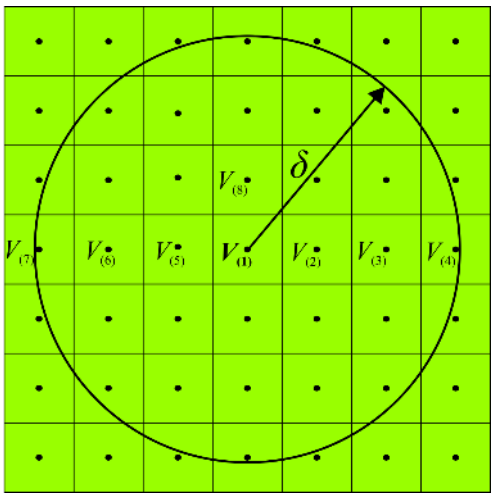

Figure 3.3 Family members of a main material point, $k=1$

In order to find the deformation of a body, other material points in a body must also be considered as the main material point. By doing so, the global static PD equation can be obtained in a matrix form as

$$\mathbf{KU}=\mathbf{B} \tag{3.6}$$

in which **K**, **U** and **B** are the global stiffness, the displacement and the body load matrices of a body. The global static PD equation, i.e. Equation (3.6), can now be solved directly to find the unknown displacement vector, **U**, by taking the inverse of stiffness matrix as

$$\mathbf{U}=\mathbf{K}^{-1}\mathbf{B} \tag{3.7}$$

However, calculating $\mathbf{K}^{-1}$ can be tedious for big and complex structures, which include many material points. In this regard, the solution methods can be exploited for simultaneously solving the linear system of equations. Such well-known and effective direct solution methods are Gaussian elimination, LU decomposition, Cholesky decomposition, QR decomposition and etc. As a result, the static and quasi – static problems can be solved directly by using the global static PD equation, given in Equation (3.6). Directly solving static PD equation may lead to very fast results for some problems compared to ADR method. However, an ill-conditioned stiffness matrix may arise regarding with the horizon size and the number of material points (Bobaru et al., 2009). Moreover, the three-dimensional and complex problems may construct very large matrices and working with them can be very challenging. In these

cases, the solution time of direct solution method can be too long. Hence, the solution capability of already existing FE software can be exploited by creating the PD model in their framework. For more information, please refer to Section 3.3.1.2. On the other hand, iterative methods, in which solution is converged iteratively, may be used to solve Equation (3.6). However, it is commonly believed that iterative methods can be unreliable and they may exhibit slow convergence characteristics.

3.2.2 Dynamic problems

In dynamic problems, the acceleration and/or inertia terms have significant effects on the results of a problem so that they cannot be ignored as in static problems. Hence, PD EOM given in Equation (2.109) can directly be used to solve the dynamic problems. In the solution procedure, two different solution methods can be used, i.e. either explicit or implicit time integration schemes. Each method has disntictive advantages and disadvantages. Therefore, the best method must be chosen depending on the type of a problem. In general, explicit time integration scheme has small time step sizes and does not solve matrix equations. On the other hand, implicit time integration scheme uses larger time step sizes but matrix equations must be solved.

3.2.2.1 Explicit Method

Explicit time integration scheme is usually the preferred method for Peridynamic analysis since it does not solve any matrix equations. The dynamic PD EOM given in Equation (2.109) is used for the explicit time integration scheme and it can be rewritten for the n^{th} time step as

$$\ddot{\mathbf{u}}_{(k)}^{n} = \frac{1}{\rho_{(k)}} \sum_{j} \mathbf{f}_{(k)(j)}^{n} V_{(j)} + \mathbf{b}_{(k)}^{n} \quad \text{and} \quad n = 0,1,2,... \tag{3.8}$$

where n indicates the time steps and zeroth step is just beginning of the analysis. Equation (3.8) is solved for the unknown term acceleration of material point k, i.e. $\ddot{\mathbf{u}}_{(k)}^{n}$, while summing the force functions, $\mathbf{f}_{(k)(j)}$, for each bond interaction. After that, the velocity of material point k, i.e. $\dot{\mathbf{u}}_{(k)}^{n+1}$, which is for the next time step, n+1, can be obtained using the forward difference method as

$$\dot{\mathbf{u}}_{(k)}^{n+1} = \ddot{\mathbf{u}}_{(k)}^{n} \Delta t + \dot{\mathbf{u}}_{(k)}^{n} \tag{3.9}$$

where Δt indicates time step size. Then, backward difference method is used to obtain the displacement of material point *k*, i.e. $\mathbf{u}_{(k)}^{n+1}$, for the next time step as

$$\mathbf{u}_{(k)}^{n+1} = \dot{\mathbf{u}}_{(k)}^{n+1} \Delta t + \mathbf{u}_{(k)}^{n} \tag{3.10}$$

Acceleration of each material point, i.e. $k = 1, 2, 3, \ldots$, can be calculated from Equation (3.8) individually. For this reason, there is no need for matrix equations. Above explained steps, i.e. Equations (3.8) through (3.10), are solved until the desired time *t* is reached,

$$t = n \times \Delta t \tag{3.11}$$

On the other hand, explicit time integration scheme can only be used for very small time step sizes and it may become unstable for larger time step sizes. The stability condition for explicit time integration scheme in PD theory is derived by Silling and Askari (2005) using the von Neumann stability as

$$\Delta t < \sqrt{\frac{2\rho_{(k)}}{\sum_j \frac{c}{\left| x_{(j)} - x_{(k)} \right|} V_{(j)}}} \times sf \tag{3.12}$$

in which sf is the safety factor and it can be taken as $sf < 1$. Safety factor ensures the stability of the analysis especially in nonlinear problems.

3.2.2.2 Implicit method

Implicit time integration scheme has the advantage of allowing the use of larger time step sizes. It is unconditionally stable for linear problems and it may also be the choice for nonlinear problems. However, it does not remain stable for very long times especially in large deformation analyses. Several implicit integration schemes are introduced in the literature, e.g. trapezoidal rule, Wilson θ method, Newmark β method, etc., and they can be used for solution of several types of problems. Specifically, Newmark β or Newmark's method is very common and is available in many software packages like ANSYS.

In implicit Newmark's time integration scheme, the PD equation of motion, provided in Equation (2.109), should be rewritten in a matrix form. The static PD equation given by Equation (3.6) can be extended with an additional acceleration term, $\ddot{\mathbf{U}}$, as

$$\mathbf{D}\ddot{\mathbf{U}} + \mathbf{K}\mathbf{U} = \mathbf{B} \tag{3.13}$$

where **K**, **U** and **B** are the stiffness matrix, the displacement vector and the body load vector, respectively.

While applying the implicit time integration steps or solving the problem quasi – statically, which is explained in Section 3.2.1.2, the failure can be incorporated by breaking the bonds. This is achieved by calculating the stretch of each bond and then checking the value of this against the critical stretch value, s_c. The stretch of each bond can be calculated as

$$s_{(k)(j)} = \frac{1}{\left|\boldsymbol{\xi}_{(k)(j)}\right|}\begin{Bmatrix} -C & -S & C & S \end{Bmatrix}\begin{Bmatrix} u_{x(k)} \\ u_{y(k)} \\ u_{x(j)} \\ u_{y(j)} \end{Bmatrix} \tag{3.14}$$

where $C = \mathrm{Cos}\,\theta_{(k)(j)}$ and $S = \mathrm{Sin}\,\theta_{(k)(j)}$ as well as θ indicates the angle of a bond with respect to *x* axis. Moreover, the bond is broken if $s_{(k)(j)} \geq s_c$.

Newmark's implicit time integration scheme can be advantageous over explicit scheme because of the larger time step sizes. Newmark's method is unconditionally stable in linear problems. However, it may become unstable in nonlinear analyses such as in large deformation and material nonlinearity problems. Implicit time integration schemes can be made more stable while checking the residuals after each time step and using the equilibrium iterations (Bathe and Baig, 2005). This may be achieved by using Newton-Raphson iterative method. FE software package, ANSYS, uses this methodology. On the other hand, one needs to solve the huge matrix equations in Newmark's method and also in other implicit time integration schemes. There are many methods, which may solve huge matrix equations as explained in Section 3.2.1.2. However the capability of ANSYS solver can also be exploited to solve these huge matrix equations as explained in Section 3.3.1.2.

3.3 Numerical Methods

PD equation of motion or static PD equation can be solved numerically with different type of discretization methods for various cases. The most commonly used methods are the quadrature formula methods (Emmrich and Weckner, 2007, 2006; Emmrich et al., 2013; Kilic, 2008), the midpoint method (Emmrich and Weckner, 2007; Madenci and Oterkus, 2014; Silling and Askari, 2005) and, recently, the finite element (FE) method (Chen and Gunzburger, 2011; Du et al., 2013a, 2013b; Emmrich and Weckner, 2007; Zhou and Du, 2010).

However, most researchers prefer the meshless midpoint rule since it is simple and easily applicable to discontinuities available in a body. In this section, firstly, the application of midpoint meshless method is introduced preceding the discussion about meshless domain in FE software, ANSYS. Apart from that the FE method can also be used for the PD solution of a body and there are few attempts in the literature. Hence, the applicability and the advantages of this mesh method are also explained.

3.3.1 Meshless methods

As mentioned in Section 3.3, solving PD domain using a meshless method is the most prevalent approach in the literature since the discontinuities can easily be represented without a mesh dependency.

3.3.1.1 Direct solution with midpoint method

The PD EOM is in integro-differential form and it can also be written in terms of summations as in Equation (2.109). Hence, the assumption used is that the infinite number of volumes composes the PD domain. From this point of view, the body can numerically be discretized into very small cubic volumes in three – dimension, quadratic areas in two – dimension or lines in one – dimension. Thus, each material point represents the center of each volume, area or line in Equation (2.109). The discretized form of two dimensional PD domain can be seen in Figure 3.3. In this figure, the main material point *k* and its volume are denoted by number 1 and $V_{(1)}$, respectively. The main material point or the material volume, $V_{(1)}$, interacts with other member material volumes, i.e. $V_{(2)}, V_{(3)}, \ldots$ etc., in its horizon, δ. Summing up the force

interactions, i.e. $\mathbf{f}_{(k)(j)}V_{(j)}$, individually for each main material point, i.e. $k=1,2,3,...$, leads to an unknown term of PD equation. This term is displacement **U** in ADR technique or in direct solution method as well as it is acceleration term $\ddot{\mathbf{u}}_{(k)}^{n}$ in explicit method or $\ddot{\mathbf{U}}^{n}$ in implicit method. The more detailed explanations for direct application of meshless method can be found in ref. (Silling and Askari, 2005) or in Chapter 7 of ref. (Madenci and Oterkus, 2014).

3.3.1.2 FE software

It is explained in Section 3.3.1.1 how the body can be discretized into many small finite volumes and how the force interactions are established between the material volumes. The same modelling procedure can also be achieved by any commercial FE software so that the meshless PD domain of a body is constructed. Thus, the solution and the post – processing capabilities of any FE software can be exploited in PD analyses. This procedure was first implemented by Macek and Silling (2007) by using the commercial FE software, ABAQUS. Furthermore, ANSYS can also be the preferred FE software for meshless implementation of PDs.

In order to solve the static problems in an FE software, the global static PD equation (Equation (3.6)) is constructed with truss elements. The dynamic problems may also be solved with an FE software and this is achieved by creating the mass elements on the nodes. This procedure forms diagonal mass matrix, **M**, for a PD domain. Similarly, multiplying both sides of dynamic PD EOM, given by Equation (3.13), with the volume of main material point, i.e. V, constructs such equation as given below.

$$\mathbf{M}\ddot{\mathbf{U}}+\mathbf{K}'\mathbf{U}=\mathbf{F} \tag{3.15}$$

where **M** is the diagonal mass matrix of a bond, which is

$$\mathbf{M}=\rho V\mathbf{I} \tag{3.16}$$

In the commercial FE software, ANSYS, the three dimensional LINK180 element can be used to model the bond interactions between the nodes and MASS21 element can be used to introduce the mass of a material volume. In this regard, LINK180 elements are created between the main material node *k* and its family member nodes *j* as in Figure 3.4a. Then, sequentially taking each node as a main and creating again the

LINK180 elements for its family members lead to network of truss elements in ANSYS as shown in Figure 3.4b. This procedure actually creates the global stiffness matrix for a body. Moreover, if the dynamic problem is intended to be solved, MASS21 elements are introduced onto the nodes. This procedure creates diagonal mass matrix for a body.

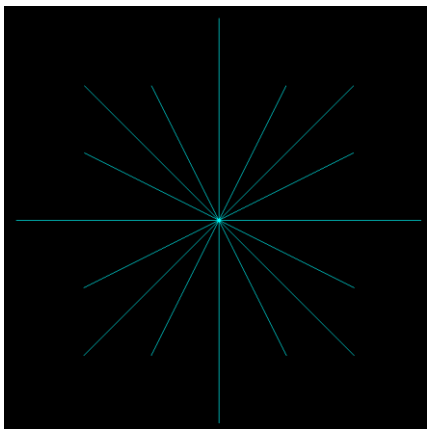

a) Link elements between the main node and its family members

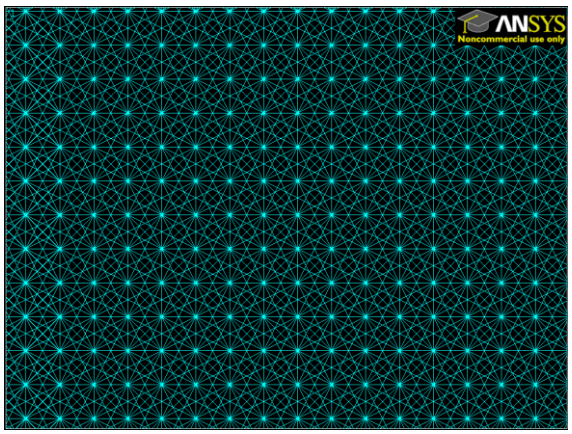

b) Network of link elements of a body

Figure 3.4 PD discretization with LINK180 and MASS21 elements in ANSYS

While solving PD problems in ANSYS, the failure can also be incorporated with a bond breakage procedure. This is achieved by calculating the stretch value of each bond and checking it against the critical value, s_c. If the stretch value of a bond exceeds the critical value, i.e. $s_{(k)(j)} \geq s_c$, it is broken with EKILL command. Thus, LINK element is deactivated in ANSYS.

In this section, it is briefly explained how the meshless PD domain can be created in any FE software and particularly in ANSYS. This introduces several advantages for solving PD meshless models. The capability of FE software in solving huge matrix equations can be utilized and its post – processor can be used for visualization of the bonds. For example, visualization of the bond interactions between material points along with their deformations can give better ideas while investigating the crack tips and openings in more detail. On the other hand, Newton – Raphson iterative scheme can be incorporated to the Newmark's method in ANSYS in order to solve nonlinear problems implicitly. Thus, the residuals of nonlinear PD equations are minimized in each step so that more stable solutions are obtained with larger time step sizes. Another point which is worth to mention is that the PD static equation or dynamic EOM, which

are introduced by Equations (3.6) and (3.13), can be solved with nonlinear option in FE software which allows larger deformations for truss elements. As a result, Equation (3.13), which is a linearized form of PD equation, converges to a nonlinear form of PD EOM, i.e. Equation (2.109).

3.3.2 Finite element method

Recently, the finite element (FE) method has attracted the researchers' attention for the solution of PD equations. Emmrich and Weckner (2007) compared all of the solution methods including the FE method by solving one-dimensional (1D) PD problem. In this problem, solution does not contain any discontinuities and it is found that FE method has the best accuracy amongst the others. However, it actually requires more computational time to solve the matrix equations. Although it is a common sense that meshless methods are the most convenient methods for PD problems with discontinuities, FE method with discontinuous piecewise finite element polynomials can solve these problems readily. Besides, the solution does not involve any jump terms as in the classical theory of elasticity because the governing equation of PD theory is derivative – free. Hence, discontinuous FE spaces are automatically conforming for the variational formulation of the PDs (Chen and Gunzburger, 2011) as in the case of continuous piecewise polynomials for smooth solutions. Chen and Gunzburger (2011) derived discontinuous piecewise - constant/linear and continuous piecewise - linear Galerkin finite element methods for 1D PDs. The convergence behaviors of these polynomial functions are studied for problems which have either smooth or discontinuous solutions. It is found that hybrid finite element spaces, which constitutes from both continuous and discontinuous FE functions, can be used effectively for problems with discontinuities in order to reduce computational time. Moreover, local gird refinement approach may also be considered for more robust results. Qiang Du et al. (2013a) studied a posteriori error estimation for PD problems comprised of discontinuous and continuous finite element functions and theoretical error estimations are verified with 1D and 2D numerical experiments. Following this, an adaptive FE method for PD models are proposed by Qiang Du et al. (2013b) and it is observed that the theoretical results of error estimations are independent from the horizon size, δ, provided that initial mesh size is smaller than $\delta/6$. Thus, horizon size

becomes merely a material parameter which only depends on nature of the material behavior. Finally, the convergence of PD – FE solutions to classical differential equations is indicated by Zhou and Du (2010) while both the mesh parameter, *h*, and the horizon size approach to zero.

To sum up, the above mentioned studies prove the strength and applicability of FE method for PD problems. In solving static problems, a body can be constructed with PD –FEs and naturally boundary elements are also formed. As a result, the global stiffness, displacement and force or body load matrices are built up. Applying the desired displacement boundary conditions to boundary elements of a body and/or applying the body loads to actual elements of a body lead to the PD construction of a problem with FE method.

It is apparent that solving PD problems with FE method may require less elements than the meshless method material volumes. Furthermore, very thin structures, e.g. plates, can be modelled with PD – FEs with the help of very thin rectangular prism form of PD – FE. On the other hand, discontinuities may also be represented in PD – FE method by using discontinuous FE functions instead of continuous ones and they are very convenient for derivative – free PD theory. However, there still can occur mesh dependency in crack propagation problems.

3.4 More Efficient PD Codes

Researchers are always in quest of very efficient and fast PD codes. This of course will make the PD theory more applicable to engineering structures and make it more ubiquitous. The in - house PD code mainly consists of 4 parts as;

1. Coordinate part; A body is composed of many small finite volumes and the center of each volume is represented by a material point. In this part, material points are created while specifying their locations in the coordinate system.
2. Family member search part; Family member points, which reside inside the horizon of each main material point, are determined and family member array is created.

3. Surface correction part; Horizon is usually truncated near the boundaries of a surface and this results in reduction of a material point stiffness. Hence, this stiffness reduction near free surfaces must be corrected. This procedure is explained in detail in Chapter 4 of ref. (Oterkus and Madenci, 2012).
4. Time integration part; PD domain of a problem is solved in time using one of the time integration methods.

In an in – house built code, the most time consuming parts are the family member search and time integration parts. In this section, two ways are proposed to improve the PD codes in these parts. Performing family member search in a very efficient way is demonstrated and argued that the search time can be reduced significantly. Then, the parallel programming procedures are discussed to reduce the solution time in the time integration part. Both or either one of these methods allow us to solve very complex problems effectively.

3.4.1 Family member search

Family member search for each main material point can be made very effective while partitioning body into many regions. By doing this, the time spent in the search of family members may be reduced dramatically. For example, the family search time of a rectangular prism, which is composed of $100\times100\times100$ material points in each direction, i.e. *x*, *y* and *z*, with a total of one million points, can be reduced roughly from 2300 seconds to 5 seconds. As a result, such significant time reduction allow us to model very complex 3 – dimensional structures in PDs.

3.4.1.1 Two – dimensional code

In order to achieve such reduction in time, a body, which is composed of many material points, should first be partitioned into many regions in the 1st (coordinate) part of a code, shown in Figure 3.5.

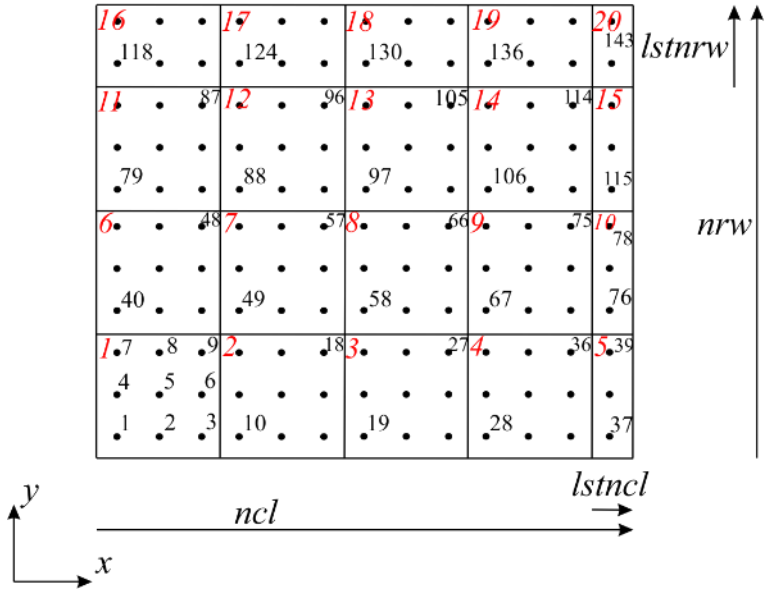

Figure 3.5 Regions in a 2 – dimensional body

In Figure 3.5, an example 2D body is shown. There, material point and region numbers are denoted by black and red colors, respectively. In constructing each region, particular attention is paid to locate 3 points along each direction, i.e. x and y, except the last regions. The reason of such partitioning is related to the horizon size, which is chosen as $\delta = 3\Delta x$, where Δx denotes the distance between adjacent material points. By doing this, family members of each main material point can only reside in its own and neighboring regions. It is also advised to define some region parameters in the 1st (coordinate) part of the code. In Figure 3.5, these parameters are shown and summarized as

ncl: Number of regions or number of columns along x – axis.

nrw: Number of regions or number of rows along y – axis.

lstncl: Number of points in the last region or in the last column along x - axis.

lstnrw: Number of points in the last region or in the last row along y - axis.

nrgn: Total number of regions.

region: An array which gives the first material point's number for each region.

Then, in the 2nd (family member search) part of the code, the family members for each material point should be decided. While family member arrays are created, the advantage of region partitioning is benefitted. Thus, the search time can be reduced

dramatically. Firstly, the main region's number and its neighboring regions' numbers are defined and searched for the family member points. For example, if the region 14 is chosen as a main region from Figure 3.5, the search for its family members is only done inside its neighboring regions, which are 8, 9, 10, 13, 15, 18, 19 and 20. Figure 3.6 shows such a search for the main material point 109 and these regions are also numbered locally which are depicted in blue color.

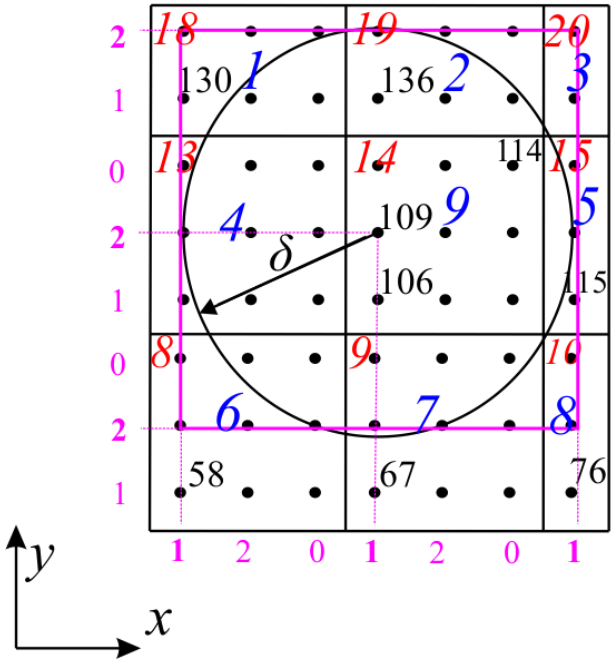

Figure 3.6 Family member search for a main material point 109

From this aspect, the main material point's number, which is in the main region, and the related family member numbers inside its horizon can be decided. Moreover, this family member search procedure can further be reduced to a pink colored rectangle area, shown in Figure 3.6. This is done by numbering the material points in each region in base 3 which is depicted in pink color numbers in Figure 3.6. For example, the main material point 109 possesses the numbers 1 and 2 in x and y directions, respectively. So, it is apparent that the borders of pink colored rectangle take also the same numbers in base 3. Thus, the family member search is only done in the pink colored rectangle area which includes 7×7 points.

3.4.2 Parallel programming procedures

PD codes, which are written by using any programming language, e.g. C, C++, FORTRAN or Java, can be solved or run with any computing facility available. This can be our desktop/laptop computer or high performance computing (HPC) facility. Generally, researchers tend to solve big and complex problems in HPC which can be made available by universities. However, without any modification to our regular codes, the advantage of such high performance computing facility can not be taken completely and even no improvement may be observed with such facilities compared to our desktops. In this regard, small modifications in our codes make possible to solve or run very huge problems. Moreover, we may not need to use HPC facility at all such that only desktops/laptops may be sufficient to solve such big problems. Nowadays, desktops/laptops include many central processing units (CPUs) and relatedly many cores in their architectures. As well as graphical processing units (GPUs) of computers have been improved above and beyond the expectations. Either one of or both of them can be employed in order to solve huge and complicated problems in our personal desktops/laptops.

In this section, the possibility of improving our codes and making them more efficient for huge problems are explained with the help of parallel programming procedures. In a common sense, engineers and researchers are not keen on engaging with parallel programming issues because they are considered complicated and time consuming. However, simple modifications may lead to a dramatic increase in computational speed.

3.4.2.1 General information

In order to solve huge and complex problems in our desktops or laptops within a reasonable time, PD codes must be modified to benefit from all processors available in the architecture. By doing such modifications, the parts of a problem can be solved independently by each processor, so-called the parallel programming procedure. The parts can either be the instructions of a code or be the huge data of a code which is in the form of arrays or matrices. In regular or serial solution procedure, the parts are executed or solved sequentially with only one processor. Figure 3.7 shows the difference between serial and parallel programming procedures.

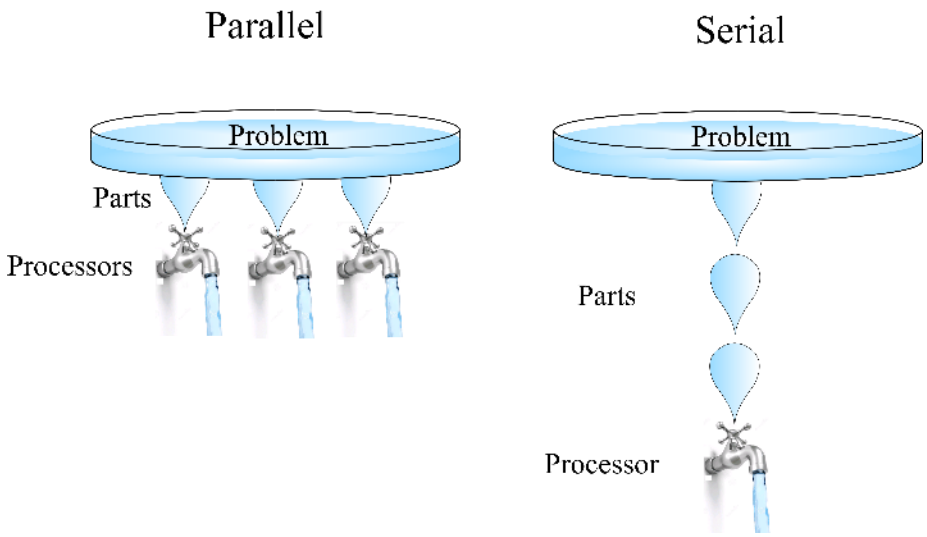

Figure 3.7 Types of programming procedures

Bearing in mind that the parts of a problem can be the instructions of a code and/or be the data in it. Hence, there are several ways of doing parallel programming and they can be named as single instruction multiple data (SIMD), multiple instruction single data (MISD) and multiple instruction multiple data (MIMD) procedures. Effectively, SIMD parallel programming type can be used to execute 4th (time integration) part of any PD code in which arrays with the huge data can be solved concurrently with many processors. In this method, all processors execute the same instruction, which is the time integration part, of a code.

To be more precise, whenever any PD code does not solve matrix equations, it is very simple to parallelize 4th (time integration) part of a code. The solution methods, which do not include matrices, are ADR and explicit methods as well as the meshless methods. In these methods, we do not have to solve linear equations simultaneously. More clearly, the force functions, $\mathbf{f}_{(k)(j)}$, are summed individually for each member material point, *j*, in time integration part and the unknown term, i.e. the acceleration or displacement term, is calculated. Due to independent calculation of the unknown term for each main material point *k*, SIMD parallel programming type is very convenient for the 4th (time integration) part of a code.

3.5 Conclusion

In this section, several solution methods in solving PD problems are demonstrated. These methods are firstly separated into groups. The first group shows the solution methods considering the problem types, i.e. static and dynamic problems and the second group comprises of numerical discretization methods. Each solution method is explained throughout the chapter while considering how and when to use them. It is believed that presenting such methods in one chapter may ease the understanding of PD theory. The literature can of course touch upon some methods in some extent regarding with the solution of an intended PD problem but the abundance of references may lead to a misunderstanding of PD theory. In addition to solution methods of PD theory, improving the PD codes and running them in a more efficient manner are also discussed. In this regard, the very efficient family member search method and the parallel programming procedures are introduced. All of these may give researcher an opportunity to solve very complex and big problems easily in PD theory. In the following chapters, the solution capacity of PD theory in solving such problems are demonstrated.

Chapter 4

Simplified Structures

4.1 Introduction

In Section 3.4, the very efficient ways of improving PD codes are explained in order to model large and complex structures. By using these methods, i.e. an efficient family member search algorithm and parallel programming procedures, the computational time can significantly be reduced. However, modeling very large and complicated structures such as aerospace and marine vehicles can still be computationally demanding. Therefore, the focus of this chapter is to propose PD eqautions of idealized or simplified structures such as beam and plate type of structures which accounts for transverse shear deformation. Thus, utilizing such simplified structures in PD modelling of engineering structures can make the computations more feasible. Moreover, the wave dispersion relations of such simplified structures can be obtained in PD theory and compared against the classical theory results. Dispersion relations basically show the wave propagation characterics of a structure in different wave lengths. The length scale parameter, which is a horizon, available in the PD theory gives a nonlocal character and the wave characteristics obtained may differ from the classical theory results in small scales such that the PD theory shows dispersion behavior similar to that observed in experiments of real materials. Hence, this property

of PD theory allows the modelling of physical phenomena not only at the macro-scale, but also at the various small scales, which leads to multi – scale analysis simulations.

4.2 Peridynamic Equations of Motions

In Section 2.4.2, it is explained how the PD equation of motion (EOM) can be obtained from principle of vitual work by using Lagrange's equation of motion. Futhermore, Madenci and Oterkus (2014) obtained an ordinary state based PD theory from the proposed strain energy density function, $W_{(k)}$, which is for three dimensional (3D) structures, in Section 2.4.3.1. Relatedly, the obtained PD force density function, $\mathbf{t}_{(k)(j)}$, given by Eqaution (2.45) is in 3D form and also substituting this into a PD equation of motion, i.e. Eqaution (2.24), results in 3D form of PD EOM. However, using the same force function, $\mathbf{t}_{(k)(j)}$, with different PD material parameters leads to PD EOM for one and two dimensional structures, named as simplified structures. Please also see the Section 2.4.4 for simplified structures in a bond based PD theory. Basically, in obtaining PD material parameters for such simplified structures, Madenci and Oterkus (2014) followed the procedure of equating the strain energy densities of CCM and PD theories for simple loading conditions, explained in Chapter 4 of Madenci and Oterkus (2014).

On the other hand, the equation(s) of motion for a simplified structure can also be obtained directly from proposed strain energy density function, which is in one or two dimensional form. Then, Lagrange's equation of motion can be benefitted to obtain the governing EOM in PDs. This is actually the similar procedure followed in Section 2.4.2 but now it is extended for simplified structures. Figure 4.1 shows the steps that must be followed in derivation process of E(s)OM with the related Peridynamic material parameter(s) for a simplified structure.

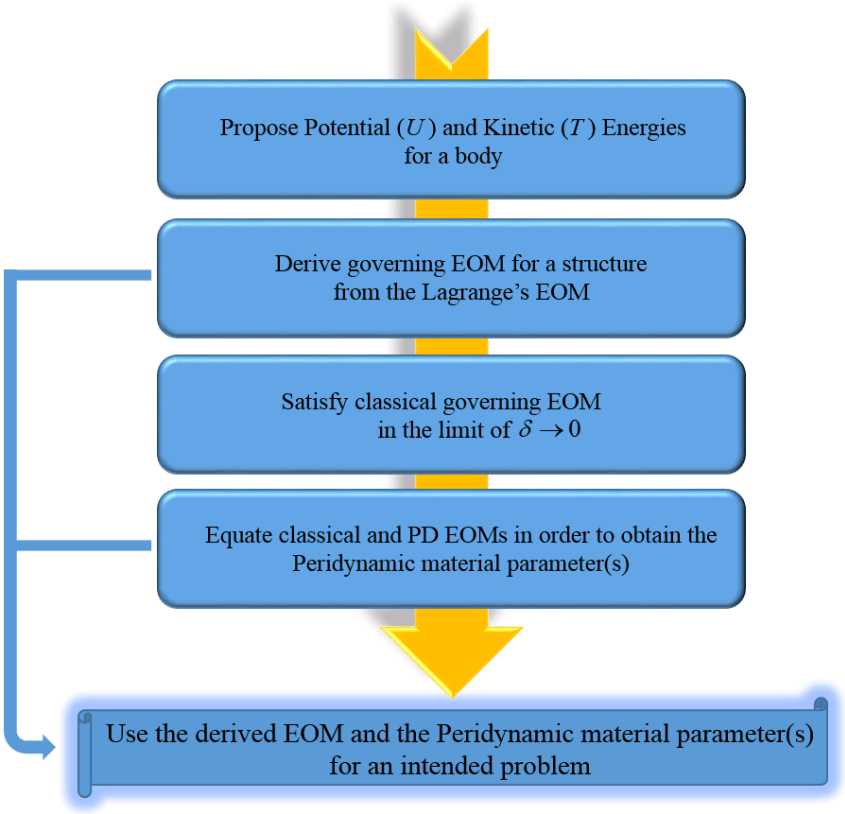

Figure 4.1 The steps of a derivation procedure for PD equations of a simplified structure

The aim of this section is to derive equation(s) of motions for beam and plate type of simplified structures in PDs and these include Timoshenko beam and Mindlin plate theories. Recently, Taylor and Steigmann (2015) proposed a plate model by using an asymptotic analysis based on a bond based PDs. However, their formulation is only capable of capturing transverse deformations of thin plates. Moreover, O'Grady and Foster (2014a, 2014b) developed a non – ordinary state based PD model for Euler beam and Kirchhoff – Love plate formulations by disregarding the transverse shear deformations. Therefore, the focus of this section is to present new PD formulations that are valid for thin and thick beams and plates. Briefly, the proposed formulations account for transverse shear deformations on a structure and the formulations are based on the bond based PD theory.

4.2.1 Timoshenko beam

4.2.1.1 Kinematics in PD theory

In Timoshenko beam theory, it is sufficient to use a single row of material points along the beam axis, *x*, in order to represent PD beam in a meshless discretizaton form as shown in Figure 4.2. Here, the shape of horizon is line however each material point has two degrees of freedom which are the transverse displacement, w, along *z* axis and the rotation of a material point, θ, about *y* axis. Below, the kinematic equations of a Timoshenko beam are derived based on the bond based PD theory.

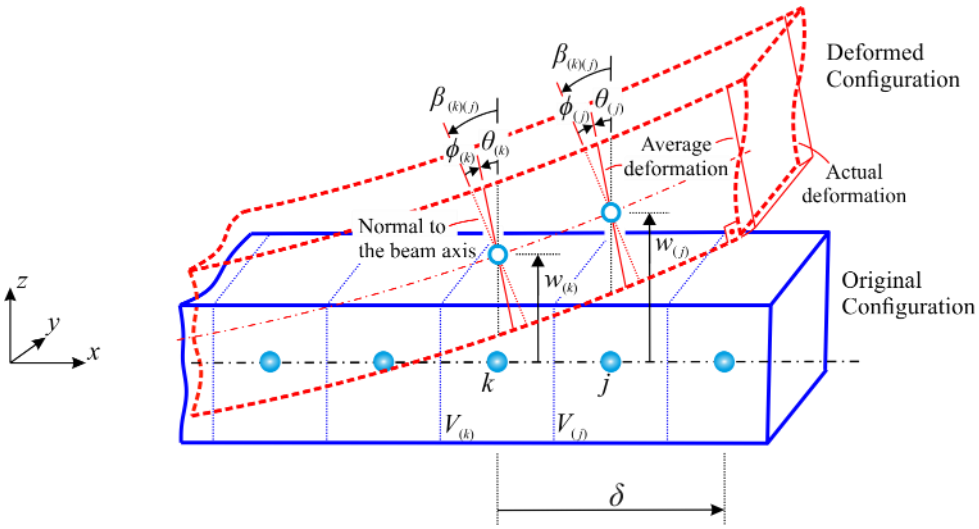

Figure 4.2 Kinematics of a Timoshenko beam in PD theory

In Figure 4.2, all of the rotations are in positive directions considering the sign convention adopted. Furthermore, $\beta_{(k)(j)}$ represents the slope of a bond between the material points, *k* and *j*, as well as ϕ denotes the shear rotation of each material point. Firstly, the slope of a bond can be expressed as

$$\beta_{(k)(j)} = \frac{w_{(j)} - w_{(k)}}{\xi_{(k)(j)}} \tag{4.1}$$

where $\xi_{(k)(j)}$ represents the distance between the material points, i.e. $\xi_{(k)(j)} = \left| x_{(k)} - x_{(j)} \right|$. This expression is very much similar to its classical counterpart, i.e. $\partial w / \partial x$, in the

limit of horizon approaches to zero, i.e. $\delta \to 0$, and it can basically be obtained from Taylor series expansion up to a first order term as

$$w_j = w_k + \frac{dw}{dx}\left(x_j - x_k\right) \quad \text{and} \quad \frac{dw}{dx} = \frac{w_j - w_k}{\xi_{(k)(j)}} \tag{4.2}$$

Apart from that, the shear rotations of material point *k* and *j* can be proposed as

$$\phi_{(j)} = \left(\frac{w_{(j)} - w_{(k)}}{\xi_{(k)(j)}} - \theta_{(j)} \operatorname{sgn}\left(x_{(j)} - x_{(k)}\right) \right) \tag{4.3}$$

$$\phi_{(k)} = \left(\frac{w_{(j)} - w_{(k)}}{\xi_{(k)(j)}} - \theta_{(k)} \operatorname{sgn}\left(x_{(j)} - x_{(k)}\right) \right) \tag{4.4}$$

It is obvious that the shear rotations of material points are very much similar to their classical counterpart, i.e. $\phi = \partial w / \partial x - \theta$, in the limit of horizon approaches to zero, i.e. $\delta \to 0$. Moreover, from Equations (4.3) and (4.4), the average transverse shear rotation of a bond, $\phi_{(k)(j)}$, can be derived as

$$\phi_{(k)(j)} = \left(\frac{w_{(j)} - w_{(k)}}{\xi_{(k)(j)}} - \frac{\theta_{(j)} + \theta_{(k)}}{2} \operatorname{sgn}\left(x_{(j)} - x_{(k)}\right) \right) \tag{4.5}$$

where the material point *k* is a point of interest and the $\operatorname{sgn}\left(x_{(j)} - x_{(k)}\right)$ function imposes a positive average shear rotation on a bond according to Figure 4.2. On the other hand, considering the material point *j* as a point of interest, the average shear rotation, $\phi_{(j)(k)}$, of a bond can be written in a similar manner with Equation (4.5) as

$$\phi_{(j)(k)} = \left(\frac{w_{(k)} - w_{(j)}}{\xi_{(k)(j)}} - \frac{\theta_{(j)} + \theta_{(k)}}{2} \operatorname{sgn}\left(x_{(k)} - x_{(j)}\right) \right) \quad \text{or} \quad \phi_{(j)(k)} = -\phi_{(k)(j)} \tag{4.6}$$

where the $\operatorname{sgn}\left(x_{(j)} - x_{(k)}\right)$ function now imposes the negative average shear rotation on a same bond according to Figure 4.2. As a result, the force densties, i.e. $\hat{t}_{(k)(j)}$ and $\hat{t}_{(j)(k)}$, arising from the shear deformations, $\phi_{(k)(j)}$ and $\phi_{(j)(k)}$, are formed in opposite directions but they have the same magnitudes in the same bond, as shown in Figure 4.3. Hence, the force densities can be assumed as

$$\hat{t}_{(k)(j)} = \frac{1}{2} c_s \left(\phi_{(k)(j)} \right) \quad \text{and} \quad \hat{t}_{(j)(k)} = \frac{1}{2} c_s \left(\phi_{(j)(k)} \right) \tag{4.7}$$

where c_s is the Peridynamic material parameter, which can also be named as shear bond constant because of its relation to the shear deformation. In Equation (4.7), $\hat{t}_{(k)(j)}$ represents the force density on a material point *k* and likewise $\hat{t}_{(j)(k)}$ is the force density on a material point *j* in the same bond. It is now obvious that these force densities are compatible with the bond based PD theory. Thus, the pairwise force function, $\hat{f}_{(k)(j)}$, related with the shear deformations of a bond can be derived from the force densities as

$$\hat{t}_{(k)(j)} = -\hat{t}_{(j)(k)} \quad \text{with} \quad \hat{f}_{(k)(j)} = 2\hat{t}_{(k)(j)} = c_s \left(\phi_{(k)(j)} \right) \tag{4.8}$$

in which $\hat{f}_{(k)(j)}$ is the pairwise force function of bond $k - j$ and it is on the material point, *k*.

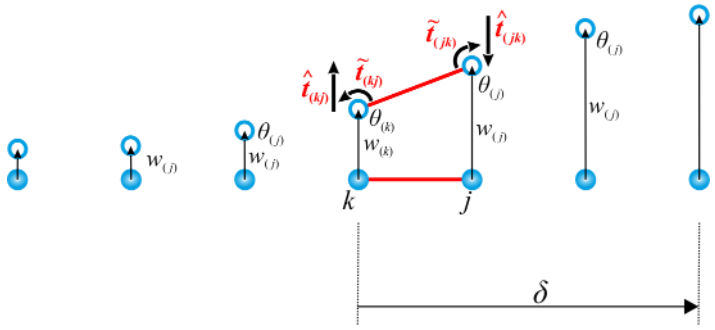

Figure 4.3 The force functions of a Timoshenko beam

Furthermore, the bending strain or curvature of a bond, i.e. $\kappa_{(k)(j)}$, between the material points, *k* and *j* can simply be proposed as

$$\kappa_{(k)(j)} = \left(\frac{\theta_{(j)} - \theta_{(k)}}{\xi_{(k)(j)}} \right) \tag{4.9}$$

where the material point *k* is a point of interest. It is apparent that Equation (4.9) is very much similar to its classical counterpart, i.e. $\kappa = \partial\theta / \partial x$, in the limit of horizon

approaches to zero, i.e. $\delta \to 0$, and it can basically be obtained from Taylor series expansion up to a first order term as

$$\theta_j = \theta_k + \frac{d\theta}{dx}\left(x_j - x_k\right) \quad \text{and} \quad \frac{d\theta}{dx} = \frac{\theta_j - \theta_k}{\xi_{(k)(j)}} \tag{4.10}$$

On the other hand, considering the material point *j* as a point of interest, the curvature, $\kappa_{(j)(k)}$, of a bond can be written in a similar manner with Equation (4.9) as

$$\kappa_{(j)(k)} = \left(\frac{\theta_{(k)} - \theta_{(j)}}{\xi_{(k)(j)}}\right) \quad \text{or} \quad \kappa_{(j)(k)} = -\kappa_{(k)(j)} \tag{4.11}$$

As a result, the force densties, i.e. $\tilde{t}_{(k)(j)}$ and $\tilde{t}_{(j)(k)}$, arising from the bending deformations, $\kappa_{(k)(j)}$ and $\kappa_{(j)(k)}$, are formed in opposite directions but they have the same magnitudes in a same bond, as shown in Figure 4.3, and so they can be assumed as

$$\tilde{t}_{(k)(j)} = \frac{1}{2} c_b\left(\kappa_{(k)(j)}\right) \quad \text{and} \quad \tilde{t}_{(j)(k)} = \frac{1}{2} c_b\left(\kappa_{(j)(k)}\right) \tag{4.12}$$

where c_b is the another Peridynamic material parameter which can also be named as bending bond constant because of its relation to the bending deformation. In Equation (4.12), the force densities are compatible with the bond based PD theory. Thus, the pairwise force function, $\tilde{f}_{(k)(j)}$, related with bending deformations of a bond can be derived from the force densities as

$$\tilde{t}_{(k)(j)} = -\tilde{t}_{(k)(j)} \quad \text{with} \quad \tilde{f}_{(k)(j)} = 2\tilde{t}_{(k)(j)} = c_b\left(\kappa_{(k)(j)}\right) \tag{4.13}$$

in which $\tilde{f}_{(k)(j)}$ is the pairwise force function of a bond $k - j$ and it is on the material point, *k*. Please also be aware that the relations given by Equations (4.8) and (4.13) are similar with the relations given by Equations (2.108) and (2.110) in Section 2.4.4.

After defining the main kinematic variables of the Timoshenko beam theory, the strain energy density function can be decomposed into two parts as

$$W_{(k)}^{PD} = W_{(k)}^{PD-bending} + W_{(k)}^{PD-shear} \tag{4.14}$$

where $W_{(k)}^{PD-bending}$ and $W_{(k)}^{PD-shear}$ represent the bending and the shear strain energy densities of a material point *k*. These strain energy densities can now be proposed as

$$\begin{aligned} W_{(k)}^{PD-bending} &= \frac{1}{2} c_b \sum_{j=1}^{\infty} \frac{1}{2} \left(\kappa_{(k)(j)} \right)^2 \xi_{(k)(j)} V_{(j)} \\ W_{(k)}^{PD-shear} &= \frac{1}{2} c_s \sum_{j=1}^{\infty} \frac{1}{2} \left(\phi_{(k)(j)} \right)^2 \xi_{(k)(j)} V_{(j)} \end{aligned} \tag{4.15}$$

where the summation function involves all the member material points, *j*, that are in the horizon of a main material point, *k.* Thus, the total potential energy of a beam is defined by summing all the main material volumes', i.e. $V_{(k)}$, strain energy densities over the domain with also considering the energies of external loads as

$$U^{PD} = \sum_{k=1}^{\infty} \left(\begin{array}{l} \frac{1}{2} c_b \sum_{j=1}^{\infty} \frac{1}{2} \left(\kappa_{(k)(j)} \right)^2 \xi_{(k)(j)} V_{(j)} + \\ \frac{1}{2} c_s \sum_{j=1}^{\infty} \frac{1}{2} \left(\phi_{(k)(j)} \right)^2 \xi_{(k)(j)} V_{(j)} - \hat{b}_{(k)} w_{(k)} - \tilde{b}_{(k)} \theta_{(k)} \end{array} \right) V_{(k)} \tag{4.16}$$

in which $\hat{b}_{(k)}$ and $\tilde{b}_{(k)}$ denote the body loads with units of "force/per unit volume" and "moment/per unit volume", respectively. Hence, they represent both the transverse load, $p(x)$, and the moment load, $m(x)$, of the classical beam theory. Then, the total kinetic energy for a beam body can be proposed with the help of its classical form as

$$T^{PD} = T_{rotational}^{PD} + T_{translational}^{PD} \tag{4.17}$$

with

$$\begin{aligned} T_{rotational}^{PD} &= \frac{1}{2} \frac{\rho I}{A} \sum_{k=1}^{\infty} \left(\dot{\theta}_{(k)} \right)^2 V_{(k)} \\ T_{translational}^{CCM} &= \frac{1}{2} \rho \sum_{k=1}^{\infty} \left(\dot{w}_{(k)} \right)^2 V_{(k)} \end{aligned} \tag{4.18}$$

Thus, the Lagrangian can be expressed as

$$
\begin{aligned}
L &= T^{PD} - U^{PD} \\
&= \frac{1}{2}\frac{\rho I}{A}\sum_{k=1}^{\infty}\left(\dot{\theta}_{(k)}\right)^2 V_{(k)} + \frac{1}{2}\rho\sum_{k=1}^{\infty}\left(\dot{w}_{(k)}\right)^2 V_{(k)} \\
&\quad - \sum_{k=1}^{\infty}\left(\begin{array}{l}
\dfrac{1}{2}c_b\displaystyle\sum_{j=1}^{\infty}\frac{1}{2}\left(\frac{\theta_{(j)}-\theta_{(k)}}{\xi_{(k)(j)}}\right)^2 \xi_{(k)(j)}V_{(j)} \\
+\dfrac{1}{2}c_s\displaystyle\sum_{j=1}^{\infty}\frac{1}{2}\left(\frac{w_{(j)}-w_{(k)}}{\xi_{(k)(j)}} - \frac{\theta_{(j)}+\theta_{(k)}}{2}\operatorname{sgn}\left(x_{(j)}-x_{(k)}\right)\right)^2 \xi_{(k)(j)}V_{(j)} - \hat{b}_{(k)}w_{(k)} - \tilde{b}_{(k)}\theta_{(k)}
\end{array}\right)V_{(k)}
\end{aligned}
\tag{4.19}
$$

It is now obvious that the Lagrangian is functions of $w_{(k)}$ and $\theta_{(k)}$ and the Euler – Lagrange equations take the form of

$$
\begin{aligned}
&\frac{d}{dt}\frac{\partial L}{\partial \dot{w}_{(k)}} - \frac{\partial L}{\partial w_{(k)}} = 0 \\
&\text{and} \\
&\frac{d}{dt}\frac{\partial L}{\partial \dot{\theta}_{(k)}} - \frac{\partial L}{\partial \theta_{(k)}} = 0
\end{aligned}
\tag{4.20}
$$

Substituting Equation (4.19) into Equation (4.20) yields the EsOM of a Timoshenko beam in PD theory as

$$
\begin{aligned}
\rho\ddot{w}_{(k)} &= c_s\sum_{j=1}^{\infty}\left(\frac{w_{(j)}-w_{(k)}}{\xi_{(k)(j)}} - \frac{\theta_{(j)}+\theta_{(k)}}{2}\operatorname{sgn}\left(x_{(j)}-x_{(k)}\right)\right)V_{(j)} + \hat{b}_{(k)} \\
\frac{\rho I}{A}\ddot{\theta}_{(k)} &= c_b\sum_{j=1}^{\infty}\left(\frac{\theta_{(j)}-\theta_{(k)}}{\xi_{(k)(j)}}\right)V_{(j)} + \frac{1}{2}c_s\sum_{j=1}^{\infty}\left(\frac{w_{(j)}-w_{(k)}}{\xi_{(k)(j)}}\operatorname{sgn}\left(x_{(j)}-x_{(k)}\right) - \frac{\theta_{(j)}+\theta_{(k)}}{2}\right)\xi_{(k)(j)}V_{(j)} + \tilde{b}_{(k)}
\end{aligned}
\tag{4.21}
$$

or they can also be expressed in the form of pairwise force functions, i.e. $\hat{f}_{(k)(j)}$ and $\tilde{f}_{(k)(j)}$, which are given by Equations (4.8) and (4.13), as

$$
\begin{aligned}
\rho\ddot{w}_{(k)} &= \sum_{j=1}^{\infty}\hat{f}_{(k)(j)}V_{(j)} + \hat{b}_{(k)} \\
\frac{\rho I}{A}\ddot{\theta}_{(k)} &= \sum_{j=1}^{\infty}\tilde{f}_{(k)(j)}V_{(j)} + \frac{1}{2}\sum_{j=1}^{\infty}\hat{f}_{(k)(j)}\operatorname{sgn}\left(x_{(j)}-x_{(k)}\right)\xi_{(k)(j)}V_{(j)} + \tilde{b}_{(k)}
\end{aligned}
\tag{4.22}
$$

In order to prove the validity of Peridynamic EsOM, given by Equations (4.21) or (4.22), it is shown that their classical counterparts, given by Equation (4.23), can be recovered in the limit of horizon size approaches to zero, i.e. $\delta \to 0$.

$$\begin{aligned} \rho\ddot{w} &= kG\left(\frac{\partial^2 w}{\partial x^2} - \frac{\partial \theta}{\partial x}\right) + p \\ \frac{\rho I}{A}\ddot{\theta} &= kG\left(\frac{\partial w}{\partial x} - \theta\right) + \frac{EI}{A}\frac{\partial^2 \theta}{\partial x^2} + m \end{aligned} \tag{4.23}$$

Therefore, the transverse displacement and the rotation of material point *j*, i.e. $w_{(j)}$ and $\theta_{(j)}$, are expressed in terms of main material point's degrees of freedom, i.e. $w_{(k)}$ and $\theta_{(k)}$, by using Taylor series expansions while ignoring the higher order terms as

$$\begin{aligned} w_{(j)} &= w_{(k)} + w_{(k),x}\xi_{(k)(j)}\,\mathrm{sgn}\left(x_{(j)} - x_{(k)}\right) + \frac{1}{2}w_{(k),xx}\xi_{(k)(j)}^2 \\ \theta_{(j)} &= \theta_{(k)} + \theta_{(k),x}\xi_{(k)(j)}\,\mathrm{sgn}\left(x_{(j)} - x_{(k)}\right) + \frac{1}{2}\theta_{(k),xx}\xi_{(k)(j)}^2 \end{aligned} \tag{4.24}$$

Substituting Equation (4.24) into PD EsOM, i.e. Equation (4.21), and performing some algebraic manipulations result in

$$\begin{aligned} \rho\ddot{w}_{(k)} &= \frac{1}{2}c_s\sum_{j=1}^{\infty}\left(w_{(k),xx} - \theta_{(k),x}\right)\xi_{(k)(j)}V_{(j)} + \hat{b}_{(k)} \\ \frac{\rho I}{A}\ddot{\theta}_{(k)} &= \frac{1}{2}c_b\sum_{j=1}^{\infty}\left(\theta_{(k),xx}\right)\xi_{(k)(j)}V_{(j)} + \frac{1}{2}c_s\sum_{j=1}^{\infty}\left(w_{(k),x} - \theta_{(k)} - \frac{1}{4}\theta_{(k),xx}\xi_{(k)(j)}^2\right)\xi_{(k)(j)}V_{(j)} + \tilde{b}_{(k)} \end{aligned} \tag{4.25}$$

where the infinitesimal volume of material point *j*, i.e. $V_{(j)}$, can also be expressed as $V_{(j)} = A\Delta\xi_{(k)(j)}$. There, $\Delta\xi_{(k)(j)}$ represents the spacing between two consecutive material points and it approaches to differential reference distance, i.e. $\Delta\xi_{(k)(j)} \to d\xi$ while converting the summation functions into integrations as

$$\begin{aligned} \rho\ddot{w} &= c_s\int_0^{\delta}\left(w_{,xx} - \theta_{,x}\right)\xi A d\xi + \hat{b} \\ \frac{\rho I}{A}\ddot{\theta} &= c_b\int_0^{\delta}\theta_{,xx}\xi A d\xi + c_s\int_0^{\delta}\left(w_{,x} - \theta - \frac{1}{4}\theta_{,xx}\xi^2\right)\xi A d\xi + \tilde{b} \end{aligned} \tag{4.26}$$

and performing the integrations in Equation (4.26) yields the PD EOM as

$$\begin{aligned}\rho\ddot{w} &= c_s \frac{A\delta^2}{2}\left(\frac{\partial^2 w}{\partial x^2} - \frac{\partial\theta}{\partial x}\right) + \hat{b} \\ \frac{\rho I}{A}\ddot{\theta} &= c_s \frac{A\delta^2}{2}\left(\frac{\partial w}{\partial x} - \theta\right) + \left(c_b \frac{A\delta^2}{2} - c_s \frac{A\delta^4}{16}\right)\frac{\partial^2\theta}{\partial x^2} + \tilde{b}\end{aligned} \tag{4.27}$$

It is now obvious that the obtained PD EsOM have the same form with their classical counterparts, given by Equation (4.23), for Timoshenko beam theory. The body loads, $\hat{b}$ and $\tilde{b}$, substitute for the transverse load, *p*, and the moment load, *m*, of the classical beam theory, respectively. Therefore, it can be concluded that the proposed potential, *U*, and kinetic, *T*, energy expressions given by Equations (4.16) and (4.17) – (4.18), are suitable for representation of the Timoshenko beam problem.

Finally, equating the coefficients of the unknown functions, i.e. *w* and θ, in the PD EsOM to the coefficients of that in the classical equation yields the relationships between the PD material parameters, c_s and c_b, and the shear and Young's moduli, *G* and *E*, as well as the second moment of the cross sectional area, *I*, and the shear correction factor, *k*, as

$$\begin{aligned}c_s &= \frac{2kG}{A\delta^2} \\ c_b &= \frac{2EI}{A^2\delta^2} + \frac{kG}{4A}\end{aligned} \tag{4.28}$$

As a result, PD EsOM, given in Equation (4.21), along with shear and bending bond constants, i.e. c_s and c_b, given in Equation (4.28) can be used for Timoshenko beam problems.

Surface corrections

Above, the Peridynamic material parameters, c_s and c_b, are derived under the assumption that the main material point, *k*, has a horizon which is completely embedded inside the beam body. Hence, the material points' stiffnesses in a beam are effected from the free surfaces or material interfaces as reductions. These reductions should be corrected with a surface correction coefficients.

The surface correction coefficients for a material point, *k*, in a beam can be calculated as

$$S_{s(k)} = \frac{W_{shear}^{CCM}}{W^{PD-shear}\left(\mathbf{x}_{(k)}\right)} \quad \text{and} \quad S_{b(k)} = \frac{W_{bending}^{CCM}}{W^{PD-bending}\left(\mathbf{x}_{(k)}\right)} \tag{4.29}$$

where $S_{s(k)}$ and $S_{b(k)}$ represent surface corrections for shear and bending Peridynamic material parameters, i.e. c_s and c_b, respectively. In order to find these parameters for near surface points, the simple loading conditions are considered as explained below.

Firslty, the beam is subjected to a simple shear loading, ζ, as shown in Figure 4.4. Under such loading condition, the shear strain energy density function, for any material point *k*, can be calculated from Equation (4.15) as

$$W_{(k)}^{PD-shear} = \frac{1}{2} c_s \sum_{j=1}^{\infty} \frac{1}{2} (\zeta)^2 \xi_{(k)(j)} V_{(j)} \quad \text{with} \quad \zeta = \phi_{(k)(j)} \tag{4.30}$$

It can be seen from Figure 4.4 that the material point, which is located nearly to the free surface, has a truncated horizon so that its shear stiffness is not complete.

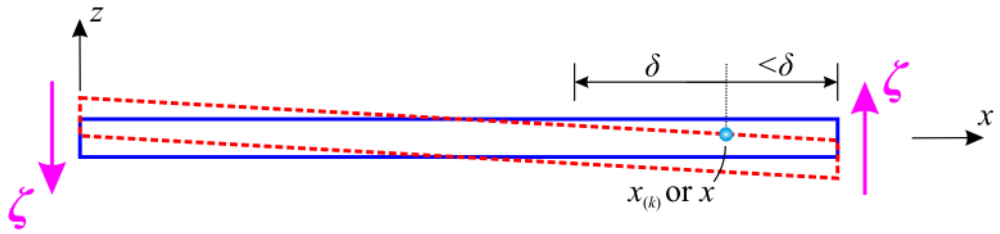

Figure 4.4 A beam subjected to a simple shear loading

Furthermore, the strain energy density of the same point can be calculated in classical theory as

$$W_{shear}^{CCM} = \frac{1}{2} kG\zeta^2 \quad \text{with} \quad \zeta = \phi \tag{4.31}$$

As a result, substituting Equations (4.30) and (4.31) into Equation (4.29) leads to a shear loading surface correction factor $S_{s(k)}$ for a material point, *k*.

Secondly, the beam is subjected to a constant curvature, ζ , as shown in Figure 4.5. Under such loading condition, the bending strain energy density function, for any material point *k*, can be calculated from Equation (4.15) as

$$W_{(k)}^{PD-bending} = \frac{1}{2} c_b \sum_{j=1}^{\infty} \frac{1}{2} (\zeta)^2 \xi_{(k)(j)} V_{(j)} \quad \text{with} \quad \zeta = \kappa_{(k)(j)} \tag{4.32}$$

It can be seen from Figure 4.5 that the material point, which is located nearly to the free surface, has a truncated horizon so that its bending stiffness is not complete.

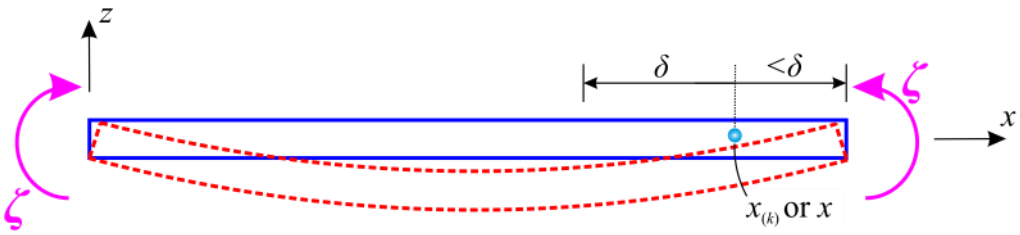

Figure 4.5 A beam subjected to a constant curvature loading

Furthermore, the strain energy density of the same point can be calculated in classical theory as

$$W_{bending}^{CCM} = \frac{1}{2} \frac{EI}{A} \zeta^2 \quad \text{with} \quad \zeta = \kappa \tag{4.33}$$

As a result, substituting Equations (4.32) and (4.33) into Equation (4.29) leads to a bending loading surface correction factor $S_{b(k)}$ for a material point, *k*.

Moreover, the surface correction factors, which are calculated for the material points *j* and *k*, can have the different values, therefore averaging these leads to the bond's surface corrections as

$$\bar{S}_s = \frac{S_{s(k)} + S_{s(j)}}{2} \quad \text{and} \quad \bar{S}_b = \frac{S_{b(k)} + S_{b(j)}}{2} \tag{4.34}$$

4.2.2 Mindlin plate

A two dimensional structure is basically considered as the extension of a one dimensional structure through second dimension, which is *y* – axis.

4.2.2.1 Kinematics in PD theory

In order to model Mindlin plate in PD theory, many rows of material points are modelled on the midplane and it is sufficient to use only single layer of material points in the thickness direction. Moreover, the shape of horizon is also a circle as in 2D plate theory. Plate bending behavior can be represented by considering Mindlin plate formulation which is an extension of Timoshenko beam formulation. In addition to the transverse displacement, *w* and rotation, θ_x, there is an additional rotational degree of freedom, θ_y for each material point, as shown in Figure 4.6.

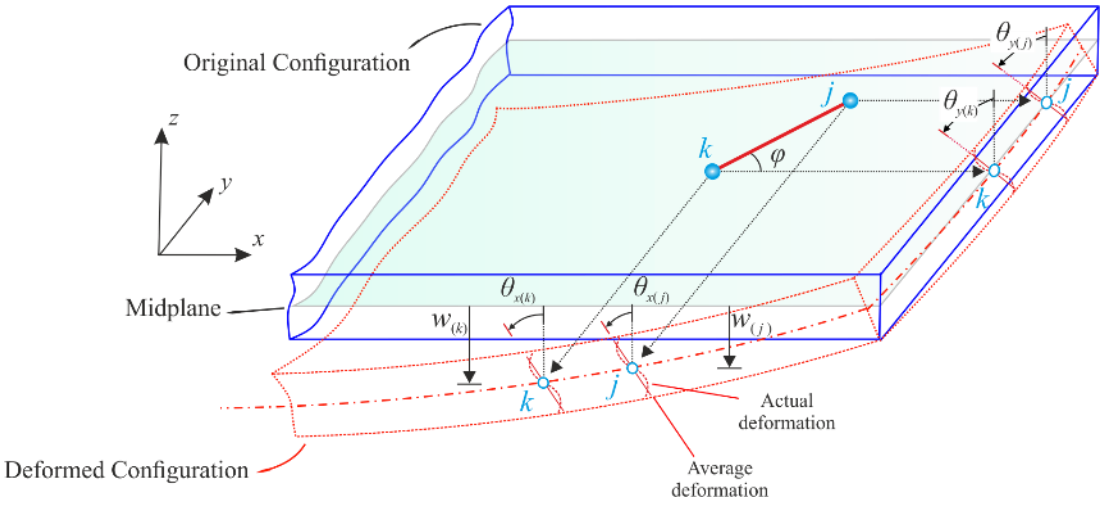

Figure 4.6 Kinematics of a Mindlin plate in PD theory

In Figure 4.6, all of the rotations are in positive directions considering the sign convention adopted. Furthermore, $\theta_{(j)}$ and $\theta_{(k)}$ represent the rotations with respect to the line of action between the material points *k* and *j*. Thus, considering the material point *k* as the point of interest, the average transverse shear rotation of a bond, $\phi_{(k)(j)}$, can be proposed as

$$\phi_{(k)(j)} = \frac{w_{(j)} - w_{(k)}}{\xi_{(j)(k)}} - \frac{\theta_{(j)} + \theta_{(k)}}{2} \tag{4.35}$$

Equation (4.35) is given with respect to a line of action and the rotations, $\theta_{(j)}$ and $\theta_{(k)}$, can be transformed to the coordinate axes, *x* and *y*, as

$$\theta_{(j)} = \theta_{x(j)} \cos\theta + \theta_{y(j)} \sin\varphi$$
$$\theta_{(k)} = \theta_{x(k)} \cos\theta + \theta_{y(k)} \sin\varphi \tag{4.36}$$

In this regard, Equation (4.35) can also be rewritten as

$$\phi_{(k)(j)} = \frac{w_{(j)} - w_{(k)}}{\xi_{(j)(k)}} - \frac{\left(\theta_{x(j)} \cos\varphi + \theta_{y(j)} \sin\varphi\right) + \left(\theta_{x(k)} \cos\varphi + \theta_{y(k)} \sin\varphi\right)}{2} \tag{4.37}$$

where "$\left(w_{(j)} - w_{(k)}\right)/\xi_{(j)(k)}$" represent the slope with respect to the line of action between the material points *j* and *k*. On the other hand, considering the material point *j* as a point of interest, the average shear rotation, $\phi_{(j)(k)}$, of a bond can be written in a similar manner with Equation (4.35) as

$$\phi_{(j)(k)} = \frac{w_{(k)} - w_{(j)}}{\xi_{(j)(k)}} - \left(-\frac{\theta_{(k)} + \theta_{(j)}}{2}\right) \tag{4.38}$$

As a result, the force densties, i.e. $\hat{t}_{(k)(j)}$ and $\hat{t}_{(j)(k)}$, arising from the shear deformations, $\phi_{(k)(j)}$ and $\phi_{(j)(k)}$, are formed in opposite directions but they have the same magnitudes in a same bond as in Timoshenko beam formulation, and so they can be assumed as

$$\hat{t}_{(k)(j)} = \frac{1}{2} c_s \left(\phi_{(k)(j)}\right) \quad \text{and} \quad \hat{t}_{(j)(k)} = \frac{1}{2} c_s \left(\phi_{(j)(k)}\right) \tag{4.39}$$

where c_s is the Peridynamic material parameter which is related to a shear deformation or shear bond constant. Thus, the pairwise force function, $\hat{f}_{(k)(j)}$, related with the shear deformations of a bond can be derived from the force densities as

$$\hat{t}_{(k)(j)} = -\hat{t}_{(k)(j)} \quad \text{with} \quad \hat{f}_{(k)(j)} = 2\hat{t}_{(k)(j)} = c_s \left(\phi_{(k)(j)}\right) \tag{4.40}$$

in which $\hat{f}_{(k)(j)}$ is the central force which is on the material point, *k*.

Furthermore, the bending strain or curvature of a bond, i.e. $\kappa_{(k)(j)}$, between the material points, *k* and *j* can be proposed as

$$\kappa_{(k)(j)} = \left(\frac{\theta_{(j)} - \theta_{(k)}}{\xi_{(k)(j)}}\right) \tag{4.41}$$

where the material point *k* is a point of interest. Again, Equation (4.41) is given with respect to a line of action and it can be rewritten along the coordinate axes, *x* and *y*, by using Equation (4.36) as

$$\kappa_{(k)(j)} = \left(\frac{\theta_{x(j)} - \theta_{x(k)}}{\xi_{(k)(j)}} \right) \cos\varphi + \left(\frac{\theta_{y(j)} - \theta_{y(k)}}{\xi_{(k)(j)}} \right) \sin\varphi \tag{4.42}$$

On the other hand, considering the material point *j* as a point of interest, the curvature, $\kappa_{(j)(k)}$, of a bond can be written in a similar manner with Equation (4.41) as

$$\kappa_{(j)(k)} = \left(\frac{\theta_{(k)} - \theta_{(j)}}{\xi_{(k)(j)}} \right) \quad \text{or} \quad \kappa_{(j)(k)} = -\kappa_{(k)(j)} \tag{4.43}$$

As a result, the force densties, i.e. $\tilde{t}_{(k)(j)}$ and $\tilde{t}_{(j)(k)}$, arising from the bending deformations, $\kappa_{(k)(j)}$ and $\kappa_{(j)(k)}$, are formed in opposite directions but they have the same magnitudes in the same bond, as in Timoshenko beam theory, and so they can be assumed as

$$\tilde{t}_{(k)(j)} = \frac{1}{2} c_b \left(\kappa_{(k)(j)} \right) \quad \text{and} \quad \tilde{t}_{(j)(k)} = \frac{1}{2} c_b \left(\kappa_{(j)(k)} \right) \tag{4.44}$$

where c_b is the another Peridynamic material parameter which is related to a bending deformation and it can also be named as bending bond constant. The pairwise force function, $\tilde{f}_{(k)(j)}$, related with the bending deformations of a bond can be derived from the force densities as

$$\tilde{t}_{(k)(j)} = -\tilde{t}_{(k)(j)} \quad \text{with} \quad \tilde{f}_{(k)(j)} = 2\tilde{t}_{(k)(j)} = c_b \left(\kappa_{(k)(j)} \right) \tag{4.45}$$

in which $\tilde{f}_{(k)(j)}$ is the central force which is on the material point, *k*.

After defining the main kinematic variables of the Mindlin plate theory, the strain energy density function can be expressed as

$$W_{(k)}^{PD} = W_{(k)}^{PD-bending} + W_{(k)}^{PD-shear} \tag{4.46}$$

where $W_{(k)}^{PD-bending}$ and $W_{(k)}^{PD-shear}$ represent the bending and the shear strain energy densities of a material point *k*. These strain energy densities can now be proposed as

$$W_{(k)}^{PD-bending} = \frac{1}{2} c_b \sum_{j=1}^{\infty} \frac{1}{2} \left(\kappa_{(k)(j)} \right)^2 \xi_{(k)(j)} V_{(j)}$$
$$W_{(k)}^{PD-shear} = \frac{1}{2} c_s \sum_{j=1}^{\infty} \frac{1}{2} \left(\phi_{(k)(j)} \right)^2 \xi_{(k)(j)} V_{(j)} \tag{4.47}$$

where $V_{(j)}$ represents infinitesimally small volume and it is in the form of $V_{(j)} = A_{(j)} h$ where $A_{(j)}$ is the surface area of the material point *j*. In Equation (4.47), the summation function involves all the member material points, *j*, that are in the horizon of a main material point, *k*. Thus, the total potential energy of a plate is defined by summing all the strain energy densities of the main material volumes, i.e. $V_{(k)}$, over the domain together with the energies of external loads as

$$U^{PD} = \sum_{k=1}^{\infty} \left(\begin{array}{l} \frac{1}{2} c_b \sum_{j=1}^{\infty} \frac{1}{2} \left(\kappa_{(k)(j)} \right)^2 \xi_{(k)(j)} V_{(j)} \\ + \frac{1}{2} c_s \sum_{j=1}^{\infty} \frac{1}{2} \left(\phi_{(k)(j)} \right)^2 \xi_{(k)(j)} V_{(j)} - \hat{b}_{(k)} w_{(k)} - \tilde{b}_{(k)} \theta_{(k)} \end{array} \right) V_{(k)} \tag{4.48}$$

or in an open form

$$U^{PD} = \sum_{k=1}^{\infty} \left(\begin{array}{l} \frac{1}{2} c_b \sum_{j=1}^{\infty} \frac{1}{2} \left(\left(\frac{\theta_{x(j)} - \theta_{x(k)}}{\xi_{(k)(j)}} \right) \cos\varphi + \left(\frac{\theta_{y(j)} - \theta_{y(k)}}{\xi_{(k)(j)}} \right) \sin\varphi \right)^2 \xi_{(k)(j)} V_{(j)} \\ + \frac{1}{2} c_s \sum_{j=1}^{\infty} \frac{1}{2} \left(\begin{array}{l} \frac{w_{(j)} - w_{(k)}}{\xi_{(j)(k)}} \\ - \frac{\left(\theta_{x(j)} \cos\varphi + \theta_{y(j)} \sin\varphi \right) + \left(\theta_{x(k)} \cos\varphi + \theta_{y(k)} \sin\varphi \right)}{2} \end{array} \right)^2 \xi_{(k)(j)} V_{(j)} \\ - \frac{\hat{b}_{(k)}}{h} w_{(k)} - \frac{\tilde{b}_{x(k)}}{h} \theta_{(k)} - \frac{\tilde{b}_{y(k)}}{h} \theta_{(k)} \end{array} \right) V_{(k)} \tag{4.49}$$

in which $\hat{b}_{(k)}$ denotes the body load related to the transver direction force as well as $\tilde{b}_{x(k)}$ and $\tilde{b}_{y(k)}$ denote the body loads related to the *x* and *y* direction moments. Moreover, they have the units of "force / unit area" and "moment / unit area", respectively. Hence, they represent both the transverse load, $p(x, y)$, and the moment

loads, $m_x(x,y)$ and $m_y(x,y)$, of the classical plate theory. Then, the total kinetic energy can be proposed with the help of its classical form as

$$T^{PD} = T^{PD}_{rotational} + T^{PD}_{translational} \tag{4.50}$$

and they can be expressed as

$$\begin{aligned} T^{PD}_{rotational} &= \frac{1}{2}\frac{\rho h^3}{12}\sum_{k=1}^{\infty}\left(\left(\dot{\theta}_{x(k)}\right)^2 + \left(\dot{\theta}_{y(k)}\right)^2\right)A_{(k)} \\ T^{PD}_{translational} &= \frac{1}{2}\rho h\sum_{k=1}^{\infty}\dot{w}^2_{(k)}A_{(k)} \end{aligned} \tag{4.51}$$

in which $A_{(k)}$ represents the infinitesimally small incremental area of each material point and *h* represents the thickness of the plate. Thus, the Lagrangian can be expressed as

$$\begin{aligned} L &= T^{PD} - U^{PD} \\ &= \frac{1}{2}\frac{\rho h^3}{12}\sum_{k=1}^{\infty}\left(\left(\dot{\theta}_{x(k)}\right)^2 + \left(\dot{\theta}_{y(k)}\right)^2\right)A_{(k)} + \frac{1}{2}\rho h\sum_{k=1}^{\infty}\dot{w}^2_{(k)}A_{(k)} \\ &\quad - \sum_{k=1}^{\infty}\left(\begin{array}{l} \frac{1}{2}c_b\sum_{j=1}^{\infty}\frac{1}{2}\left(\left(\frac{\theta_{x(j)}-\theta_{x(k)}}{\xi_{(k)(j)}}\right)\cos\varphi + \left(\frac{\theta_{y(j)}-\theta_{y(k)}}{\xi_{(k)(j)}}\right)\sin\varphi\right)^2\xi_{(k)(j)}V_{(j)} \\ +\frac{1}{2}c_s\sum_{j=1}^{\infty}\frac{1}{2}\left(\frac{w_{(j)}-w_{(k)}}{\xi_{(j)(k)}} - \frac{\left(\theta_{x(j)}\cos\varphi+\theta_{y(j)}\sin\varphi\right)+\left(\theta_{x(k)}\cos\varphi+\theta_{y(k)}\sin\varphi\right)}{2}\right)^2\xi_{(k)(j)}V_{(j)} \\ -\frac{\hat{b}_{(k)}}{h}w_{(k)} - \frac{\tilde{b}_{x(k)}}{h}\theta_{(k)} - \frac{\tilde{b}_{y(k)}}{h}\theta_{(k)} \end{array}\right)V_{(k)} \end{aligned} \tag{4.52}$$

It is now obvious that the Lagrangian is a function of $w_{(k)}$, $\theta_{x(k)}$ and $\theta_{y(k)}$ so that Euler – Lagrange equations take the form of

$$\frac{d}{dt}\frac{\partial L}{\partial \dot{w}_{(k)}}-\frac{\partial L}{\partial w_{(k)}}=0$$
$$\frac{d}{dt}\frac{\partial L}{\partial \dot{\theta}_{x(k)}}-\frac{\partial L}{\partial \theta_{x(k)}}=0 \tag{4.53}$$
and
$$\frac{d}{dt}\frac{\partial L}{\partial \dot{\theta}_{y(k)}}-\frac{\partial L}{\partial \theta_{y(k)}}=0$$

Substituting Equation (4.52) into Equation (4.53) yields the EsOM of a Mindlin plate in PD theory as

$$\rho h\ddot{w}_{(k)}=c_s\sum_{j=1}^{\infty}\left(\frac{w_{(j)}-w_{(k)}}{\xi_{(j)(k)}}-\frac{\theta_{x(j)}+\theta_{x(k)}}{2}\cos\varphi-\frac{\theta_{y(j)}+\theta_{y(k)}}{2}\sin\varphi\right)V_{(j)}+\hat{b}_{(k)}$$
$$\rho\frac{h^3}{12}\ddot{\theta}_{x(k)}=c_b\sum_{j=1}^{\infty}\left[\left(\frac{\theta_{x(j)}-\theta_{x(k)}}{\xi_{(j)(k)}}\right)\cos\varphi+\left(\frac{\theta_{y(j)}-\theta_{y(k)}}{\xi_{(j)(k)}}\right)\sin\varphi\right]\cos\varphi\,V_{(j)}$$
$$+\frac{1}{2}c_s\sum_{j=1}^{\infty}\xi_{(j)(k)}\left(\frac{w_{(j)}-w_{(k)}}{\xi_{(j)(k)}}-\frac{\theta_{x(j)}+\theta_{x(k)}}{2}\cos\varphi-\frac{\theta_{y(j)}+\theta_{y(k)}}{2}\sin\varphi\right)\cos\varphi\,V_{(j)}+\tilde{b}_{x(k)}$$
and
$$\rho\frac{h^3}{12}\ddot{\theta}_{y(k)}=c_b\sum_{j=1}^{\infty}\left[\left(\frac{\theta_{x(j)}-\theta_{x(k)}}{\xi_{(j)(k)}}\right)\cos\varphi+\left(\frac{\theta_{y(j)}-\theta_{y(k)}}{\xi_{(j)(k)}}\right)\sin\varphi\right]\sin\varphi\,V_{(j)}$$
$$+\frac{1}{2}c_s\sum_{j=1}^{\infty}\xi_{(j)(k)}\left(\frac{w_{(j)}-w_{(k)}}{\xi_{(j)(k)}}-\frac{\theta_{x(j)}+\theta_{x(k)}}{2}\cos\varphi-\frac{\theta_{y(j)}+\theta_{y(k)}}{2}\sin\varphi\right)\sin\varphi\,V_{(j)}+\tilde{b}_{y(k)} \tag{4.54}$$

In order to prove the validity of Peridynamic EsOM, it is shown that their classical counterparts, given by Equation (4.55), can be recovered in the limit of horizon size approaches to zero, i.e. $\delta\to 0$.

$$\rho h\ddot{w}=k^2Gh\left(\frac{\partial^2 w}{\partial x^2}+\frac{\partial^2 w}{\partial y^2}-\frac{\partial\theta_x}{\partial x}-\frac{\partial\theta_y}{\partial y}\right)+p$$
$$\frac{\rho h^3}{12}\ddot{\theta}_x=D\theta_{x,xx}+D\frac{1}{2}(1-\nu)\theta_{x,yy}+D\frac{1+\nu}{2}\theta_{y,xy}+k^2Gh\left(\frac{\partial w}{\partial x}-\theta_x\right)+m_x \tag{4.55}$$
and
$$\frac{\rho h^3}{12}\ddot{\theta}_y=D\theta_{y,yy}+D\frac{1}{2}(1-\nu)\theta_{y,xx}+D\frac{1+\nu}{2}\theta_{x,xy}+k^2Gh\left(\frac{\partial w}{\partial y}-\theta_y\right)+m_y$$

Therefore, the transverse displacement and the rotations of the material point *j*, i.e. $w_{(j)}$, $\theta_{x(j)}$ and $\theta_{y(j)}$, are expressed in terms of main material point's degrees of freedom, i.e. $w_{(k)}$, $\theta_{x(k)}$ and $\theta_{y(k)}$, by using Taylor series expansions while ignoring the higher order terms as

$$\begin{aligned}
w_{(j)} &= w_{(k)} + w_{(k),x}\xi_{(k)(j)}\cos\varphi + w_{(k),y}\xi_{(k)(j)}\sin\varphi + \frac{1}{2}w_{(k),xx}\xi^2_{(k)(j)}\cos^2\varphi \\
&\quad + w_{(k),xy}\xi^2_{(k)(j)}\cos\varphi\sin\varphi + \frac{1}{2}w_{(k),yy}\xi^2_{(k)(j)}\sin^2\varphi \\
\theta_{x(j)} &= \theta_{x(k)} + \theta_{x(k),x}\xi_{(j)(k)}\cos\varphi + \theta_{x(k),y}\xi_{(j)(k)}\sin\varphi + \frac{1}{2}\theta_{x(k),xx}\xi^2_{(j)(k)}\cos^2\varphi \\
&\quad + \theta_{x(k),xy}\xi^2_{(j)(k)}\cos\varphi\sin\varphi + \frac{1}{2}\theta_{x(k),yy}\xi^2_{(j)(k)}\sin^2\varphi \\
\theta_{y(j)} &= \theta_{y(k)} + \theta_{y(k),x}\xi_{(j)(k)}\cos\varphi + \theta_{y(k),y}\xi_{(j)(k)}\sin\varphi + \frac{1}{2}\theta_{y(k),xx}\xi^2_{(j)(k)}\cos^2\varphi \\
&\quad + \theta_{y(k),xy}\xi^2_{(j)(k)}\cos\varphi\sin\varphi + \frac{1}{2}\theta_{y(k),yy}\xi^2_{(j)(k)}\sin^2\varphi
\end{aligned} \tag{4.56}$$

The summation functions given in Equation (4.54) can simply be converted into integrations and the infinitesimal volume of material point *j*, i.e. $V_{(j)}$, can be expressed as $V_{(j)} = h\xi_{(k)(j)}\Delta\xi_{(k)(j)}\Delta\varphi_{(k)(j)}$. There, $\Delta\xi_{(k)(j)}$ represents the spacing between two consecutive material points and $\Delta\varphi_{(k)(j)}$ the angle between two consecutive bonds. These expressions approach to differentials as $\Delta\xi_{(k)(j)} \to d\xi$ and $\Delta\varphi_{(k)(j)} \to d\varphi$. Thus, the conversion process from summations to integrations can be achieved by "$\int_0^{2\pi}\int_0^{\delta} ....h\xi d\xi d\varphi$" expression. Substituting Equation (4.56) into PD EsOM, i.e. Equation (4.54), and converting the summation functions into integrations result in

$$\begin{aligned}
\rho h\ddot{w} &= \frac{\pi}{2}c_s h\frac{\delta^3}{3}\left(w_{,xx} + w_{,yy} - \theta_{x,x} - \theta_{y,y}\right) + \hat{b} \\
\rho\frac{h^3}{12}\ddot{\theta}_x &= \frac{\pi}{16}h\delta^3\left(c_b\frac{2}{3} - c_s\frac{\delta^2}{10}\right)\left[3\theta_{x,xx} + \theta_{x,yy} + 2\theta_{y,xy}\right] - \frac{\pi}{2}c_s h\frac{\delta^3}{3}\left(-w_{,x} + \theta_x\right) + \tilde{b}_x \\
\rho\frac{h^3}{12}\ddot{\theta}_y &= \frac{\pi}{16}h\delta^3\left(c_b\frac{2}{3} - c_s\frac{\delta^2}{10}\right)\left[3\theta_{y,yy} + \theta_{y,xx} + 2\theta_{x,xy}\right] - \frac{\pi}{2}c_s h\frac{\delta^3}{3}\left(-w_{,y} + \theta_y\right) + \tilde{b}_y
\end{aligned} \tag{4.57}$$

It is now obvious that the obtained PD EsOM have the same form with their classical counterparts, given by Equation (4.55). As mentioned before, the body loads, $\hat{b}$, $\tilde{b}_x$ and $\tilde{b}_y$, substitute for the transverse load, *p*, and the moment loads, m_x and m_y, of the classical plate theory, respectively. Therefore, it can be concluded that the proposed potential, *U*, and kinetic, *T*, energy expressions given by Equations (4.48) – (4.49) and (4.50) – (4.51), are suitable for representation of the Mindlin plate problem.

Finally, equating the coefficients of the unknow functions, i.e. *w*, θ_x and θ_y, between the PD EsOM and the classical equations yields the relationships between the PD material parameters, c_s and c_b, and the Young's modulus, *E*, as well as the shear correction factor, k^2, as

$$c_s = \frac{9E}{4\pi\delta^3}k^2 \quad \text{and} \quad c_b = \frac{E}{\pi\delta}\left(\frac{3h^2}{4\delta^2}+\frac{27}{80}k^2\right) \tag{4.58}$$

with

$$\nu = \frac{1}{3} \tag{4.59}$$

Again, the constraint on the Poisson's ratio is found and it is the same value with the 2D plate under in – plane loads problem. Hence, the flexural rigidty, *D*, and the shear modulus, *G*, are defined as

$$D = \frac{Eh^3}{12\left(1-\nu^2\right)} = \frac{3Eh^3}{32} \quad \text{and} \quad G = \frac{E}{2\left(1+\nu\right)} = \frac{3E}{8} \tag{4.60}$$

As a result, the PD EsOM, given in Equation (4.54), along with shear and bending bond constants, i.e. c_s and c_b, given in Equation (4.58) can be used for Mindlin plate problems.

Surface corrections

The surface correction are again the two dimensional extended form of Timoshenko beam problem. Here, the strain energy density of a Mindlin plate can be separated into two parts that are the bending and shear energy densities. Strain energy density due to bending in the classical theory can be expressed as

$$W_{bending}^{CCM}\left(x_{(k)}\right)=\frac{1}{2}D\left(\kappa_x^2+2\nu\kappa_x\kappa_y+\kappa_y^2+\frac{1-\nu}{2}\kappa_{xy}^2\right) \tag{4.61}$$

where the curvatures are; $\kappa_x=\theta_{x,x}$, $\kappa_y=\theta_{y,y}$, and $\kappa_{xy}=\theta_{x,y}+\theta_{y,x}$. Its counterpart in the PD theory can be expressed in discretized form as

$$W_{bending}^{PD}\left(x_{(k)}\right)=\frac{1}{2}\sum_{j=1}^{\infty}\frac{c_b}{2}\left(\kappa_{(k)(j)}\right)^2\xi_{(j)(k)}V_{(j)} \tag{4.62}$$

Considering pure bending loading along the *x* and *y* directions, i.e. $M_x=M_y\neq 0$, and $M_{xy}=0$, results in curvatures

$$\kappa_x=\kappa_y\neq 0 \quad \text{and} \quad \kappa_{xy}=0. \tag{4.63}$$

The classical and PD strain energy densities for this loading condition become

$$W_{bending}^{CCM}\left(x_{(k)}\right)=\frac{1}{2}D\left(\kappa_x^2+2\nu\kappa_x\kappa_y+\kappa_y^2\right) \tag{4.64}$$

and

$$W_{bending}^{PD}\left(x_{(k)}\right)=\frac{1}{2}\sum_{j=1}^{\infty}\frac{c_b}{2}\left(\kappa_x\cos^2(\varphi)+\kappa_y\sin^2(\varphi)\right)^2\xi_{(j)(k)}V_{(j)} \tag{4.65}$$

Hence, the surface correction factor for pure bending can be defined as

$$S_b\left(x_{(k)}\right)=\frac{W_{bending}^{CCM}\left(x_{(k)}\right)}{W_{bending}^{PD}\left(x_{(k)}\right)} \tag{4.66}$$

On the other hand, the strain energy density due to transverse shear deformation in the classical theory can be written as

$$W_{shear}^{CCM}\left(x_{(k)}\right)=\frac{1}{2}Gk^2h\left(\left(\phi_x\right)^2+\left(\phi_y\right)^2\right) \tag{4.67}$$

where $\phi_x=w_{,x}-\theta_x$ and $\phi_y=w_{,\mathrm{y}}-\theta_y$. Its counterpart in the PD theory can be expressed in discretized form as

$$W_{shear}^{PD}\left(x_{(k)}\right)=\frac{1}{2}\sum_{j=1}^{\infty}\frac{c_s}{2}\left(\phi_{(k)(j)}\right)^2\xi_{(j)(k)}V_{(j)} \tag{4.68}$$

Applying pure shear loading along the x – direction, i.e. $Q_x \neq 0$ and $Q_y = 0$, results in shear angles

$$\phi_x \neq 0 \text{ and } \phi_y = 0. \tag{4.69}$$

Then, classical and PD strain energy densities for this loading condition become

$$W_{shear}^{CCM}\left(x_{(k)}\right) = \frac{1}{2} G k^2 h \left(\phi_x\right)^2 \tag{4.70}$$

and

$$W_{shear}^{PD}\left(x_{(k)}\right) = \frac{1}{2} \sum_{j=1}^{\infty} \frac{c_s}{2} \left(\phi_x \cos\left(\varphi\right)\right)^2 \xi_{(j)(k)} V_{(j)} \tag{4.71}$$

Similar results can also be obtained for pure shear loading along the y – direction as

$$W_{shear}^{CCM}\left(x_{(k)}\right) = \frac{1}{2} G k^2 h \left(\phi_y\right)^2 \tag{4.72}$$

and

$$W_{shear}^{PD}\left(x_{(k)}\right) = \frac{1}{2} \sum_{j=1}^{\infty} \frac{c_s}{2} \left(\phi_y \sin\left(\varphi\right)\right)^2 \xi_{(j)(k)} V_{(j)} \tag{4.73}$$

Similar to pure bending, the correction factor for pure shear loading can be obtained as

$$S_s\left(x_{(k)}\right) = \frac{W_{shear}^{CCM}\left(x_{(k)}\right)}{W_{shear}^{PD}\left(x_{(k)}\right)} \tag{4.74}$$

The surface correction factors for material point j and material point k can have different values; therefore, the surface correction factors for an interaction between material point j and material point k can be taken as their average

$$\overline{S}_b = \frac{S_b\left(x_{(k)}\right) + S_b\left(x_{(j)}\right)}{2} \tag{4.75}$$

and

$$\overline{S}_s = \frac{S_s\left(x_{(k)}\right) + S_s\left(x_{(j)}\right)}{2} \tag{4.76}$$

4.2.3 Boundary conditions

The boundary conditions are imposed through a nonzero volume of fictitious boundary layers. This necessity arises because the PD field equations do not contain any spatial derivatives; therefore, constraint conditions are, in general, not necessary for the solution of an integro-differential equation. However, such conditions can be imposed by prescribing constraints through a fictitious boundary layer. In simplified structure theories, displacement or rotation constraint is introduced outside the actual material with introducing a fictitious boundary layer, R_c, as shown in Figure 4.7. The size of this layer is equivalent to the horizon. An external load, such as a moment or a transverse load, can be applied in the form of body loads through a layer within the actual material, R_ℓ. This layer can be 1/3 of the horizon size.

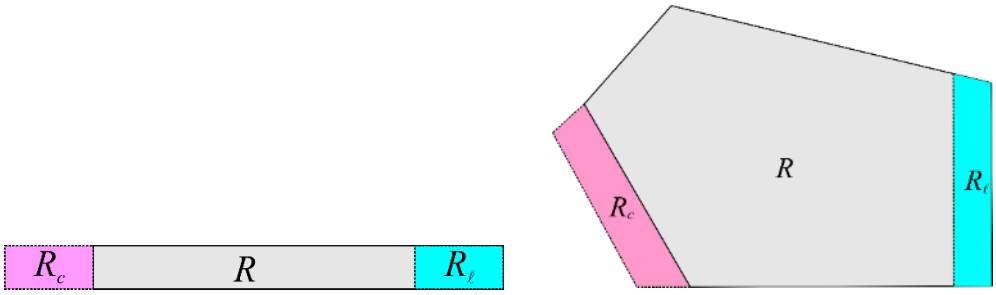

(a) (b)

Figure 4.7 Application of boundary conditions in Peridynamics: (a) beam and (b) plate

4.2.4 Critical values

The incorporation of damage to a Mindlin plate theory is a bit different than the usual calculations given in Section 2.4.5. In order to include failure in the material response, again the response functions, i.e. force – stretch/curvature relations, in the governing equations for the Mindlin plate should be modified through a history – dependent scalar value function, $H(x_{(j)} - x_{(k)}, t)$ as

$$\hat{f}_{(k)(j)} = c_s H\left(x_{(j)} - x_{(k)}, t\right)\left(\phi_{(k)(j)}\right) \tag{4.77}$$

and

$$\tilde{f}_{(k)(j)} = c_b H\left(x_{(j)} - x_{(k)}, t\right)\left(\kappa_{(k)(j)}\right) \tag{4.78}$$

and it is defined as

$$H\left(x_{(j)} - x_{(k)}, t\right) = \begin{cases} 1 & \text{if } \left|\kappa_{(k)(j)}\left(x_{(j)} - x_{(k)}, t'\right)\right| < \kappa_c \text{ and } \left|\varphi_{(k)(j)}\left(x_{(j)} - x_{(k)}, t'\right)\right| < \varphi_c \\ 0 & \text{otherwise} \end{cases} \tag{4.79}$$

Critical curvature and angle values can be expressed in terms of the critical energy release rate of the material. In order to find these relationships, the total strain energy required to remove all of the interactions across a newly created crack surface, *A*, shown in Figure 2.17, must be determined and equated to the corresponding critical energy release rate value.

The total bending strain energy required to remove all of the interactions across the new crack surface *A* is

$$W^c_{bending} = \sum_{k=1}^{K^+}\sum_{j=1}^{J^-}\frac{1}{2}c_b\left(\kappa_c\right)^2\left(\left|\mathbf{x}_{(j^-)} - \mathbf{x}_{(k^+)}\right|\right)V_{(k^+)}V_{(j^-)} \tag{4.80}$$

The total bending strain energy, $W^c_{bending}$, can be equated to the mode – I critical energy release rate, G_{Ic}, in order to determine the value of the bending critical curvature as

$$G_{Ic} = \frac{\frac{1}{2}c_b\left(\kappa_c\right)^2\sum_{k=1}^{K^+}\sum_{j=1}^{J^-}\left(\left|\mathbf{x}_{(j^-)} - \mathbf{x}_{(k^+)}\right|\right)V_{(k^+)}V_{(j^-)}}{A} \tag{4.81}$$

Based on the expression derived by Silling and Askari, 2005 and Madenci and Oterkus (2014) for the critical energy release rate, it is evident that

$$\frac{\sum_{k=1}^{K^+}\sum_{j=1}^{J^-}\left(\left|\mathbf{x}_{(j^-)} - \mathbf{x}_{(k^+)}\right|\right)V_{(k^+)}V_{(j^-)}}{A} = \frac{h\delta^4}{2} \tag{4.82}$$

Finally, the critical curvature can be expressed as

$$\kappa_c = \sqrt{\frac{4G_{Ic}}{c_b h\delta^4}} \tag{4.83}$$

Similarly, the total shear strain energy required to remove all of the interactions across the surface *A* is

$$W_{shear}^{c} = \sum_{k=1}^{K^{+}} \sum_{j=1}^{J^{-}} \frac{1}{2} c_s \left(\phi_c\right)^2 \left(\left| \mathbf{x}_{(j^-)} - \mathbf{x}_{(k^+)} \right| \right) V_{(k^+)} V_{(j^-)} \tag{4.84}$$

This total shear strain energy, W_{shear}^{c}, can be equated to the mode – III critical energy release rate, G_{IIIc}, in order to determine the value of the critical shear angle as

$$G_{IIIc} = \frac{\frac{1}{2} c_s \left(\phi_c\right)^2 \sum_{k=1}^{K^{+}} \sum_{j=1}^{J^{-}} \left(\left| \mathbf{x}_{(j^-)} - \mathbf{x}_{(k^+)} \right| \right) V_{(k^+)} V_{(j^-)}}{A} \tag{4.85}$$

By using the relationship given in Equation (4.82), the critical shear angle can be obtained as

$$\phi_c = \sqrt{\frac{4G_{IIIc}}{c_s h \delta^4}} \tag{4.86}$$

4.3 Peridynamic Dispersion Relations

4.3.1 Introduction

Dispersion relation is basically the propagation bevahiour of a wave in a structure at very small length scales. In classical theory only special case in the long wavelength limit can be captured; however, the PD theory results shows the dispersion behavior similar to that observed in real material experiments. In principle, the length – scale parameter, i.e. horizon, is the advantage of the PD theory over the classical continuum mechanics. The horizon size introduces PD theory a nonlocal character. Hence, physical phenomena can be captured not only at the macro – scale, but also at other scales.

It is proven that multi-scale analysis simulations can be performed with PD theory and also with the proposed simplified structures given in this section. With the increase of use of micro and nano structures in engineering systems, i.e. micro-electro-mechanical

systems (MEMS) and nano-electro-mechanical systems (NEMS), it is inevitable to take advantage of simplified structures, such as beam, plate etc., in these systems.

The advantage of Peridynamic theory over the other non local theories is that there is no need to deal with adaptation of appropriate boundary conditions to non local effects. Because EsOMs do not involve any derivatives of stresses or displacements. Thus, PD theory of simplified stuructures can take the place of non local theories explained here. Micro and nano structures can be easily modelled with the simplified theories of PDs. There have been already some attempts found in the literature for the application of Peridynamic theory to micro or nano structures. However, EsOMs for Timoshenko beam and Mindlin plate have not been used before in the literature. These theories are very important to utilize the Peridynamic theory for MEMS and NEMS because they also have the ability of modelling thick structures. The purpose of this section is to show dispersion relations of simplified structures in order to prove the applicability of PD theory for small scale simplified structures.

4.3.2 Timoshenko beam

The governing equation of motion for Timoshenko beam is given in Equation (4.21) in summation form and it can also be expressed in integral form when the elements of summation go to infinity as

$$\begin{aligned}\rho\ddot{w} &= Ac_s\int_{\delta}\left(\frac{w'-w}{\xi}-\frac{\theta'+\theta}{2}\operatorname{sgn}\left(x'-x\right)\right)d\xi \\ \frac{\rho I}{A}\ddot{\theta} &= Ac_b\int_{\delta}\frac{\theta'-\theta}{\xi}d\xi+\frac{1}{2}Ac_s\int_{H}\left(\frac{w'-w}{\xi}\operatorname{sgn}\left(x'-x\right)-\frac{\theta'+\theta}{2}\right)\xi d\xi\end{aligned} \tag{4.87}$$

where w' and θ' indicate member material points inside the horizon of w and θ. The differential volume has the form of $dV = Ad\xi$. Equation (4.87) can also be expressed in the limit of horizon approaches to zero, $\delta \to 0$, as given in Equation (4.26), which is the similar form with the classical theory of elasticity. However, the long range forces have also effect in Peridynamic theory for which the horizon values are not equal to zero.

Again, Peridynamic dispersion relations are compared against the classical Timoshenko theory. In the derivation of these dispersion relations, the wave number,

the wave frequency and phase velocity of the wave are denoted by κ, ω, and υ, respectively. The relationship among these parameters is $\omega = \kappa\upsilon$. The compressional and shear wave speeds are defined by $\upsilon_c^2 = E/\rho$ and $\upsilon_s^2 = G/\rho$, respectively, where *G* and *E* are the shear and Young's moduli of the material. The wave number is related to the half-wavelength, Γ, by the relationship $\kappa = \pi/\Gamma$.

In this regard, dispersion relations are determined by considering a wave propagating in the *x* direction. Therefore, wave solutions for material points located at *x* and x' can be expressed as

$$w(x,t) = w_0 e^{i(\kappa x - \omega t)} \text{ and } w(x',t) = w_0 e^{i(\kappa x - \omega t + \text{sgn}(x'-x)\kappa\xi)} \tag{4.88}$$

$$\theta(x,t) = \theta_0 e^{i(\kappa x - \omega t)} \text{ and } \theta(x',t) = \theta_0 e^{i(\kappa x - \omega t + \text{sgn}(x'-x)\kappa\xi)} \tag{4.89}$$

in which w_0 and θ_0 represent the amplitudes of waves and $\kappa\xi$ is the phase difference between the material points located at *x* and x'. The $\text{sgn}(x'-x)$ function here represents both the left and right going wave. Substituting these wave solutions into the PD equations of motion given in Equation (4.87) leads to a homogeneous set of equations for θ_0 and w_0 and for a nontrivial solution to exist, the determinant of their coefficient matrix must vanish, resulting in the wave dispersion relation as

$$\begin{vmatrix} 2Ac_sB_2 - \rho\omega^2 & Ac_sB_3 \\ -Ac_sB_3 & 2Ac_bB_2 + \frac{1}{2}Ac_sB_1 - \rho\frac{I}{A}\omega^2 \end{vmatrix} = 0 \tag{4.90}$$

The terms appearing in Equation (4.90) are defined as

$$B_1 = \int_0^\delta \left(1 + \cos(\kappa\xi)\right)\xi d\xi \tag{4.91}$$

$$B_2 = \int_0^\delta \frac{\left(1 - \cos(\kappa\xi)\right)}{\xi} d\xi \tag{4.92}$$

and

$$B_3 = \int_0^\delta i\sin(\kappa\xi)\, d\xi \tag{4.93}$$

and they are dependent on the phase difference and the horizon. As suggested by Silling (2000), in the limit of long wavelength (or small κ), these integrals can be analytically evaluated by considering the first three terms of the Taylor series expansion of the cosine and sine functions

$$\cos(\kappa\xi) = 1 - \frac{(\kappa\xi)^2}{2!} + \frac{(\kappa\xi)^4}{4!} - \ldots \tag{4.94}$$

and

$$\sin(\kappa\xi) = \kappa\xi - \frac{(\kappa\xi)^3}{3!} + \frac{(\kappa\xi)^5}{5!} - \ldots \tag{4.95}$$

With the evaluation of these integrals and considering the PD material parameters, the determinant from Equation (4.90) can be expressed as

$$\Omega_{pd}^4 - \Omega_{pd}^2\left(2(1+\nu)\zeta^2 + k\zeta^2 + mk - \frac{(1+\nu)\zeta^4}{12t^2} - \frac{k\zeta^4}{24t^2} + \frac{mk\zeta^4}{576t^4}\right) + \frac{k(1+\nu)\zeta^8}{288t^4} + \frac{mk^2\zeta^8}{2560t^6}$$
$$- \frac{k(1+\nu)\zeta^6}{6t^2} - \frac{31mk^2\zeta^6}{2880t^4} + 2k(1+\nu)\zeta^4 - \frac{mk^2\zeta^{10}}{129600t^8} + \frac{mk^2\zeta^4}{8t^2} = 0 \tag{4.96}$$

in which ν is the Poisson's ratio. The nondimensional wave frequency and wave number, Ω_{pd} and ζ, respectively, are defined as

$$\Omega_{pd} = \frac{\omega h}{\upsilon_s} \quad \text{and} \quad \zeta = \kappa h \tag{4.97}$$

The non-dimensional geometric parameters, *m* and *t*, are defined as

$$m = \frac{Ah^2}{I} \text{ and } t = \frac{h}{\delta} \tag{4.98}$$

Disregarding the higher order terms of the horizon simplifies the wave dispersion relation for long wavelength limit (or small ζ) as

$$\Omega_{pd}^4 - \Omega_{pd}^2\left(2(1+\nu)\zeta^2 + k\zeta^2 + mk\right) + 2k(1+\nu)\zeta^4 = 0 \tag{4.99}$$

As expected, this equation recovers the nondimensional wave dispersion relation in the classical theory (Amirkulova, 2011) for a long wavelength limit. It leads to four

different values for wave frequency, which represent two waves traveling to the right and two waves traveling to the left of the beam. Therefore, there are two distinct modes that can propagate in a Timoshenko beam (Reis, 1978). The first mode yields zero frequency ($\Omega = 0$) when the wave number is equal to zero ($\zeta = 0$)

$$\Omega_{ccm} = \Omega_{pd} = \sqrt{\zeta^2(1+\nu) + \frac{\zeta^2 k}{2} + \frac{km}{2} - \sqrt{\left(\zeta^2(1+\nu) + \frac{\zeta^2 k}{2} + \frac{km}{2}\right)^2 - \zeta^4\left(2k(1+\nu)\right)}} \tag{4.100}$$

and the second mode can be expressed as

$$\Omega_{ccm} = \Omega_{pd} = \sqrt{\zeta^2(1+\nu) + \frac{\zeta^2 k}{2} + \frac{km}{2} + \sqrt{\left(\zeta^2(1+\nu) + \frac{\zeta^2 k}{2} + \frac{km}{2}\right)^2 - \zeta^4\left(2k(1+\nu)\right)}} \tag{4.101}$$

The wave dispersion relations for long wavelength limit are shown in Figure 4.8 and Figure 4.9 for the specified values of $E = 200$ GPa, $\rho = 7850$ kg/m^3, $k = 5/6$, $h = 10^{-7}$ m, $\nu = 0.3$, and horizon size, $\delta = 10^{-8}$ m.

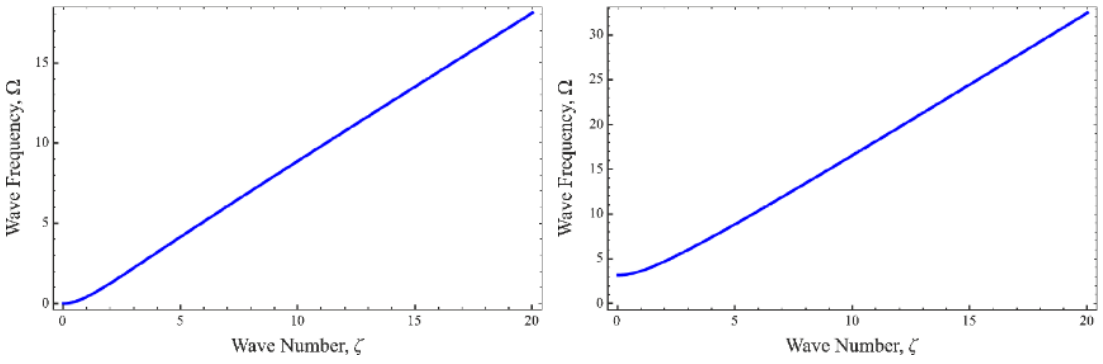

(a) (b)

Figure 4.8 Classical wave frequency dispersion for the (a) first and (b) second modes

As can be seen from Figure 4.8b, the wave number of the second mode is real for $\Omega \geq 3.16$. This indicates that the first mode is a propagating mode for any wave frequency, while the second mode only propagates for wave frequencies $\Omega \geq 3.16$ and is exponentially attenuated for $\Omega < 3.16$, as discussed by Reis (1978). Therefore, $\Omega = 3.16$ is the cut-off frequency for the second mode.

The variations of nondimensional phase speed, $\upsilon = \Omega / \left(\zeta \sqrt{k} \right)$ and $\upsilon = \Omega / \left(\zeta \sqrt{E/G} \right)$, as a function of the wave number are shown in Figure 4.9 for the first and second modes.

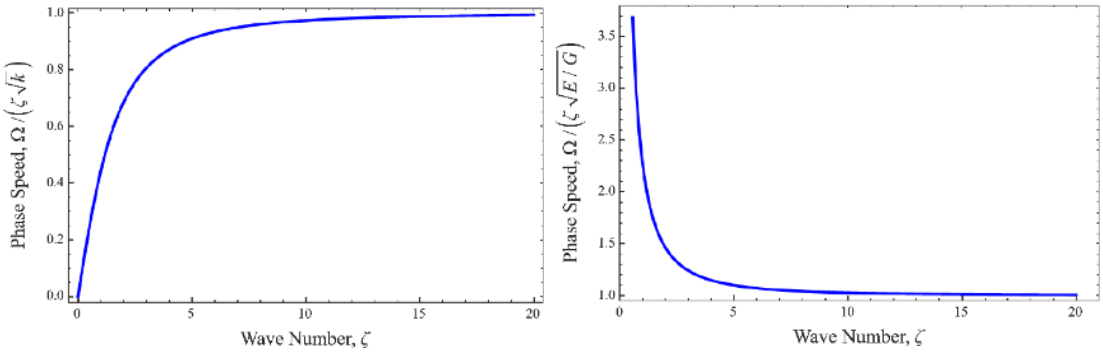

(a) (b)

Figure 4.9 Classical wave speed dispersion for the (a) first and (b) second modes

The phase speed, $\upsilon = \Omega / \left(\zeta \sqrt{k} \right)$ or $\upsilon = \Omega / \left(\zeta \sqrt{E/G} \right)$, converges to unity as the wave number, ζ, increases. Hence, the phase speed for the first mode, $\upsilon = \Omega / \left(\zeta \sqrt{k} \right)$, converges to the shear wave speed, υ_s, of the CCM, since

$$\upsilon = \frac{\omega}{\kappa} \quad \text{and} \quad \frac{\Omega}{\zeta \sqrt{k}} = \frac{\upsilon}{\upsilon_s \sqrt{k}} \tag{4.102}$$

Moreover, the phase speed for the second mode, $\upsilon = \Omega / \left(\zeta \sqrt{E/G} \right)$, converges to the compressional wave speed, υ_c, of the CCM, since

$$\frac{\Omega}{\zeta \sqrt{\frac{E}{G}}} = \frac{\upsilon}{\upsilon_c} \tag{4.103}$$

As a summary, for long wavelength (or small wave number, κ), the resulting wave dispersion relations are the same as that of the classical theory (Amirkulova, 2011). As expected, both theories yield the same relationship for long wavelength.

For specified values of $E = 200$ GPa, $\rho = 7850$ kg/m^3, $k = 5/6$, $h = 10^{-7}$ m, $\nu = 0.3$, and finite horizon size, $\delta = 10^{-8}$ m, the evaluation of the determinant without any simplification leads to the variation of the wave frequency, ω, as a function of the

wave number, κ, for the first and second modes as shown in Figure 4.10. For both modes, the PD wave dispersions level off as the wave number increases. However, the wave frequency always increases linearly according to the classical theory (CCM). Similar to the dispersion curves found by Silling (2000), it is apparent that the PD theory captures the experimentally observed characteristics of real materials.

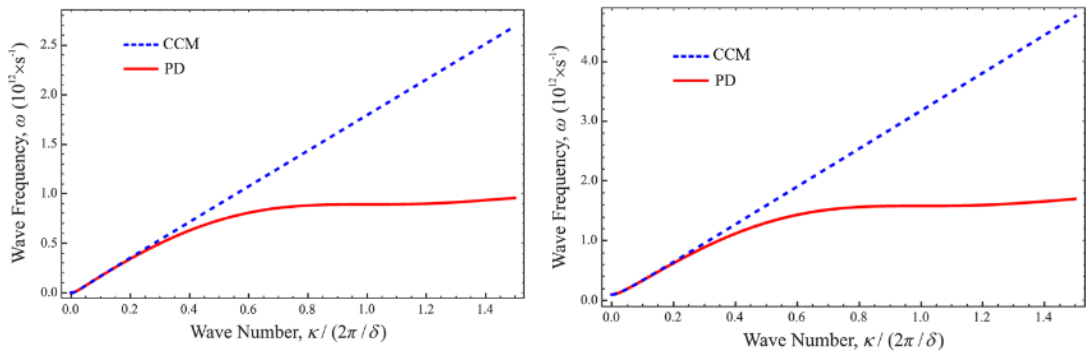

(a) (b)

Figure 4.10 Comparison of PD and CCM wave frequency dispersions: (a) first mode and (b) second mode

The variation of the normalized phase speed, $\upsilon/\left(\upsilon_s\sqrt{k}\right)$ as a function of wave number, κ, for the first mode is shown in Figure 4.11a. As shown in Figure 4.11, both PD and CCM predict zero speed in the limit as κ approaches zero. The phase speed of the CCM reaches a constant value close to the shear wave speed of a bar for short wavelengths (or relatively large wave numbers). For the second mode, both theories predict comparable results for the long wavelengths (or relatively small wave numbers) while classical phase speed reaches the compressional wave speed, υ_c, of a bar for short wavelengths (or relatively large wave numbers), as depicted in Figure 4.11b. However, the phase speed decreases as the wave number increases according to the PD theory as observed in real materials.

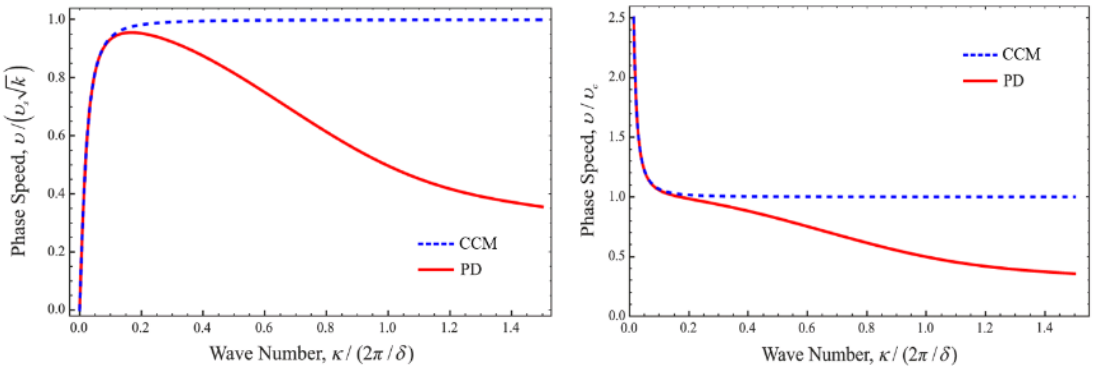

(a) (b)

Figure 4.11 Comparison of PD and CCM wave speed dispersions: (a) first mode and (b) second mode.

4.3.3 Mindlin plate

The governing equation of motion for Mindlin plate is given in Equation (4.54) in summation form and it can also be expressed in integral form when the elements of summation go to infinity as

$$\rho h\ddot{w} = c_s \int_0^{2\pi}\int_0^{\delta}\left(\frac{w'-w}{\xi} - \frac{\theta'_x+\theta_x}{2}\cos\varphi - \frac{\theta'_y+\theta_y}{2}\sin\varphi\right)dV$$

$$\rho\frac{h^3}{12}\ddot{\theta}_x = c_b \int_0^{2\pi}\int_0^{\delta}\left[\left(\frac{\theta'_x-\theta_x}{\xi}\right)\cos\varphi + \left(\frac{\theta'_y-\theta_y}{\xi}\right)\sin\varphi\right]\cos\varphi dV$$

$$+\frac{1}{2}c_s \int_0^{2\pi}\int_0^{\delta}\xi\left(\frac{w'-w}{\xi} - \frac{\theta'_x+\theta_x}{2}\cos\varphi - \frac{\theta'_y+\theta_y}{2}\sin\varphi\right)\cos\varphi dV \qquad (4.104)$$

and

$$\rho\frac{h^3}{12}\ddot{\theta}_y = c_b \int_0^{2\pi}\int_0^{\delta}\left[\left(\frac{\theta'_x-\theta_x}{\xi}\right)\cos\varphi + \left(\frac{\theta'_y-\theta_y}{\xi}\right)\sin\varphi\right]\sin\varphi dV$$

$$+\frac{1}{2}c_s \int_0^{2\pi}\int_0^{\delta}\xi\left(\frac{w'-w}{\xi} - \frac{\theta'_x+\theta_x}{2}\cos\varphi - \frac{\theta'_y+\theta_y}{2}\sin\varphi\right)\sin\varphi dV$$

Where w', θ'_x and θ'_y indicate member material points inside the horizon of w, θ_x and θ_y. The differential volume has the form of $dV = h\xi d\xi d\varphi$. Equation (4.104) can also be expressed in the limit of horizon approaches to zero, $\delta \to 0$, as given in Equation (4.57), which is the similar form with the classical theory of elasticity. However, the long range forces have also effect in Peridynamic theory for which the horizon values are not equal to zero.

Again, Peridynamic dispersion relations are compared against the classical Mindlin theory. In the derivation of these dispersion relations, the wave number, the wave frequency and phase velocity of the wave are denoted by κ, ω, and υ, respectively. The relationship among these parameters is $\omega = \kappa\upsilon$. The compressional and shear wave speeds are defined by $\upsilon_c^2 = E/\rho$ and $\upsilon_s^2 = G/\rho$, respectively, where *G* and *E* are the shear and Young's moduli of the material. The wave number is related to the half-wavelength, Γ, by the relationship $\kappa = \pi/\Gamma$.

In this regard, as in the case of a beam, dispersion relations are determined by considering a wave propagating in the *x* direction. Therefore, wave solutions for material points located at *x* and x' can be expressed as

$$w(\mathbf{x},t) = w_0 e^{i(\kappa x - \omega t)} \quad \text{and} \quad w(\mathbf{x}',t) = w_0 e^{i(\kappa x - \omega t + \kappa\xi\cos(\varphi))} \tag{4.105}$$

$$\theta_x(\mathbf{x},t) = \theta_{x0} e^{i(\kappa x - \omega t)} \quad \text{and} \quad \theta_x(\mathbf{x}',t) = \theta_{x0} e^{i(\kappa x - \omega t + \kappa\xi\cos(\varphi))} \tag{4.106}$$

$$\theta_y(\mathbf{x},t) = \theta_{y0} e^{i(\kappa x - \omega t)} \quad \text{and} \quad \theta_y(\mathbf{x}',t) = \theta_{y0} e^{i(\kappa x - \omega t + \kappa\xi\cos(\varphi))} \tag{4.107}$$

in which w_0, θ_{x0} and θ_{y0} represent the amplitudes of waves and $\kappa\xi\cos(\varphi)$ is the phase difference between the material points located at *x* and x'. Substituting these wave solutions into the PD equations of motion given in Equation (4.104) leads to a homogeneous set of equations for θ_{x0}, θ_{y0} and w_0 and for a nontrivial solution to exist, the determinant of their coefficient matrix must vanish, resulting in the wave dispersion relation as

$$\begin{vmatrix} c_s M_1 + \rho h\omega^2 & -c_s M_2 & -c_s M_3 \\ \frac{1}{2} c_s M_6 & c_b M_4 - \frac{1}{2} c_s M_7 + \frac{\rho h^3}{12}\omega^2 & c_b M_5 - \frac{1}{2} c_s M_8 \\ \frac{1}{2} c_s M_{10} & c_b M_5 - \frac{1}{2} c_s M_8 & c_b M_9 - \frac{1}{2} c_s M_{11} + \frac{\rho h^3}{12}\omega^2 \end{vmatrix} = 0 \tag{4.108}$$

The terms appearing in Equation (4.108) are defined as

$$M_1 = \int_0^{2\pi}\int_0^{\delta} \frac{e^{i\kappa\xi\cos(\varphi)} - 1}{\xi} dV \tag{4.109}$$

$$M_2 = \int_0^{2\pi}\int_0^{\delta} \frac{e^{i\kappa\xi\cos(\varphi)}+1}{2}\cos(\varphi)\,dV \tag{4.110}$$

$$M_3 = \int_0^{2\pi}\int_0^{\delta} \frac{e^{i\kappa\xi\cos(\varphi)}+1}{2}\sin(\varphi)\,dV \tag{4.111}$$

$$M_4 = \int_0^{2\pi}\int_0^{\delta} \frac{e^{i\kappa\xi\cos(\varphi)}-1}{\xi}\cos^2(\varphi)dV \tag{4.112}$$

$$M_5 = \int_0^{2\pi}\int_0^{\delta} \frac{e^{i\kappa\xi\cos(\varphi)}-1}{\xi}\sin(\varphi)\cos(\varphi)dV \tag{4.113}$$

$$M_6 = \int_0^{2\pi}\int_0^{\delta} \left(e^{i\kappa\xi\cos(\varphi)}-1\right)\cos(\varphi)dV \tag{4.114}$$

$$M_7 = \int_0^{2\pi}\int_0^{\delta} \frac{e^{i\kappa\xi\cos(\varphi)}+1}{2}\xi\cos^2(\varphi)dV \tag{4.115}$$

$$M_8 = \int_0^{2\pi}\int_0^{\delta} \frac{e^{i\kappa\xi\cos(\varphi)}+1}{2}\xi\sin(\varphi)\cos(\varphi)dV \tag{4.116}$$

$$M_9 = \int_0^{2\pi}\int_0^{\delta} \frac{e^{i\kappa\xi\cos(\varphi)}-1}{\xi}\sin^2(\varphi)dV \tag{4.117}$$

$$M_{10} = \int_0^{2\pi}\int_0^{\delta} \left(e^{i\kappa\xi\cos(\varphi)}-1\right)\sin(\varphi)dV \tag{4.118}$$

$$M_{11} = \int_0^{2\pi}\int_0^{\delta} \frac{e^{i\kappa\xi\cos(\varphi)}+1}{2}\xi\sin^2(\varphi)dV \tag{4.119}$$

where the terms M_i with $i = 1,.....,11$ are dependent on the phase difference and the horizon. Evaluation of these integrals yields Bessel functions of the first kind, $J_0(\kappa\delta)$ and $J_1(\kappa\delta)$, and Struve functions, $H_0(\kappa\delta)$ and $H_1(\kappa\delta)$.

As indicated bySilling (2000), in the limit of a long wavelength (Γ) or for a very small wave number ($\kappa \to 0$), the integrals in Equations (4.109) – (4.119) can be simplified by using the first three terms of the Taylor series expansion for cosine and sine functions

$$\cos\left(\kappa\xi\cos\left(\varphi\right)\right)=1-\frac{\left(\kappa\xi\cos\left(\varphi\right)\right)^2}{2!}+\frac{\left(\kappa\xi\cos\left(\varphi\right)\right)^4}{4!}-\ldots \tag{4.120}$$

and

$$\sin(\kappa\xi\cos\left(\varphi\right))=\kappa\xi\cos\left(\varphi\right)-\frac{\left(\kappa\xi\cos\left(\varphi\right)\right)^3}{3!}+\frac{\left(\kappa\xi\cos\left(\varphi\right)\right)^5}{5!}-\ldots \tag{4.121}$$

Substituting the relationships given in Equations (4.120) and (4.121) into integrations given in Equations (4.109) – (4.119) and solving the determinant equation given in Equation (4.108), while ignoring higher order terms of horizon size, yield the dispersion relationship for a long wavelength limit in the PD theory

$$\begin{vmatrix} -k^2Gh\kappa^2+\rho h\omega^2 & -k^2Ghi\kappa & 0 \\ k^2Ghi\kappa & -D\kappa^2-k^2Gh+\frac{\rho h^3}{12}\omega^2 & 0 \\ 0 & 0 & -\frac{D}{2}(1-\nu)\kappa^2-k^2Gh+\frac{\rho h^3}{12}\omega^2 \end{vmatrix}=0 \tag{4.122}$$

with the constraint on Poisson's ratio ($\nu=1/3$).

This relationship is equivalent to the dispersion relationship obtained from the classical theory (CCM). Moreover, roots of Equation (4.122) correspond to three different natural frequencies. Soedel (2004) explained that the lowest of these frequencies is the one that the transverse deflection mode dominates and other two are considered as shear modes.

Shown in Figure 4.12 are the nondimensionalized phase speed (υ/υ_s) dispersion relationships with the change of wave number (h/Γ) for three different wave modes for the long wavelength limit while considering the following properties of a plate; $k^2=5/(6-\nu)$ and $\nu=1/3$.

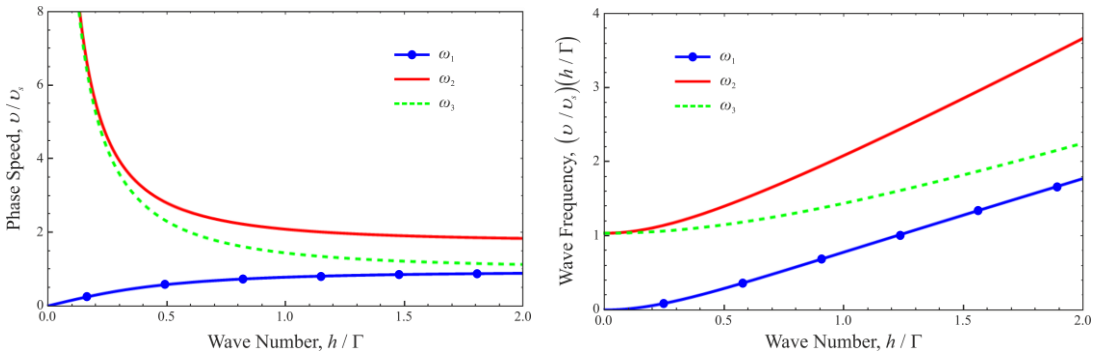

(a) (b)

Figure 4.12 Classical (a) phase speed and (b) wave frequency dispersions

Variations similar to those in Figure 4.12 and comparisons with Rayleigh – Lamb waves, which have the property of waves in a plate with infinite extent, can be seen in ref. (Stephen, 1997). Also, in ref. (Stephen, 1997), ω_1 is named as the lowest flexural mode, ω_2 as the thickness – shear mode, and ω_3 as the thickness-twist mode. In Figure 4.12a, when the wave number (h/Γ) reaches the value of two, which means the wave length is now comparable with the thickness of a plate, all the phase speeds become flat.

Figure 4.12b shows the nondimensionalized wave frequency ($(\upsilon/\upsilon_s)(h/\Gamma)$) dispersions with the change of wave number (h/Γ) for three wave modes of the CCM or for the PD theory in the long wavelength limit. As a summary, for long wavelength (or small wave number, κ), the resulting wave dispersion relation is the same as that of the CCM (Soedel, 2004). Thus, both theories give the same relationship for long wavelength.

For specified values of $E = 200$ GPa, $\rho = 7850$ kg/m^3, $h = 5\times10^{-8}$ m, $k^2 = 5/(6-\nu)$, $\nu = 1/3$ and finite horizon size, $\delta = 10^{-8}$m, the evaluation of the determinant without any simplifications leads to the variation of the wave frequency, ω, as a function of the wave number, κ. Figure 4.13 shows comparisons of nondimensionalized phase speed ($\upsilon/\left(\upsilon_s\sqrt{k^2}\right)$) as a function of wave number, $\kappa/(2\pi/\delta)$, for the first three modes; lowest flexural mode ω_1, thickness-shear mode ω_2, and thickness – twist mode ω_3.

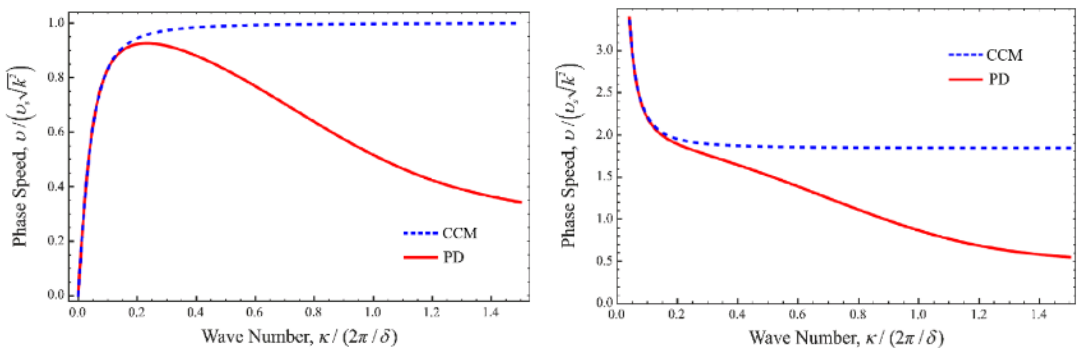

(a) (b)

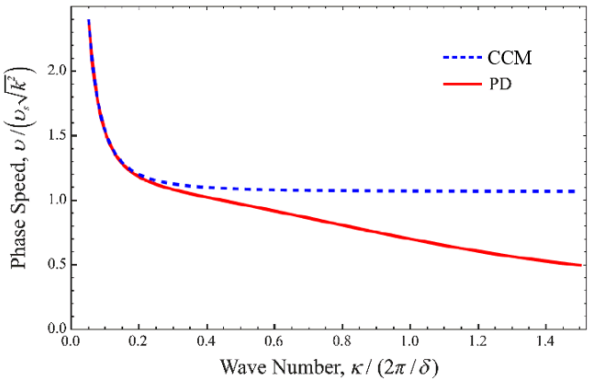

(c)

Figure 4.13 Comparison of wave speed dispersions: (a) lowest flexural mode ω_1, (b) thickness – shear mode ω_2, and (c) thickness-twist mode ω_3

As observed in Figure 4.13a, both the classical and PD theories estimate zero speed in the limit as wave number, κ, approaches zero, whereas the classical theory phase speed nearly approaches the Rayleigh surface wave speed, $\upsilon/\upsilon_s = 0.9274$, for Poisson's ratio of $\nu = 0.30$ as wave number, κ, increases (Stephen, 1997). In Figure 4.13b – c, both theories estimate comparable results for the long wavelengths (or relatively small κ). However, PD theory captures the feature of real materials that phase velocity decreases as the wave number increases.

Also comparisons of wave frequency dispersions for increasing wave number are shown in Figure 4.14. As a characteristic of real materials, dispersion curves of the peridynamic theory for all modes level off as the wave number increases and exceeds a value of $2\pi/\delta$ (Silling, 2000). Thus, PD theory captures the experimentally observed feature of real materials, which are always dispersive as a result of long-range forces.

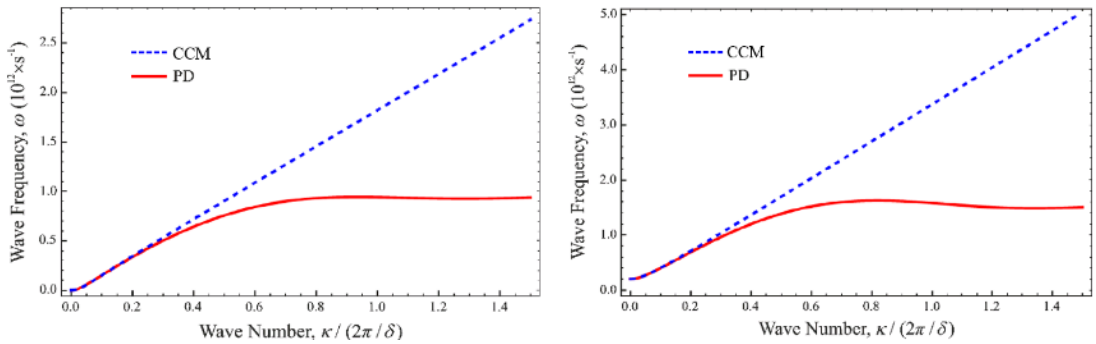

(a)

(b)

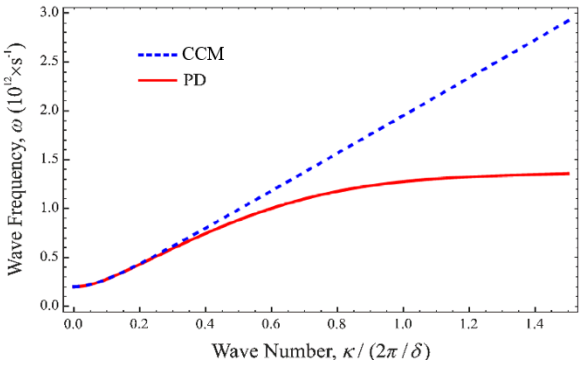

(c)

Figure 4.14 Comparison of wave frequency dispersions: (a) lowest flexural mode ω_1, (b) thickness – shear mode ω_2, and (c) thickness – twist mode, ω_3

4.4 Benchmark Problems

In order to validate the proposed peridynamic formulations, simple loading cases are first considered for which analytical solutions are also available.

Lastly, a plate with a center crack under bending is considered to show the capability of Mindlin plate theory in capturing the crack propagation behavior.

4.4.1 Timoshenko beam

In order to obtain the static solutions, the adaptive dynamic relaxation (ADR) technique is used and the horizon size is chosen as $\delta = 3.015\Delta x$, where Δx is the uniform grid spacing.

The length of the beam is $L = 1\text{m}$, with a cross sectional area of $A = 0.1 \times 0.1\text{m}^2$. Its Young's modulus is specified as $E = 200\text{GPa}$. Only a single row of material (collocation) points are necessary to discretize the beam. The distance between material points is $\Delta x = 0.01\text{m}$. The left edge is constrained by introducing a fictitious region with a size of δ. The beam is first subjected to transverse loading, as shown in Figure 4.15. The loading is applied to a single material point at the right end of the bar as a body load of $\hat{b} = 5 \times 10^9\ \text{N/m}^3$ for the transverse loading, corresponding to a transverse load of $P = 5 \times 10^5\ \text{N}$.

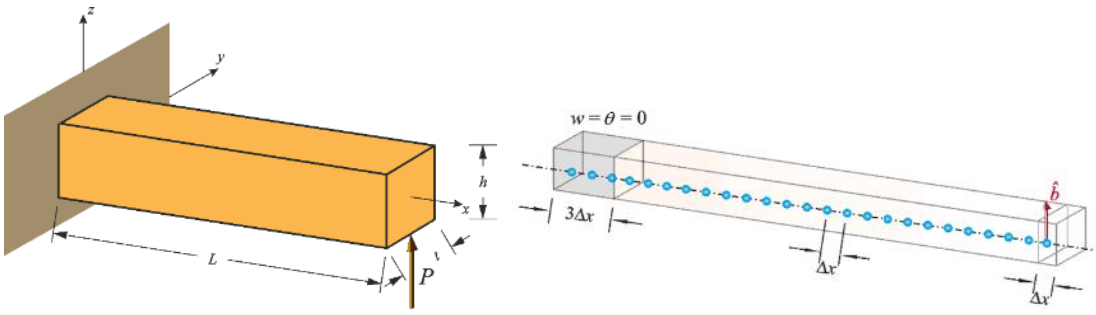

(a) (b)

Figure 4.15 (a) Timoshenko beam subjected to transverse loading and (b) its discretization

Under the transverse loading case, the analytical solutions for the transverse displacement and the rotation are given as

$$w = \frac{Px}{kGA} + \frac{P}{2EI}\left(Lx^2 - \frac{x^3}{3}\right) \quad \text{and} \quad \theta = \frac{P\left(2Lx - x^2\right)}{2EI} \tag{4.123}$$

As shown in Figure 4.16, the PD and the analytical solutions also agree well with each other. This verifies that the PD equations of motion accurately captures the deformation behavior of a Timoshenko beam.

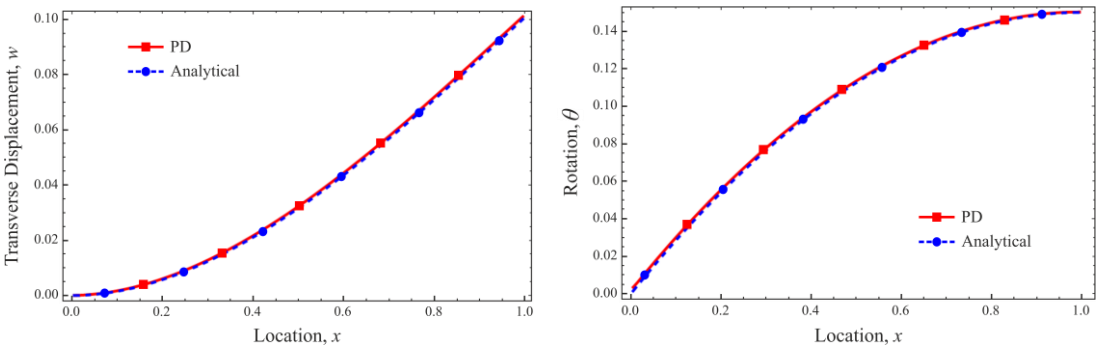

Figure 4.16 Variation of (a) transverse displacement and (b) rotation along a Timoshenko beam subjected to transverse force loading

4.4.2 Mindlin plate

In order to obtain the static solutions, the adaptive dynamic relaxation (ADR) technique is used and the horizon size is chosen as $\delta = 3.015\Delta x$, where Δx is the uniform grid spacing.

As shown in Figure 4.17, the length and width of the plate is $L = W = 1\text{m}$ with a thickness of $h = 0.1$ m. The Young's modulus of the plate is specified as $E = 200\,\text{GPa}$. Only a single row of material (collocation) points in the thickness direction is necessary to discretize the domain. The distance between material points is $\Delta x = 0.01\text{m}$. The left edge is constrained by introducing a fictitious region with a size of $3\Delta x$. The loading is applied to a single row of material points at the right end of the plate as a resultant body load of $\tilde{b}_x = 3.33\times10^8$ N/m for bending loading.

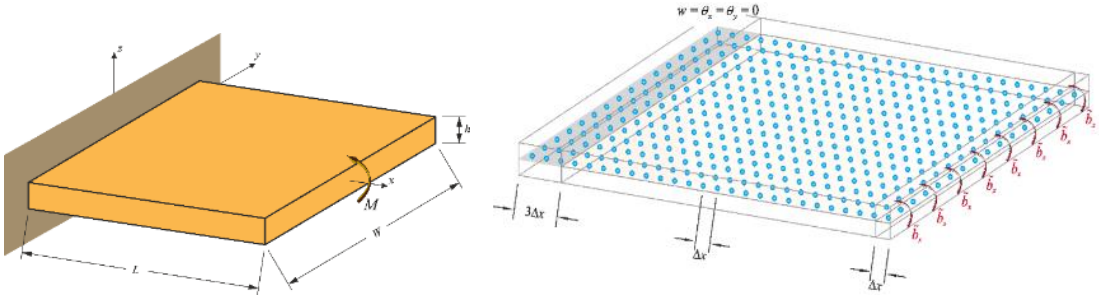

(a) (b)

Figure 4.17 (a) Mindlin plate subjected to pure bending loading and (b) its discretization

The peridynamic solutions of the transverse displacement and the x direction rotation for bending moment loading are compared with finite element (FE) solutions by using a shell element, which is suitable for thick shell structures, available in commercial software, ANSYS.

As depicted in Figure 4.18, the PD and the FE solutions agree well with each other. This verifies that the PD equation of motion given in Equation (4.54) can accurately capture the deformation behavior of a Mindlin plate.

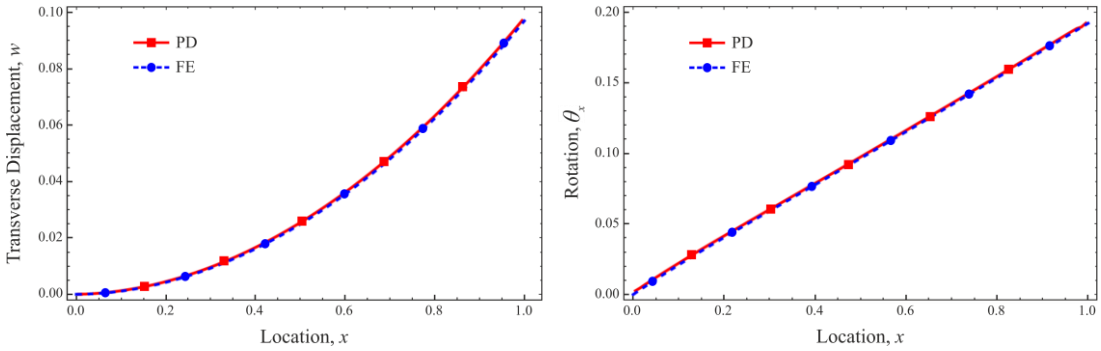

Figure 4.18 Variation of (a) transverse displacement and (b) rotation along a Mindlin plate subjected to pure bending loading

4.4.2.1 Mindlin plate with central crack

Crack growth in a square plate with an initial central crack aligned with the x – axis, as shown in Figure 4.19, is analyzed. The length and width of the plate are $L = W = 1\text{m}$ with a thickness of $h = 0.1\,\text{m}$. Plate thickness to crack length ratio is $h/2a = 0.5$, which has the properties of a thick plate, where $2a$ is the initial crack length. The Young's modulus of the plate is specified as $E = 3.227\,\text{GPa}$ and the shear modulus is $G = 1.21\text{GPa}$. Only a single row of material (collocation) points in the thickness direction is necessary to discretize the domain. The distance between material points is $\Delta x = 2\times10^{-3}\,\text{m}$. The horizon size is chosen as $\delta = 3.015\Delta x$.

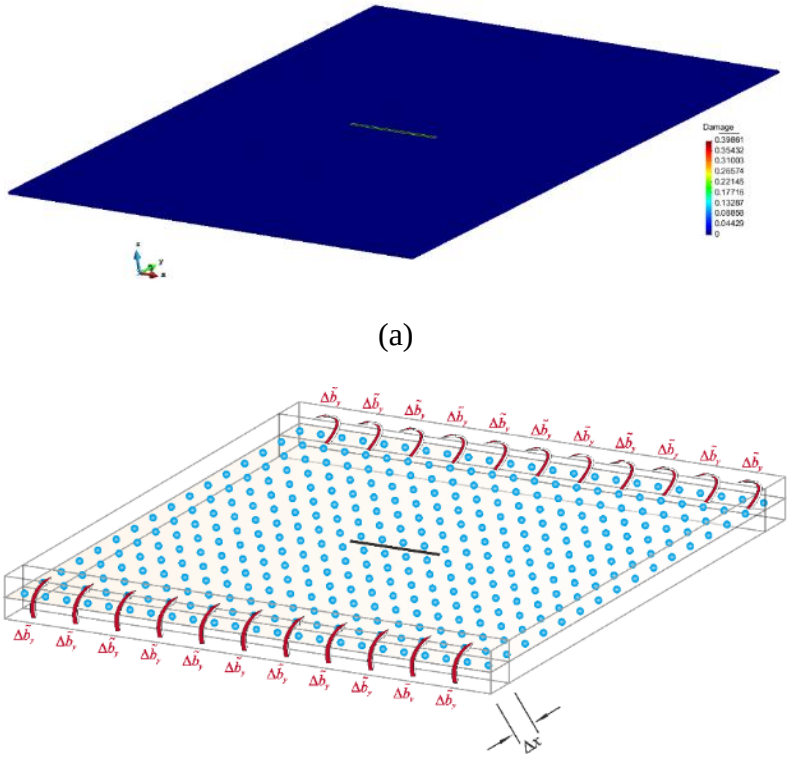

(a)

(b)

Figure 4.19 (a) Mindlin plate with a central crack subjected to pure bending loading and (b) its discretization

The material is chosen as polymethyl-methacrylate (PMMA), which shows a brittle fracture behavior. Mode – I fracture toughness of this material is given as $1.33\ \text{MPa}\sqrt{\text{m}}$ (Ayatollahi and Aliha, 2009) and mode – III fracture toughness is given as $7.684\ \text{MPa}\sqrt{\text{m}}$ (Farshad and Flüeler, 1998). The critical energy release rates of mode – I and mode – III can be found from

$$G_{Ic} = \frac{K_{Ic}^2}{E} \quad \text{and} \quad G_{IIIc} = \frac{K_{IIIc}^2}{2G} \tag{4.124}$$

In order to show simple mode – I crack growth, a bending moment loading is applied through a single row of material points at the horizontal boundary regions of the plate. Small increments of resultant body loading of $\Delta\tilde{b}_y = \pm 250\ \text{N/m}$ are induced in order to achieve stable crack growth. Under the applied uniform bending, the crack starts to grow at the end of nearly 66000 time steps, and as expected, it propagates towards the edges of the plate, as shown in Figure 4.20.

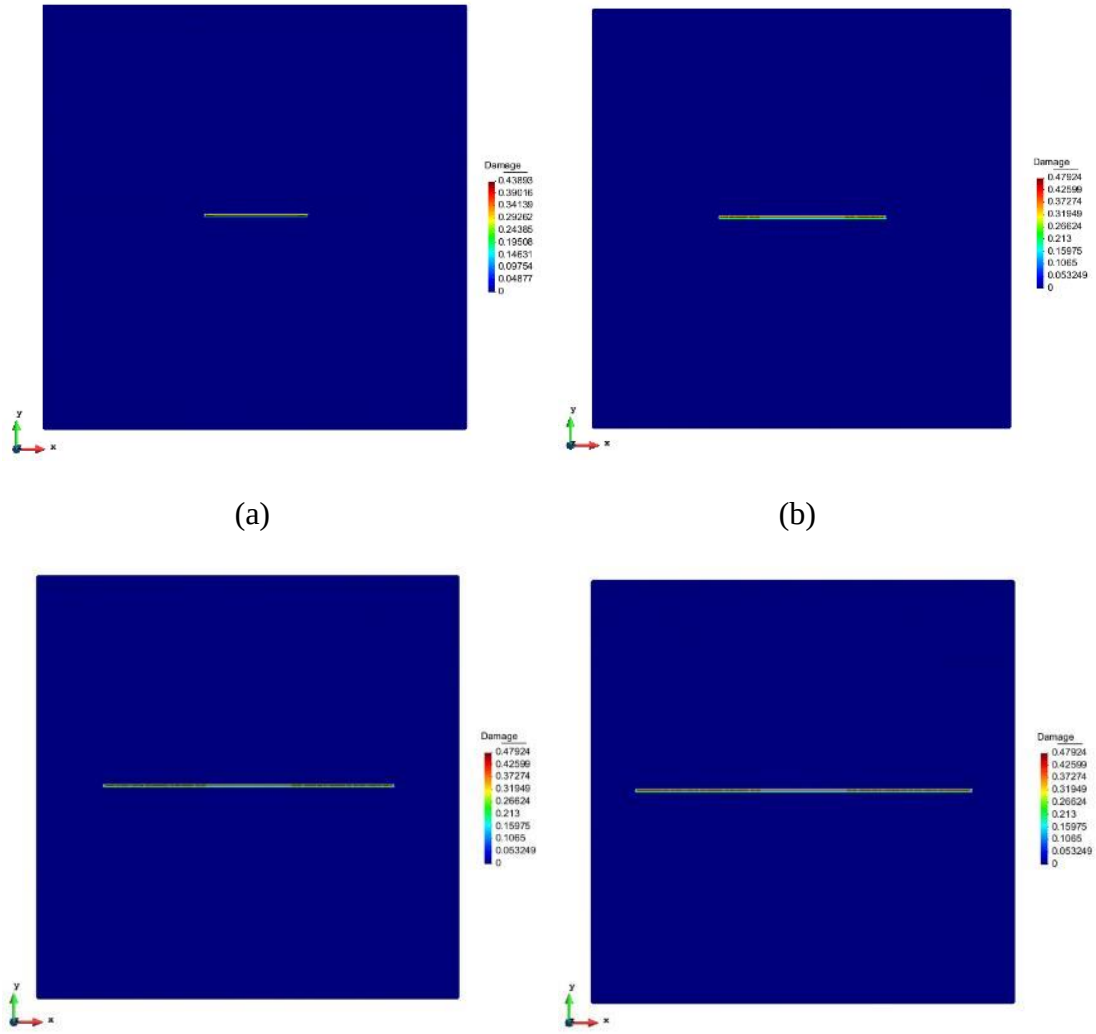

(a) (b)

(c) (d)

Figure 4.20 Crack evolution at (a) 66000th, (b) 67000th, (c) 68000th and (d) 69000th time steps

4.5 Conclusion

In this section, PD theories for simplified structures are derived while using a proposed procedure. These structures are very important to model complex and big structures such as ships and aeroplanes. Here, the proposed PD Timoshenko beam and Mindlin plate theories are new to the literature and this brings many advantages for modelling engineering structures. Since they have the ability of capturing transverse shear deformations, the thick beam and plate structures can be represented with these

theories. As a result, such thick engineering structures can only be modelled with a single layer of material points in the thickness direction and this brings computational advantage on PD simulations of complex structures. Moreover, the Timoshenko beam and Mindlin plate theories can be extended considering ordinary based PD theory. By doing this, the constraint on Poisson's ratio for the plate theory can be removed.

Apart from that, PD dispersion relationships were also obtained for simplified structures and it was concluded that the wave dispersion characteristics, which are also observed in experiments, of real materials can be captured with PD theory. However, using the classical theory can not incorporate such characteristics to a material behaviour because it does not have a length – scale parameter as in the PD theory. Hence, the classical theory is incapable of capturing phenomena occurring at lower scales that can affect the macro scale behavior. On the other hand, the horizon parameter in Peridynamics, which defines the domain of influence of peridynamic interactions, serves as a length – scale parameter. Due to this parameter, PDs is capable of capturing phenomena occurring at different length scales, including the nano – scale.

After establishing the PD equation(s) of motion(s) for simplified structures, they are validated with simple benchmark problems. Furthermore, the expressions for critical curvature and shear angle values in terms of mode – I and mode – III critical energy release rates of the material were also utilized to predict crack growth in a plate under pure bending.

Chapter 5

Underwater Shock Response of Marine Structures

5.1 Introduction

In recent years, composite structures have found extensive application area in marine field. Especially, they have received a lot of interest in military applications, such as naval ships, submarines and torpedoes (Mouritz, 2001), because these structures may be exposed to extreme loading conditions in their life time and their design must resist such conditions without any compromise from its weight. In this sense, composites are the best option with their high strength and low weight properties. Besides, they are also advantageous over metallic structures with their high corrosion resistance and low noise transmission behaviours (Kalavalapally et al., 2006). After all, composite materials took a lot attraction from the designers because of such superior characteristics. However, several types of material, which possess different mechanical characteristics, are involved in their design and construction process. Hence, they are rather complex and understanding dynamic behaviour of composite materials is not easy especially under extreme loading conditions. Therefore, various

studies concentrate on investigating dynamic deformation and/or failure characteristics of composite structures under shock loading conditions.

In order to get quick solutions without any computational cost in the initial design stage (Li et al., 2013), analytical solutions were proposed to investigate dynamic behaviour of composite structures exposed to underwater shock loading. Librescu et al. (2004) investigated the dynamic response of composite sandwich panels analytically while considering several effects such as anisotropy of the face sheets, orthotropy of the core layer, geometrical nonlinearities and initial geometric imperfections. Later on, Librescu et al. (2006) incorporated the effect of core layer on induced pressure-time history to the structure from both air and underwater explosions. In these two parametric studies, comparisons were done for several geometrical and mechanical configurations of sandwich panels which also include the effect of charge weights and stand-off distances. Lam et al. (2003) developed an effective semi-analytical method to study composite laminated pipeline subjected to underwater shock loading. In their analysis, fluid-structure interaction effect was considered and pipeline was modelled with Reissner-Mindlin assumptions assuming that it is a thick cylindrical shell. Finally, results were obtained by using modal analysis technique. Schiffer and Tagarielli (2014) developed analytical models, which incorporate cavitation effect on the fluid-structure interaction phenomena, for predicting dynamic behaviour of fiber reinforced laminated circular and clamped composite plates. Optimal design procedure for selection of plate geometries and its constituents were accounted for the developed analytical model. Wang et al. (2013) developed a novel analytical technique, which uses three-dimensional elastic fundamental equations instead of laminated plate theories, in order to obtain exact solution to the underwater explosion (UNDEX) problem. In this study, dynamic elastic response of laminated plates is obtained by using state space-numerical inversion of Laplace transform (SS-NILT) method with considering fluid-structure interaction effects and results were compared with both finite element (FE) analysis and experiments from the literature. Panciroli and Abrate (2012) formulated dynamic response of composite structures which also incorporates the effect of core layer for straight and curved beams as well as for cylindrical and spherical shell structures. Moreover, geometric nonlinearities were considered for plates. Since the formulations were derived in curvilinear

coordinates, they can easily be extended to different geometries using the same kinematic assumptions. They also found that higher modes are effective for curved structures whereas they are negligible for plates and beams. These analytical studies are limited in beam, plate or shell geometries and difficult to implement for more complex structures. Moreover, no damage evolution predictions have been done analytically so far. Therefore, several numerical studies were carried out for more complex structures exposed to underwater shock loading. Gong and Lam (1998) studied transient stress response of submersible stiffened cylindrical composite hull by using finite element and boundary element methods. Fluid-structure interaction was also included with doubly asymptotic approximation (DAA) method and from comparisons against its steel counterpart, it was found that composite hull dissipates higher kinetic energy. Young et al. (2009) investigated the effect of fluid – structure-interaction (FSI) on the dynamic response of sandwich composite structures. They used two-dimensional Eulerian – Lagrangian FSI solver in order to capture complex phenomena such as shock-bubble interactions, phase changes within the fluid and cavitation effects. Thus, it was concluded that UNDEX loading may lead to a very complex impact on the structure rather than uniform loading. However, both studies didn't consider any damage in the structure. Some limited damage prediction analyses were carried out numerically by McCoy and Sun (1997) and Kalavalapally et al. (2006). McCoy and Sun (1997) performed stress analysis of hollow composite cylinder with FE method and FSI effects are also included. The effective modulus theory, which separates thick composite laminate section into a periodic sublaminate stacking sequence instead of considering each individual lamina, is used for dynamic application. After all, delamination damage can be predicted if radial stress reaches some particular value. Kalavalapally et al. (2006) made some optimization analyses for both metallic and composite models of torpedoes and it is found that composite model is stronger and lighter than its metallic counterpart. They also used maximum stress and strain failure criteria for damage prediction. However, both studies lack to show full perspective of damage evolution process and final failure considering each constituent of composite structures. Recently, the detailed failure and damage characteristics of composite structures were studied extensively for underwater shock loading by using FE method. Motley et al. (2011) numerically investigated initial

failure loads of fully submerged composite plates while taking the advantage of Hashin's failure initiation criteria. A more complex study was carried out by Batra and Hassan (2007) for a laminated composite plate subjected to underwater shock loading and an FE computational framework, which incorporates rate-dependent damage evolution equations, was developed. Thus, evolution of several damage types, i.e. fiber/matrix debonding, matrix cracking, fiber breakage and delamination, can be predicted in the structure. Moreover, LeBlanc (2011) used a commercial FE software, i.e. LS-DYNA, in which specific material model incorporating progressive damage property is used. Hereby, final failure characteristics of a circular composite plate were found to be in agreement with experimental results obtained from conical shock tube test setup. Gauch et al. (2012) investigated the effect of preloading, which may be a hydrostatic pressure experienced by submersible vehicles, on the response of structure. Material damage and delamination were observed in thin E-Glass reinforced composite plates by using similar material model as in ref. (LeBlanc, 2011), which incorporates degradation of a composite material stiffness during the simulation. Wei et al. (2013b) proposed progressive degradation model in order to analyse different damage mechanisms in composite structures and they compared their results with experimental observations obtained from underwater shock tube. Later on these results were improved by considering strain-rate effects on mechanical behaviour of constituents of composites (Wei et al., 2013a).

Experiments are also carried out in order to gain better understanding on dynamic and damage behaviour of composite structures under shock loadings. Hence, some of the above mentioned analytical and numerical studies were supported by experiments. In general, experiments were carried out using either explosives directly or with shock tubes in laboratory scale. Shock tubes are more favourable than using explosives (Arora et al., 2012) because field experiments can be expensive, dangerous and harmful to environment (Bachynski et al., 2011). In experiments, small target dimensions may lead to small impacted region and subsequently localized damage (Latourte et al., 2011). Therefore scaling relations, which considers plate dimensions, explosive intensity and other parameters, are pretty important. Bachynski et al. (2011) derived scaling relations for composite structures in order to make laboratory scale experiments. Espinosa et al. (2006) developed a novel experimental setup, which is

based on scaling analysis, in order to represent full field experiments in laboratory scale. Other kinds of shock tube test setups have been used in the literature, e.g. (Avachat, 2012; LeBlanc, 2011; Schiffer et al., 2012), to understand deformation and failure characteristics of composite structures. Mouritz (2001) carried out prototype-scale experiments and showed the effect of stitching on improving damage characteristics, especially delamination damage, of Glass/vinyl ester composites. Arora et al. (2012) carried out large scale field experiments and investigated failure mechanisms of E-Glass fiber reinforced sandwich panels and laminated tubes. Latourte et al. (2011) investigated failure modes and damage mechanisms of composite laminated and sandwich structures using shock tube defined by Espinosa et al. (2006). Their study also confirmed the performance improvement of composite sandwich panels under shock loadings. Avachat and Zhou (2013) used novel gas-gun based Underwater Shock Loading Simulator (USLS) for investigating damage characteristics of composite structures and comparisons were done with FE simulations perfomed by Avachat (2012).

In summary, several numerical techniques based on FE analysis technique were used collaboratively with experimental studies in order to develop most powerful numerical model. However, numerical studies, which have been carried out to date, only used FE analysis technique. FE analysis greatly suffers from mesh sensitivity in impact analyses (Raimondo et al., 2012) and its equation of motion is based on local continuum theory which needs additive kinematic relations and/or damage evolution equations for the damage prediction analysis. In this section, Peridynamics is used for the first time in literature for analysing underwater shock responses of composite structures. The governing equations of peridynamics are in the form of integro-differential equations, which naturally incorporates damage into the structure, and no additional equations are needed. Moreover, its numerical implementation is done by meshless approach which does not result in unrealistic energy dissipations as in the FE theory (Raimondo et al., 2012). In this regard, we first briefly explain implementation of peridynamic formulation for composite structures. Then, peridynamic analysis of a 4-ply composite structure subjected to underwater shock loading is carried out and results are compared against a previous study done by Batra and Hassan (2007). Since, only numerical results were provided by Batra and Hassan (2007), Peridynamic

computational results are further verified with the experimental results given by LeBlanc (2011) where conical shock tube (CST) test setup was used. Furthermore, in the latter case, a more complex 13-cross ply composite structure is analysed.

5.2 Peridynamic Theory for a Composite Lamina

In this section, we briefly explain Peridynamic formulation of a two-dimensional composite lamina, which shows anisotropic material property, explained in Chapter 5 of ref. (Madenci and Oterkus, 2014). Lamina constitutes from fibers and matrix materials. Fibers are oriented along x_1 axis and fiber orientation angle is defined as θ with respect to a reference axis, x, as shown in Figure 5.1. The directional dependent property of composite lamina is provided by introducing fiber direction bonds in addition to arbitrary direction bonds. In Figure 5.1, the main material point, i, interacts with other material points, p and q, through arbitrary direction bonds while it is also connected with material point, q, through fiber direction bond inside its horizon, $H_{\mathbf{x}}$.

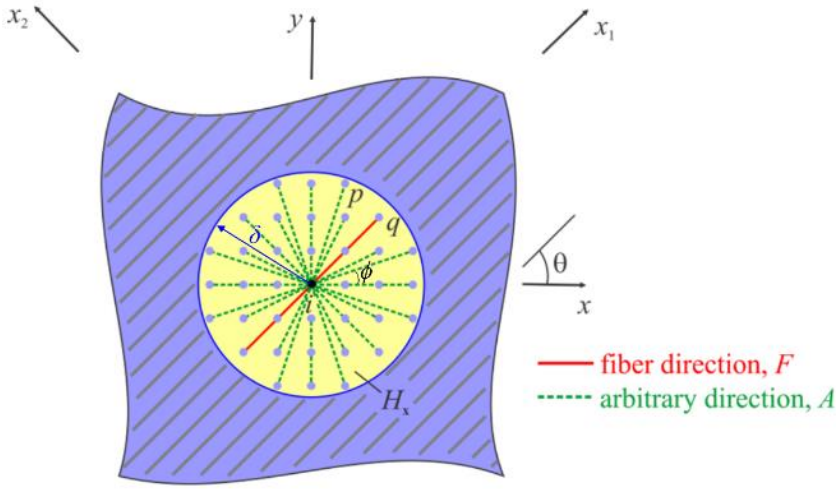

Figure 5.1 Fiber orientation with respect to x axis

Due to the fact that two types of interactions or peridynamic bonds are defined for the composite lamina, the bond constant, c, which is available in the original PD theory, is replaced by directional dependent bond constant, $c(\phi)$, as

$$c(\phi)=\begin{cases} c_F + c_A & \phi = \theta \\ c_A & \phi \neq \theta \end{cases} \tag{5.1}$$

where ϕ, c_F and c_A are referred as angle of the peridynamic bond with respect to *x* axis, fiber direction bond constant and arbitrary direction bond constant, respectively. As mentioned earlier in Section 2.4.4, the bond constants, c_F and c_A, can be obtained in terms of engineering material constants by equating strain energy densities based on the CCM and PD theories for simple loading conditions. Following the procedure defined by Oterkus and Madenci (2012), the bond constants are expressed as

$$c_F = \frac{2E_1\left(E_1 - E_2\right)}{\left(E_1 - \frac{1}{9}E_2\right)\left(\sum_{q=1}^{Q}\xi_{qi}V_q\right)} \tag{5.2}$$

$$c_A = \frac{8E_1E_2}{\left(E_1 - \frac{1}{9}E_2\right)\pi h\delta^3} \tag{5.3}$$

where E_1 and E_2 are the Young's moduli along the fiber direction and perpendicular to the fiber direction, respectively. In Equations (5.2) and (5.3), *Q*, *h*, V_q and ξ_{qi} define the number of material points in the fiber direction, the thickness of the lamina, the incremental volume of material point *q* and the reference distance between material points *q* and *i* in the undeformed configuration, $\xi_{qi} = \left|\mathbf{x}_q - \mathbf{x}_i\right|$, respectively. The force-stretch relationship for a composite lamina can be written by slightly modifying the force – stretch relation given in Section 2.4.4 as

$$\mathbf{f} = c(\phi)s\frac{\mathbf{y}' - \mathbf{y}}{\left|\mathbf{y}' - \mathbf{y}\right|} \tag{5.4}$$

The force – stretch relationships, which are along the arbitrary and fiber directions, are linear in PD theory, as shown in Figure 5.2. Failure has direct relationship with critical parameters or stretches of the peridynamic bonds. The critical stretches of fiber direction and arbitrary direction bonds can be determined based on experimental measurements of different lay-up configurations as indicated by Oterkus et al. (2012). Failure of arbitrary and fiber direction bonds, shown in Figure 5.2, are directly related with matrix and fiber failures, respectively, in the material. Moreover, it is assumed that fiber and arbitrary direction bonds are failed at the same stretch value under

compression because microbuckling is the dominant failure mechanism for fiber-reinforced composites under compression loading.

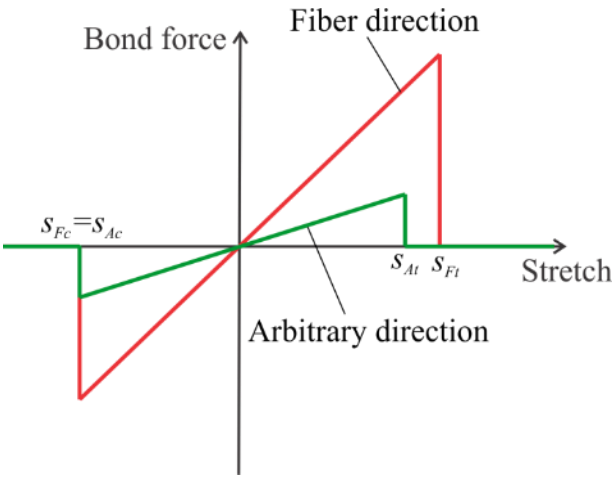

Figure 5.2 Force-stretch relationships in a composite lamina

After defining the critical stretch values, failure is incorporated by terminating the interactions between material points or generally speaking by breaking the bonds in Peridynamics. Thus, the Peridynamic force relation given in Equation (5.4) is further modified by introducing the history-dependent failure parameter, $\mu\left(\mathbf{x}'-\mathbf{x},t\right)$, as

$$\mathbf{f}=\mu\left(\mathbf{x}'-\mathbf{x},t\right)c\left(\phi\right)s\frac{\mathbf{y}'-\mathbf{y}}{\left|\mathbf{y}'-\mathbf{y}\right|} \tag{5.5}$$

and

$$\mu\left(\mathbf{x}'-\mathbf{x},t\right)=\begin{cases}1 & \text{if } s_c<s\left(\mathbf{x}'-\mathbf{x},t'\right)<s_t \text{ for all } 0<t'<t\\ 0 & \text{otherwise}\end{cases} \tag{5.6}$$

where s_c and s_t represent critical stretches of the peridynamic bonds in compression and tension, respectively. They can either be related to arbitrary direction bonds, i.e. s_{At} and s_{Ac}, or fiber direction bonds, i.e. s_{Ft} and s_{Fc}, depending on which bond is being evaluated. Thus, failure parameter, $\mu\left(\mathbf{x}'-\mathbf{x},t\right)$, is split into two parts, i.e. for matrix (μ_A) and fiber (μ_F) failures, and each type of failure parameter is further integrated into the horizon of a material point in order to find the local damage, $\Phi\left(\mathbf{x},t\right)$, at a material point as

$$\Phi(\mathbf{x},t) = 1 - \frac{\int_H \mu(\mathbf{x}' - \mathbf{x}, t) dH}{\int_H dH} \tag{5.7}$$

As a result, local damage of a material point is characterised for both matrix (Φ_A) and fiber (Φ_F) damages in the material.

5.3 Peridynamic Theory for a Composite Laminate

Peridynamic formulation of a two-dimensional composite lamina was further extended to a three-dimensional composite laminate as is done by Oterkus and Madenci (2012). A laminate constitutes from more than one lamina with particular mechanical property stacked at different orientation angles. Thus, laminate can resist complex loading conditions with improved stiffness properties (Kaw, 2006). However, the resin-rich layer, which strongly bonds laminae to each other, is responsible for cracking and delamination (Madenci and Oterkus, 2014). In PD theory, the thickness direction deformations of a laminate are provided by additional peridynamic bonds, i.e. interlayer and shear bonds, between plies. In Figure 5.3, two plies of a laminate are shown with peridynamic bonds. The main material points, *i*, in both plies are connected with interlayer bond as well as shear bonds between plies connecting the main material point *i* in the k^{th} ply with family members of *i*, i.e. *p* and *q*, in the $(k+1)^{th}$ ply and the same follows for the main material point *i* in the $(k+1)^{th}$ ply. In total, four types of peridynamic bonds exist in a laminate. While in-plane bonds, i.e. fiber and arbitrary direction bonds, resist in-plane normal and shear deformations, thickness direction bonds, i.e. interlayer and shear bonds, resist transverse normal and shear deformations.

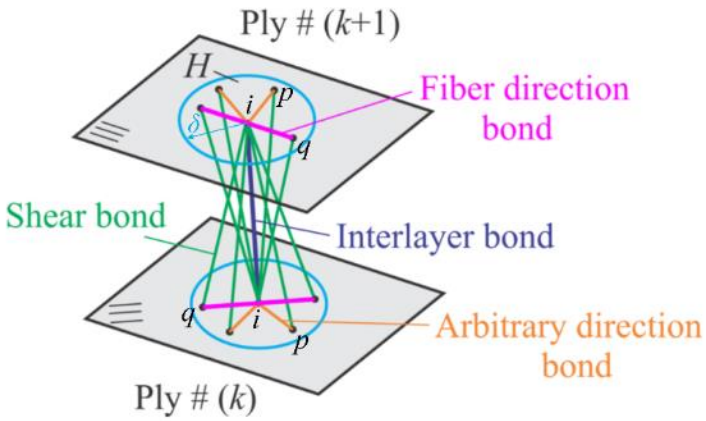

Figure 5.3 Peridynamic bonds in a composite laminate

Interlayer and shear bonds are related with bond constants c_N and c_S, respectively. Equating the strain energy densities based on the CCM and PD theories for simple loading conditions, they are obtained in terms of the engineering material constants as derived by Oterkus and Madenci (2012)

$$c_N = \frac{E_m}{h\bar{V}} \tag{5.8}$$

$$c_S = \frac{2G_m}{\pi h}\frac{1}{\left(\delta^2 + h^2 \ln\left(\frac{h^2}{\delta^2 + h^2}\right)\right)} \tag{5.9}$$

where E_m, G_m are the elastic and shear moduli of the matrix material, respectively and $\bar{V}$ is the incremental volume of the material point, i. The force-stretch relationships for interlayer bonds and shear bonds are expressed as

$$\mathbf{f}_N = c_N\, s\frac{\mathbf{y}' - \mathbf{y}}{|\mathbf{y}' - \mathbf{y}|} \tag{5.10}$$

and

$$\mathbf{f}_S = c_S\, \varphi(\Delta x)^2 \frac{\mathbf{y}' - \mathbf{y}}{|\mathbf{y}' - \mathbf{y}|} \tag{5.11}$$

where $\mathbf{f}_N$ and $\mathbf{f}_S$ are the peridynamic forces for normal and shear deformations, respectively and φ, Δx represent shear angle of the diagonal shear bonds and spacing between material points on the plane of the lamina, respectively. It is apparent that

peridynamic force for shear deformation, i.e. Equation (5.11), is different than the usual since it relates the force density with shear angle, φ, instead of the stretch, s, of the bonds. Figure 5.4 shows the diagonal shear bonds in deformed and undeformed configurations of the fictitious plane between the plies of a laminate. When the diagonal shear bonds in the fictitious plane deform, the change in angles between the perpendicular edges of the undeformed form of fictitious plane are φ_{ii} and φ_{pp} and they can be defined as

$$\varphi_{ii} = \frac{u_{ii}}{h} \tag{5.12}$$

and

$$\varphi_{pp} = \frac{u_{pp}}{h} \tag{5.13}$$

where u_{ii} and u_{pp} represent the relative displacements of corners, i and p, in the plane, respectively and they are also nearly equal to the change in length of diagonal shear bonds. In the light of above derivations, average shear deformation of fictitious plane is approximated by averaging the shear angles φ_{ii} and φ_{pp} as

$$\varphi = \frac{\varphi_{ii} + \varphi_{pp}}{2} \tag{5.14}$$

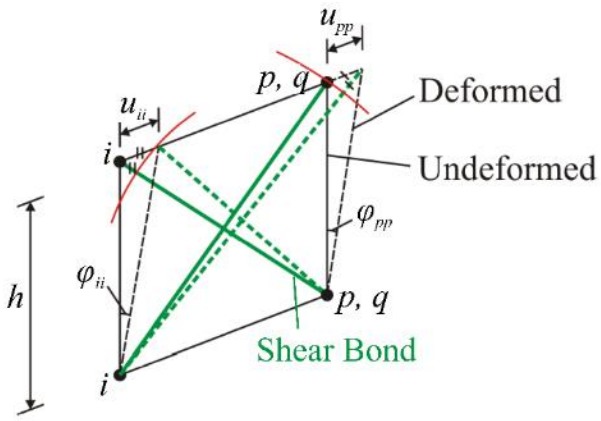

Figure 5.4 Diagonal shear bonds in deformed and undeformed configurations

Similar with in-plane bonds, force-stretch relationships of interlayer bonds and force-shear angle relationships of shear bonds are linear, as shown in Figure 5.5. Failures of

peridynamic bonds are related with critical stretches of interlayer bonds, s_N, and critical angles of diagonal shear bonds, φ_S. Since it is assumed that the plies are bonded with resin-rich matrix material, delamination is the dominated failure mechanism between plies of a laminate. Accordingly, mode – I and mode – II crack propagations are related with transverse normal and transverse shear deformations, respectively. Thus, Oterkus and Madenci (2012) proposed formulations for critical parameters of interlayer and shear bonds as

$$s_N = \sqrt{\frac{2G_{IC}}{h E_m}} \tag{5.15}$$

and

$$\varphi_S = \sqrt{\frac{G_{IIC}}{h G_m}} \tag{5.16}$$

where G_{IC} and G_{IIC} are the mode – I and mode – II critical energy release rates of the matrix material. The underlying idea on derivations of Equations (5.15) and (5.16) is that energies required to break all interlayer or shear bonds between the plies of a laminate are the same with mode – I or mode – II critical energy release rates, respectively. It is also important to note that the interlayer bonds are assumed to fail only in tension because of the predominant mechanism of the delamination between the plies of a laminate.

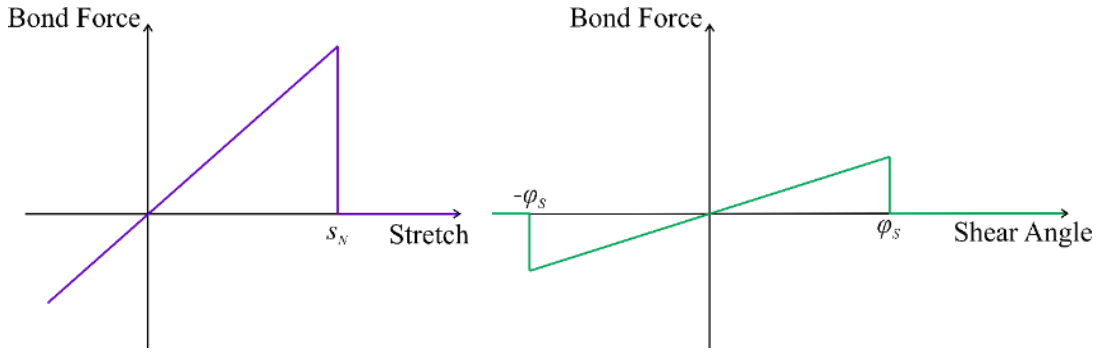

(a) Interlayer bond (b) Diagonal shear bonds

Figure 5.5 Force-stretch and force-shear angle relationships in a composite laminate

Peridynamic force relations given in Equations (5.10) and (5.11) are further modified by introducing the history-dependent failure parameter as

$$\mathbf{f}_N = \mu_N\left(\mathbf{x}'-\mathbf{x},t\right) c_N\, s \frac{\mathbf{y}'-\mathbf{y}}{\left|\mathbf{y}'-\mathbf{y}\right|} \tag{5.17}$$

where μ_N is the failure parameter for a mode I crack in delamination and it is defined as

$$\mu_N\left(\mathbf{x}'-\mathbf{x},t\right) = \begin{cases} 1 & \text{if } s\left(\mathbf{x}'-\mathbf{x},t'\right) < s_N \text{ for all } 0<t'<t \\ 0 & \text{otherwise} \end{cases} \tag{5.18}$$

and

$$\mathbf{f}_S = \mu_S\left(\mathbf{x}'-\mathbf{x},t\right) c_S\, \varphi\left(\Delta x\right)^2 \frac{\mathbf{y}'-\mathbf{y}}{\left|\mathbf{y}'-\mathbf{y}\right|} \tag{5.19}$$

where μ_S is the failure parameter for a mode II crack in delamination and it is defined as

$$\mu_S\left(\mathbf{x}'-\mathbf{x},t\right) = \begin{cases} 1 & \text{if } \left|\varphi\left(\mathbf{x}'-\mathbf{x},t'\right)\right| < \varphi_S \text{ for all } 0<t'<t \\ 0 & \text{otherwise} \end{cases} \tag{5.20}$$

Integrating each of the failure parameter inside the horizon of a material point as in Equation (5.7), local damage at a material point can be found for delamination damage related with mode I (Φ_N) and mode II (Φ_S) cracks in the material.

Finally, all peridynamic force relations for composite lamina and laminate, i.e. Equations (5.5), (5.17) and (5.19), are summed and written in a summation form to solve the problem in three-dimensions as

$$\rho_{(i)}^{(k)}\, \ddot{\mathbf{u}}_{(i)}^{(k)} = \sum_{p=1}^{\infty} \mu_{(i)(p)}^{(k)} c\left(\phi_{(i)(p)}^{(k)}\right) s_{(i)(p)}^{(k)} \frac{\mathbf{y}_{(p)}^{(k)} - \mathbf{y}_{(i)}^{(k)}}{\left|\mathbf{y}_{(p)}^{(k)} - \mathbf{y}_{(i)}^{(k)}\right|} V_{(p)}^{(k)} + \sum_{m=k+1,k-1} \mu_{N(i)(i)}^{(k)(m)} c_N\, s_{(i)(i)}^{(k)(m)} \frac{\mathbf{y}_{(i)}^{(m)} - \mathbf{y}_{(i)}^{(k)}}{\left|\mathbf{y}_{(i)}^{(m)} - \mathbf{y}_{(i)}^{(k)}\right|} V_{(i)}^{(m)}$$

$$+ \sum_{m=k+1,k-1} \sum_{p=1}^{\infty} \mu_{S(i)(p)}^{(k)(m)} c_S\, \varphi_{(i)(p)}^{(k)(m)} \left(\Delta x\right)^2 \frac{\mathbf{y}_{(p)}^{(m)} - \mathbf{y}_{(i)}^{(k)}}{\left|\mathbf{y}_{(p)}^{(m)} - \mathbf{y}_{(i)}^{(k)}\right|} + \mathbf{b}_{(i)}^{(k)} \tag{5.21}$$

where superscript k shows the ply number of a laminate and subscripts i, p are the material points in a lamina. For example, $s_{(i)(p)}^{(k)}$ is the stretch between material points i and p in the k^{th} ply and $\varphi_{(i)(p)}^{(k)(m)}$ is the shear angle between material points i in the k^{th} ply and p in the m^{th} ply. Please also note that the bond constants, c, c_S and c_N, are derived under the assumption that the horizon of the main material point, $H_{\mathbf{x}}$, is completely inside the body. However, this is not generally the case for real problems because the horizon is usually truncated near the boundaries of a surface, as shown in Figure 5.6, and this results in a reduction in material point stiffness. Hence, the stiffness reduction of a material point near the free surfaces must be corrected by calculating the strain energy density of a material point with truncated horizon and equating it with CCM theory. Following this, surface correction factor of each bond is determined by averaging through the material points associated with the bond and the peridynamic force of the bond is further modified. The procedure of applying surface corrections can be viewed in detail in ref. (Oterkus and Madenci, 2012).

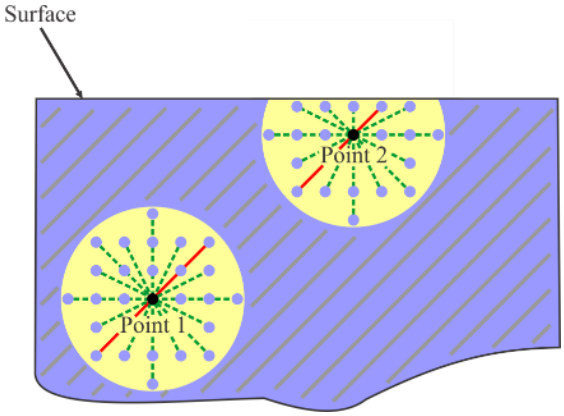

Figure 5.6 Surface effects in the body

As mentioned in Section 3.2.2.1, after obtaining the acceleration, $\ddot{\mathbf{u}}_{(i)}^{(k)}$, from Equation (5.21), the velocity and displacement of each material point can be determined for the next time step by using explicit time integration schemes. The advantage of explicit schemes over implicit time integration methods is that there is no need to solve equation of motion using large matrices because each equation related to the main material point, i, can be solved independently. However, the explicit schemes are stable only if the time step size, Δt, is smaller than a particular value. The stability

condition for isotropic materials was given by Silling and Askari (2005) using von Neumann stability analysis and this can be slightly modified for a composite laminate as

$$\Delta t < \sqrt{\frac{2\rho_{(i)}^{(k)}}{\sum_p c \frac{1}{\left|\xi_{(i)(p)}\right|} V_{(p)}^{(k)} + \frac{1}{h}\sum_m c_N V_{(i)}^{(m)} + \frac{1}{2h} c_S \left(\Delta x\right)^2}} \times sf \tag{5.22}$$

where sf is the safety factor, $0 < sf < 1$, and $\xi_{(i)(p)}$ represents reference distance between material points *p* and *i* in the undeformed configuration, $\xi_{(i)(p)} = \left|\mathbf{x}_{(p)} - \mathbf{x}_{(i)}\right|$.

5.4 Damage Evolution in a 4 – Ply Composite Laminate

In this section, damage evolution in a 4-ply composite laminate subjected to underwater shock loading is analysed using PD theory and the results are compared against a previous study done by Batra and Hassan (2007). In ref. (Batra and Hassan, 2007), an FE computational framework based on additive damage evolution equations was developed in order to capture several damage types, i.e. fiber/matrix debonding, matrix cracking, fiber breakage and delamination, of a composite laminate under shock loading. The geometry, loading condition and mechanical properties of the composite plate used here are the same with ref. (Batra and Hassan, 2007).

5.4.1 Geometry and loading condition

A 4-ply composite plate, which can be a part of surface ship, with fibers of each ply are oriented along the *x* or x_1 direction, $\theta = 0^\circ$, is considered. All the edges of the plate are assumed to be clamped and in Peridynamics the displacement boundary condition is implemented by creating fictitious boundary region, which may have a depth of δ, as shown Figure 5.7. The length and width of the plate is specified as $L = W = 22$ cm , respectively and each lamina has a thickness of $h = 10$ mm. These geometrical properties are consistent with test plates, which have been used in experiments to date, subjected to air and underwater shock loadings (Batra and Hassan, 2007).

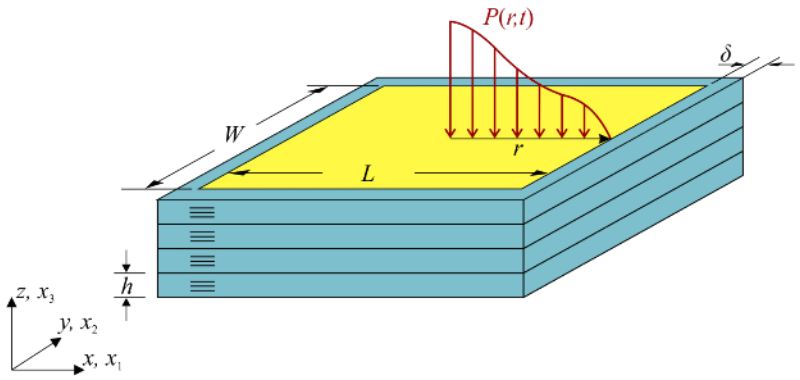

Figure 5.7 4-ply composite laminate under shock loading

The chosen composite square plate can be a part of surface ship below the water line and if an explosive charge is detonated far from the target surface, the generated high pressure shock wave propagates towards the target, as shown in Figure 5.8. Whenever the shock wave strikes on a ship surface, it may cause sudden severe damage on the structure. For this reason, only the first impact of the shock wave can be considered with neglecting other effects, i.e. bubble pulsation, reflection of the shock wave from bottom or free surfaces and FSI.

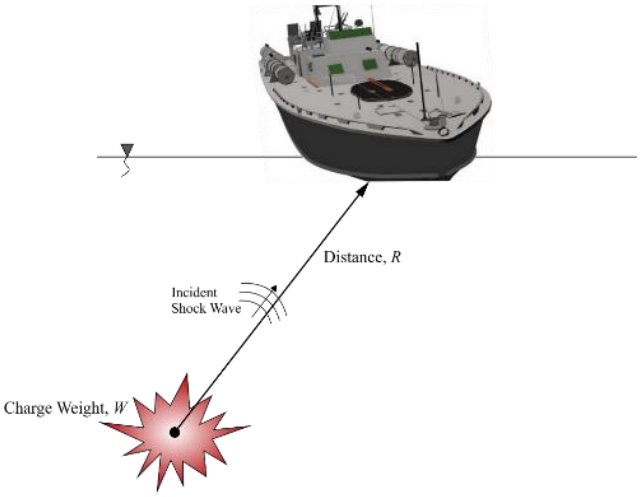

Figure 5.8 Schematic representation of underwater explosion phenomena

Whenever the explosive charge is detonated in an open water, the pressure, *P*, rapidly increases to an extremely high value in a very small time range, which may be less than 10^{-7} s, and it is followed by an exponential decay function (Liang and Tai, 2006) which can be represented by an empirical expression as (Batra and Hassan, 2007)

$$P(t) = P_{\max} e^{-t/\lambda} \tag{5.23}$$

where P_{max}, t and λ denote the peak pressure, time and the decay constant, respectively. The decay constant, λ, which depends on the explosive type, the weight of charge, W, and the standoff distance, R, between the charge and the target, can be expressed as

$$\lambda = K_2 W^{1/3} \left(\frac{W^{1/3}}{R} \right)^{A_2} \tag{5.24}$$

where K_2 and A_2 are parameters related with the explosive type. Their values for several types of explosives (Batra and Hassan, 2007) are given in Table 5.1.

Table 5.1 Shock wave parameters

	Explosive Type			
	TNT	**HBX-1**	**PETN**	**Nuclear**
K_1	52.12	53.51	56.21	1.06×10^4
A_1	1.18	1.144	1.194	1.13
K_2	0.0895	0.092	0.086	3.627
A_2	-0.185	-0.247	-0.257	-0.22

The peak pressure, P_{max}, is extremely high in the vicinity of the charge and it decays with an increasing standoff distance between the charge and the target by

$$P_{max} = K_1 \left(\frac{W^{1/3}}{R} \right)^{A_1} \tag{5.25}$$

where K_1 and A_1 are also explosive type related parameters which can be obtained from Table 5.1. To sum up, the pressure profile for $W = 64$ kg of TNT, which is placed beneath the ship surface with a standoff distance of $R = 10$ m between the charge and the target, is obtained from Equations (5.23) – (5.25) as

$$P(t) = 17.678 e^{-t/0.424} \tag{5.26}$$

and it is plotted in Figure 5.9.

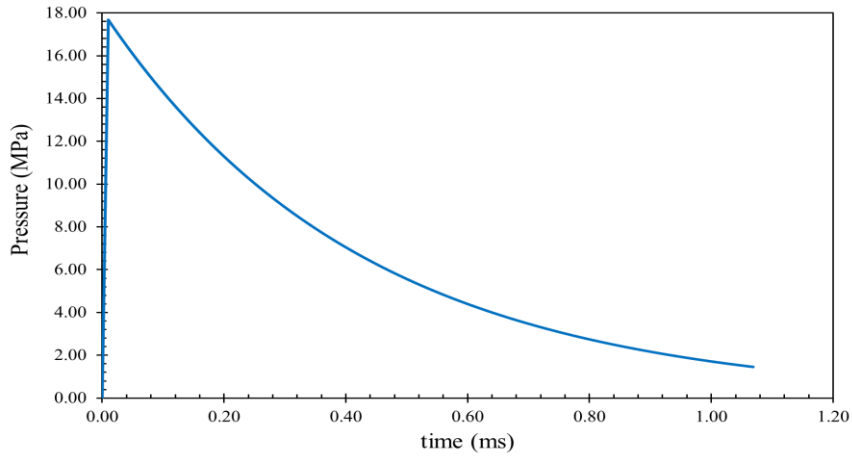

Figure 5.9 The pressure profile of the shock wave in an open water

Furthermore, spherical shock wave propagates from the charge and it becomes nearly planar far away from the charge. However, Batra and Hassan (2007) assumed nonlinear pressure distribution, $P(r,t)$, over the plate and it is expressed by a polynomial function, which is experimentally derived by Turkmen and Mecitoglu (1999), as

$$P(r,t) = \left(-0.0005r^4 + 0.01r^3 - 0.0586r^2 - 0.001r + 1\right)P(t) \tag{5.27}$$

where r is the distance from the centre of a plate in "cm", shown in Figure 5.7. Equation (5.27) is derived from air blast experiments and it is assumed that similar conditions may be satisfied underwater as well. Figure 5.10 shows the plot of polynomial function, Equation (5.27), at time which peak pressure, $P(t) = P_{\max}$, is applied to the centre of a plate, $r = 0$, and diminishing property of the pressure values towards the edges can be observed from the figure.

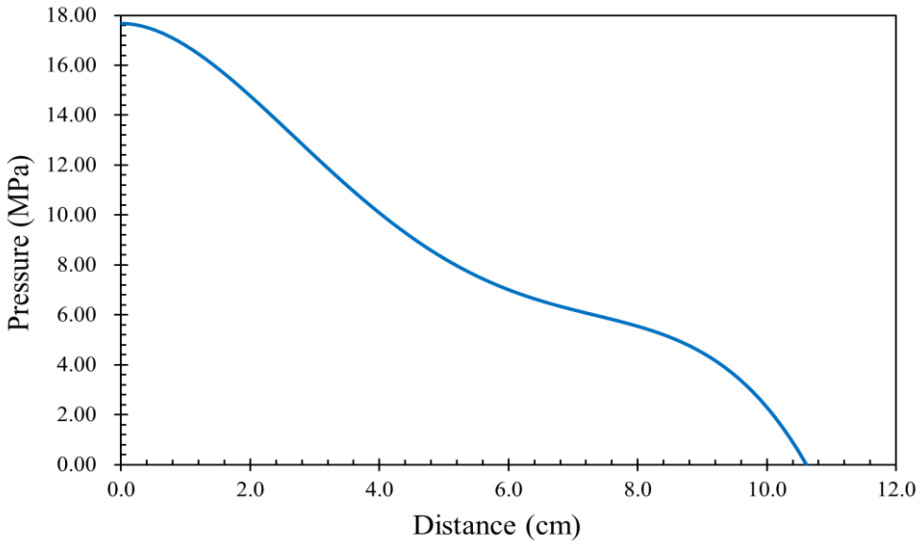

Figure 5.10 The change in shock pressure towards the edges of a plate

5.4.2 Mechanical properties and Peridynamic parameters

Each ply of a laminated composite plate is composed of AS4 carbon fiber and PEEK matrix with a fiber volume fraction of $V^f = 0.6$ (Batra and Hassan, 2007) and all fibers are oriented along the *x* direction. The isotropic material properties of PEEK matrix and AS4 carbon fiber are given in Table 5.2 (Batra and Hassan, 2007). Furthermore, with an assumption of each material is homogeneously distributed over the plate, unidirectional lamina has the generalized properties shown in Table 5.3 (Hassan, 2005).

Table 5.2 Material properties of each element in a lamina

	PEEK Matrix	**AS4 Carbon Fiber**
Young's Modulus, E	6.14 GPa	214 GPa
Shear Modulus, G	2.264 GPa	84.7 GPa
Poisson's Ratio, ν	0.356	0.263
Mass Density, ρ	1.44	1.78

Table 5.3 Material properties of the unidirectional lamina

	AS4/PEEK
Longitudinal Young's Modulus, E_1	130.86 GPa
Transverse Young's Modulus, E_2	14.70 GPa
Shear Modulus, G_{12}	5.44 GPa
Major Poisson's Ratio, ν_{12}	1/3
Mass Density, ρ	1640 kg/m^3

*Subscripts 1 and 2 denote the x_1 and x_2 axes, respectively.

As for the numerical solution of the problem, laminated composite plate, shown in Figure 5.7, is discretised into many material points such that each lamina has a single layer of material points with a grid size of $\Delta x = 1\times10^{-3}$ m and each material point has a horizon radius of $\delta = 3.015\Delta x$, as in Figure 5.11.

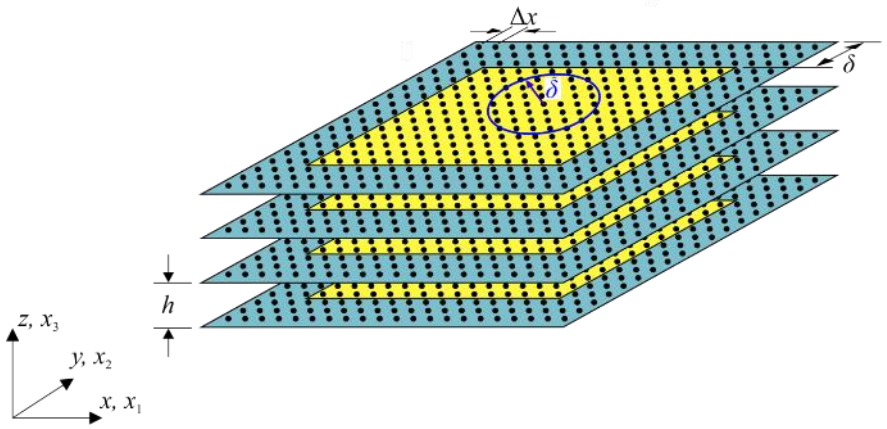

Figure 5.11 Discretization of a 4-ply composite plate

Substituting values of geometrical and material properties as well as that of peridynamic parameters into Equations (5.2), (5.3), (5.8) and (5.9), properties of all types of bonds, i.e. bond constants c_F, c_A, c_N and c_S, can be determined for a composite plate.

As mentioned in Section 5.2, critical stretch values of fiber direction and arbitrary direction bonds may be determined from several experiments of different lay-up configurations of AS4/PEEK laminated composites as in ref. (Oterkus et al., 2012).

However, we are limited in number of experiments and failure strains can only be obtained from experimental stress-strain curves of an axially loaded AS4/PEEK unidirectional lamina specimen (cf. Figs. (2.9-11) in ref. (Hassan, 2005)) or from different configurations of 4-ply composites with identically oriented fibers in each ply (cf. Fig. 2.41 in ref. (Hassan, 2005)). Even, the strain rate effects of composites can also be observed from Figs. (2.18-21) in ref. (Hassan, 2005). Tensile failure strains of an axially loaded unidirectional lamina can be read as 0.01075 in the fiber direction, i.e. x_1 direction, and as 0.0081 in the perpendicular direction to the fibers, i.e. x_2 direction. In the light of above considerations, critical stretch value of fiber direction bonds in tension is taken as $s_{Ft} = 0.006$ and critical stretch value of arbitrary direction bonds in tension is taken as $s_{At} = 0.004$. Apart from that, fiber and arbitrary direction bonds are only allowed to fail in tension and no compressive failure is considered.

As mentioned in Section 5.3, critical stretch value of interlayer bonds, i.e. s_N, and critical shear angle value of shear bonds, i.e. φ_S, may be determined by substituting material properties of a PEEK matrix material, i.e. E_m, G_m, G_{IC} and G_{IIC}, as well as thickness of a lamina, h into Equations (5.12) and (5.13). Critical energy release rates of PEEK matrix material are chosen from "APC-2 PEEK Thermoplastic Polymer Technical Data Sheet" (2012) where mode I and mode II interlaminar fracture toughness values of APC-2 PEEK/AS4 unidirectional tape are provided as $G_{IC} = 1.7$ kJ/m^2 and $G_{IIC} = 2.0$ kJ/m^2, respectively. Thus, critical values of interlayer and shear bonds are found as, $s_N = 0.01488$ and $\varphi_S = 0.0188$, respectively.

5.4.3 Underwater shock analysis results of a 4 – ply composite laminate

Underwater shock analysis of a 4-ply laminated composite plate is carried out for 230 μs because at this instant complete failure takes place. The time step size for an explicit time integration is chosen according to Equation (5.22) as $\Delta t = 7.12 \times 10^{-8}$ s with a safety factor of $sf = 0.5$. Peridynamic results are compared against FE results of ref. (Batra and Hassan, 2007). Peridynamic damage results are demonstrated for all 4 plies of a composite plate whereas FE results are only for three surfaces, i.e. top, middle and

bottom. The plies are numbered from bottom ply to top ply as 1st to 4th ply, respectively. While Peridynamic damage parameters represent matrix damage, fiber damage, delamination damages for mode I and mode II cracks, FE method has matrix cracking, fiber/matrix debonding, fiber breakage, and delamination damage variables. Hence, matrix damage in peridynamics is a combination of matrix cracking and fiber/matrix debonding damage variables of FE method. Moreover, delamination damage variable in FE method is a combination of mode I and mode II cracks of delamination damage in Peridynamics.

5.4.3.1 Displacement evolution in time

The evolution of vertical displacement values (u_z) of central material points in each ply are the same and only one ply's material point values are plotted against time in Figure 5.12a. The results are compared with FE results provided by Batra and Hassan (2007), shown in Figure 5.12b, and it is found that they are in good agreement although there is a difference between the two displacement values after 150 μs. However, it is also important to note that FE results have a tendency towards PD results from mesh 1 to mesh 4 which show refinement in mesh sizes.

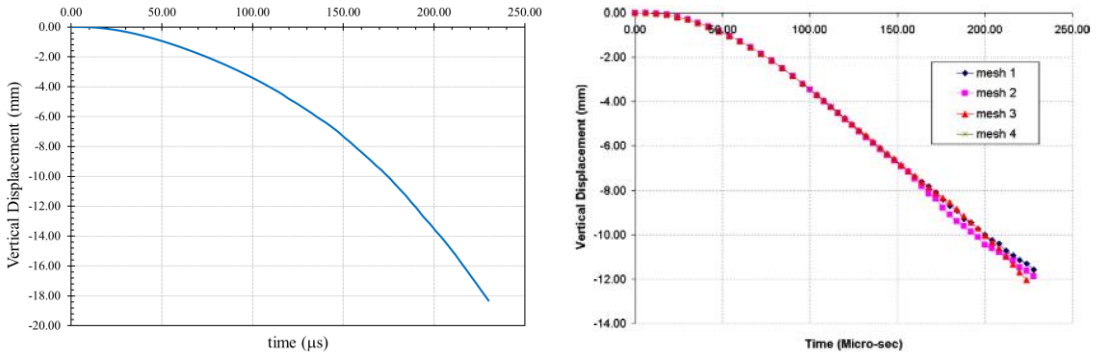

(a) PD theory (b) FE method (Batra and Hassan, 2007)

Figure 5.12 Comparison of the change of vertical displacement values of central point in time

5.4.3.2 Matrix cracking damage

Matrix damage (Φ_A) commences from the centre of horizontal edges of top ply at about 54 μs, which is along the fiber direction, and it propagates towards the both vertical edges until it is arrested nearly at 108 μs, as shown in Figure 5.13. The matrix

damage in PD theory involves both matrix cracking and fiber/matrix debonding damage variables of FE method. These failure modes can also be identified in PD theory comparing both results by means of occurrence region and propagation direction. Hence, matrix cracking damage in PD theory is shown as encircled region in Figure 5.13. A similar matrix cracking damage behaviour is also observed for 2nd and 3rd plies and even if their emergence time is later than the top ply, they nearly reach the similar extent at the same time. Batra and Hassan (2007) also observed the matrix cracking damage variable at the same region of the top surface as shown in Figure 5.14b but its propagation path seems different than the PD theory which is shown in Figure 5.14a.

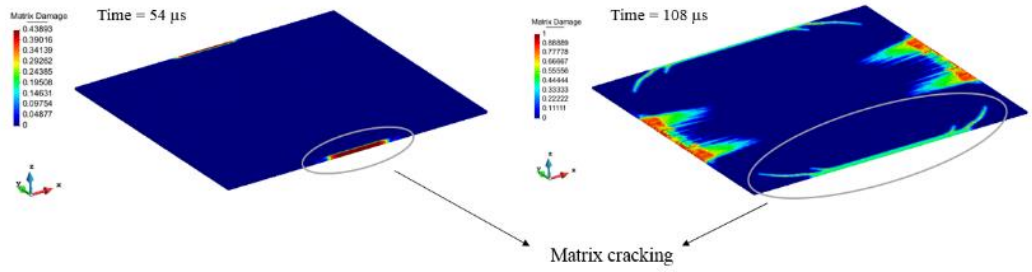

Figure 5.13 Top ply matrix damage evolution in time

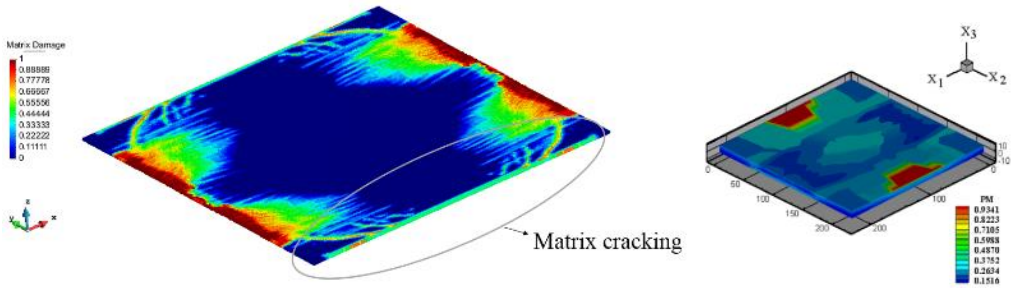

(a)Top ply in PD theory at 160 μs (b) Top surface in FE method at 160 μs (Batra and Hassan, 2007)

Figure 5.14 Comparison of top surface matrix damages

Matrix damage emerges from the centre of bottom ply at about 108 μs which is exactly the same observed time in FE method. Furthermore, propagation of damage is very fast along the fiber direction as in FE method. From the comparisons, shown in Figure 5.15, it is observed that damage propagation behaviour and its path are very similar in both results.

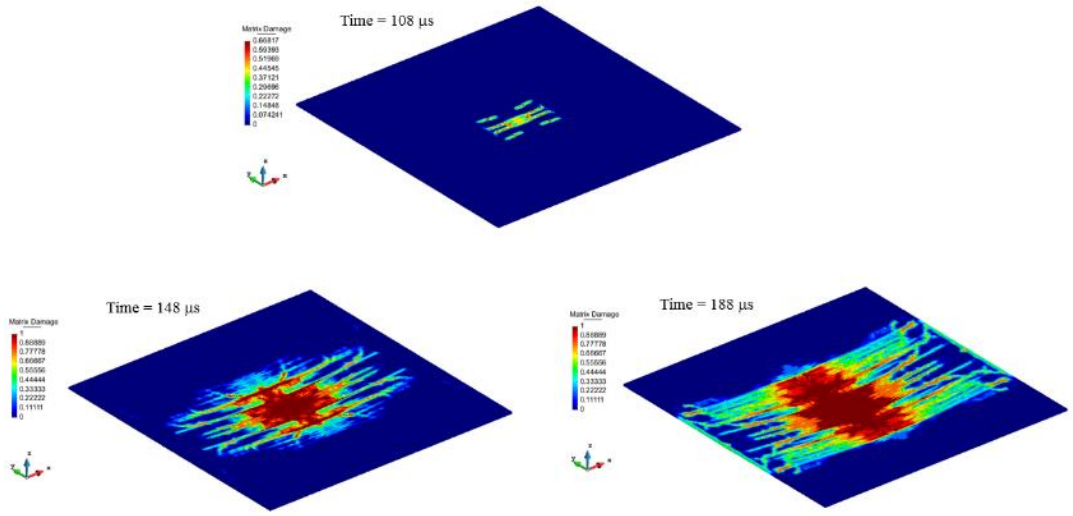

(a) Bottom ply in PD theory

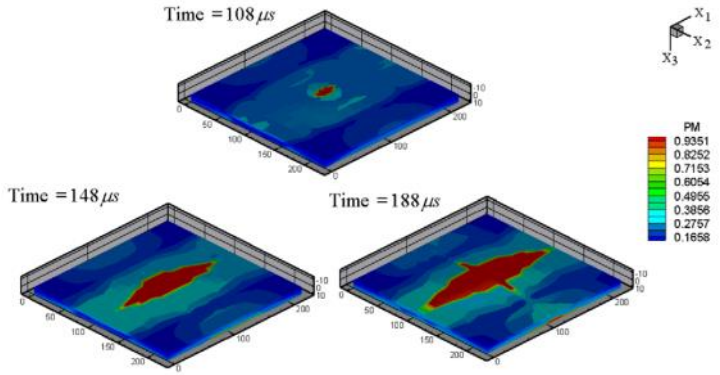

(b) Bottom surface in FE method (Batra and Hassan, 2007)

Figure 5.15 Comparison of bottom surface matrix damage evolution in time

After the emergence of the matrix damage in the bottom ply, it also diffuses into upper plies and central matrix damage is observed in the second ply nearly at 130 µs, as shown in Figure 5.16a. The diffusion time of central matrix damage to the middle surface is about 125 µs in FE method and this is nearly the same observation time with PD results. Moreover, bottom and top surface matrix damage regions are similar in both results and this can be seen from Figure 5.14 and Figure 5.16 for $t = 160\ \mu s$. It can also be noticed that even if the induced shock loading is circular and maximum at the centre of a top ply, central damage cannot be observed in the top ply at that time. Instead, bottom plies have the central damage and this is probably the result of wave

reflection from the bottom ply where compressive wave is transformed into a tension wave (Batra and Hassan, 2007).

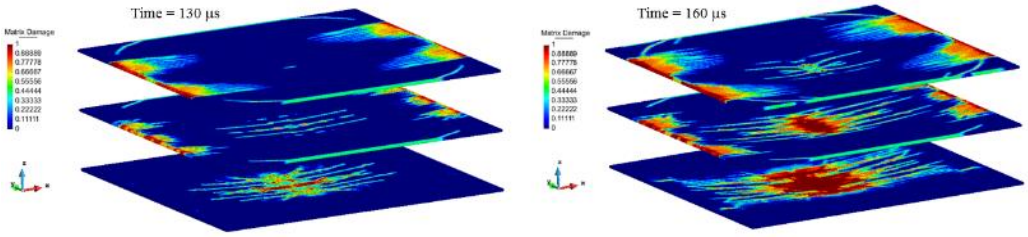

(a) Matrix damage evolution in bottom three plies in PD theory

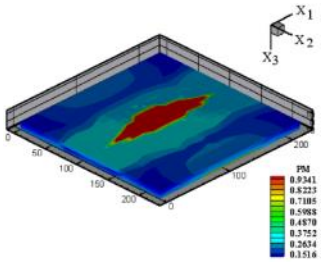

(b) Bottom surface in FE method (Batra and Hassan, 2007) at 160 μs

Figure 5.16 Comparison of bottom surface matrix damages

Later in time, central matrix damage reaches the top ply nearly at 220 μs, shown in Figure 5.17, and this indicates that the wave reflected from the bottom surface has just reached the top surface.

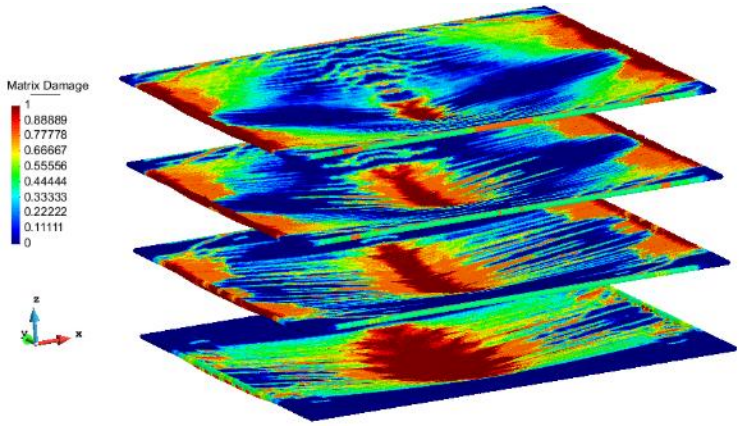

Figure 5.17 Matrix damage results of all plies at 220 μs

5.4.3.3 Fiber/matrix debonding damage

In FE method debonding damage propagates from the vertical edges towards the centre of the plate along the fiber direction and the similar propagation behaviour is also observed in PD theory for top three plies. It first evolves in top two plies at 108 μs and propagates towards the centre while extending along the edges until nearly 160 μs. At that time 2nd ply also has the similar damage with top two plies. This fiber/matrix debonding damage propagation behaviour is shown in Figure 5.18a and it is comparable with FE results, shown in Figure 5.18b. Besides, Batra and Hassan (2007) also observed debonding damage in all surfaces of the laminate instantaneously. The ideas developed here can also supported by commonly known behaviour of debonding damage that it usually occurs along the fibers rather than in the perpendicular direction to the fibers.

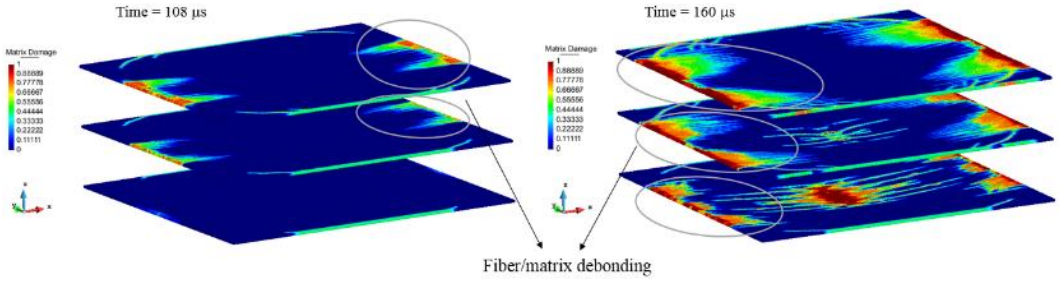

(a) Matrix damage evolution of top three plies in PD theory

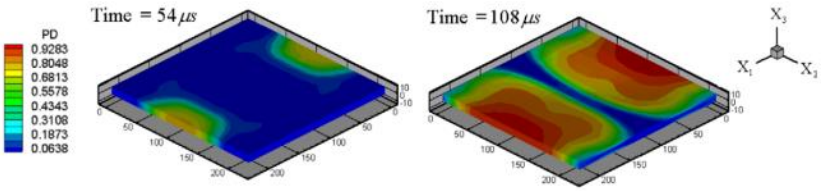

(b) Debonding damage evolution in FE method (Batra and Hassan, 2007)

Figure 5.18 Comparison of matrix damages in PD theory with a debonding damage in FE method

5.4.3.4 Fibrer breakage damage

Fiber damage (Φ_F) commences from vertical edges of the top two plies nearly at 108 μs and it grows through the edges until 160 μs. The same damage behaviour at the edges is also observed in the 2nd ply with a little later emergence time but they are at

the same length at 160 μs, as can be seen in Figure 5.19a from the plot of top three plies. These damage patterns are well comparable with FE method fiber breakage damage variable which emerges with a very small value from the edges of bottom surface at 160 μs, as shown in Figure 5.19b. Furthermore, a similar damage pattern for the edges of bottom ply is also observed in PD theory but with a later emergence time which is about 180 μs.

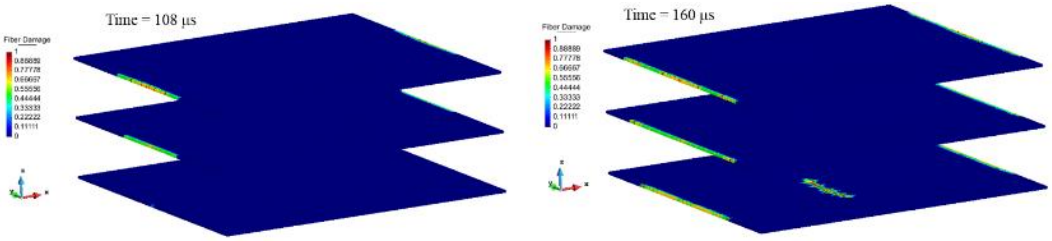

(a) Fiber damage evolution of top three plies in time in PD theory

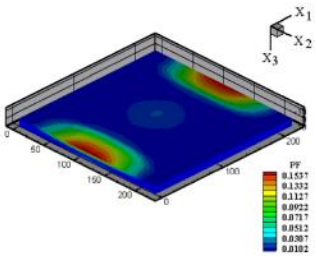

(b) Bottom surface in FE method at 160 μs (Batra and Hassan, 2007)

Figure 5.19 Comparison of fiber damages at the edges

On the other hand, central fiber damage develops at the bottom ply at 130 μs and it propagates along the perpendicular direction to the fibers, i.e. *y* axis. This propagation behaviour can also be seen in FE method for the bottom surface. The comparison of bottom surface central fiber damage propagation behaviour can be seen in Figure 5.20. Although the fiber damage initiation time in PD theory seems earlier than the FE results, the same propagation behaviour is captured. Furthermore, the central fiber damage grows quite fast in the bottom surface in less than 20 μs in FE method. Similarly, in PD theory, it grows until 160 μs quite fast within 30 μs. Apart from that, the further growth is observed in PD theory after 188 μs and completed at 220 μs.

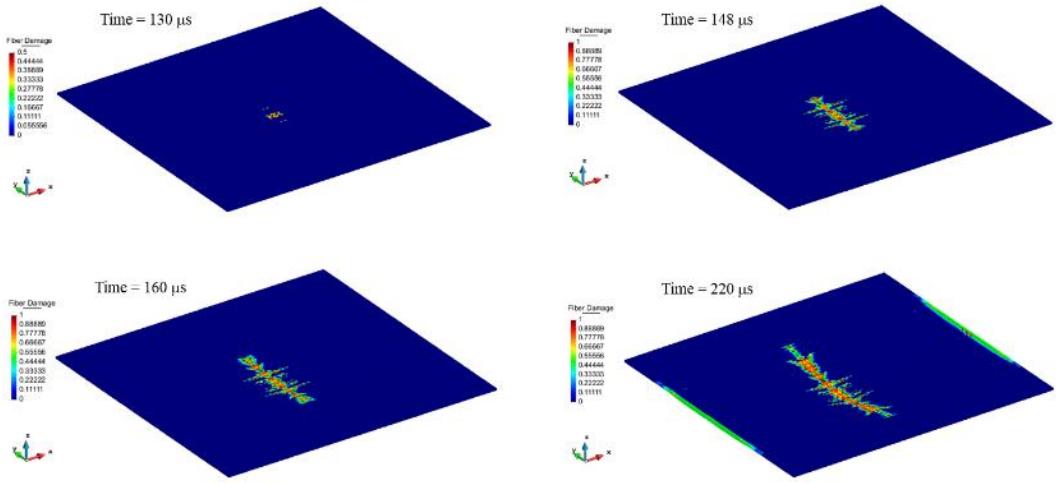

(a) Bottom ply in PD theory

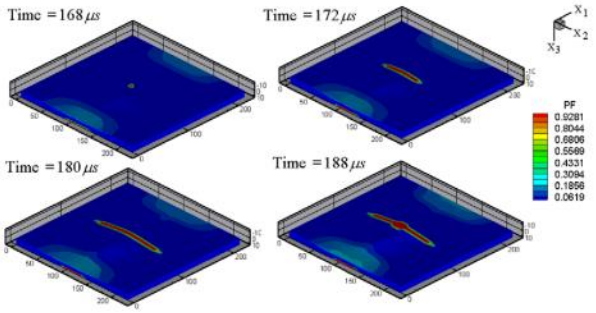

(b) Bottom surface in FE method (Batra and Hassan, 2007)

Figure 5.20 Comparison of bottom surface fiber damage evolution in time

Besides, fiber damage diffuses into upper plies with time, shown in Figure 5.21, and it reaches to the top ply at about 220 μs. In FE method, central fiber breakage damage variable gradually develops in the top ply until nearly 210 μs but it still has very small value of 0.20 at that time. The fiber damage in the top surface at 160 μs is shown in Figure 5.22. Batra and Hassan (2007) also mentioned that the central damage in the top surface grows instantaneously to a very high value, i.e. to the order of 1.0, at about 210 μs. As a result, central fiber damage of the top ply at 220 μs in PD theory is well comparable with FE result of top ply at 210 μs. Although, the damage plot of top surface is not provided for FE method at that time, the damage extent given in Figure 5.22 can be compared with PD result, given in Figure 5.21.

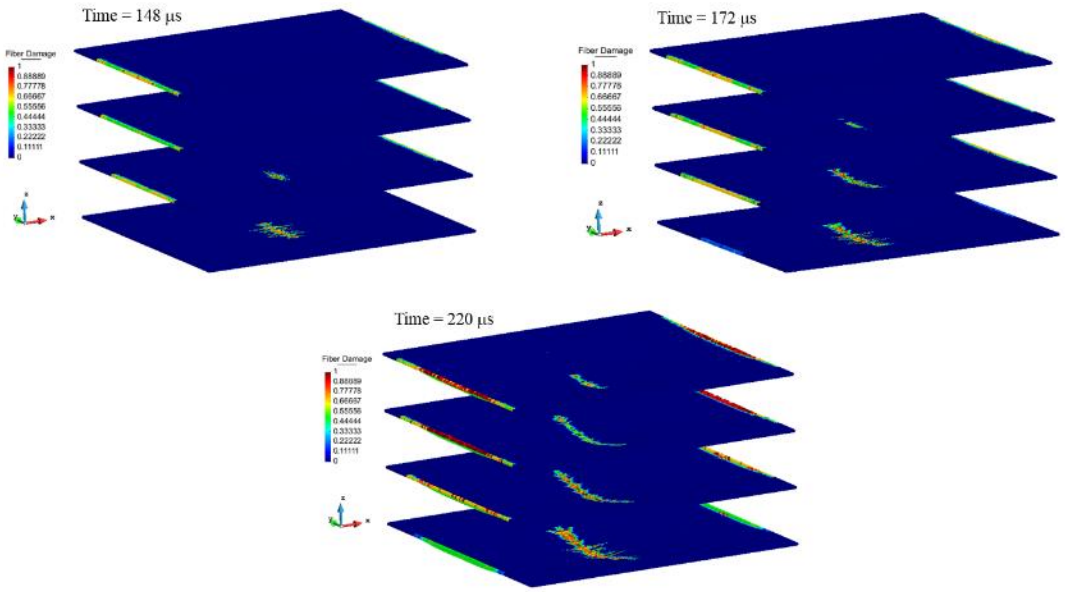

Figure 5.21 Central fiber damage diffusion from bottom to top ply with time in PD theory

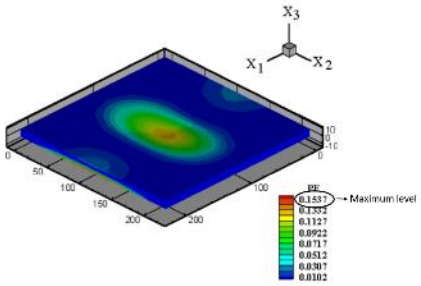

Figure 5.22 Top surface central fiber breakage damage at 160 μs in FE method (Batra and Hassan, 2007)

5.4.3.5 Delamination damage

As mentioned in Section 5.4.3, delamination damage can either be related with mode I (Φ_N) or mode II (Φ_S) cracks in PD theory. Mode II cracks emerge from the vertical edges of top three plies nearly at 108 μs with a very small extent and they develop through the edges with the inclusion of bottom ply cracks, as shown in Figure 5.23. The observed initiation place of delamination damage from the edges is also mentioned by Batra and Hassan (2007) in FE method. They support their idea with the given transverse shear stress values (S_{13}) for the top and bottom surfaces as shown in Figure 5.24. The provided high stress values reveal that delamination may initiate from the

edges (Batra and Hassan, 2007). At the time of 148 μs, delamination damage is also observed at the centre of bottom three plies in peridynamics as can be seen in Figure 5.23. The central damage and the damage at the edges develop gradually in the perpendicular direction to the fibers, i.e. *y* axis, and severe delaminated regions are observed both at the edges and at the centre of the all plies at 220 μs, as shown in Figure 5.23.

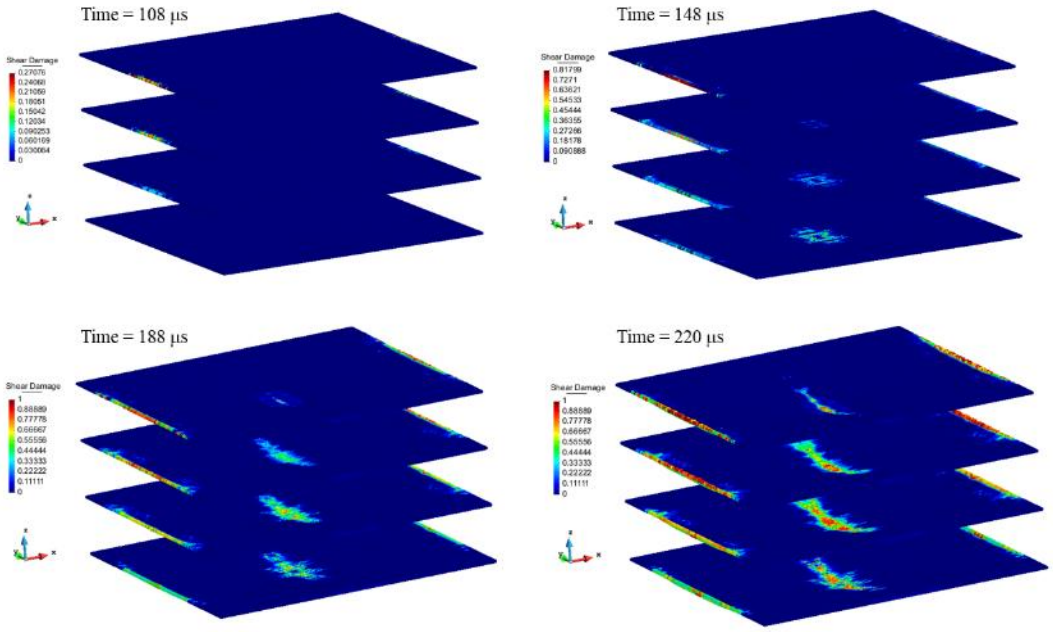

Figure 5.23 Evolution of mode II delamination damage cracks in PD theory

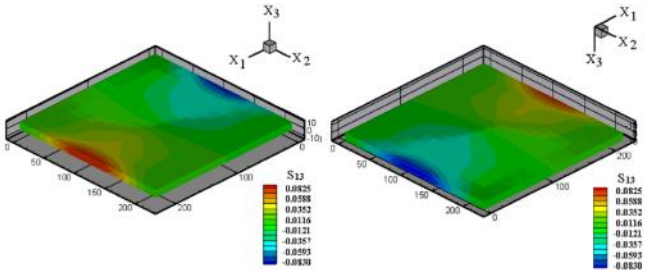

Figure 5.24 Transverse shear stress values for top (left) and bottom (right) surfaces in FE method at 160 μs (Batra and Hassan, 2007)

On the other hand, mode I delamination damage cracks emerge later than the mode II cracks from the vertical edges of middle plies at about 160 μs and they are in a very small extent compared to mode II cracks. As the time progresses, the central region of

middle plies are also damaged. The delaminated areas as a result of mode I cracks are shown in Figure 5.25 at the end of 220 μs.

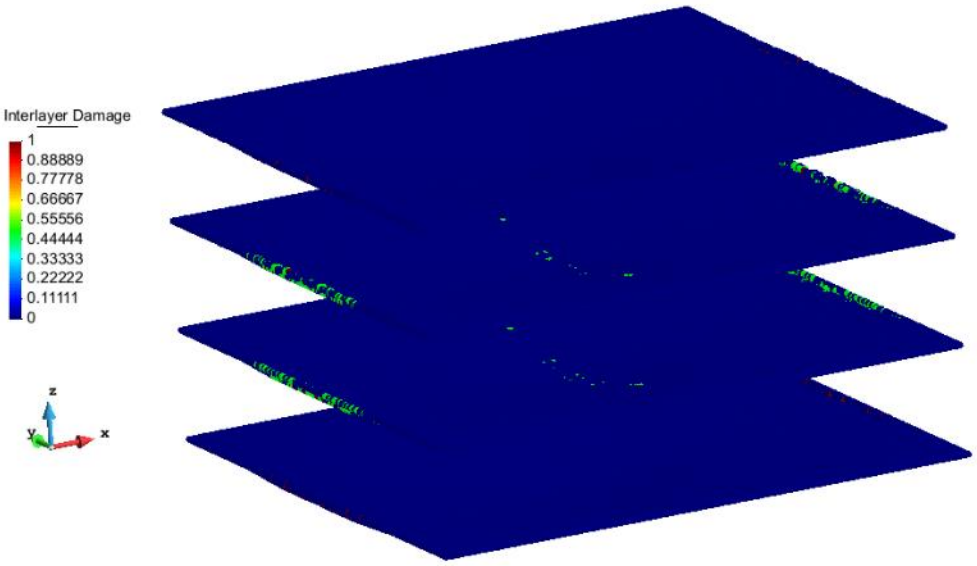

Figure 5.25 Mode I delamination damage cracks at all plies in PD theory at 220 μs

Batra and Hassan (2007) provided top view of the final delaminated regions from all surfaces at the end of analysis, i.e. at 220 μs, as shown in Figure 5.26a. For comparison purposes, mode II and mode I delamination damage cracks as well as damage at each ply are combined and plotted in Figure 5.26b. As a result, an agreement between FE method and Peridynamics are evident by means of delaminated regions from the figures.

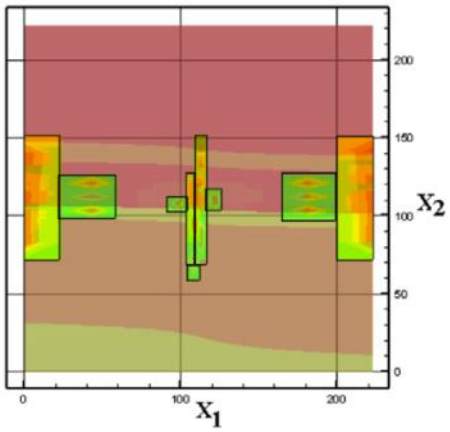

(a) Top view of delaminated regions in FE method (Batra and Hassan, 2007)

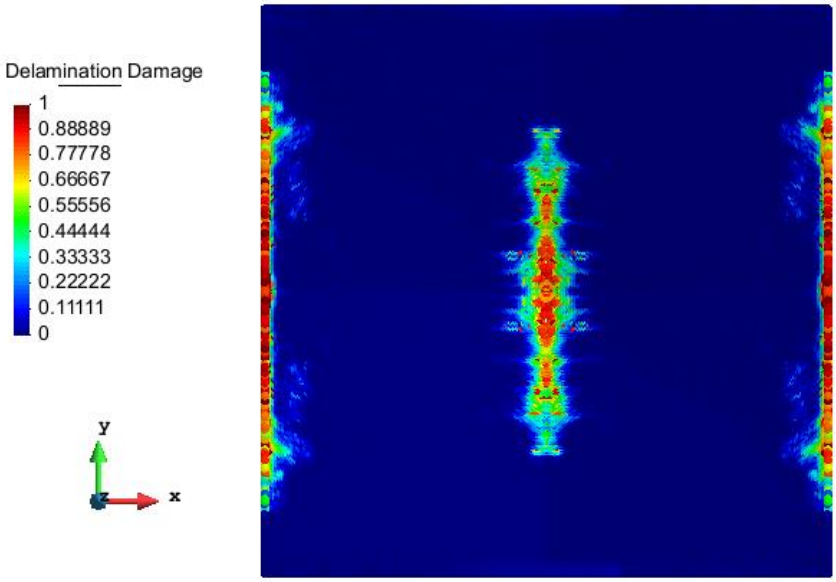

(b) Top view of combined delamination damage of all plies in PD theory

Figure 5.26 Comparison of delaminated regions at 220 μs

5.5 Damage Evolution in a 13 – Ply Composite Laminate

In this section, damage evolution in a 13-ply composite laminate structure is investigated and the results are compared against experimental study done by LeBlanc (2011). In ref. (LeBlanc, 2011), CST (Conical Shock Tube) test setup is used to

replicate underwater shock phenomena. The geometry and mechanical properties of the composite plate used in this study are the same with ref. (LeBlanc, 2011).

5.5.1 Geometry and loading condition

The CST experimental setup used by LeBlanc (2011) is shown in Figure 5.27. Walls of the tube are very thick in order to provide rigid boundary conditions and the conical shape tube is filled with water. Shock wave propagates from the breech, at which charge is located, and strikes to the test plate. The test plate is constrained with fixed end cap using mounting fixtures and this ensures fully clamped air backed conditions. Test plate used by LeBlanc (2011) is shown in Figure 5.28 and it is clamped from the boundary region, which has the yellow colour in the figure, using bolts. The bolt holes are oriented such that they have an equal distance between each other and they have a radius of $r = 4$ mm. The inner and outer radii of the plate are specified as $R_u = 11.43$ cm and $R = 13.2715$ cm, respectively. The thickness of each lamina of the test plate is $h = 0.254$ mm.

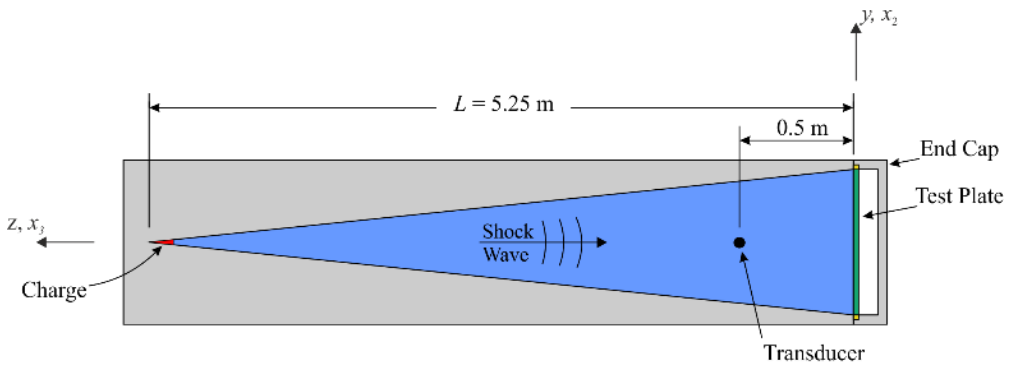

Figure 5.27 Representative CST test setup (LeBlanc, 2011)

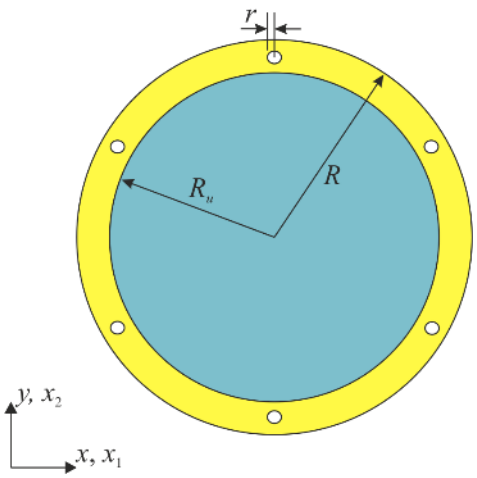

Figure 5.28 Composite test plate

As in the previous case, which is explained in Section 5.4.1, only the first impact of the shock wave is considered so that pressure generated by an incident shock wave alone is induced to the test plate. Practically, the walls of the CST confine spherical shock wave and only the conical section of the spherical wave is represented in the experiment as shown in Figure 5.29. For this reason, the charge with a spherical shape, which is used in open water experiments, is replaced with its conical sector in order to generate conical shape shock wave (Poche and Zalesak, 1992). While shock wave propagates along the tube, reflected waves from the rigid boundaries lead to intensification of shock pressure values. Thus, Poche and Zalesak (1992) derived a theoretical amplification factor (AF) based on the ratio of volume of spherical explosive to the volume of conical sector of it as

$$AF = \frac{1}{\sin^2(\alpha/4)} \tag{5.28}$$

in which α is the plane angle of the cone. However, Equation (5.28) underestimates the weight of an explosive charge which results in lower pressure values than expected from the CST setup. The reason of this performance decline is the elastic deformation losses which can occur along walls of the tube. In reality, practical AF is much lower than the theory and it can be calculated by considering weights of spherical (W) and conical charges (w) as

$$AF = \frac{W}{w} \tag{5.29}$$

Thus, the energy dissipation from the elastic walls can be calculated by using Equations (5.28) and (5.29).

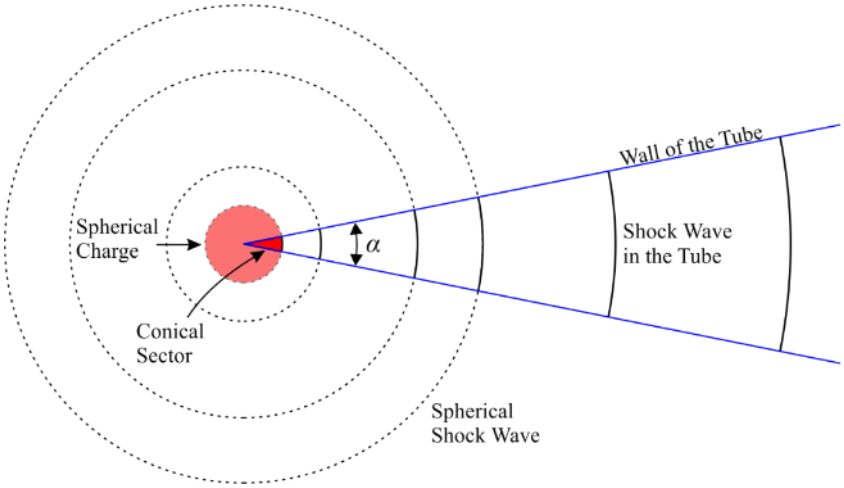

Figure 5.29 Shock wave in CST

The CST test setup used by LeBlanc (2011) has the internal cone angle of $\alpha = 2.6°$ and shock wave pressure values are measured by a transducer which is located at 0.5 m in front of the test specimen as shown in Figure 5.27. Several experimental studies with CST were carried out by LeBlanc (2011) and it was mentioned that the maximum pressure value (P_{max}) of 10.3 MPa can be measured at the transducer location using M6 blasting cap – 1.32 g TNT Equivalency. The pressure profile of this charge at the transducer location is plotted in Figure 5.30. However, the maximum pressure value (P_{max}) of 11.7 MPa was measured at the transducer location for the test considered here. Unfortunately, the pressure profile was not provided for this level by LeBlanc (2011) as well as the profile at the test plate location, $L = 5.25\,\text{m}$, rather than transducer location must be known in order to induce shock loading during the PD simulation. Hence, the empirical formulations of open water, given in Section 5.4.1, can be utilized.

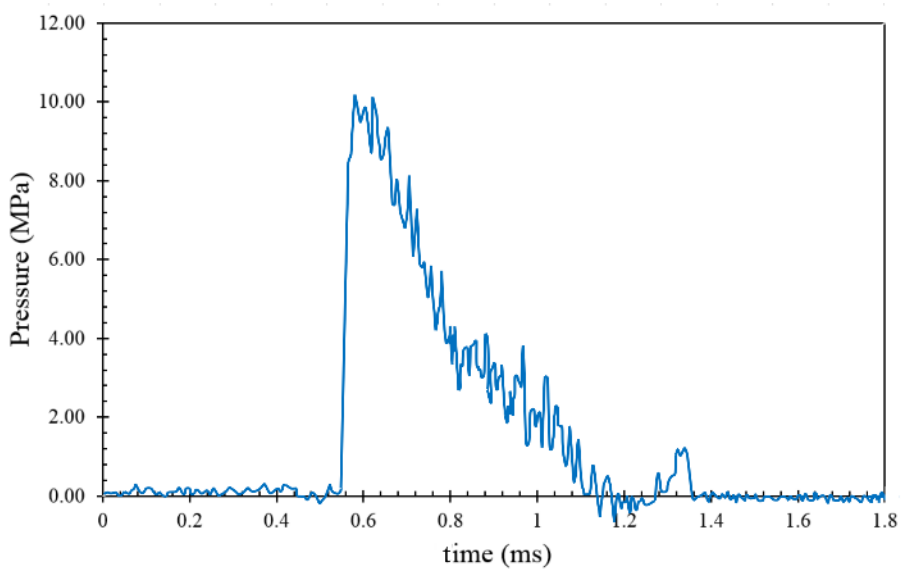

Figure 5.30 Pressure profile at the transducer in CST (LeBlanc, 2011)

In the light of Equation (5.25), it can be found that the maximum pressure, $P_{\max} = 10.3$ MPa, can be measured at the transducer location with 1.7283 kg TNT equivalency in open water. Thus, practical AF is found as 1309.318 from Equation (5.29). This value is also based on empirical Equation (5.25), but it is much closer to reality than theoretical AF. However, theoretical AF may also be found from Equation (5.28) as 7730.3. Theoretical AF is 5.9 times the practical one and this is in the order of dissipated energy from the walls of the tube by elastic deformation. Therefore, charge weight must be 5.9 times more than the weight found from theoretical AF.

On the other hand, it can be clearly seen from Figures 5.9 and 5.30 that the pressure profile obtained from open water is much smoother than the experimental CST profile. Poche and Zalesak (1992) made some experimental comparisons between two profiles (cf. Figs. 8 and 9 in ref. (Poche and Zalesak, 1992)) and similar behaviour is observed. In their study, it is mentioned that the reason of distorted shock wave profile obtained from CST is the sound propagated through steel walls of the tube which also tends to re-radiate into water. However, high frequency energy, which appears to distort the pressure profile, does not contribute much to the total energy (Poche and Zalesak, 1992) of the profile. Besides, based on comparisons, sharp peak in open water profile seems to be rounded off in CST profile (Poche and Zalesak, 1992). This rounded peak is also observed in the CST experiment done by LeBlanc (2011) as shown in Figure

5.30. Moreover, on the basis of CST experiments carried out by Poche and Zalesak (1992), it is observed that the shock wave nearer to explosive source shows more rounded peak than the far away wave and from here it may be deduced that while the shock wave becomes more planar, it does not interact much with the walls of the tube as in the spherical wave nearer the source.

Considering the test that is carried out to find damage characteristics of a 13-ply composite plate done by LeBlanc (2011), 11.7 MPa peak pressure (P_{max}) value is measured at the transducer location. By using Equation (5.25), it is found that the same maximum pressure, P_{max}, can be measured at the same location with 2.39 kg TNT equivalency in open water and considering the practical AF value for the CST experiment, which was found as 1309.318, the same conditions can be replicated in the tube with 1.825 gr TNT Equivalency, which may be used in experiments carried out by LeBlanc (2011). Besides, it is found that shock wave has a peak pressure value of, P_{max} = 10.3765 MPa, at the test plate location, $L = 5.25\ \text{m}$. After this value is reached in a very small time range at the test plate location, it decays exponentially to zero value. The exponential decay function is provided in Equation (5.23) for open water and it takes the form of

$$P = 10.3765e^{-t/0.154} \tag{5.30}$$

which is at the test plate location, $L = 5.25\ \text{m}$. As Equation (5.28) is based on open water conditions and considering the above mentioned discrepancies between the pressure profiles, the peak pressure value is rounded off as in the Figure 5.30 and exponential decay function is slightly modified as

$$P = 10.3765e^{-t/0.2} \tag{5.31}$$

As a summary, whenever the shock wave reaches the test plate, pressure rises up linearly to a peak value (P_{max}) between the time range of, $0\ \text{ms} \le t \le 0.04\ \text{ms}$, then it constantly keeps its peak value until t = 0.08 ms before diminishing in the form of exponential decay function, Equation (5.31). This pressure profile, which 13-ply composite test plate resists, is shown in Figure 5.31.

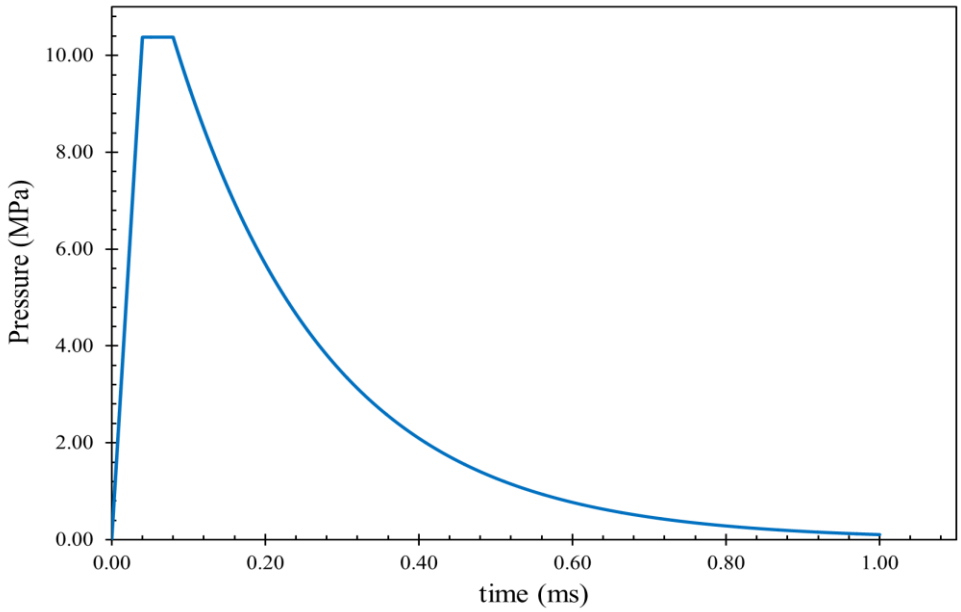

Figure 5.31 Pressure profile at the test plate in CST

Distribution of shock loading over the plate can either be uniform or non-uniform. In order to examine the shape of shock wave front, Poche and Zalesak (1992) carried out some measurements with two gages inside the CST test setup. Gages are placed to the same cross section at central axis of the tube and near the tube wall. The peak pressure values measured from two gages show slight difference in time. This may be rephrased as non-planar shock wave front inside the tube and it can be supported by several experimental studies done by Comtois et al. (1999); Langdon et al. (2005); Nurick and Shave (1996); Nurick et al. (1996); Teeling-Smith and Nurick (1991); Wierzbicki and Nurick (1996); Yuen and Nurick (2005) where response of structures under shock loading is investigated. Unlike the experiments carried out by Nurick and Shave (1996), Yuen and Nurick (2005) and Langdon et al. (2005), all other studies are related to circular plate structures as in here. Furthermore, the common failure mode is tensile tearing from the supports, shown in Figure 5.32. Teeling-Smith and Nurick (1991) as well as Nurick and Shave (1996) showed the complete tearing failure of clamped plates under uniformly distributed impulsive loading. Comtois et al. (1999) also expressed the importance of attachments on the damage behaviour of composites and severe tearing failure is observed for clamped specimens even the loading is less than the others. The importance of boundary conditions on the tearing failure was also studied by Nurick et al. (1996) for uniformly loaded plates in air blast loading. Most

importantly, Wierzbicki and Nurick (1996) observed transition from discing failure, which is in the form of disc in thin membranes preceded by tensile necking, to tearing failure with the increase of loading radius. They concluded that the more distributed load causes tearing failure at the clamped boundary. Lastly, from the experiments that were carried out by Yuen and Nurick (2005) as well as by Langdon et al. (2005) for stiffened plate structures under uniform and localised blast loadings, it was concluded that loading condition significantly designates the damage characteristics of structures and it must be ensured that no premature failure should occur during the design process. Moreover, tearing failure was observed from the boundaries of plates under uniform loading in these experimental studies. To sum up above findings explained in experimental studies, circular test plate structure with clamped boundary condition can indicate premature failure under uniform shock loading and the same behaviour, shown in Figure 5.33, is also observed in PD results for the test plate considered here under uniform shock loading. The conclusion drawn here that the damage evolution characteristics of a CST test plate can be captured by using non-uniform shock loading. This conclusion is also supported by LeBlanc (2011) from the numerical experiments. Since, it was observed that nearly planar shock waves are transformed into non-uniform waves immediately after the impact to a test plate.

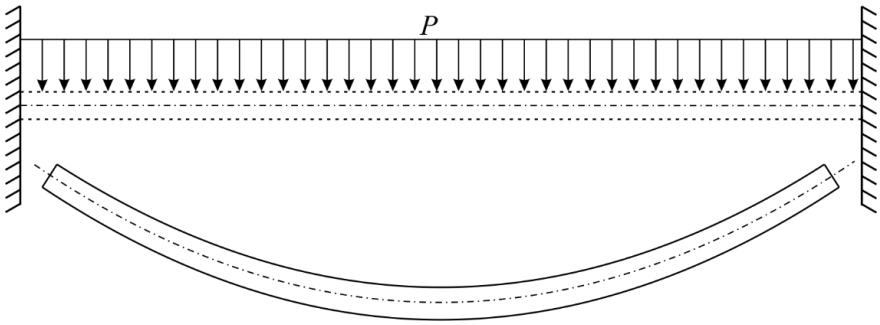

Figure 5.32 Tensile tearing failure from the supports (Teeling-Smith and Nurick, 1991)

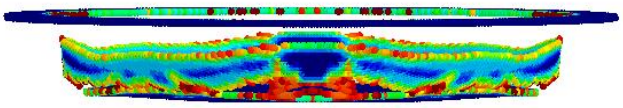

Figure 5.33 Premature failure of a test plate under uniform shock loading

Non-uniform shock pressure distribution is implemented over a test plate as explained in Section 5.4.1 and as given by Equation (5.27). However, the test plate radius, R, is slightly larger than what was used by Turkmen and Mecitoglu (1999). For this reason, the peak pressure, P_{max}, is slightly extended over the central region of the test plate and final distribution takes the form as in Figure 5.34.

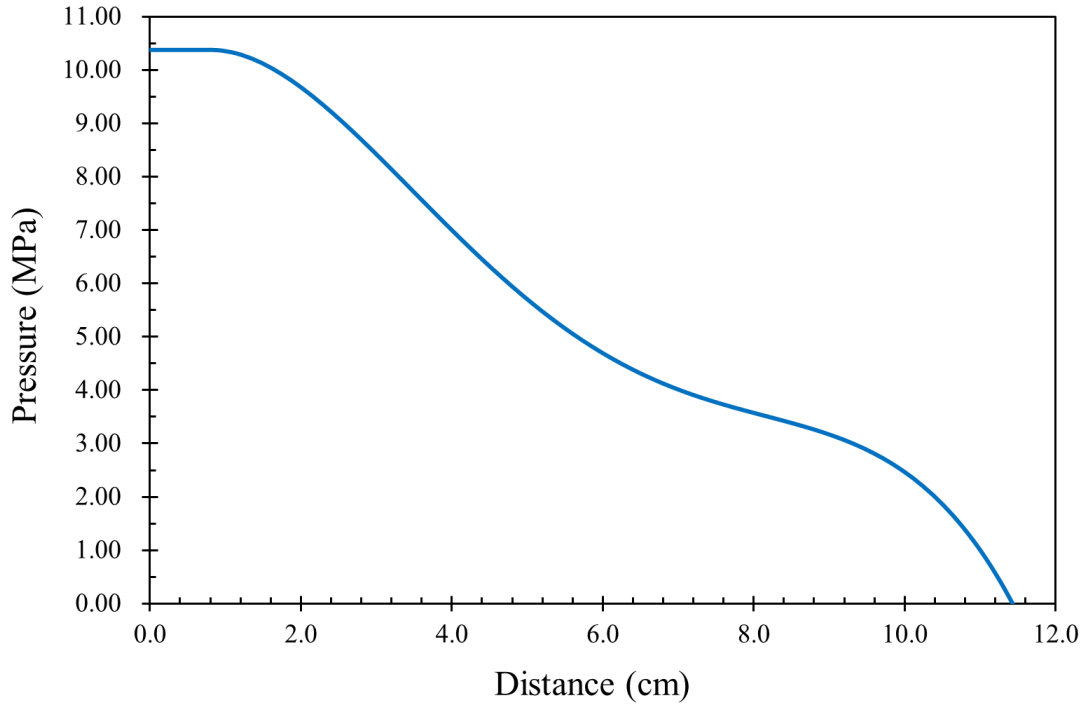

Figure 5.34 The distribution of a shock pressure over the test plate

5.5.2 Mechanical properties and Peridynamic parameters

The test plate used by LeBlanc (2011) is Cyply® 1002, which is manufactured by Cytec Engineering Materials ("Cyply 1002 Reinforced Plastic," 2002). It is a 13-ply composite plate which has a cross stacked configuration as $\left[0/90/0/90/0/90/\bar{0}\right]$. The mid 0° ply, which is denoted by over bar, is the plane of symmetry of the laminate. Each ply is composed of cured epoxy matrix and parallel E-Glass filament materials. The isotropic material properties of epoxy matrix and E-Glass are given in Table 5.4 (Kaw, 2006). Each material is homogeneously distributed over the plate and unidirectional lamina has the generalized properties shown in Table 5.5 ("Cyply 1002 Reinforced Plastic," 2002).

Table 5.4 Material properties of each element in a lamina

	Epoxy Matrix	**E-Glass**
Young's Modulus, *E*	3.792 GPa	72.40 GPa
Shear Modulus, *G*	1.422 GPa	35.42 GPa
Poisson's Ratio, ν	0.30	0.20
Mass Density, ρ	1.28	2.54

Table 5.5 Material properties of the unidirectional lamina

	Cyply® 1002
Longitudinal Young's Modulus, E_1	39.30 GPa
Transverse Young's Modulus, E_2	9.70 GPa
Shear Modulus, G_{12}	9.70 GPa
Mass Density, ρ	1850 kg/m^3

*Subscripts 1 and 2 denote the x_1 and x_2 axes, respectively.

As for the numerical solution of the problem, the laminated composite plate, shown in Figure 5.28, is discretised into many material points such that each lamina has a single layer of material points with a grid size of $\Delta x = 1.32715\times10^{-3}$ m and each material point has a horizon radius of $\delta = 3.015\Delta x$, as in Figure 5.35. Besides, fully clamped condition, which is ensured by mounting fixtures in the supported or boundary region (shown in yellow colour), is satisfied by only constraining bottom and top plies in *z* direction and leaving them free in other directions (*x* and *y*).

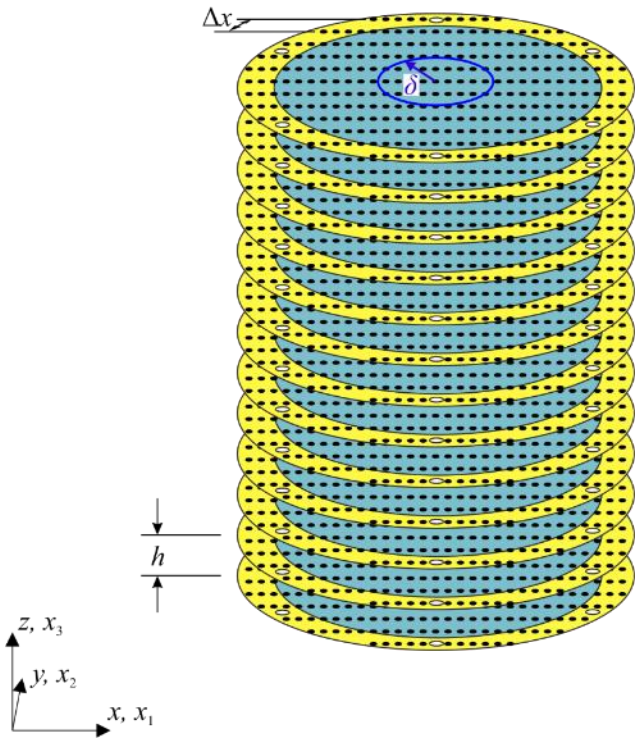

Figure 5.35 Discretization of a 13-ply composite plate

Substituting values of geometrical and material properties as well as that of peridynamic parameters into Equations (5.2) – (5.3) and (5.8) – (5.9), properties of all types of bonds, i.e. bond constants c_F, c_A, c_N and c_S, can be determined for the composite plate.

As mentioned in Section 5.2, critical stretch values of fiber direction and arbitrary direction bonds may be determined from several experiments. However, in the absence of necessary experiments, it is assumed that the critical stretch value of fiber direction bonds (s_{Ft}) is high enough to provide material integrity during the analysis and critical stretch value of arbitrary direction bonds (s_{At}) can be found from critical stretch formulation of an isotropic material (Oterkus and Madenci, 2012)

$$s_{At} = \sqrt{\frac{5G_{IC}}{9\kappa_m \delta}} \tag{5.32}$$

where G_{IC} and κ_m can be taken as mode I critical energy release rate and bulk modulus of the epoxy matrix material. Equation (5.32) may be valid because arbitrary direction bonds are distributed over two dimensional lamina homogenously. So, G_{IC} value for

the epoxy matrix material in the lamina is approximately taken as 11.85×10^{-3} MPa-m and critical stretch value of arbitrary direction bonds is found as $s_{At}=2.1\times10^{-2}$. Apart from that, arbitrary direction bonds are only allowed to fail in tension and no compressive failure is considered.

As mentioned in Section 5.3, critical stretch value of interlayer bonds (s_N) and critical shear angle value of shear bonds (φ_S) may be determined by substituting material properties of the epoxy matrix material, i.e. E_m, G_m, G_{IC} and G_{IIC}, as well as the thickness of a lamina, h, into Equations (5.15) and (5.16). Mode I critical energy release rate (G_{IC}) of the epoxy matrix material between the plies of a laminate is approximately taken as the same value given by Oterkus and Madenci (2012) as, $G_{IC}=2.37\times10^{-3}$ MPa-m and accordingly mode II critical energy release rate of the epoxy matrix material (G_{IIC}) is chosen as nearly 3 times the G_{IC}. In light of this, critical parameters between the plies of a laminate are found as $s_N=7.015\times10^{-2}$ and $\varphi_S=0.1$.

5.5.3 Underwater shock analysis results of a 13 – ply composite laminate

Underwater shock analysis of a 13-ply laminated composite plate is carried out for 1 ms and at this instant pressure profile nearly approaches to zero. However, damage results are demonstrated here until 0.452 ms because the bolt holes are fragmentized and plate is pulled apart from the mounting fixtures. The time step size for an explicit time integration is chosen according to Equation (5.22) as $\Delta t=7.69\times10^{-8}$ s with a safety factor of $sf=0.5$. Peridynamic results are compared with damaged test plate after the CST experiment. Moreover, Peridynamic damage results are demonstrated for all 13 plies of a composite plate and the plies are numbered from bottom to top ply as 1st to 13th ply, respectively. Furthermore, peridynamic damage parameters represent matrix damage in a lamina and delamination damage for mode I and mode II types of cracks between the plies of a laminate.

5.5.3.1 Displacement evolution in time

Before investigating damage characteristics of the test specimen, Peridynamic analysis is carried out without allowing damage in the structure in order to verify dynamic vibration behaviour under shock loading. By doing this, we can observe fundamental vibration behaviour of the test plate.

Only in this analysis, bolt holes are disregarded and all plies are clamped from the supported region (shown in yellow colour in Figure 5.35), where *x*, *y* and *z* directions are all fixed. Moreover, uniform pressure distribution is considered over the plate for simplicity. During the analysis, the evolution of vertical displacement values (u_z) of central material points in each ply are the same and only one ply's material point values are plotted against time in Figure 5.36.

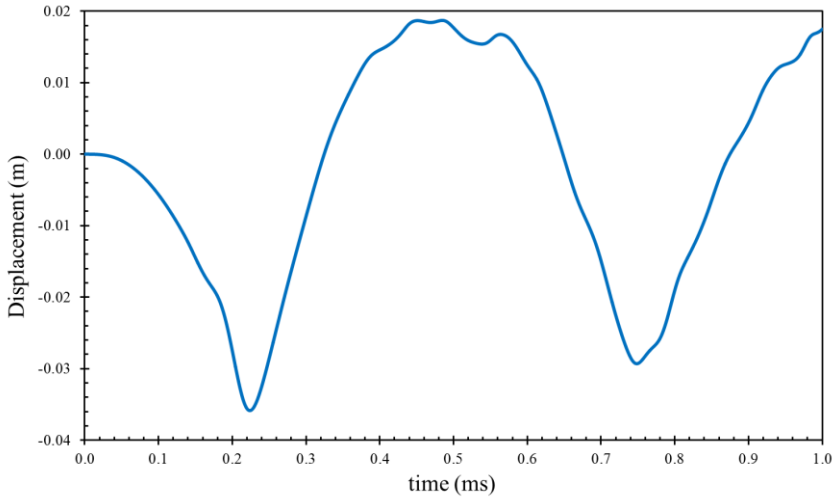

Figure 5.36 Change of vertical displacement values of central point in time

With regard to pressure profile given in Figure 5.31, whenever the peak pressure, P_{max}, is reached just before the exponential decay at 0.08 ms, test plate deforms very little from the centre at which vertical displacement is in the order of 10^{-3} m. After a while, when the pressure decreases to a half way of the exponential decay, $P = P_{max}/2$, at 0.224 ms, central deformation of the plate takes its maximum value, $u_z = -3.58\times10^{-2}$ m and the contour plot of one ply is shown in Figure 5.37. Later in time, plate continues its vibration behaviour in a very similar manner, even if the pressure diminishes. Another important observation is that the test plate structurally

responds shock loading long after maximum impact, so that there is a time lag between loading and deformation as also being supported by LeBlanc (2011).

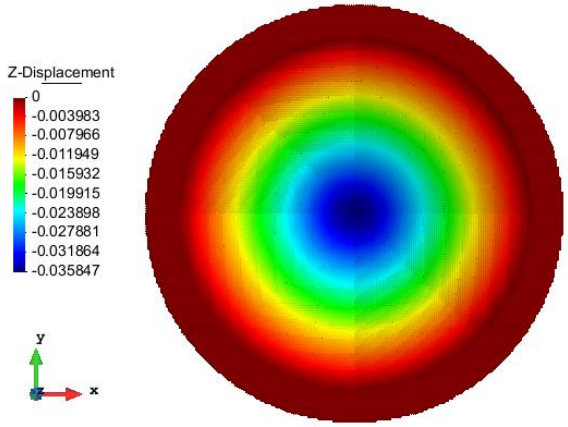

Figure 5.37 Vertical displacements of the middle ply at 0.224 ms

5.5.3.2 Matrix damage

Matrix damage (Φ_A) of a 13-ply composite test plate is investigated under non-uniform pressure distribution. Since the structural response to the shock loading is very late, no damage is observed until 0.08 ms. Matrix damage commences just before the shock loading decrease and it takes very critical values around the bolt holes in the top plies. Moreover, matrix damage is observed at the central region of four quadrants in the bottom plies. As a result of this, damage behaviours of top and bottom plies are very distinctive because while top plies are compressed under shock loading, bottom plies resist tensile stresses. These distinctive behaviours can also be observed for top and bottom plies of a 4-ply composite plate studied in Section 5.4.3.2. Matrix damage of all plies, when the loading is at the half way of the exponential decay, $P_{(t)} = P_{\max.} / 2$, at 0.224 ms, is shown in Figure 5.38. Furthermore, top views of top, middle and bottom plies are plotted in Figure 5.39 for comparison purposes. In light of Section 5.4.3.3, damage in the bottom plies can be attributed to matrix cracking while it can be both matrix cracking and fiber/matrix debonding near the bolt holes in the top plies.

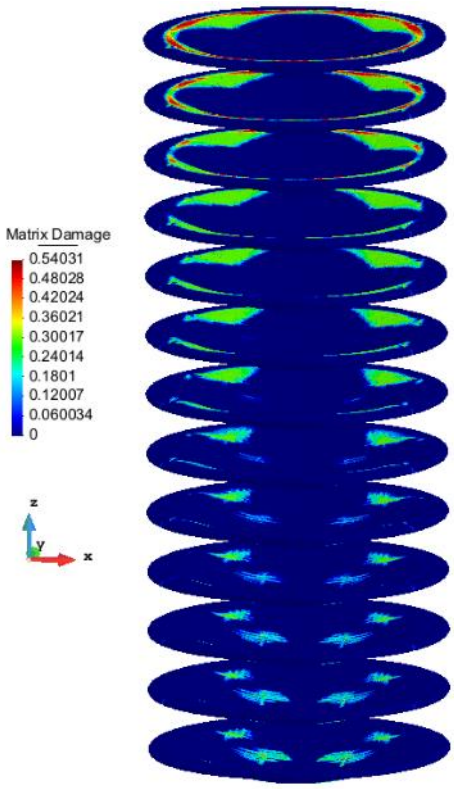

Figure 5.38 Matrix damage results of all plies at 0.224 ms

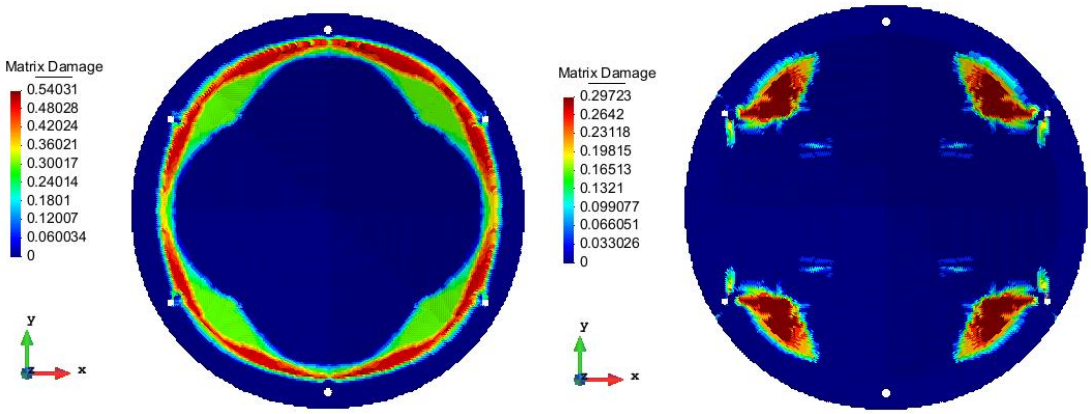

(a) (b)

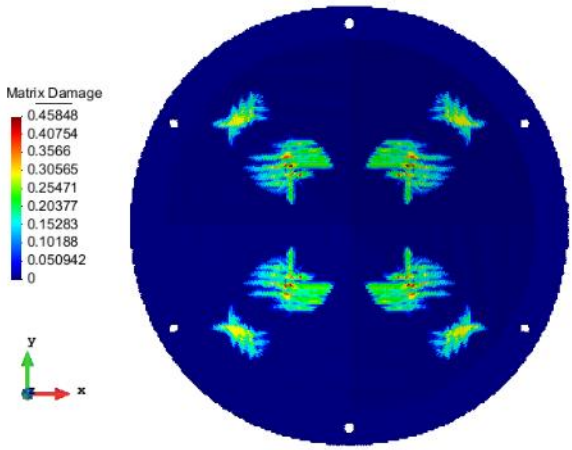

(c)

Figure 5.39 Top views of matrix damage results of (a) top, (b) middle and (c) bottom plies at 0.224 ms

After a while, at 0.325 ms, the values of matrix damage in the vicinity of bolt holes rise but keep the same extent while damage is observed over the plate with very small values except at the middle region for the top plies. As for the bottom plies, damage increases to higher values at the centre of four quadrants, in the meantime critical matrix damage emerges right at the central region. This latter damage behaviour can be attributed to a reflected compressive wave which transforms into a tension wave at the bottom surface as also explained in Section 5.4.3.2. Figure 5.40 shows matrix damage results of all plies at 0.325 ms. Moreover, top views of top, middle and bottom plies are shown in Figure 5.41 for comparison purposes.

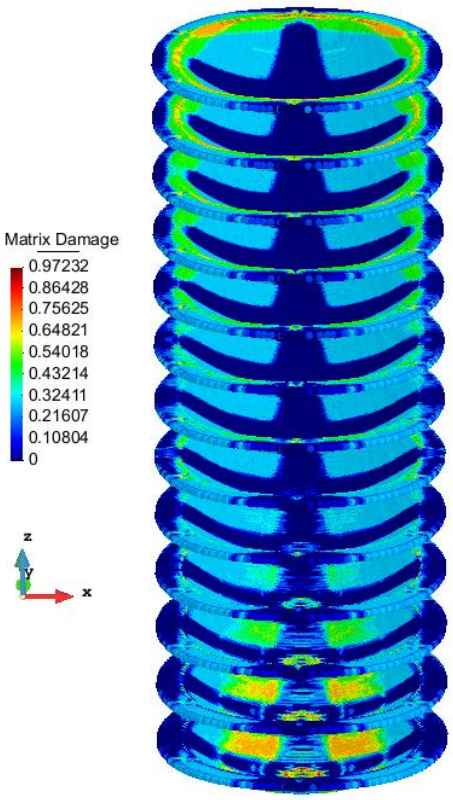

Figure 5.40 Matrix damage results of all plies at 0.325 ms

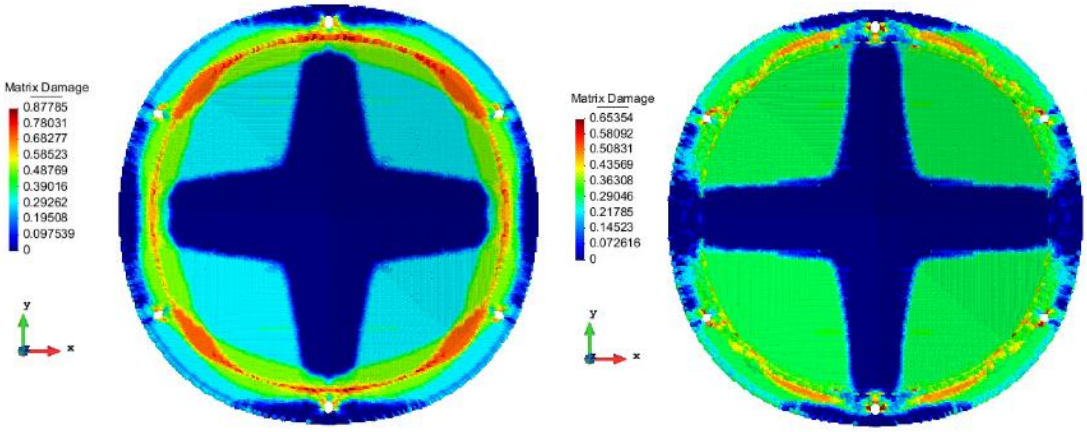

(a) (b)

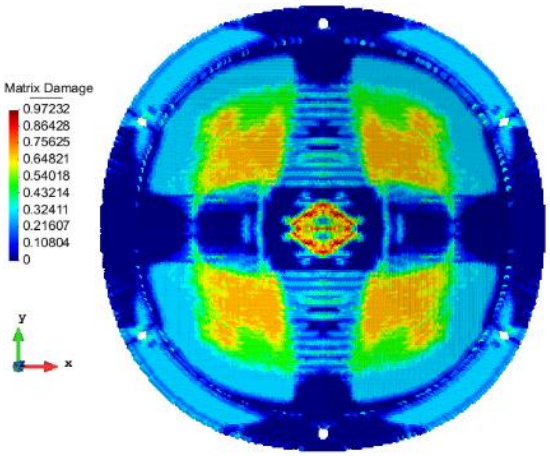

(c)

Figure 5.41 Top views of matrix damage results of (a) top, (b) middle and (c) bottom plies at 0.325 ms

Furthermore, Batra and Hassan (2007) observed high shear stress regions, as shown in Figure 5.42, in their study of underwater shock problem of a 4-ply composite plate explained in Section 5.4. From this point of view, matrix damage, which is observed right at the centre of four quadrants in the bottom plies, as shown in Figure 5.41c, may be the result of high shear stresses occurred in these regions.

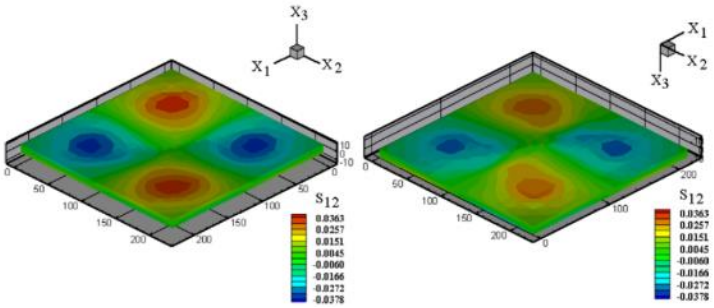

Figure 5.42 In-plane shear stresses of top and bottom surfaces under shock loading (Batra and Hassan, 2007)

As the time progresses, matrix damage takes very considerable values in all plies. However, damage characteristics between top and bottom plies are still distinguishable. Matrix damage in the bottom plies, which is observed at the central region and at the centre of four quadrants, diffuses sequentially into upper plies. Interestingly, central damage is faster than the latter one and it just reaches the middle ply at 0.452 ms. Moreover, damage in the vicinity of bolt holes is now spreaded to all

plies where top and bottom bolt holes are fragmentized dramatically. Thus, rupture of the plate from the top and bottom clamped regions is observed. Another point worth mentioning is that remarkable amount of damage propagates towards the centre from top and bottom bolt holes for all plies. All of the above described damage evolution characteristics are evident in the Figures 5.43 and 5.44 which are for 0.452 ms.

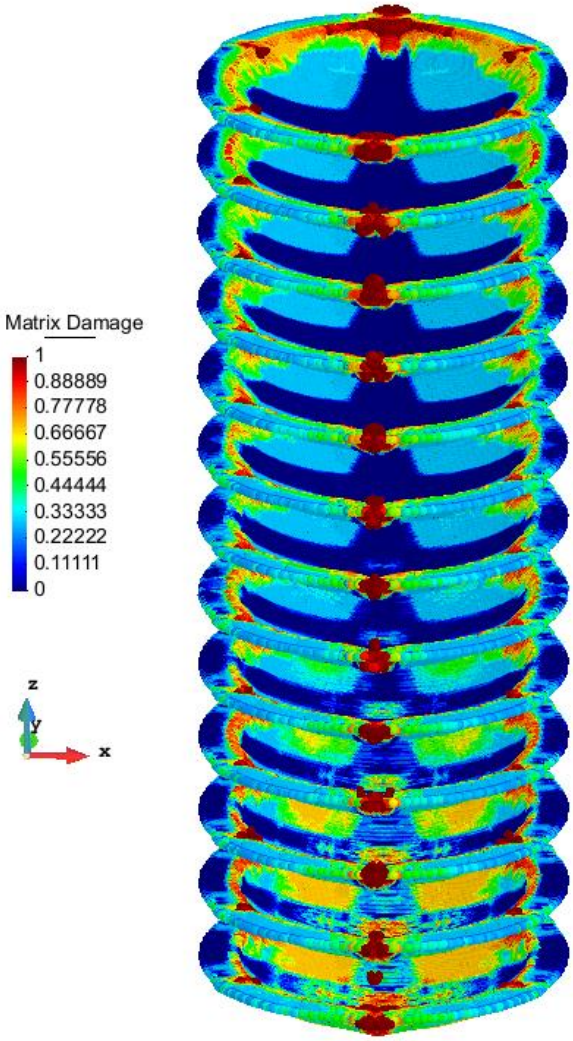

Figure 5.43 Matrix damage results of all plies at 0.452 ms

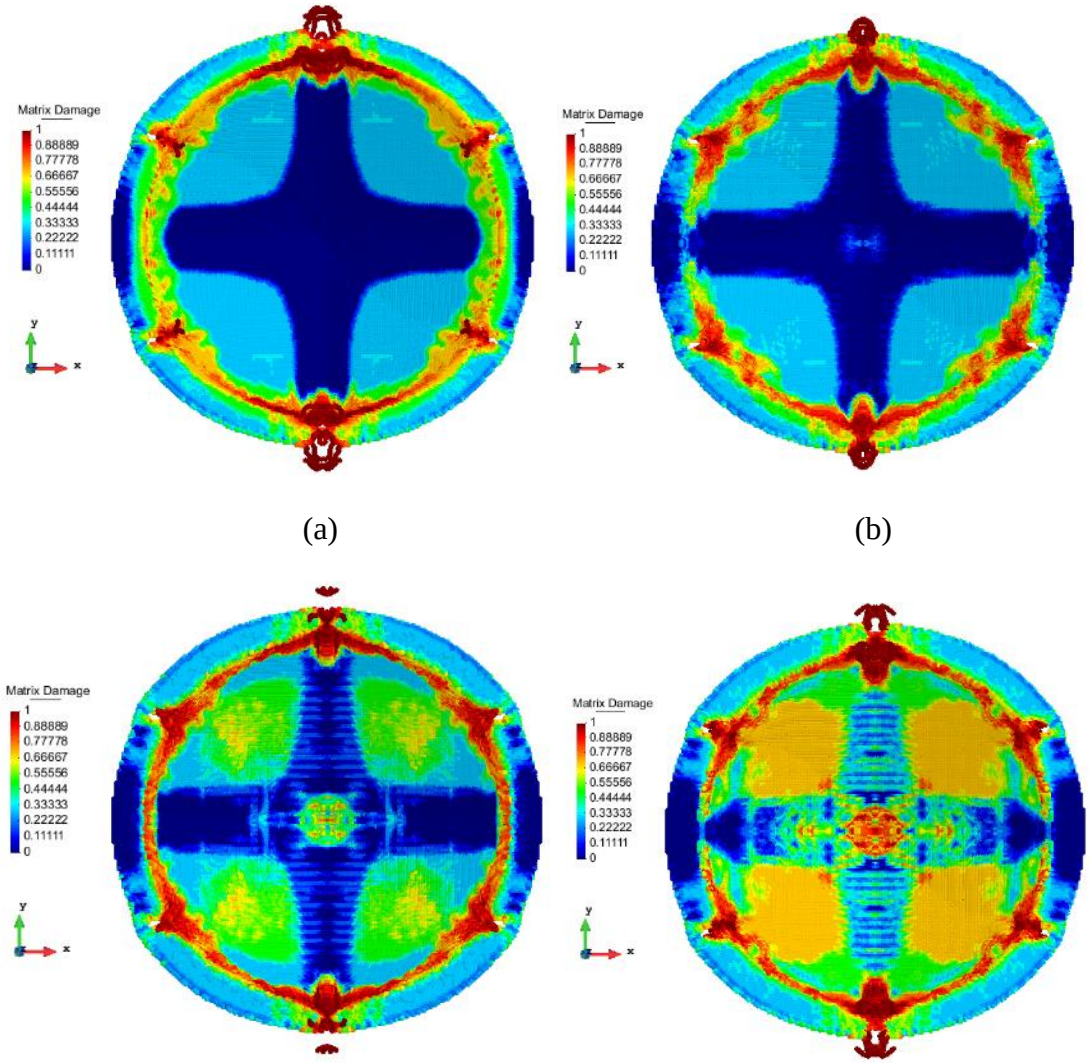

Figure 5.44 Top views of matrix damage results of (a) top, (b) middle, (c) 4th and (d) bottom plies at 0.452 ms

5.5.3.3 Delamination damage

As mentioned in Section 5.5.3, delamination damage can either be related with mode I (Φ_N) or mode II (Φ_S) cracks in PD theory. Unlike the matrix damage, mode II or shear cracks (Φ_S) commences at a later time about 0.325 ms. Mode II cracks in delamination damage are especially observed at the clamped or supported region of all plies but are more considerable in the middle plies. Particularly, middle (7th) and 6th plies have extensive damage regions around the top, bottom, left and right sides of clamped region as shown in Figure 5.46. Apart from that, there are small interactions

with bolt holes and the vicinities of top and bottom bolt holes are delaminated considerably to a small extent, as can be seen from Figures 5.45 and 5.46.

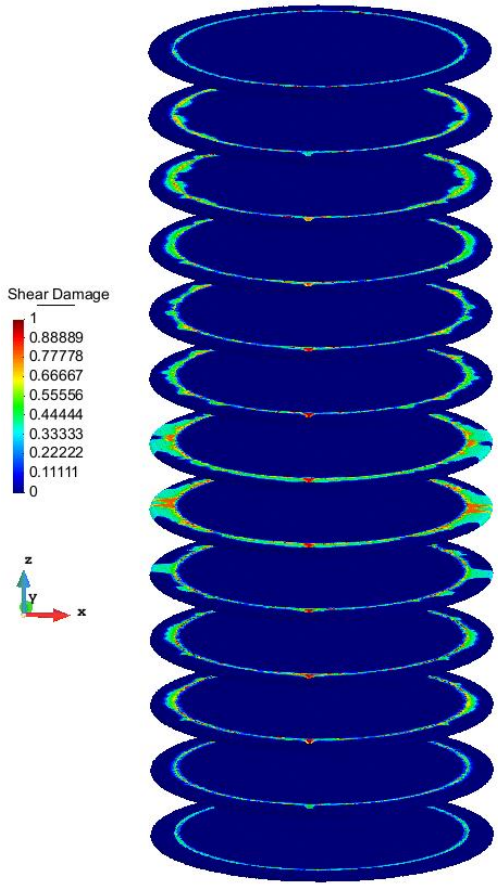

Figure 5.45 Mode II delamination damage cracks for all plies at 0.325 ms

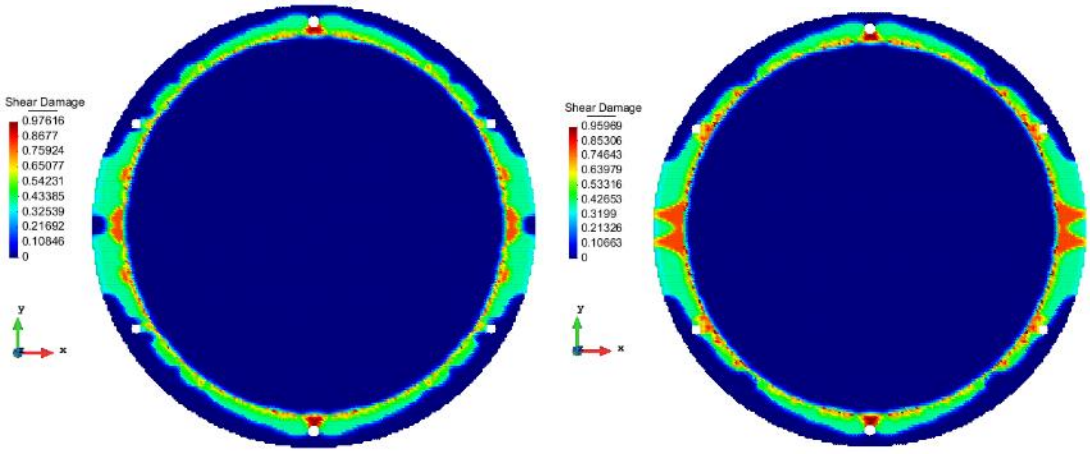

(a) (b)

Figure 5.46 Top views of mode II delamination damage cracks for (a) middle and (b) 6^{th} plies at 0.325 ms

Later in time, at 0.452 ms, mode II delamination damage cracks takes very critical values and all plies are delaminated from the circumference of supported region, as shown in Figure 5.47, as well as very significant concentrations of the damage are evident around the bolt holes as shown in Figure 5.48. Interestingly, delamination damage also propagates towards the centre of the plate from top and bottom bolt holes and a similar propagation behaviour is observed in matrix damage results at 0.452 ms.

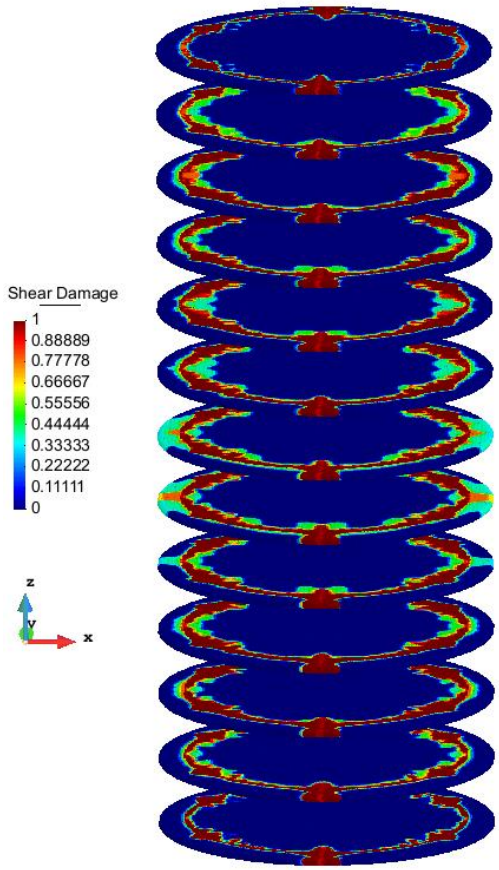

Figure 5.47 Mode II delamination damage cracks for all plies at 0.452 ms

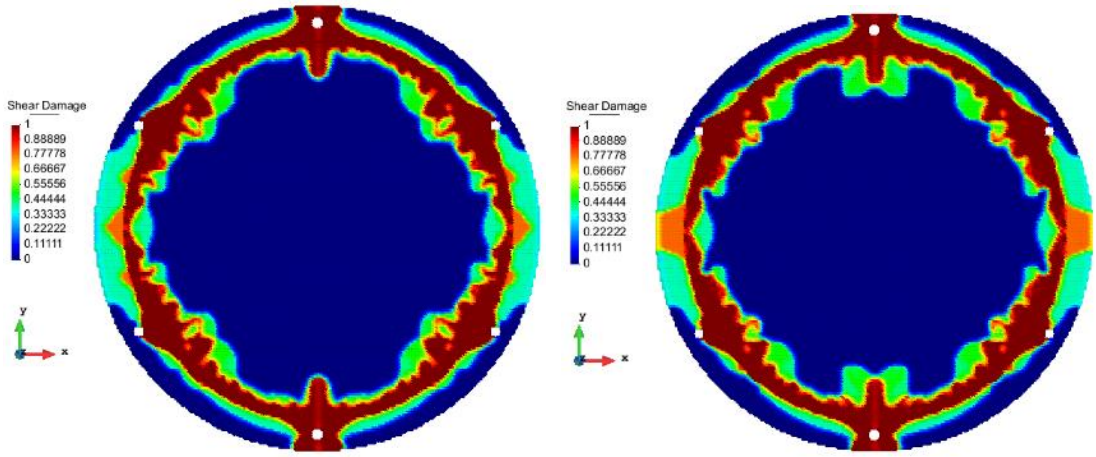

(a) (b)

Figure 5.48 Top views of mode II delamination damage cracks for (a) middle and (b) 6^{th} plies at 0.452 ms

Comtois et al. (1999) observed similar delamination damage as in Figure 5.48 from several experiments of circular specimens, which are either adhesively bonded or clamped, in air shock loading. They also emphasized more severe delamination damage for clamped specimens. Furthermore, damage propagates towards the inner region from the clamped areas and it spreads all over the specimen associated with the increase of charge weight. Please refer to ref. (Comtois et al., 1999) and cf. Figs. 6-9.

Mode-I cracks in delamination damage (Φ_N) commence at the same time, t = 0.325 ms, with mode II cracks. However, it is in very small amounts and concentrated around the circumference of unsupported region in top three plies, as shown in Figure 5.49.

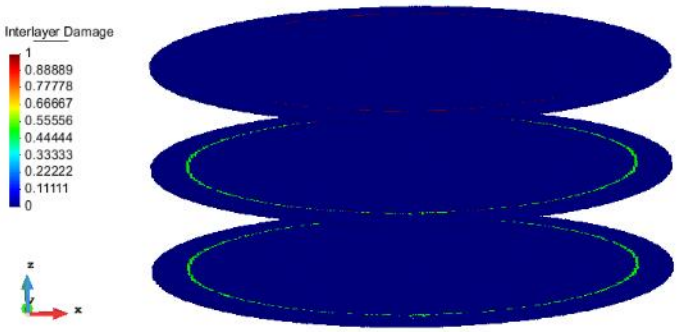

Figure 5.49 Mode I delamination damage cracks for top three plies at 0.325 ms

As the time progresses, mode I delamination damage cracks concentrate around the bolt holes and they are very significant at the top and bottom holes from which damage

spreads along the circumference of unsupported region especially for the top plies as can be seen from Figures 5.50 and 5.51.

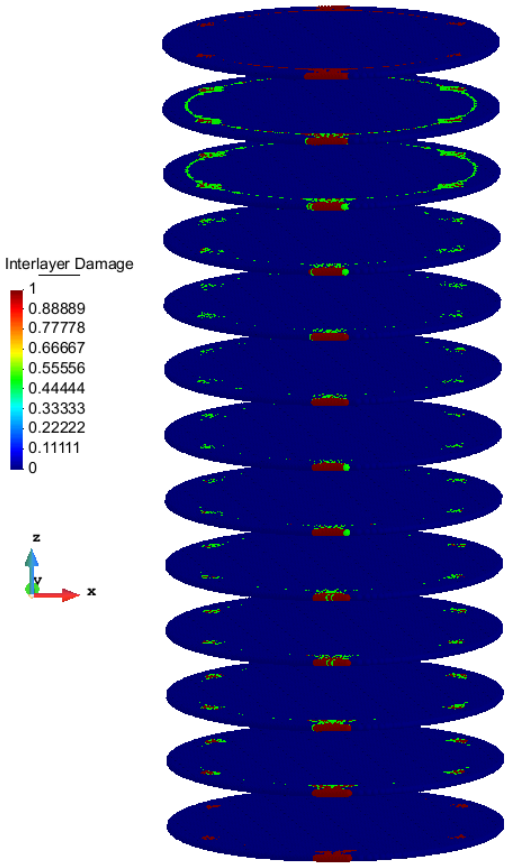

Figure 5.50 Mode I delamination damage cracks for all plies at 0.452 ms

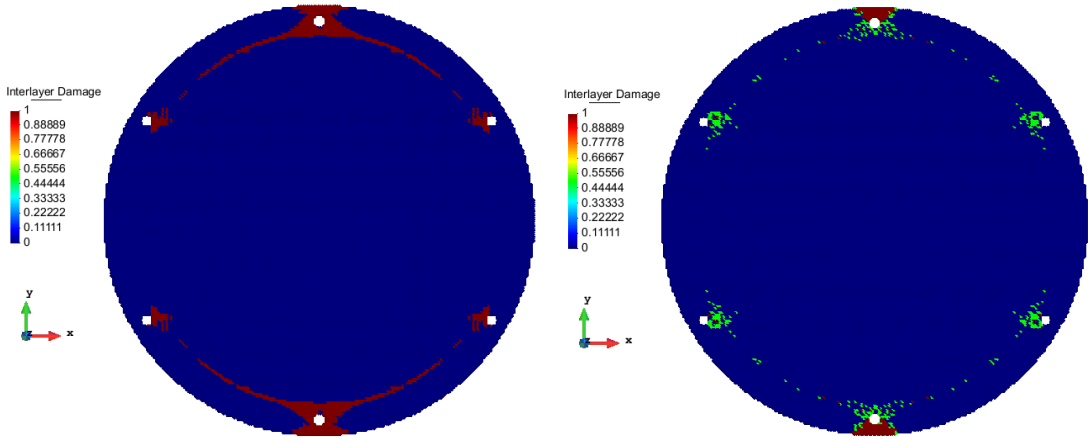

(a) (b)

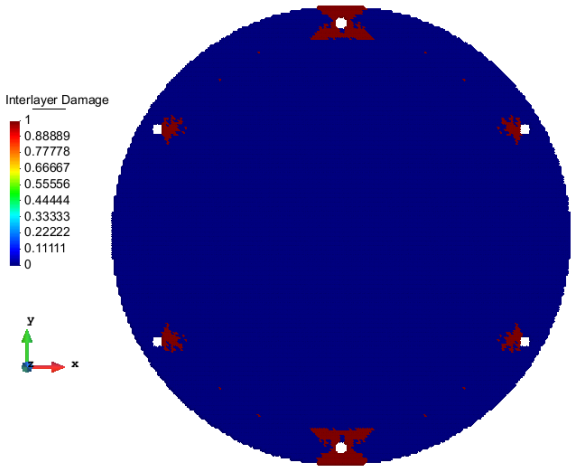

(c)

Figure 5.51 Top views of mode I delamination damage cracks for (a) top, (b) middle and (c) bottom plies at 0.452 ms

5.5.3.4 Evaluation of results with respect to damaged test specimen

During Peridynamic simulation, test plate is torn off from the mounting fixtures at 0.452 ms and it reaches the complete damage state. Thus, the results are comparable with the image of damaged test plate provided by LeBlanc (2011), shown in Figure 5.52, after the impact of underwater shock loading in CST test setup.

All bolt holes of the test plate are damaged and the damage around the top and bottom holes are more considerable than the others as well as total rupture from the top takes place. Besides, propagation of damage from the top and bottom holes to the centre is quite significant. Similar damage behaviours can also be observed in PD theory matrix damage results (Figures 5.43 and 5.44). As we are not supplied other detailed images of the test plate, it is difficult to comment on central matrix damage results observed in bottom and middle plies. However, it is very well known damage characteristic of composite plates under shock loading, as also explained in Sections 5.4.3.2 and 5.5.3.2.

In the test plate, delaminated areas can be seen more or less from transparent regions of the image because the image was lightened from the back (LeBlanc, 2011). Considerable amount of delamination can be observed at the top and right sides of the test plate. In addition to this, the vicinity of all bolt holes are delaminated. Interestingly,

delaminated areas are quite remarkable at the top and bottom bolt holes. Moreover, there is a propagation towards the centre. The unsymmetrical damage characteristic of the test plate is also notable for the delaminated areas. However, this property is very common in real materials due to the defects which may occur during the manufacturing processes. As for the PD theory results, mode II delamination damage cracks take place at the top, bottom, left and right sides of the plate quite significantly and accumulation around the bolt holes are evident (Figures 5.47 and 5.48). Furthermore, more extensive damage is observed at the top and bottom holes and the propagation from there to the centre is evident. On the other hand, mode I delamination damage cracks, which are around the top and bottom holes as well as along the circumference of the unsupported region (Figures 5.50 and 5.51), can exactly be observed from the experimental results. After all, PD theory and experimental results are well comparable for delaminated regions.

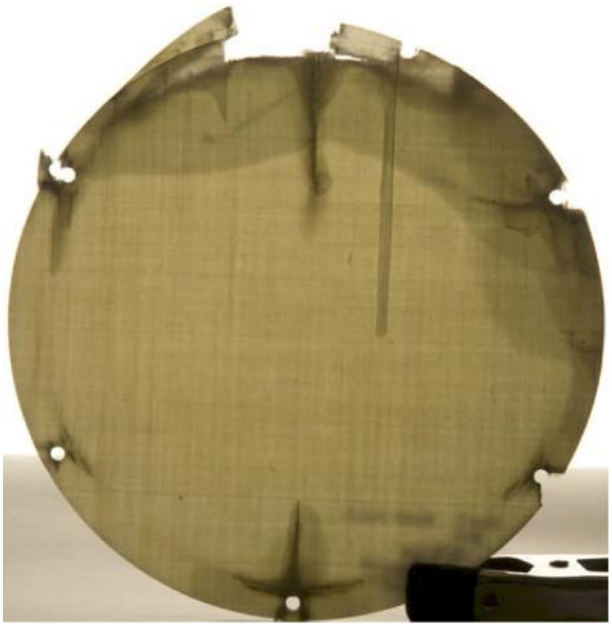

Figure 5.52 Damaged test plate after the shock loading in CST (LeBlanc, 2011)

5.6 Conclusion

The capability of PD theory for the prediction of damage patterns of complex structures under shock loading is demonstrated with several examples. In the first case, damage evolution characteristic of simple composite structure, in which all fibers are

oriented in the same direction, is analysed and the results are verified with numerical study done by Batra and Hassan (2007). It is shown that PD theory is able to provide more detailed damage for the structure and it does not use any additional kinematic equations for the damage predictions as well as damage initiates and propagates spontaneously without any triggering effect or introducing pre-cracks. This superior capability of PD theory can also be combined with simple numerical implementation property. Since meshless approach is performed in the implementation, no mesh dependent errors are observed as in the FE methods. Lastly, damage prediction capability of PD theory is proven with experimental result given by LeBlanc (2011). In this case, the more complex composite structure with cross-ply configuration is used and damage evolution characteristic of each ply is demonstrated successfully, in conjunction with the detailed descriptions of when and where damage emerges as well as how it evolves by the progression of time, without any additional effort in the analysis. Furthermore, it is concluded that ultimate damage of the test plate can correctly be captured with Peridynamics. As a result, Peridynamics can be used as a very effective computational framework in order to capture complicated damage behaviours of composite structures. This is the first time in the literature that PD theory is used for the underwater shock problems and it is realized that Peridynamics is a very suitable tool for this purpose. By exploiting exceptional characteristics of PD theory, better understanding on damage behaviour of complex composite structures is gained so that damage tolerable structures can be designed with a minimal weight for extreme and/or complicated loading conditions.

Chapter 6

Collision and Grounding Phenomena

6.1 Introduction

An accident can happen at any time, anywhere. It can happen due to human error, technical problems or harsh environmental conditions. In maritime sector, biggest accidents occur during ship-ship collision, ship-offshore structure collision and during grounding. All of these cases may result in undesirable and catastrophic consequences including human life loses, environmental problems such as oil spill, etc. As an engineer, it is important to take into account all the possible accidents during the design process in order to reduce the unexpected outcome of these accidents.

In literature, various analytical solutions to predict ship collision and grounding phenomena are presented (Minorsky, 1959; Terndrup Pedersen and Zhang, 1998). In these studies, either external dynamics or internal mechanic of ship structures are investigated. External dynamic is mainly interested in ships and their motion before, during and after collision. However, internal mechanics is interested in structural response of the struck ship. The structural response of the ship may result in complete failure. Analytical solutions offer a quick method for representing the deformation and failure characteristics of a complex ship structures. However, several assumptions have to be made for analytical solutions. Many studies have been found on

experimental and numerical analysis of ship collision (Ehler and Romanoff, 2010). These studies are mainly focuses on collision of ships and grounding phonomena. In ship collision, the impact of bulbous bow of striking ship with the side structure of another ship is the main concern and the most critical scenario is when both ships are perpendicular during collsion, i.e. right angle collision. Most of the numerical and experimental studies focus on these critical scenarios. In most of these studies, striking bow is mostly assumed as a rigid body since it is composed of many stiffners. Some of the studies focus on the calculation of the absorbed energy resulting from penetration of a struck object and some concentrate on fracture patterns formed on the structure. For the studies related with grounding phenomena, the striking object is seabed, i.e. rock, shoal or reef. Depending on the striking object, the structure may fail in different forms. For instance, grounding of a ship onto sharp rock may lead to tearing failure which may result in total destruction of bottom plate. On the other hand, grounding on blunt objects, such as shoals, may result in denting failure of bottom structure. Even the ship collision does not cause any failure, it can affect the ship's integrity which may result in hull collapse. For ship structures, it is also important to find crashworthiness of ship structures which is necessary for collision and grounding analyses. The crashworthiness of ship is the highest possible amount of energy that can be observed by the structure. The calculation is based on amount of energy that can be absorbed by the structure until fracture initiates for the side or bottom plating.

As a result, ship structure possibly shows material and geometrical nonlinearities in numerical analyses for the above mentioned situations. Apart from that, detailed crack propagation behaviours should be investigated in order to find final failure point or to decide critical energy absorption limit of a ship structure. In this regard, although there are various experimental studies done in this field, it is obvious that performing an experiment of a real size ship structure is very expensive. Instead, a smaller size of the ship structure can be tested. However, this may not really represent the behaviour of the actual ship because of its complicated structure. Hence, computational tools can be a suitable option due to their flexibility and widely applicability for complex structures. In the literature, many FE analyses have been carried out however the accuracy of these studies is questionable since the approaches used in these studies are either in their development stage or strictly criticized by many other researchers. The

issues related with the finite element method for the failure prediction arise probably due to the governing equations that is based on. Because the spatial derivatives in its governing equation are not defined if there is any discontinuity within the structure such as a crack. Furthermore, the FE simulations also suffers from mesh sensitivity (Alsos et al., 2009) since failure is represented by deleting the failed element, according to an adopted criteria in simulations. Also, the failure criteria is very sensitive to selected element size. These conditions show that FE analysis is very rough and it definitely omits local fracture behaviours of a structure. Hence, the final failure expectations as well as the energy absorption calculations may possibly fail. To conclude, it is essential to use an advanced level tool which has superb capability for fracture and failure analysis of structures, i.e. Peridynamics. It is an excellent candidate to investigate complex problems such as the collision and grounding damage analysis of ship structures. Furthermore, in a general sense, it may bring a new dimension to the analysis of marine structures.

6.1.1 Description

In this section, it is shown that PD can be used to model damage and failure during ship collision or grounding. In this sense, stiffened plates are modelled both by using PDs and a FE solver, ANSYS, as explained in Section 3.3.1.2. In PD models, it is shown that a smaller horizon, $\delta = 1.732\Delta x$, can be used to represent the bending deformation of ship structures. It is also found that sufficient number of material points has to be used through the thickness of the plate in order to get accurate deformations. By using smaller size horizon and sufficient number of material points through the thickness direction, while exploiting the ANSYS solver for PD analysis, actual size stiffened and unstiffened panels can be modelled successfully. The panel dimensions and loading conditions for collision considered in the model are chosen according to previous studies ((Alsos and Amdahl, 2009) and (Alsos et al., 2009)). In these studies, actual sized ship structures are analysed experimentally and numerically.

Finally, in order to simulate rock or bulbous bow structure impacting on ship structures, contact analysis capability of PD theory is investigated.

It is shown that impact analysis by using PDs can be done in two different ways;

1. By using PD Fortran model while adding contact analysis capability,
2. By exploiting the ANSYS contact capability for PD analysis.

In the former one, the translational and also rotatory inertia effects of a rigid body are considered in addition to proposed model of Madenci and Oterkus (2014). Apart from that, the latter model uses contact and target elements of FE software, ANSYS, in order to incorporate contact capability to a current PD model. The latter modelling procedure is validated with a previous collision study (Alsos and Amdahl, 2009) for an unstiffened ship panel structure.

6.2 Three Dimensional Plate Models

PD models of several actual sized panel structures are solved by using the ANSYS solver as explained in Section 3.3.1.2. The problems are considered for static analysis. The optimum horizon size and the number of material points through the thickness direction are chosen.

6.2.1 Plates subjected to in – plane loading

6.2.1.1 Plate subjected to displacement constraint

A relatively thick plate is subjected to a tension loading by means of applied displacement constraints to its vertical edges, as shown in Figure 6.1. The plate is made up of an isotropic material and its Young's modulus as well as the Poisson's ratio are given as $E = 200$ GPa and $\nu = 1/4$, respectively. The length, width and thickness dimensions of the plate are, $L = W = 1$ m and $H = 0.2$ m, respectively. The loading is applied as axial displacements onto the edges with a value of $u_x = 0.001$ m. In order to implement such displacement constraints, the fictitious boundary regions are created along the vertical edges with a width of $bn = \delta$, shown in Figure 6.2.

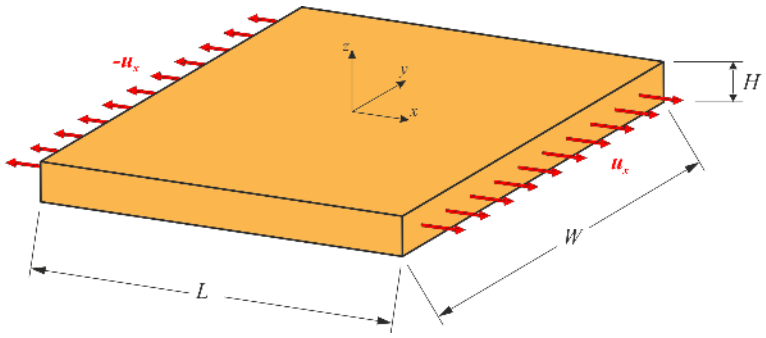

Figure 6.1 Tension loading by means of displacement constraints for a plate

The horizon sizes are chosen as $\delta = 3.015\Delta x$ and $1.733\Delta x$, respectively. Moreover, the analyses are carried out for the number of material points; 20, 10 and 5 through the thickness direction of a plate and they represent the discretization sizes of $\Delta x = H/20, H/10$ and $H/5$, respectively. In Figure 6.2, the meshless discretization of PD plate model is shown for the model with 5 material points in the thickness direction.

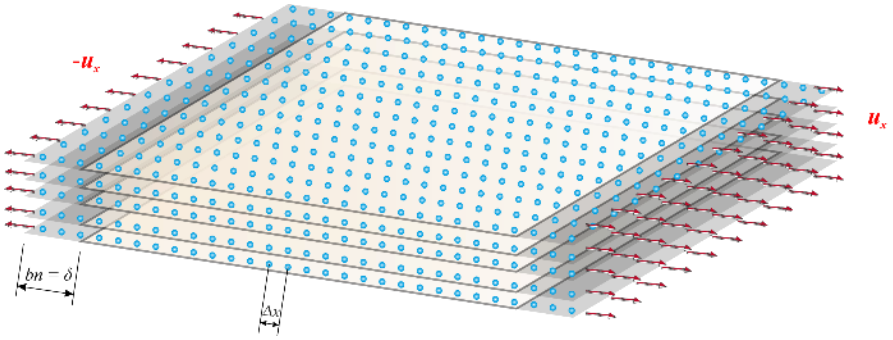

Figure 6.2 Meshless discretization of a PD model

The *x* and *y* direction displacement results of the central midplane material points for the models with different horizon sizes, δ, as well as with different discretization sizes, Δx, are shown in Figure 6.3. In these figures, horizon and discretization sizes are denoted by $\text{hor1} = 3.015\Delta x$, $\text{hor2} = 1.733\Delta x$, $\text{disc1} = H/20$, $\text{disc2} = H/10$ and $\text{disc3} = H/5$. Moreover, the classical theory results, solved by FE method, are shown in the figure for the comparison purposes.

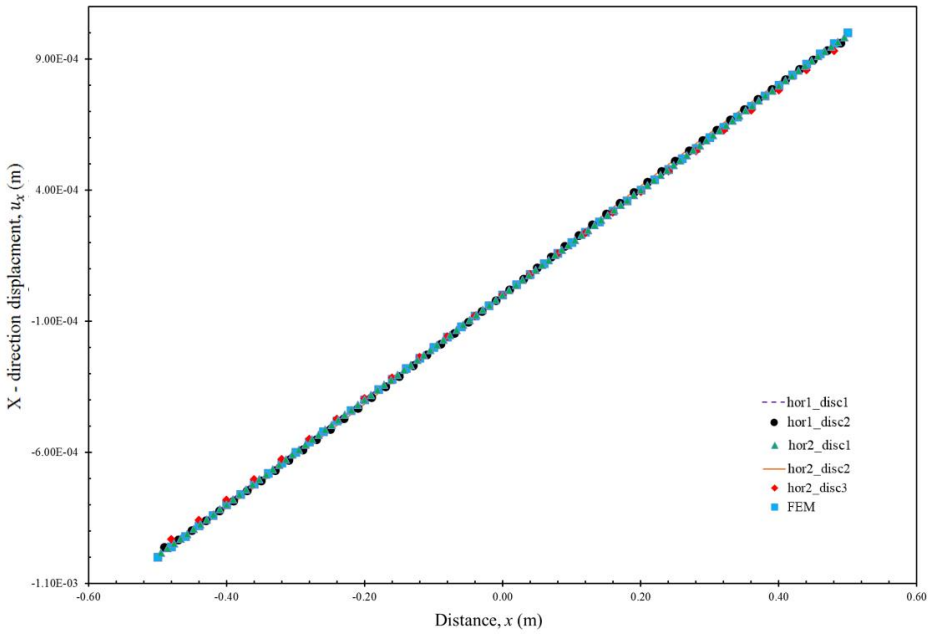

(a) x – direction displacement results along the central x axis

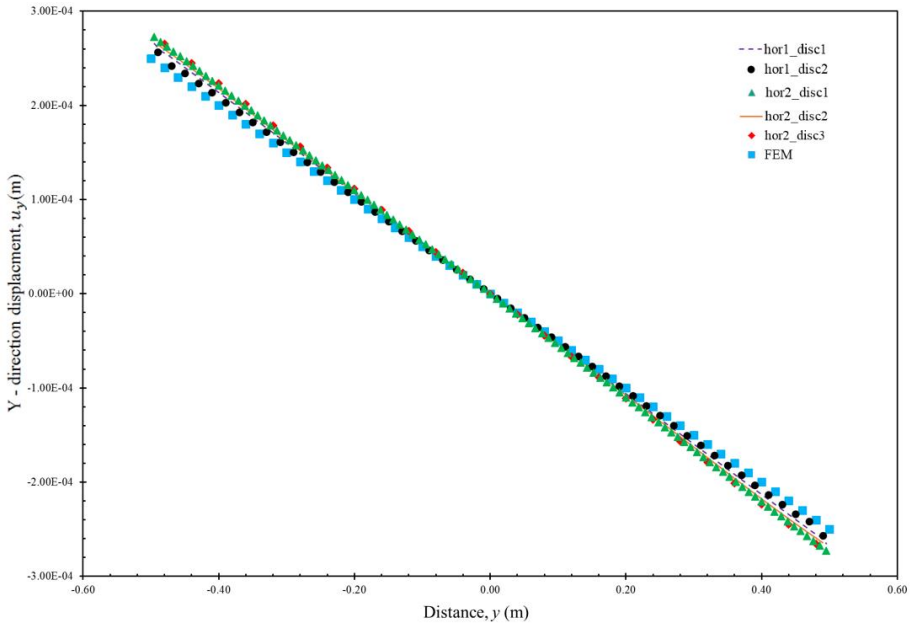

(b) y – direction displacement results along the central y axis

Figure 6.3 Comparison of the displacement results on a central midplane

The central x – displacements, shown in Figure 6.3a, are in agreement with each other as well as with the FE method results. However, some discrepencies can be seen in central y – direction displacement results, shown in Figure 6.3b. Chosing the horizon size of $\delta = 1.733\Delta x$ instead of $\delta = 3.015\Delta x$ may lead to very small changes in y

direction displacement results. However, these are in the acceptable ranges and it is also apperant that the number of material points, which are in the thickness direction, does not affect the results significantly. In light of these observations, the most efficient model, which has the values of $\text{hor2} = 1.733\Delta x$ and $\text{disc3} = H/5$, can be chosen to model plates under tension loading and is depicted with a red line in Figure 6.3b. In this case the least number of bonds or link elements are created in FE software. On the other hand, the computational burden of horizon value, $\delta = 3.015\Delta x$, is much higher than the $\delta = 1.733\Delta x$ case and it can be restrictive for the analysis of larger size models which will be analysed later in Section 6.3. Futhermore, the other discretization sizes, i.e. $\Delta x = H/20$ and $H/10$, also increases the total number of material points and the total number of link elements in the model. However, they do not improve the accuracy of results significantly compared to the $\Delta x = H/5$ case, which can also be seen from the displacement plots in Figure 6.4.

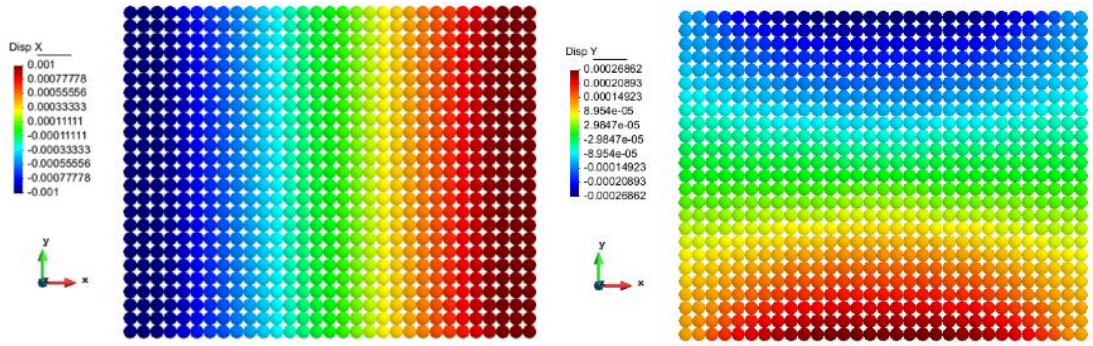

(a) *x* and *y* direction displacement plots for $\delta = 1.733\Delta x$ and $\Delta x = H/5$

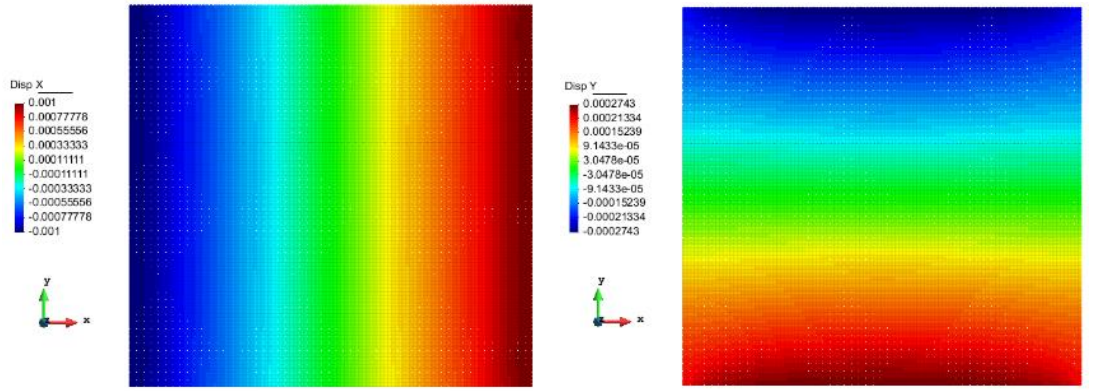

(b) *x* and *y* direction displacement plots for $\delta = 1.733\Delta x$ and $\Delta x = H/20$

Figure 6.4 Displacement results for different horizon and discretization sizes of a plate model

As a summary, for 3D plates, the horizon value of $\delta = 1.733\Delta x$ and the discretization size of $\Delta x = H/5$ can be chosen if tension loading is applied as displacement constraints to the boundaries.

6.2.1.2 Plate subjected to forces through boundaries

A relatively thick plate is subjected to a tension loading by means of applied forces to its vertical edges, as shown in Figure 6.5. The material properties and the geometrical parameters of the plate are the same with the model shown in the previous section, i.e. Section 6.2.1.1. However, the loading is applied as a line force through the vertical edges with a value of $P = 5\times10^4$ N/m. In PD theory, the application of tension loading must be done by means of body load as $b = P/(H\Delta x)$, in which A denotes the cross sectional area. The body loads, b, are implemented through actual domain of a model with a width of $bn = \Delta x$, shown in Figure 6.6.

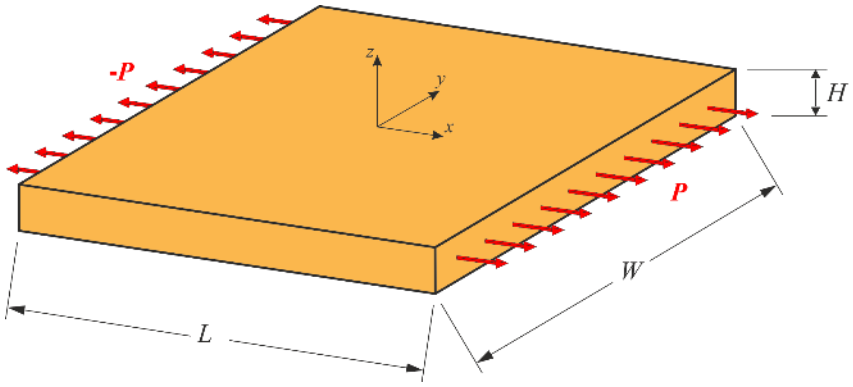

Figure 6.5 Tension loading by means of applied forces for a plate model

The meshless discretization of PD plate model can be seen in Figure 6.6. In PD model of a plate, the discretization sizes of $\Delta x = H/20, H/10$ and $H/5$ are used. Moreover, the horizon size is chosen as $\delta = 1.733\Delta x$ for all cases. Since, it is mentioned in the previous section, i.e. Section 6.2.1.1, that using the horizon value of $\delta = 3.015\Delta x$ can make the computations restrictive. Besides, the acceptable displacement values can also be achieved with a horizon size of $\delta = 1.733\Delta x$, as shown Figure 6.3.

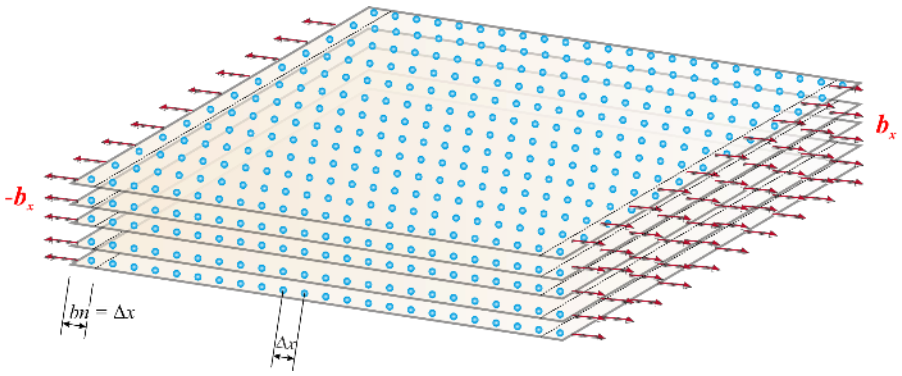

Figure 6.6 Meshless discretization of a PD model

The x and y direction displacement results of the central midplane material points for the models with different discretization sizes, Δx, are shown in Figure 6.7. In these figures, the discretization sizes are denoted by, $\text{disc1} = H/20$, $\text{disc2} = H/10$ and $\text{disc3} = H/5$. Moreover, the classical theory results, solved by FE method, are shown in the figure for comparison purposes.

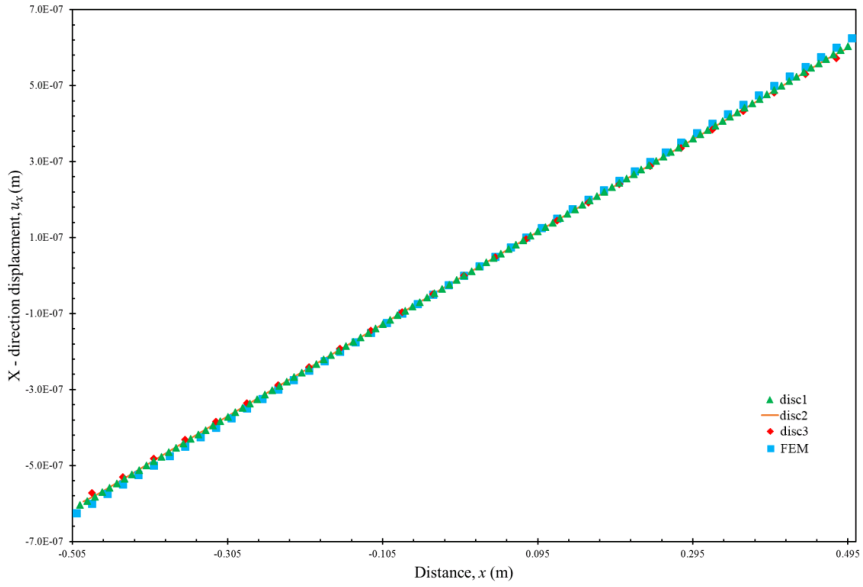

(a) x – direction displacement results along the central x axis

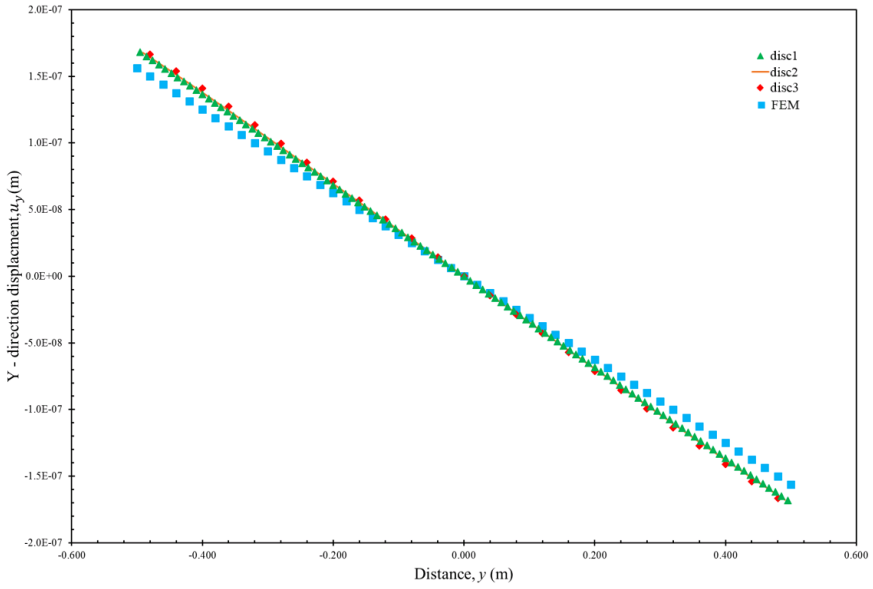

(b) y – direction displacement results along the central y axis

Figure 6.7 Comparison of the displacement results for a central midplane

The central x – displacements, shown in Figure 6.7a, are in close agreement with each other as well as with the FE method results. However, the discrepencies are observed in central y – direction displacements compared to FE method results, shown in Figure 6.7b. Again, these are in acceptable ranges and it can be concluded that the number of material points used in the thickness direction or the discretization size, Δx, does not affect the results significantly. Thus, chosing $\Delta x = H/5$ is reasonable by considering the total number of material points and the number of link elements compared to other discretization sizes. Comparison of the displacement plots for two different discretization sizes are also shown in Figure 6.8.

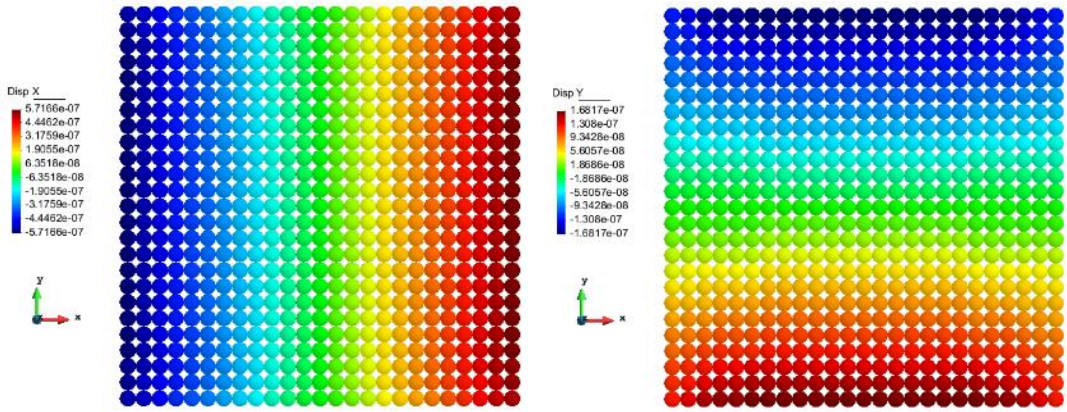

(a) x and y direction displacement plots for $\delta = 1.733\Delta x$ and $\Delta x = H/5$

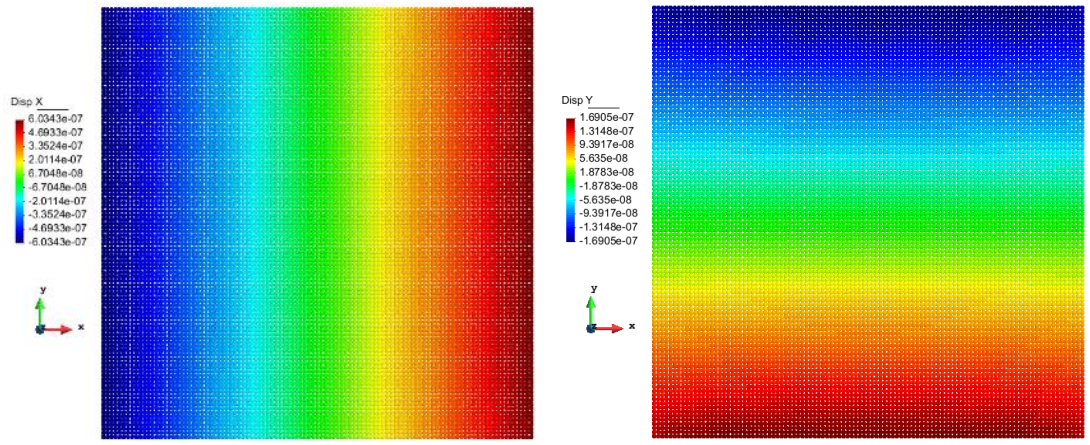

(b) *x* and *y* direction displacement plots for $\delta = 1.733\Delta x$ and $\Delta x = H/20$

Figure 6.8 Displacement results for different horizon and discretization sizes of a plate model

As a summary, for 3D plates, the horizon value of $\delta = 1.733\Delta x$ and the discretization size of $\Delta x = H/5$ can be chosen if tension force loading is applied to the boundaries.

6.2.1.3 Clamped plate

After it is demonstrated that the three dimensional PD plate models with the horizon value of $\delta = 1.733\Delta x$ and the discretization size of $\Delta x = H/5$ are capable of capturing accurate in – plane deformation behaviour, as given in Sections 6.2.1.1 and 6.2.1.2, the clamped plate under in – plane tension loading is studied. A relatively thick plate, which is clamped from its left edge, is subjected to a tension loading from its right edge, as shown in Figure 6.9. The material properties and geometrical parameters of the plate are the same with the models in the previous sections, i.e. Sections 6.2.1.1 and 6.2.1.2. The clamped boundary condition is imposed through a fictitious boundary region, which is created at the left edge, with a width of $bn_c = \delta \approx \Delta x$, as shown in Figure 6.10. On the other hand, the line force is applied through the right vertical edge with a value of $P = 5\times10^4$ N/m and it can be converted to a body load of $b = P/(H\Delta x)$. As mentioned before, it is implemented inside an actual domain of plate model with a width of $bn_l = \Delta x$, as shown in Figure 6.10.

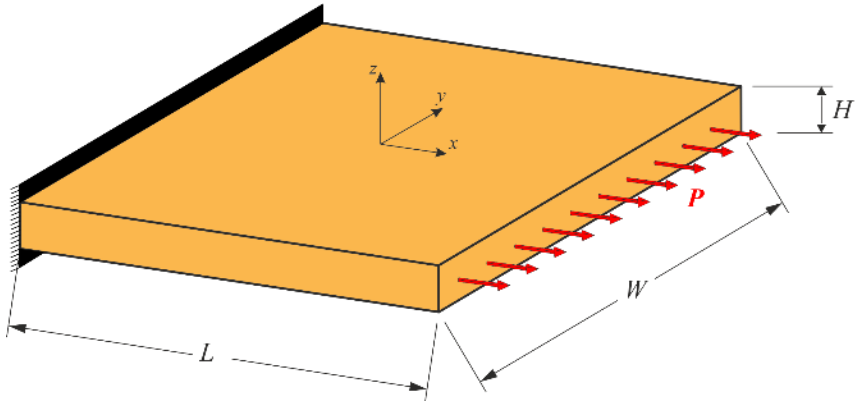

Figure 6.9 Clamped plate model under tension loading

In PD model of the plate, only the discretization size of $\Delta x = H/5$ is used and the horizon size is chosen as $\delta = 1.733\Delta x$ as mentioned earlier. Since, these are sufficient and computationally efficient values for modelling plate structures.

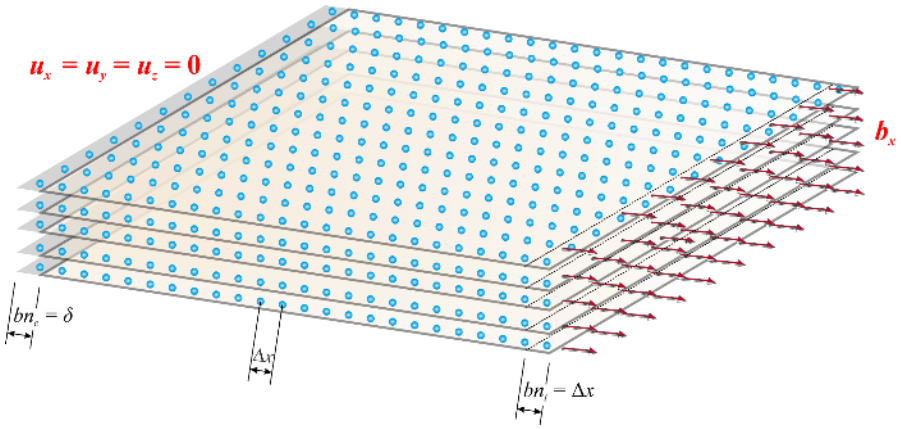

Figure 6.10 Meshless discretization of a clamped plate model

The *x* and *y* direction displacement results of the central midplane material points are shown in Figure 6.11. In these figures, the classical theory results are obtained by using FE method and compared with the PD results.

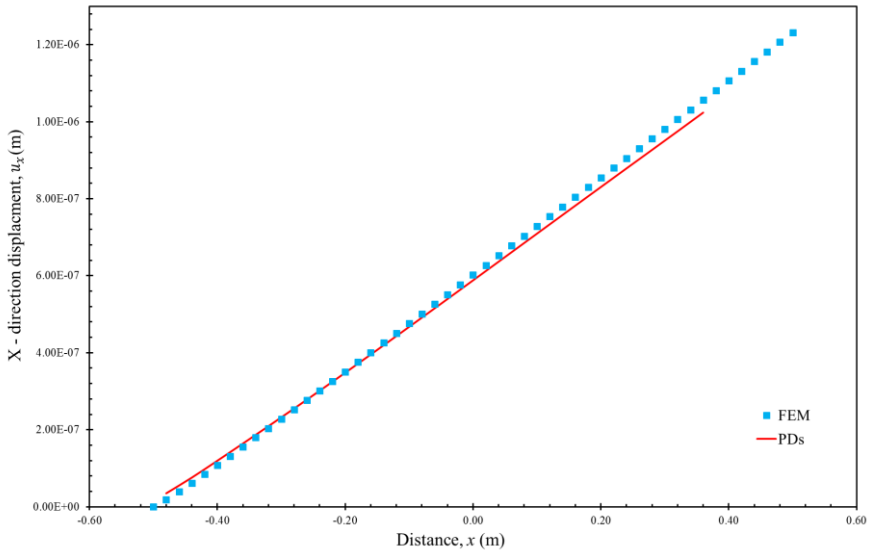

(a) x – direction displacement results along the central x axis

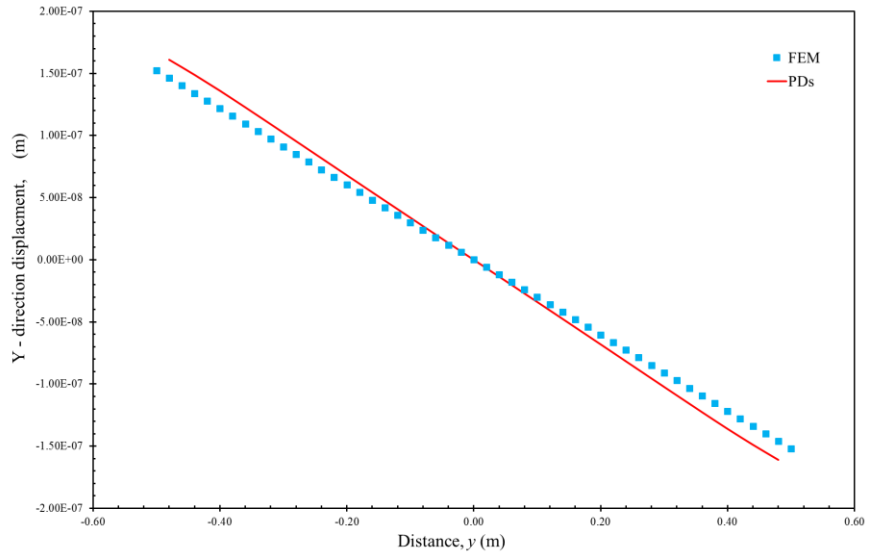

(b) y – direction displacement results along the central y axis

Figure 6.11 Comparison of the displacement results for a central midplane

The central x and y displacements are in close agreement with the FE method results. Please also keep in mind that the discretization size, i.e. element edge length, of FE model is not same with the PD model discretization size. In FE model, the solid element's average edge length is equal to $\Delta x/10$. A smaller discretization size is used in order to get closer results to analytical results. This is the reason that x – direction displacement result seems to be extended along the x axis in FE method. Furthermore, Figure 6.12 shows the plots of displacement results for PD theory and FE model. Even

though larger discretization size is used in PD model, the results are in good agreement with each other.

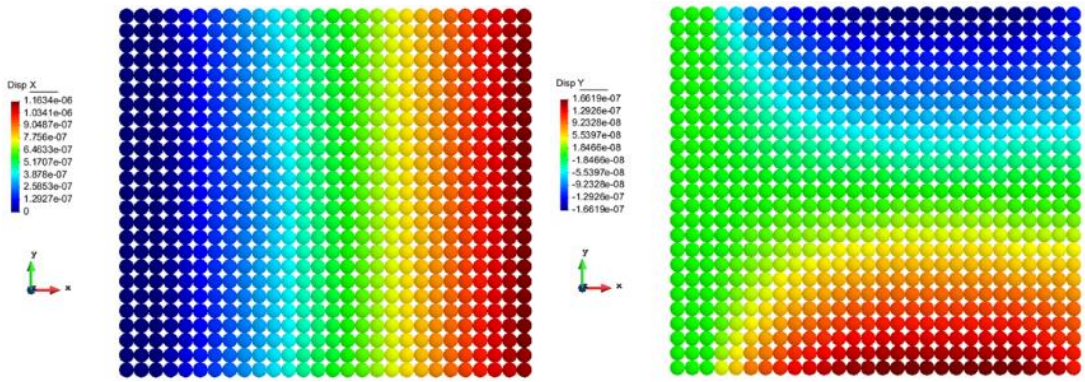

(a) *x* and *y* direction displacement plots of a PD plate model

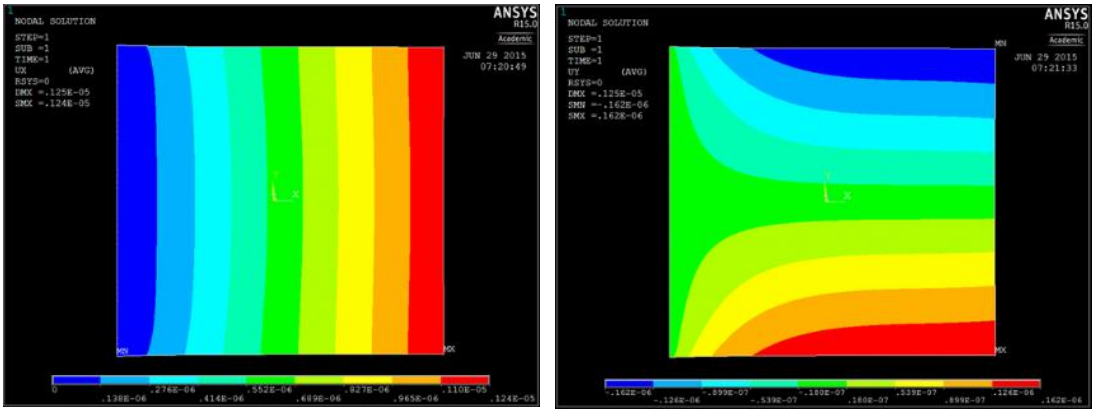

(b) *x* and *y* direction displacement plots of a FE plate model

Figure 6.12 Comparison of the displacement results for a clamped plate model

Hence, the clamped 3D plate can be modelled successfully with the horizon and the discretization sizes of $\delta = 1.733\Delta x$ and $\Delta x = H/5$, respectively.

6.2.2 Plates subjected to transverse loading

In this section, transversely loaded plates are studied and it is shown that three dimensional PD models with proposed horizon and discretization sizes are able to capture the bending deformation behaviour successfully.

6.2.2.1 Clamped thick plate

A relatively thick plate, which is clamped from its left edge, is subjected to a transverse loading as shown in Figure 6.13. In this study, it is shown that 3D PD plate model with

the horizon value of $\delta = 1.733\Delta x$ and the discretization size of $\Delta x = H/5$ can successfully capture the bending deformations of a thick plate. The material properties and geometrical parameters of the plate are the same with the models in the previous sections, i.e. Sections 6.2.1.1 – 6.2.1.2 and 6.2.1.3. The clamped boundary condition is imposed through a fictitious boundary region, created at the left edge, with a width of $bn_c = \delta \approx \Delta x$, as shown in Figure 6.14. On the other hand, a line force is applied onto the right vertical edge with a value of $P = 5\times10^4$ N/m and it can be converted to a body load of $b = P/(\Delta x)^2$. This load is only applied to a single layer of material points, which are on the top layer of the right edge, in PD model. Moreover, the boundary layer for the body load has a width of $bn_l = \Delta x$, as shown in Figure 6.14.

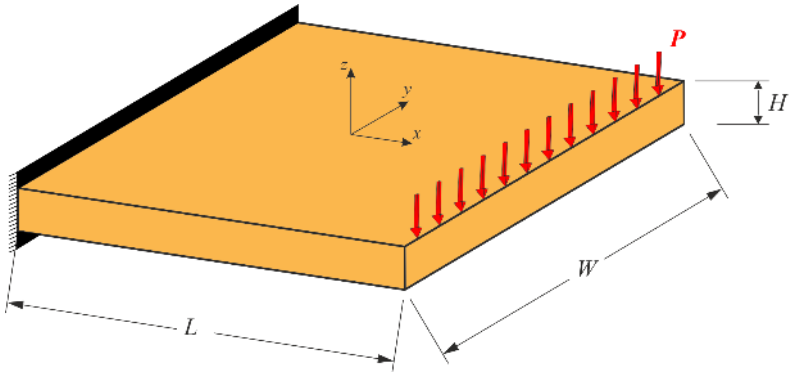

Figure 6.13 Clamped plate model under transverse loading

The meshless discretization of a PD plate model can be seen in Figure 6.14. The PD plate model has the horizon and discretization sizes of $\delta = 1.733\Delta x$ and $\Delta x = H/5$, respectively.

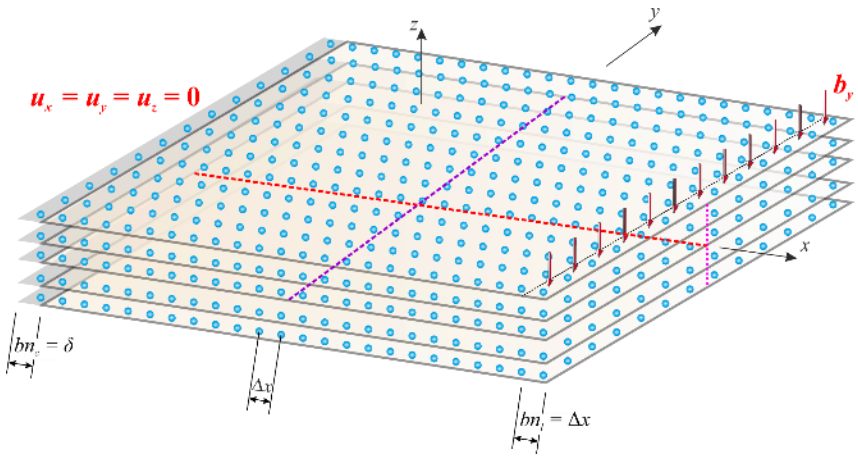

Figure 6.14 Meshless discretization of a clamped thick plate model

The central *x*, *y* and *z* direction displacement results are plotted in Figure 6.15 for the material points on the pink, purple and red coloured dotted lines, respectively, as shown in Figure 6.14. Moreover, the PD results are compared with the classical theory results, obtained by FE method.

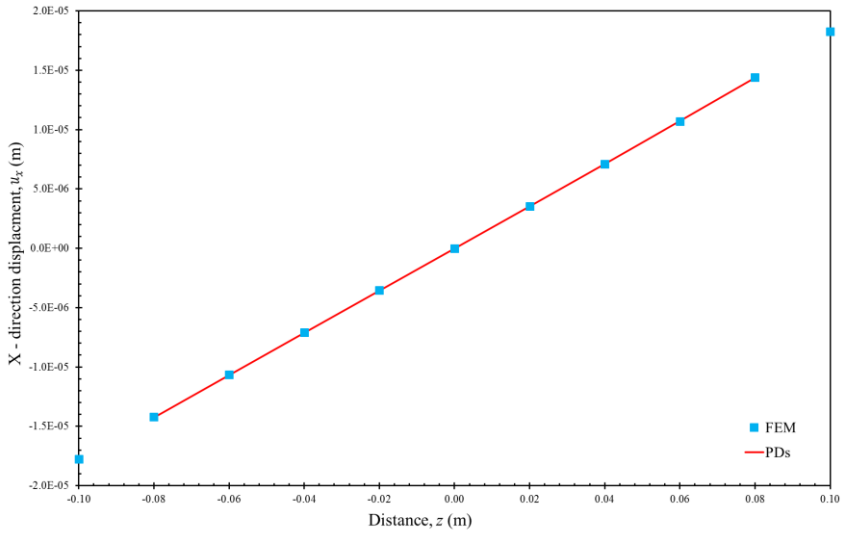

(a) *x* – direction displacement results through the thickness direction

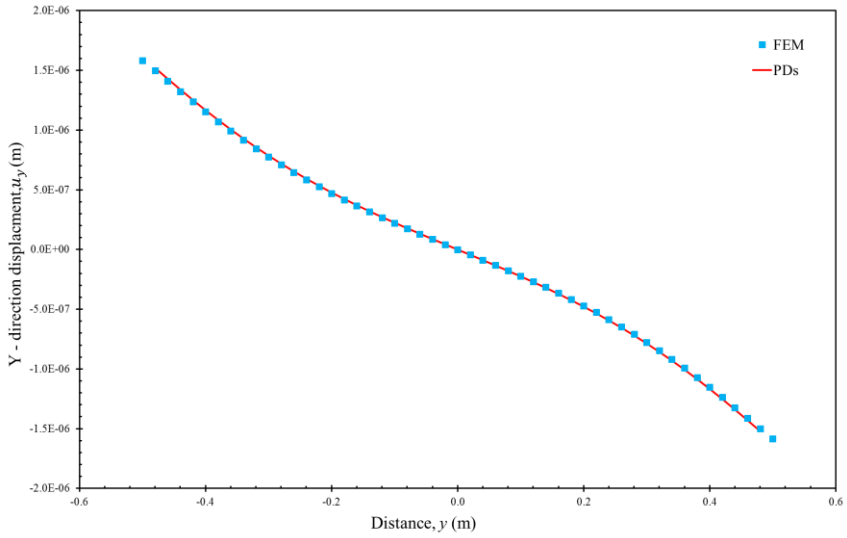

(b) y – direction displacement results along the central y axis

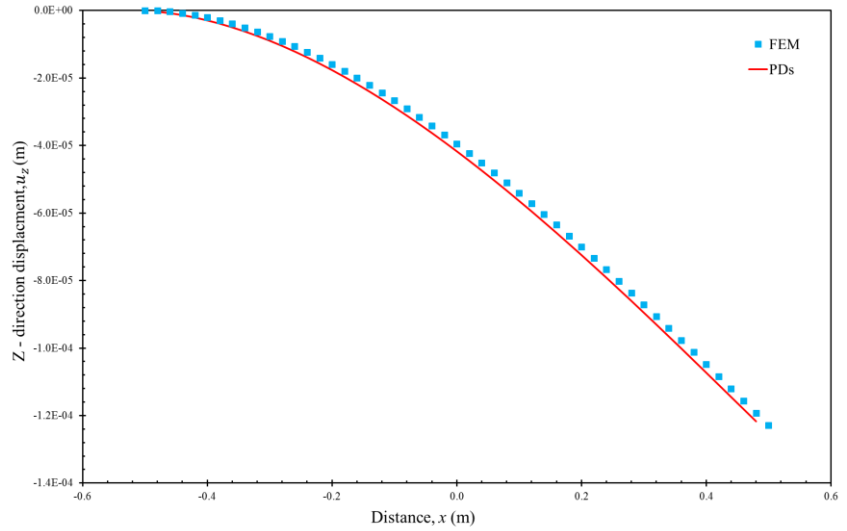

(c) z – direction displacement results along the central x axis

Figure 6.15 Comparison of the displacement results for a transversely loaded thick plate

The x direction displacements taken from the right edge are in good agreement with FE method results. Thus, it can be concluded that in – plane bending behaviour of a clamped plate can be captured very well. Again, the discrepancy seen along the z direction is due to the FE model discretization size, i.e. element edge length, difference compared to the PD model discretization size. Furthermore, the central y displacements are in close agreement with the FE model results. Hence, the contraction

of a plate along *y* axis can also be captured well. Most importantly, the transverse direction displacements, shown in Figure 6.15c, are in also close agreement with the FE model results. Thus, the out – of – plane displacement behavior can also be successfully captured with the 3D PD plate model. In Figures 6.16 and 6.17, the plots of displacement results are shown for PD theory and FE model. The displacement results are in good agreement with FE model results although a larger discretization size is used in PD model.

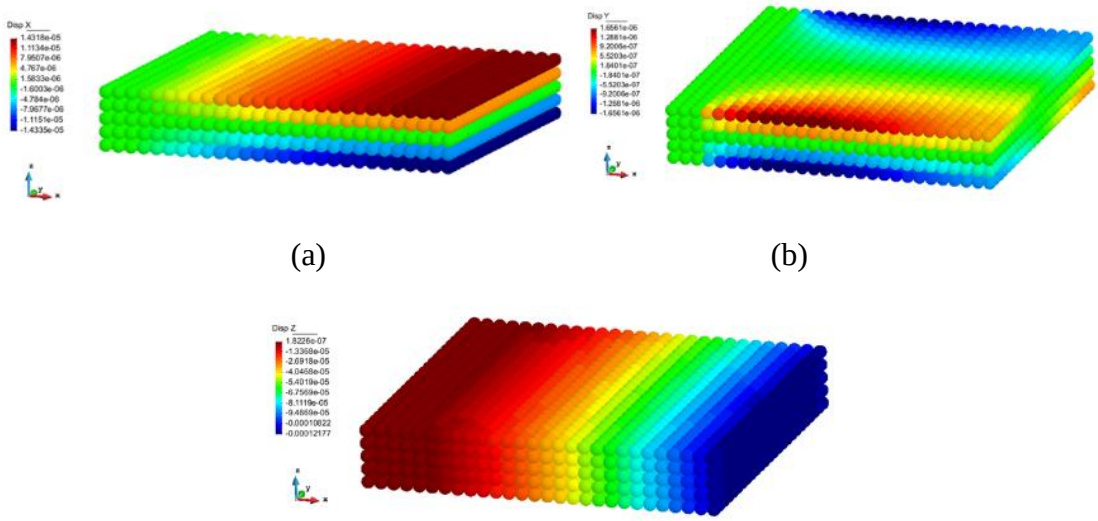

(a) (b)

(c)

Figure 6.16 (a) *x* and (b) *y* and (c) *z* direction displacement plots for a PD thick plate model

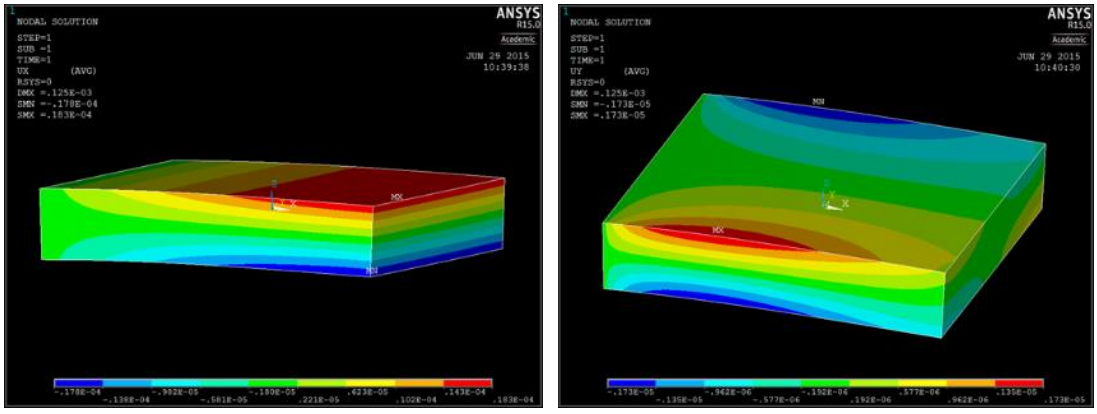

(a) (b)

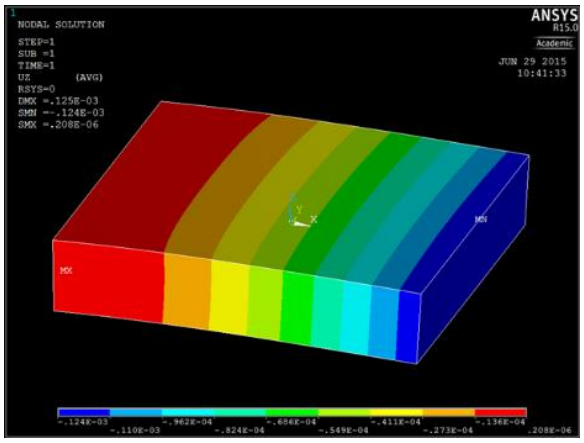

(c)

Figure 6.17 (a) *x* and (b) *y* and (c) *z* direction displacement plots for a FE thick plate model

As a summary, the in – plane and out – of plane bending behaviours as well as the contraction of a plate are successfully captured for 3D PD model of thick clamped plate modelled with horizon and discretization sizes of $\delta = 1.733\Delta x$ and $\Delta x = H/5$, respectively.

6.2.2.2 Clamped thin plate

In this section, the in – plane and out – of plane bending behaviours of clamped thin plate are investigated. A relatively thin plate, which is clamped from its left end, is subjected to a transverse loading as shown in Figure 6.13. The length, width and thickness dimensions of a plate are, $L = W = 4$ m and $H = 0.2$ m, respectively. Moreover, the material properties are the same with the model in the previous section, i.e. Section 6.2.2.1. The clamped boundary condition is imposed through a fictitious boundary region with a width of $bn_c = \delta \approx \Delta x$, as shown in Figure 6.14. On the other hand, the line force is applied in the same manner as in the previous thick plate model, i.e. Section 6.2.2.1. The magnitude of the line force is $P = 5\times10^4$ N/m and it can be converted to a body load of $b = P/(\Delta x)^2$. Since, the boundary layer for the body load has a width of $bn_l = \Delta x$.

The PD thin plate model has the horizon and discretization sizes of $\delta = 1.733\Delta x$ and $\Delta x = H/5$, respectively, as in the thick plate model.

The central *x*, *y* and *z* direction displacement results are plotted in Figure 6.18 for the material points on the pink, purple and red coloured dotted lines, respectively, as shown in Figure 6.14. Moreover, PD results are compared with the classical theory results obtained by using FE method.

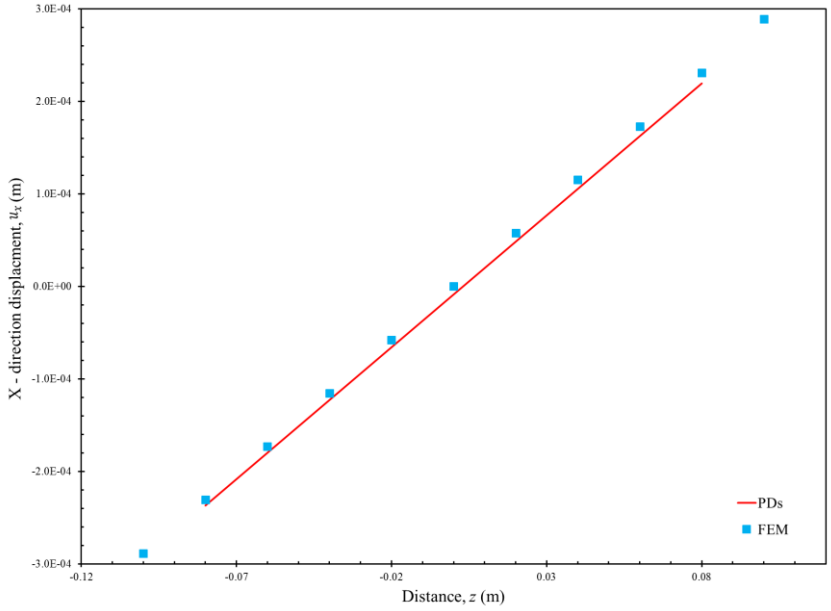

(a) *x* – direction displacement results through the thickness direction

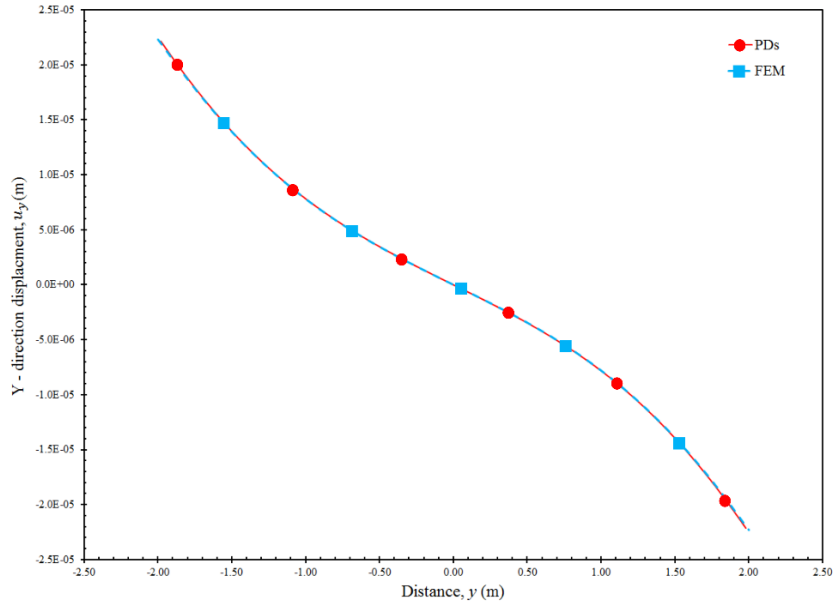

(b) *y* – direction displacement results along the central *y* axis

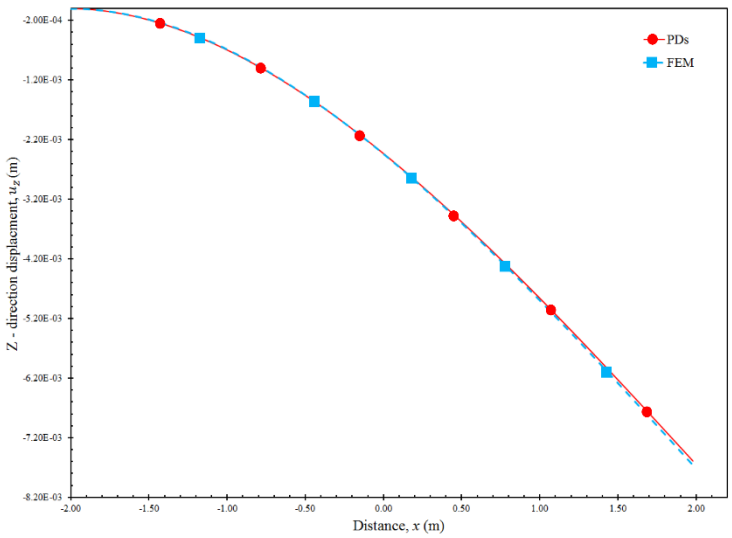

(c) z – direction displacement results along the central x axis

Figure 6.18 Comparison of the displacement results for a transversely loaded thin plate

It can be observed from x direction displacement results that in – plane bending behaviour of a clamped thin plate is successfully captured with PD model. Furthermore, the amount of contractions of the plate along y axis are in good agreement between two solutions as can be seen from Figure 6.18b. It is also remarkable that the out – of – plane displacement behavior also captured well with the 3D PD thin plate model since it is in close agreement with the FE model results. In Figures 6.19 and 6.20, the plots of PD displacements results are also shown for the comparison purposes along with FE model and they are in good agreement although a larger discretization size is used for the PD model.

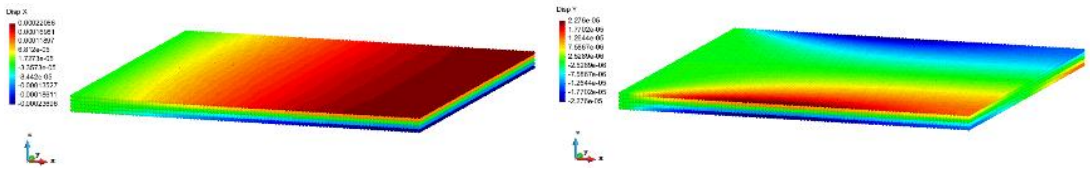

(a) (b)

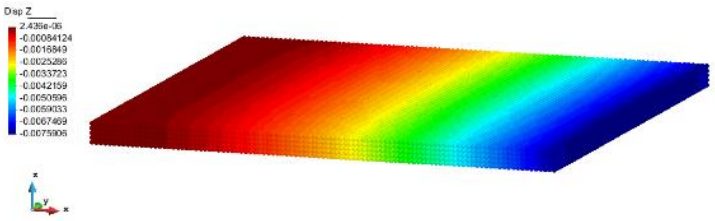

(c)

Figure 6.19 (a) *x* and (b) *y* and (c) *z* direction displacement plots of a PD thin plate model

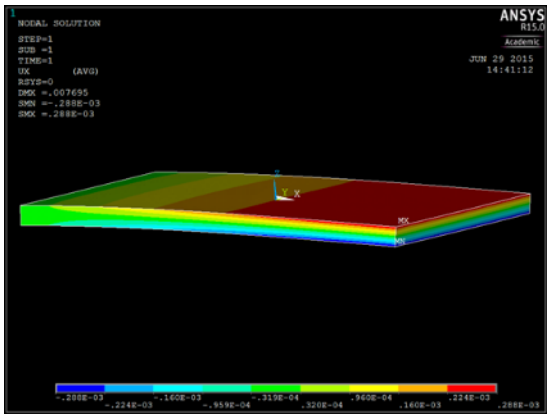

(a)

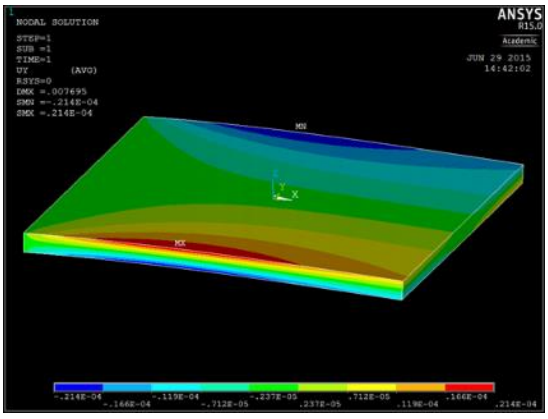

(b)

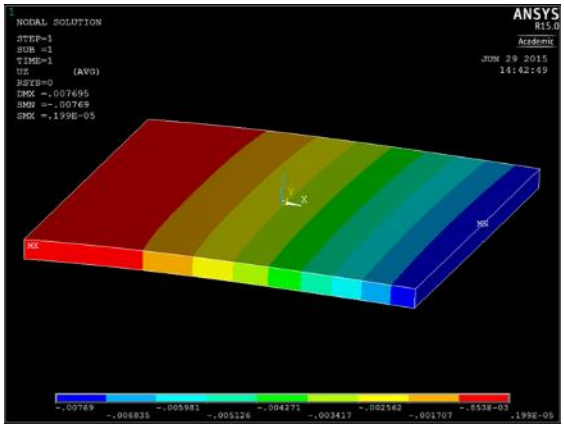

(c)

Figure 6.20 (a) *x* and (b) *y* and (c) *z* direction displacement plots of a FE thin plate model

As a summary, the in – plane and out – of plane bending behaviours as well as the contraction of a thin plate are successfully captured for the 3D PD model with discretization sizes of $\delta = 1.733\Delta x$ and $\Delta x = H/5$, respectively.

6.2.2.3 Stiffened plate

One of the most prevalent ship structure, stiffened plate, is studied here and the in – plane and out – of plane bending behaviours are investigated. As shown in Figure 6.21, the stiffened plate structure is clamped from its left end and it is subjected to a transverse loading. The length, width and thickness dimensions of the top plate are, $L = 0.12$ m, $W = 0.144$ m and $H = 0.005$ m, respectively. Moreover, the stiffener attached to it has dimensions of $l = 0.024$ m and $h = 0.006$ m. Its material properties are the same with the clamped thin model given in previous section, i.e. Section 6.2.2.2. The clamped boundary condition is imposed through a fictitious boundary region with a width of $bn_c = \delta \approx \Delta x$, as shown in Figure 6.22. On the other hand, a line force is applied in a same manner as the previous thin plate model, i.e. Section 6.2.2.2. The total magnitude of the line force is $P = 0.15$ kN and it can be converted to a body load of $b = P/\left(W\Delta x^2\right)$. Since, the boundary layer for a body load has a width of $bn_l = \Delta x$, as shown in Figure 6.22.

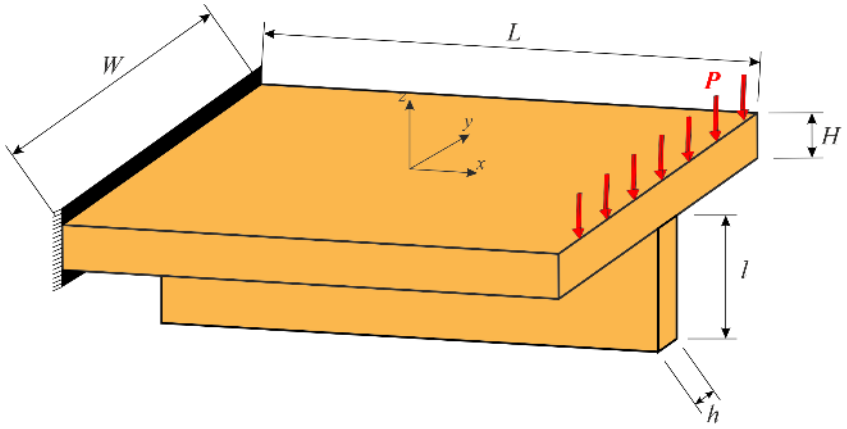

Figure 6.21 A stiffened plate model under transverse loading

The horizon and discretization sizes are chosen as $\delta = 1.733\Delta x$ and $\Delta x = H/5$, respectively.

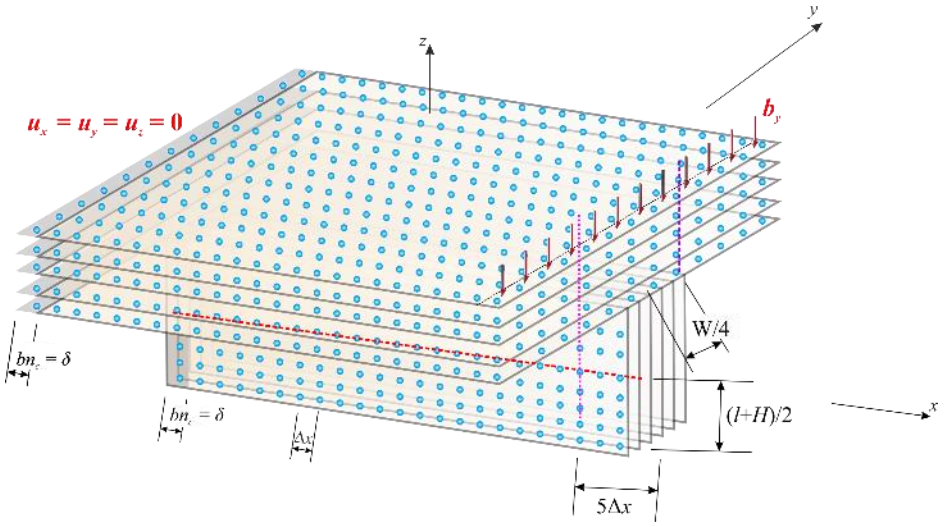

Figure 6.22 Meshless discretization of a stiffened plate model

In Figure 6.22, the pink, purple and red coloured dotted lines show where the *x*, *y* and *z* direction displacement results are extracted and they are given in Figure 6.23. Moreover, the PD results are compared with the classical theory results obtained by using FE method.

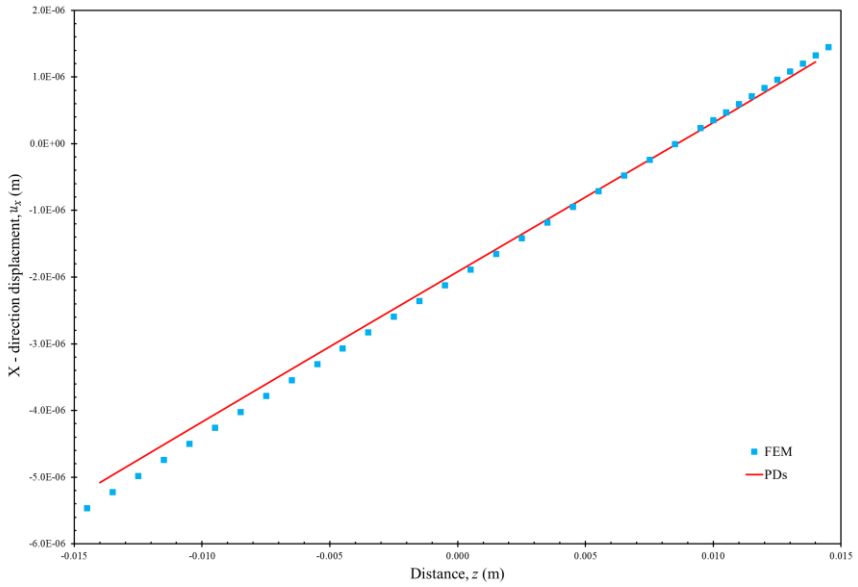

(a) *x* – direction displacement results through the thickness direction

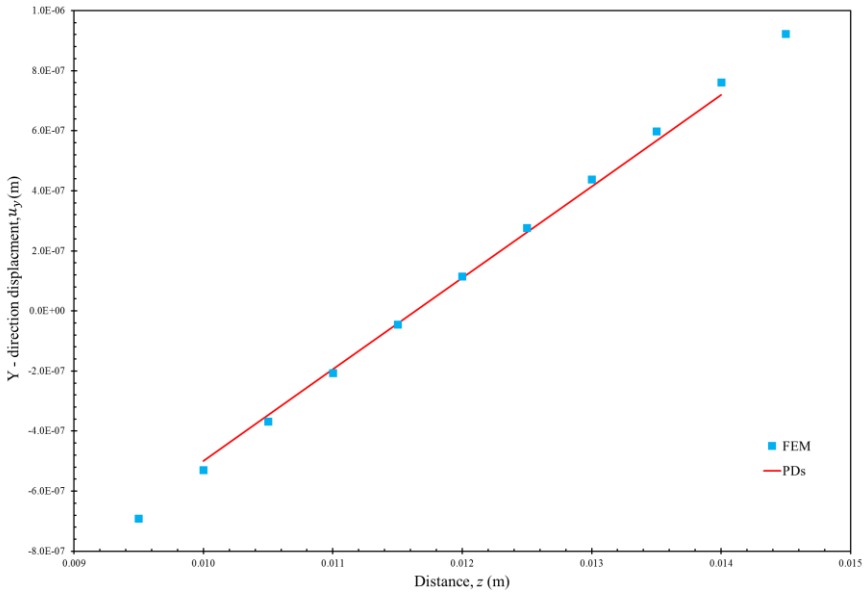

(b) y – direction displacement results through the thickness of a top plate

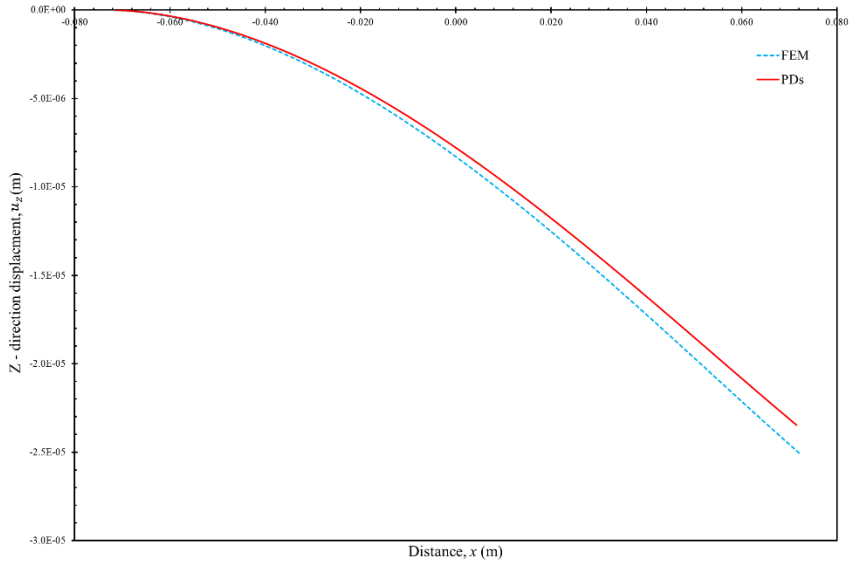

(c) z – direction displacement results along the central x axis

Figure 6.23 Comparison of the displacement results for a transversely loaded stiffened plate

It can be observed from x direction displacement results, which are extracted from very close to the free end, that they are in good agreement with FE model results. Thus, it can be said that in – plane bending deformations can be captured successfully in PD stiffened plate model. Furthermore, the contraction of the stiffened plate along y axis

may reach considerable magnitudes towards to horizontal edges of a plate, as shown in Figure 6.23b and these are also captured in PD model. Finally, the out – of – plane displacements are measured along the *x* axis for the material points on the stiffener. By comparing against FE model results, it is apperant that 3D PD stiffened plate model results are very well in agreement with FE model results. Also, Figures 6.24 and 6.25 show the displacement plots of PD theory and FE method stiffened plate models. It can be seen that PD theory very well captures the bending deformation behaviour of stiffened plate model even though larger discretization size is used in PD model compared to FE model.

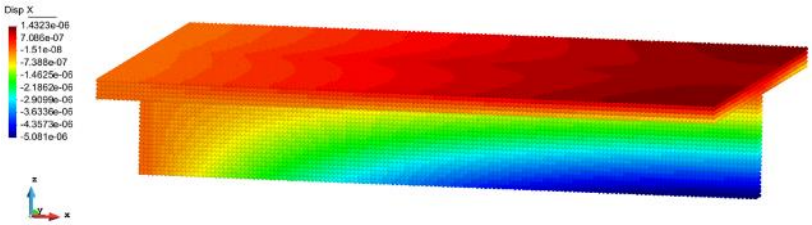

(a)

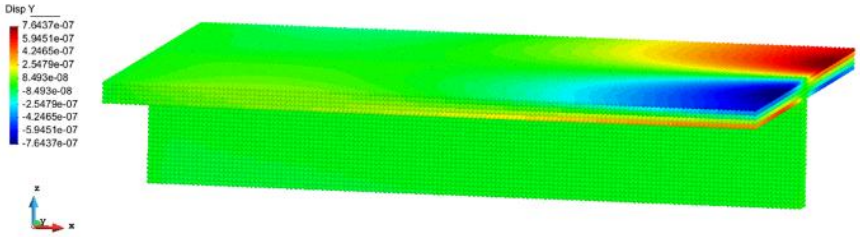

(b)

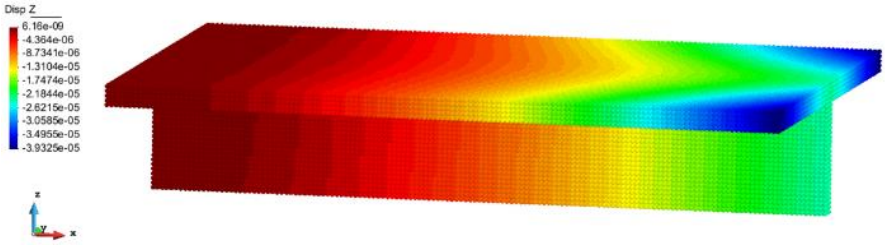

(c)

Figure 6.24 (a) *x* and (b) *y* and (c) *z* direction displacement plots of a PD stiffened plate model

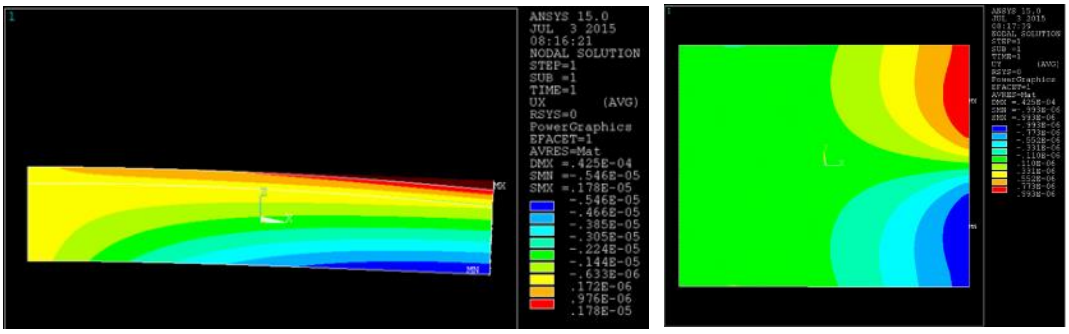

(a) front view (b) top view

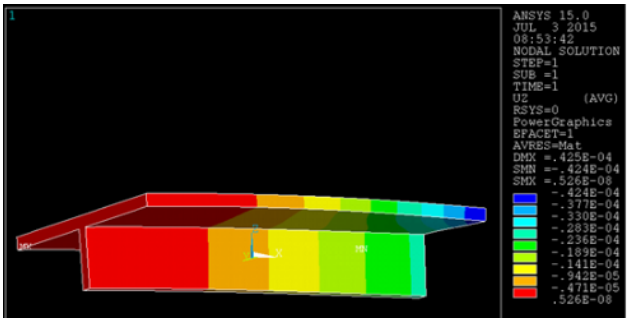

(c)

Figure 6.25 (a) *x* and (b) *y* and (c) *z* direction displacement plots of a FE stiffened plate model

As a summary, 3D PD stiffened plate model with the horizon and discretization sizes of $\delta = 1.733\Delta x$ and $\Delta x = H/5$, respectively, has a capability of successfully capturing in – plane as well as out – of – plane bending behaviours.

6.3 Collision and Grounding of Ship Structures

As mentioned in Section 6.1, collision of ships and grounding phenomena are studied by many researchers numerically and experimentally. In these studies, striking object is generally assumed as rigid body since it can either be bulbous bow of ship, which is composed of many stiffeners, or seabed topology, which can mostly be in the form of sharp rock. One of the most important studies in this regard are done by Alsos and Amdahl (2009) and Alsos et al. (2009), which present the experimental and numerical results, respectively. In experiments, the panels are loaded from its central region by a cone shaped indenter until failure of a plate, as shown in Figure 6.26, and the loading

direction is in the transverse direction to the ship panels. These experiments may represent the phenomena of grounding of a ship onto a sharp rock or bulbous bow impact on a ship side panel or the dropped object on a deck structure, as shown in Figure 6.27.

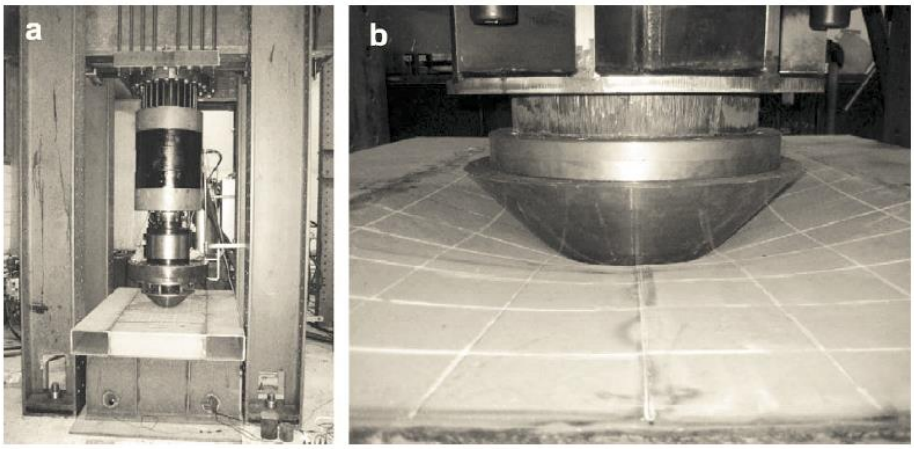

Figure 6.26 (a) Experimental setup of indenter mechanism and (b) cone shape indenter acting on a plate (Alsos and Amdahl, 2009)

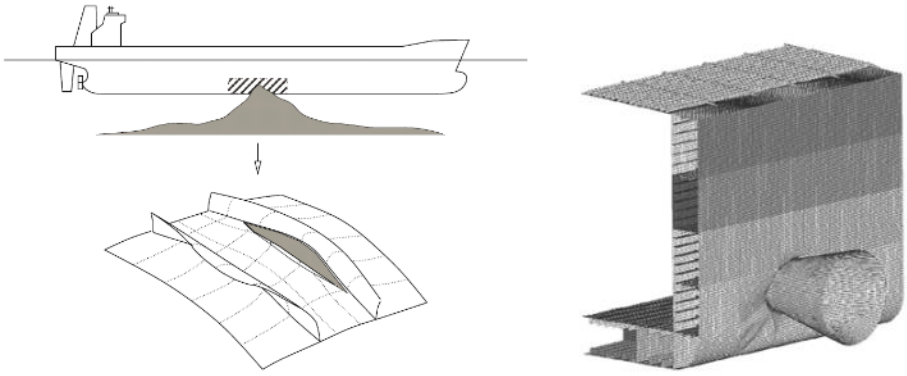

(a) Ship grounding (Alsos and Amdahl, 2009) (b) Collision of rigid bulbous bow (Klanac et al., 2010)

(c) Experimental study for the dropped object on a deck (Kozak, 2010)

Figure 6.27 Collision and grounding phenomena

In experiments, unstiffened and stiffened panels, which may represent the ship side or bottom shell structures of a ship, are used and the dimensions can be seen in Figure 6.28b. Moreover, they are supported by strong massive steel boxes from their edges as shown in Figure 6.28a.

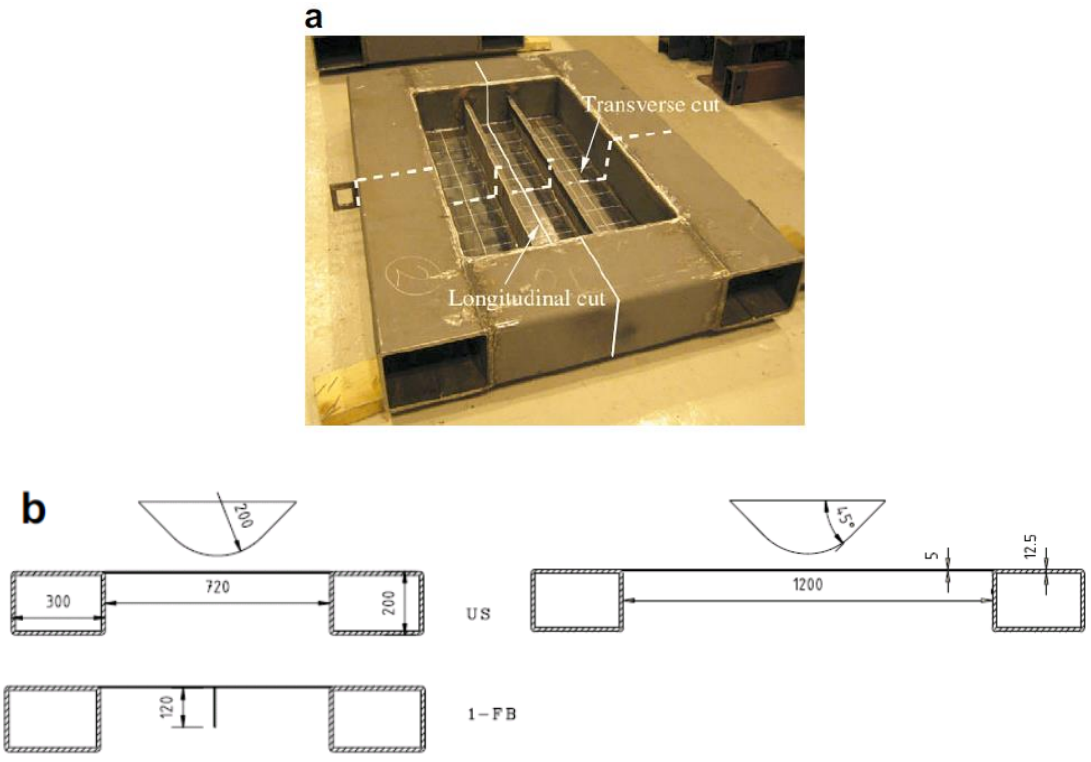

Figure 6.28 (a) Panel structure supported with steel boxes from their edges and (b) the geometrical parameters of the panels used in experiments

After all, the bending deformation behaviors of these panels are studied while rigid cone shape indenter penetrates with very small motion towards to them. Furthermore,

the force – displacement curves are plotted until final failure of panel structures is encountered.

6.3.1 Transversely loaded ship panel structures

In this section, the ship panel structures, which are studied in refs. (Alsos and Amdahl, 2009; Alsos et al., 2009), are analysed by using 3D PD plate models. In the simulations, the cone shape indenter is not actually modelled. Instead, the loading resulting from its penetration is directly induced on central region of plate models. The magnitude of transverse loading is taken as 1500 kN as mentioned in ref. (Alsos and Amdahl, 2009) and it is given as maximum load until unstiffened panel suddenly fractures. Furthermore, the distribution of loading on a plate is determined considering its shape, and dimensions, given in Figure 6.29. The PD model of cone shape indenter and its impact on a plate are presented later in Section 6.3.2.

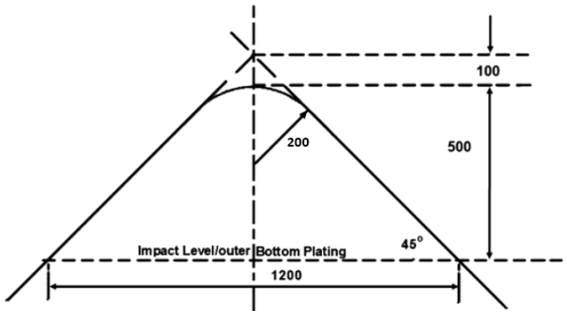

Figure 6.29 The shape and dimensions of conical shape indenter (AbuBakar and Dow, 2013)

6.3.1.1 Unstiffened panel

In light of above considerations, which are made in Sections 6.3 and 6.3.1, the unstiffened panel structure is modelled as in Figure 6.30. A plate is clamped from its edges, which are depicted in black colour in Figure 6.30. The dimensions of the plate are given as $L = 1200$ mm, $W = 720$ mm and $H = 5$ mm, respectively, and the central loading is applied onto a plate with a span length of $sp = 280$ mm. Material properties are chosen according to the provided data in ref. (Alsos and Amdahl, 2009), so that isotropic steel material is used with the properties of $E = 200$ GPa and $\nu = 1/4$.

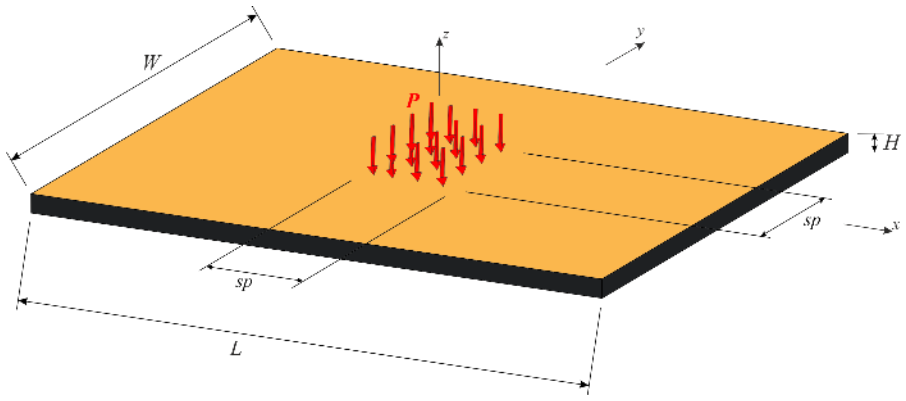

Figure 6.30 Unstiffened panel under transverse loading

The clamped boundary conditions are imposed through fictitious boundary regions with a width of $bn_c = \delta \approx \Delta x$, as shown in Figure 6.31. On the other hand, distributed load has the magnitude of $P = 1500$ kN and it is applied as a body load in PD theory. The body load of each material volume can be calculated from the formulation of $b = P/\left(sp^2 \Delta x\right)$, which is only induced on a single layer of material points. Apart from that, PD model horizon and discretization sizes are chosen as as $\delta = 1.733\Delta x$ and $\Delta x = H/5$, respectively, as proven earlier in Section 6.2 that these values can successfully represent bending behaviour of plates.

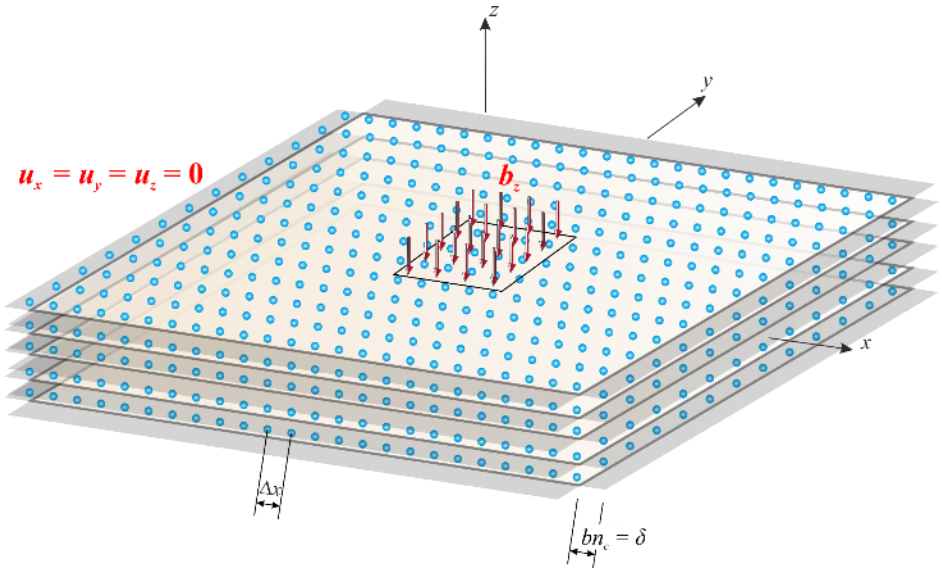

Figure 6.31 Meshless discretization of an unstiffened panel

In Figure 6.32, the *x*, *y* and *z* direction displacement results for the material points on the central axes are shown. Moreover, the PD results are compared with the classical theory results obtained by using FE method.

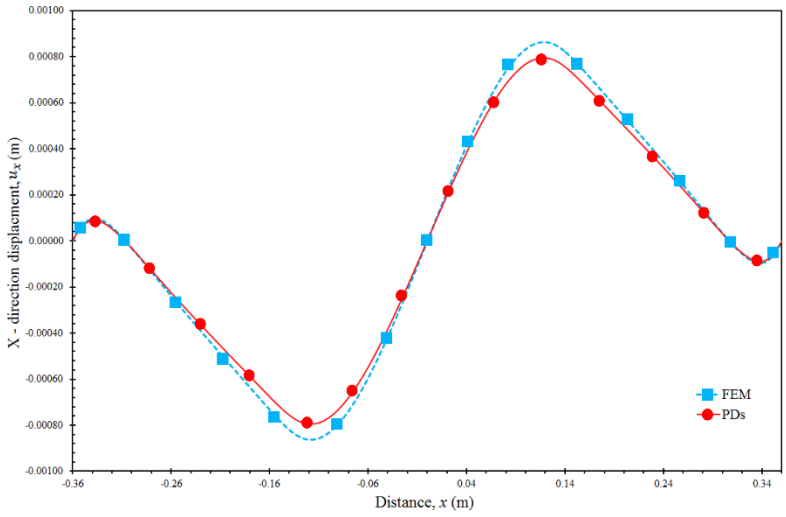

(a) *x* – direction displacement results along the *x* axis

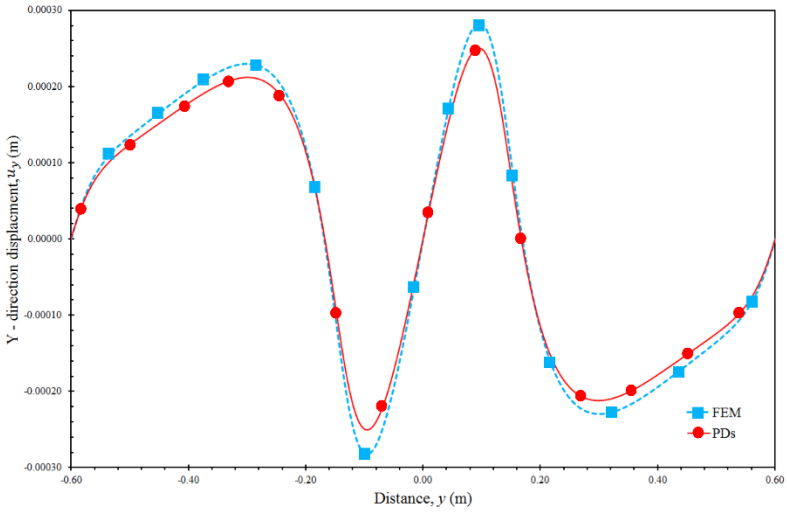

(b) *y* – direction displacement results along the *y* axis

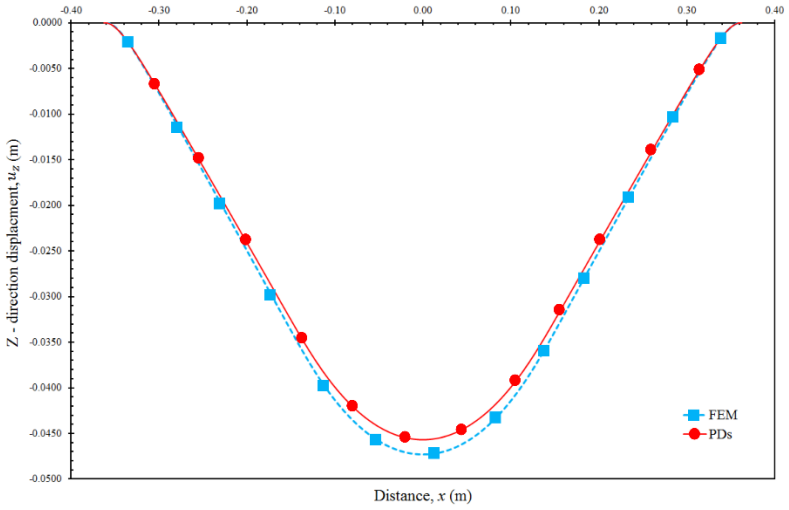

(c) z – direction displacement results along the x axis

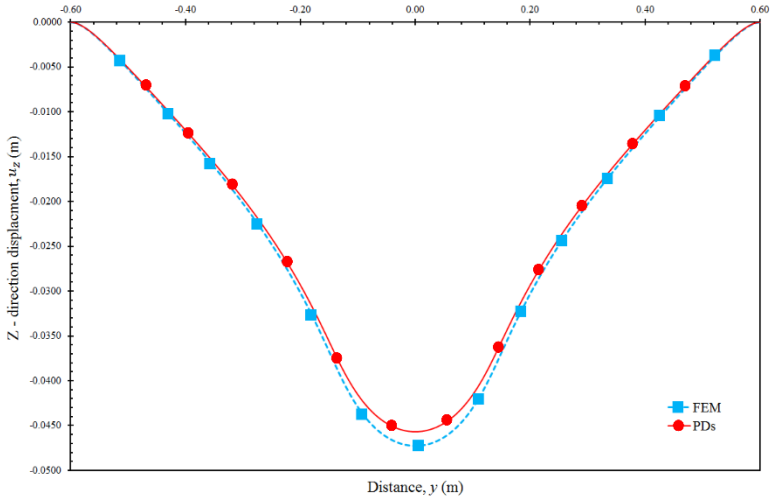

(d) z – direction displacement results along the y axis

Figure 6.32 Comparison of the displacement results for a transversely loaded unstiffened panel

It is observed that x and y direction displacement results show remarkable agreement with each other. Hence, in – plane bending deformation behaviours are represented successfully in PD theory. Moreover, out – of – plane deformations, given in Figure 6.32c and d, are also in agreement with FE model results. As mentioned by Alsos and Amdahl (2009), unstiffened plate show membrane deformations under such high level loading and this can also be seen in Figures 6.33 and 6.34 both for PD and FE model results.

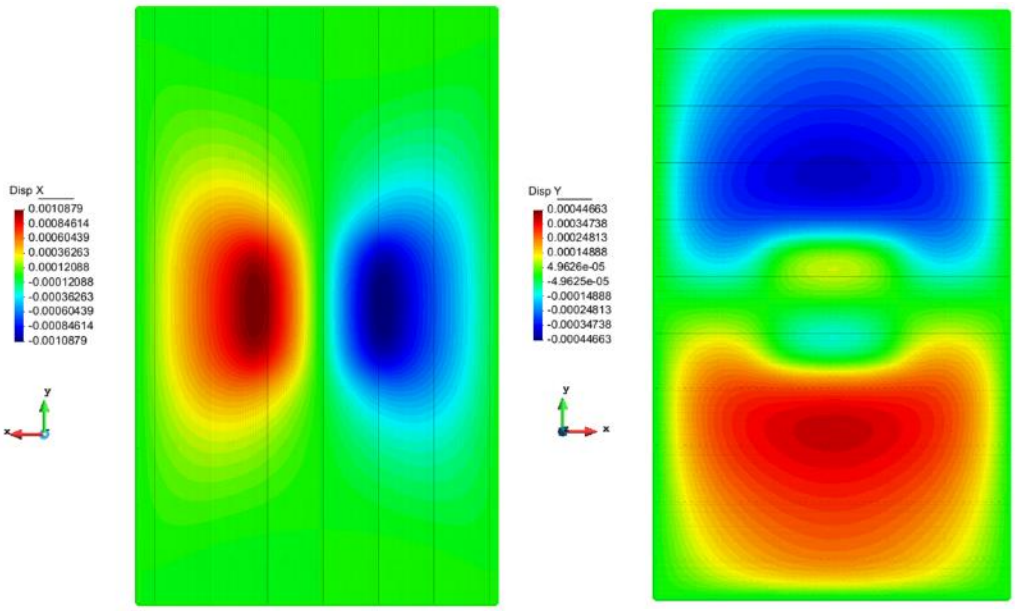

(a) Bottom view (b) Top view

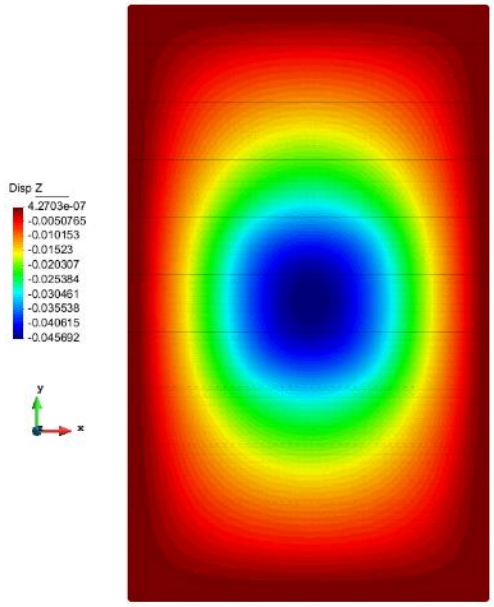

(c) Top view

Figure 6.33 (a) *x* and (b) *y* and (c) *z* direction displacement plots of a PD model for unstiffened panel

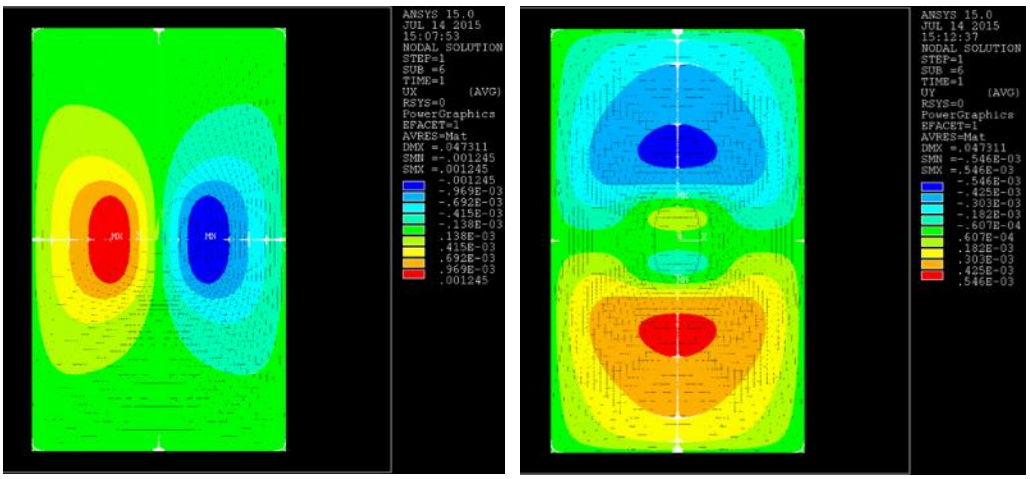

(a) Bottom view (b) Top view

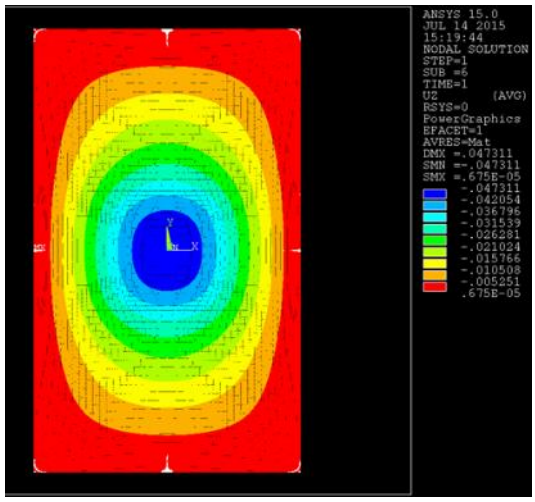

(c) Top view

Figure 6.34 (a) *x* and (b) *y* and (c) *z* direction displacement plots of a FE model for unstiffened panel

As a summary, the in – plane and out – of – plane bending deformations of an unstiffened panel can be captured well with PD theory for such a high level of transverse loading. Note that this loading results in significant amount of transverse deformations which can only be solved in classical theory including geometrical nonlinearities. However, PD theory already has capability of capturing such geometrical nonlinearities in its mathematical model.

6.3.1.2 Stiffened panel

In light of considerations made in Sections 6.3 and 6.3.1, the stiffened panel structure is modelled as shown in Figure 6.35. A plate is clamped from its edges which are depicted in black colour. The dimensions of the top plate are given as $L = 1200$ mm, $W = 720$ mm and $H = 5$ mm, respectively, and the stiffener attached to it has the dimensions of $l = 120$ mm and $h = 6$ mm. As in the unstiffened plate model, the loading is applied at the central region of the top plate with a span length of $sp = 280$ mm, which corresponds to conical shape indenter. The material properties are specified as $E = 200$ GPa and $\nu = 1/4$.

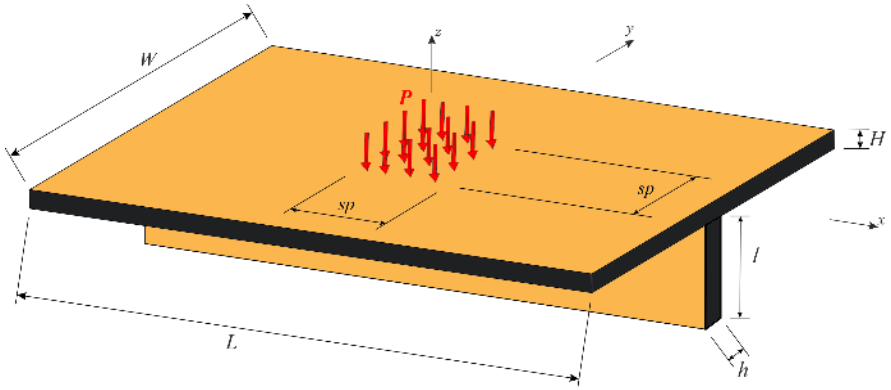

Figure 6.35 Stiffened panel under transverse loading

The clamped boundary conditions are imposed through fictitious boundary regions with a width of $bn_c = \delta \approx \Delta x$, as shown in Figure 6.36. The distributed load has a magnitude of $P = 1500$ kN and it is applied as a body load in PD theory. The body load for each material volume can be calculated from $b = P/\left(sp^2 \Delta x\right)$ and it is only induced on single layer of material points. Moreover, the horizon and discretization sizes are chosen as $\delta = 1.733\Delta x$ and $\Delta x = H/5$, respectively, since it was shown that these values can capture the bending deformations of plates.

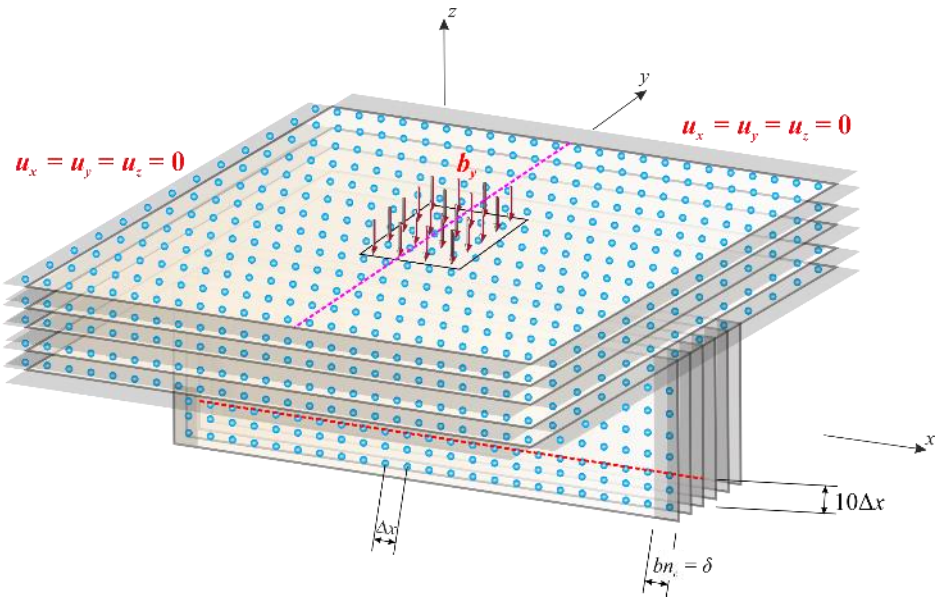

Figure 6.36 Meshless discretization of a stiffened panel

In Figure 6.36, the pink and red coloured dotted lines show where the plots of the *x*, *y* and *z* direction displacement results are extracted from and they are given in Figure 6.37. In this regard, *x* direction displacements are plotted for the material points along the pink coloured dotted line whereas *y* and *z* direction displacements are plotted for the material points along the red coloured dotted line. These locations are chosen considering the critical deformations of a plate. Moreover, the PD results are compared with the classical theory results obtained by using FE method.

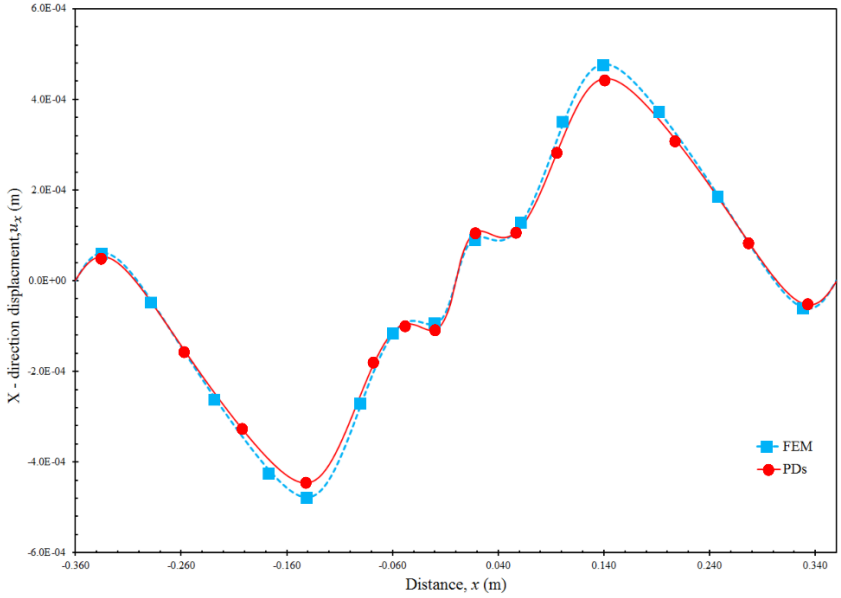

(a) *x* – direction displacement results along the width of the plate

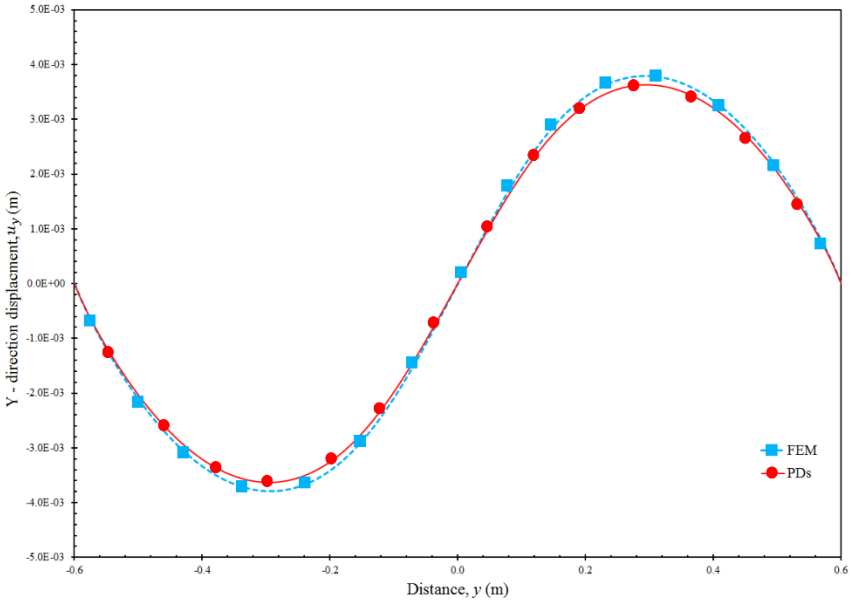

(b) y – direction displacement results along the length of the plate

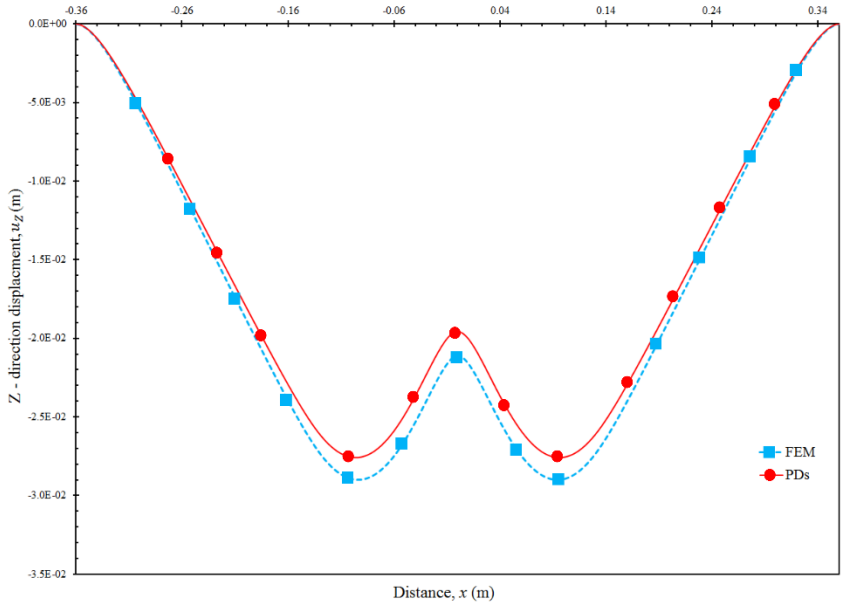

(c) z – direction displacement results along the width of the plate

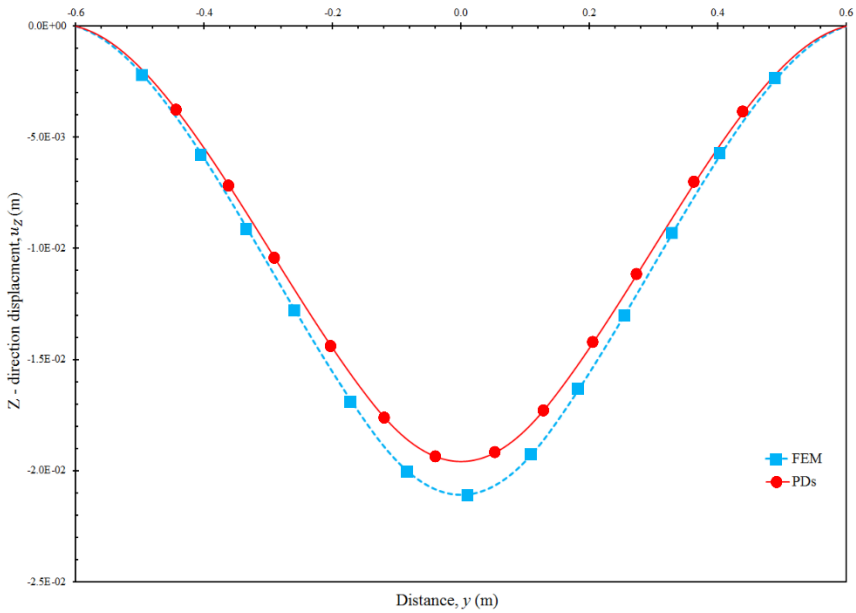

(d) z – direction displacement results along the length of the plate

Figure 6.37 Comparison of the displacement results for a transversely loaded stiffened panel

It can be observed from x direction displacement results that in – plane bending deformations, which are observed on the top plate, can be captured accurately with PD theory. Furthermore, the stiffener of the plate shows out – of – plane deformations in the y direction and this behaviour, i.e. folding effect, is also captured with PD theory results as well as with FE model results. Lastly, out – of – plane deformations through the thickness direction for the stiffener and the top plate are shown in Figure 6.37c and d. As compared to FE model results, PD stiffened model is able to capture these effects as well. The deformation plots of both models are also shown in Figures 6.38 and 6.39.

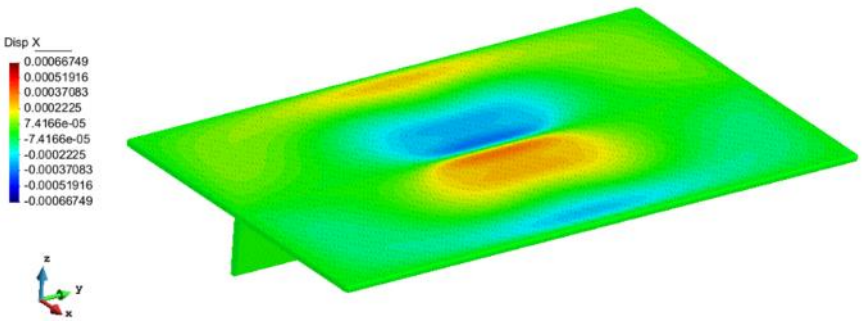

(a) Top view

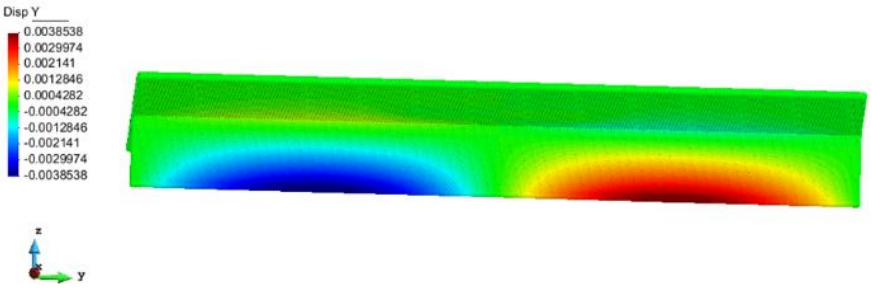

(b) Profile view

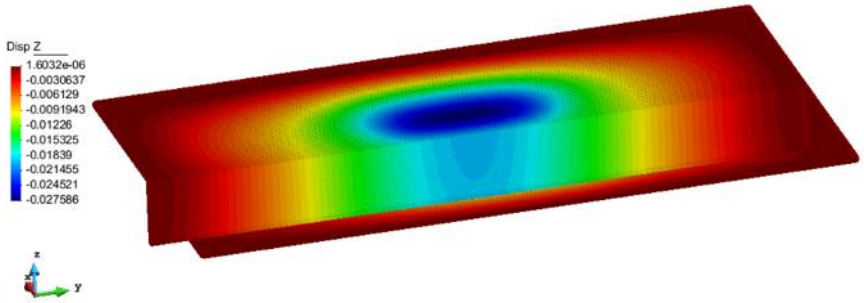

(c) Bottom view

Figure 6.38 (a) *x* and (b) *y* and (c) *z* direction displacement plots for a PD model of a stiffened panel

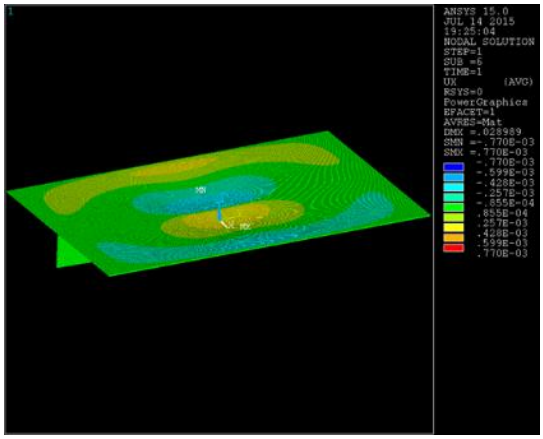

(a) Top view

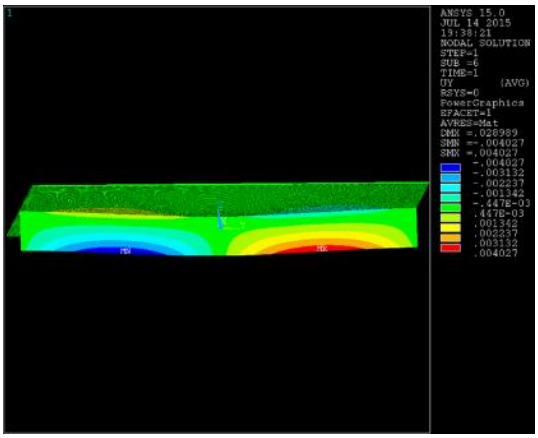

(b) Profile view

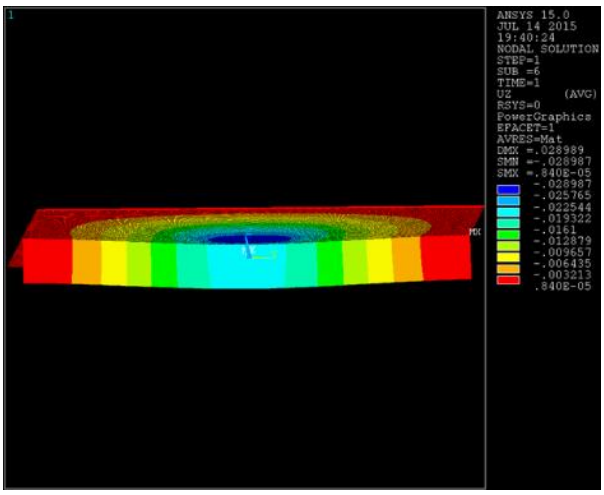

(c) Profile view

Figure 6.39 (a) *x* and (b) *y* and (c) *z* direction displacement plots for a FE model of a stiffened panel

As a summary, the in – plane and out – of – plane bending deformations of a stiffened panel can be captured with PD theory under such a high level of transverse loading. Note that this loading leads to significant amount of transverse direction deformations which can only be solved in classical theory including geometrical nonlinearities. However, PD theory already has the capability of capturing such geometrical nonlinearities in its mathematical model.

6.3.2 Impact study

In this section, we first discuss the ways of incorporating rigid body impact capability to current PD codes and then a benchmark problem, which models conical shape indenter shown in Figure 6.29, is solved. There are mainly two ways for modelling rigid targets in PD theory. One way is to add contact capability to a current PD code and the other one is to exploit contact capability of FE software.

6.3.2.1 Improving current PD codes

The contact analysis capability can be incorporated into current PD codes as explained in Chapter 10 of ref. (Madenci and Oterkus, 2014). Here, the procedure of treating material points when they are in contact with rigid body is discussed and the total reaction force on the rigid body is calculated. Please see this Chapter for more details.

The purpose of this section is to discuss how the rigid body motions can be dealt with after the total reaction force acting on it is calculated.

Equations of motion for translational motion

In rigid body dynamics, the translational motion of rigid body can basically be calculated from total forces acting on it as

$$\sum \mathbf{F} = m\mathbf{a}_{\mathbf{G}} \tag{6.1}$$

where $\mathbf{F}$, m and $\mathbf{a}_{\mathbf{G}}$ denote the total force acting on a rigid body, the mass and the acceleration of its centre of gravity. After the total reaction force acting on a rigid body is calculated, it is easy to find displacement vector, $\mathbf{u}$, while using explicit time integration scheme as explained in Section 3.2.2.1.

Equations of motion for rotational motion

On the other hand, the rotational motion of rigid body can be calculated from total moments acting on it as

$$\sum \mathbf{M}_{\mathbf{G}} = \dot{\mathbf{H}}_{\mathbf{G}} \tag{6.2}$$

where $\mathbf{M}_{\mathbf{G}}$ and $\dot{\mathbf{H}}_{\mathbf{G}}$ denote the total moments about mass centre, *G*, and the rate of angular momentum, respectively. The angular momentum is calculated with respect to rotating axes, which rotates with an angular velocity of $\boldsymbol{\Omega}$, on the rigid body. Hence, Equation (6.2) can be expressed as

$$\sum \mathbf{M}_{\mathbf{G}} = \left(\dot{\mathbf{H}}_{\mathbf{G}}\right)_{xyz} + \boldsymbol{\Omega} \times \mathbf{H}_{\mathbf{G}} \tag{6.3}$$

where $\left(\dot{\mathbf{H}}_{\mathbf{G}}\right)_{xyz}$ denotes the rate of angular momentum relative to *xyz* axes on the rigid body. If the rotating axes are fixed to the rigid body's centre of mass, *G*, the angular velocity, $\boldsymbol{\omega}$, can be expressed as equal to angular velocity of axes, $\boldsymbol{\Omega}$, i.e. $\boldsymbol{\omega} = \boldsymbol{\Omega}$. Thus, the inertia, *I*, and the moment terms become constant so that Equation (6.3) can be rewritten as

$$\sum \mathbf{M}_{\mathbf{G}} = \left(\dot{\mathbf{H}}_{\mathbf{G}}\right)_{xyz} + \boldsymbol{\omega} \times \mathbf{H}_{\mathbf{G}} \tag{6.4}$$

or it is expressed with scalar terms as (Hibbeler, 2007)

$$\sum M_x = I_{xx}\dot{\omega}_x - \left(I_{yy} - I_{zz}\right)\omega_y\omega_z - I_{xy}\left(\dot{\omega}_y - \omega_z\omega_x\right) - I_{yz}\left(\omega_y^2 - \omega_z^2\right) - I_{zx}\left(\dot{\omega}_z + \omega_x\omega_y\right)$$
$$\sum M_y = I_{yy}\dot{\omega}_y - \left(I_{zz} - I_{xx}\right)\omega_z\omega_x - I_{yz}\left(\dot{\omega}_z - \omega_x\omega_y\right) - I_{zx}\left(\omega_z^2 - \omega_x^2\right) - I_{xy}\left(\dot{\omega}_x + \omega_y\omega_z\right) \quad (6.5)$$
$$\sum M_z = I_{zz}\dot{\omega}_z - \left(I_{xx} - I_{yy}\right)\omega_x\omega_y - I_{zx}\left(\dot{\omega}_x - \omega_y\omega_z\right) - I_{xy}\left(\omega_x^2 - \omega_y^2\right) - I_{yz}\left(\dot{\omega}_y + \omega_z\omega_x\right)$$

On the other hand, locating the coordinate axes to the principal axes of inertia can reduce Equation (6.5) to a form of

$$\begin{aligned}\sum M_x &= I_x\dot{\omega}_x - \left(I_y - I_z\right)\omega_y\omega_z \\ \sum M_y &= I_y\dot{\omega}_y - \left(I_z - I_x\right)\omega_z\omega_x \\ \sum M_z &= I_z\dot{\omega}_z - \left(I_x - I_y\right)\omega_x\omega_y\end{aligned} \quad (6.6)$$

where I_x, I_y and I_z denote the principal moments of inertia and Equation (6.6) can also be named as Euler equations of motion. Calculation of principal moments of inertia is a simple eigenvalue problem (Thornton and Marion, 2004) which can be expressed as

$$\left(I_{ij} - I\delta_{ij}\right)\omega_{ij} = 0 \quad (6.7)$$

and the determinant of coeficient matrix of Equation (6.7) must vanish

$$\left|I_{ij} - I\delta_{ij}\right| = 0 \quad (6.8)$$

which leads to principal moments of inertia. Besides, eigenvectors, i.e. ω_j, of Equation (6.8) results in orientation of each axis.

Euler Angles

Angular velocities, i.e. ω_x, ω_y and ω_z, of body axes can not be integrated in order to find angular displacements. For this reason, a set of generalized coordinates are selected to describe the orientation of the rigid body in terms of Euler angles, i.e. ϕ, θ and Ψ (D'Souza and Garg, 1984). Thus, the ω_x, ω_y and ω_z components of angular velocity can be expressed in terms of Euler angles. The definitions of these angles are not unique. Here, the study of Greenwood (1988) is taken as reference. As shown in Figure 6.40, Euler angles define the orientation of *xyz* coordinate system or body axes relative to the fixed *XYZ* system.

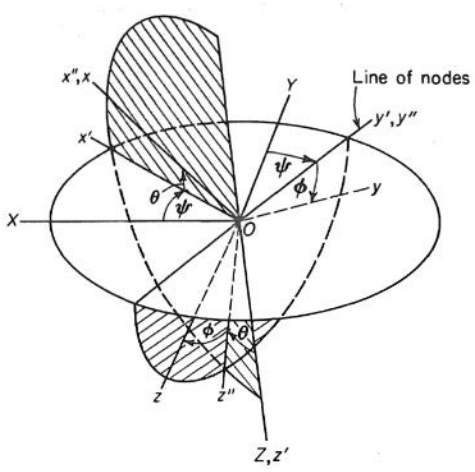

Figure 6.40 Definition for Euler angles (Greenwood, 1988)

In order to define Euler angles, firstly, it is considered that two coordinate systems are coincident and then series of three rotations about the body axes, in a proper sequence, are performed. Thus, the final orientation of the axes or the body is found from these rotations as

1. A positive rotation, Ψ, about Z axis leads to primed coordinate system as

$$\{r'\} = [\psi]\{R\} \tag{6.9}$$

and it can be expressed in an explicit form as

$$\begin{Bmatrix} x' \\ y' \\ z' \end{Bmatrix} = \begin{bmatrix} \cos\psi & \sin\psi & 0 \\ -\sin\psi & \cos\psi & 0 \\ 0 & 0 & 1 \end{bmatrix} \begin{Bmatrix} X \\ Y \\ Z \end{Bmatrix} \tag{6.10}$$

2. A positive rotation, θ, about y' axis leads to double primed coordinate system as

$$\{r''\} = [\theta]\{r'\} \tag{6.11}$$

and in an explicit form as

$$\begin{Bmatrix} x'' \\ y'' \\ z'' \end{Bmatrix} = \begin{bmatrix} \cos\theta & 0 & -\sin\theta \\ 0 & 1 & 0 \\ \sin\theta & 0 & \cos\theta \end{bmatrix} \begin{Bmatrix} x' \\ y' \\ z' \end{Bmatrix} \tag{6.12}$$

3. A positive rotation, ϕ, about x'' axis leads to final coordinate system, i.e. *xyz*, as

$$\{r\} = [\phi]\{r''\} \tag{6.13}$$

and in an explicit form as

$$\begin{Bmatrix} x \\ y \\ z \end{Bmatrix} = \begin{bmatrix} 1 & 0 & 0 \\ 0 & \cos\phi & \sin\phi \\ 0 & -\sin\phi & \cos\phi \end{bmatrix} \begin{Bmatrix} x'' \\ y'' \\ z'' \end{Bmatrix} \tag{6.14}$$

In light of above considerations, the final orientation of rigid body can be found from

$$\{r\} = [\lambda]\{R\} \tag{6.15}$$

where λ indicates the transformation matrix, which is in the form of $[\lambda] = [\phi][\theta][\psi]$ and it can be rewritten in an explicit form as

$$[\lambda] = \begin{bmatrix} \cos\psi\cos\theta & \sin\psi\cos\theta & -\sin\theta \\ -\sin\psi\cos\phi + \cos\psi\sin\theta\sin\phi & \cos\psi\cos\phi + \sin\psi\sin\theta\sin\phi & \cos\theta\sin\phi \\ \sin\psi\sin\phi + \cos\psi\sin\theta\cos\phi & -\cos\psi\sin\phi + \sin\psi\sin\theta\cos\phi & \cos\theta\cos\phi \end{bmatrix} \tag{6.16}$$

To conclude, any possible orientation of rigid body can be found by using Equation (6.15) while performing rotations in a proper order as defined above.

Furthermore, the angular velocity, i.e. $\boldsymbol{\omega}$, of a body can be expressed by means of time rate of change of Euler angles as

$$\boldsymbol{\omega} = \dot{\boldsymbol{\psi}} + \dot{\boldsymbol{\theta}} + \dot{\mathbf{f}} \tag{6.17}$$

Equation (6.17) can also be expressed in the matrix form as

$$\{\omega\} = [J]\{\omega_e\} \tag{6.18}$$

where ω_e and J denote the Euler – rate vector and the transformation matrix, respectively. An explicit form of Equation (6.18) is

$$\begin{Bmatrix}\omega_x\\ \omega_y\\ \omega_z\end{Bmatrix}=\begin{bmatrix}1 & 0 & -\sin\theta\\ 0 & \cos\phi & \cos\theta\sin\phi\\ 0 & -\sin\phi & \cos\theta\cos\phi\end{bmatrix}\begin{Bmatrix}\dot{\phi}\\ \dot{\theta}\\ \dot{\psi}\end{Bmatrix} \tag{6.19}$$

However, $\dot{\boldsymbol{\psi}}$, $\dot{\boldsymbol{\theta}}$ and $\dot{\mathbf{f}}$ are the non – orthogonal components of $\boldsymbol{\omega}$. Therefore, *J* does not satisfy orthogonal transformation property, i.e. $[J]^{-1} \neq [J]^{T}$. Thus, the Euler – rate vector can be expressed from Equations (6.18) or (6.19) as

$$\{\omega_e\}=[J]^{-1}\{\omega\} \quad \text{where} \quad [J]^{-1}=\begin{bmatrix}1 & \sin\phi\tan\theta & \cos\phi\tan\theta\\ 0 & \cos\phi & -\sin\phi\\ 0 & \sin\phi\sec\theta & \cos\phi\sec\theta\end{bmatrix} \tag{6.20}$$

Note that $[J]^{-1}$ is singular for the cases of $\theta=\pm 90^{\circ}$. In such cases, the kinematic equations can be solved by four – parameter method based on quaternions. Thus, the singularity of matrix can be avoided by using four parameters (Fossen, 1987).

Solution procedure in order to find final orientation of body

In light of above discussed procedures, Equations (6.6) and (6.20) are solved simultaneously for Euler angles, ψ, θ and ϕ, and then substituting these angles into Equation (6.15) results in final orientation of the body. In order to achieve these, 4th order Runge Kutta time integration method can be utilized. Runge Kutta method is basically derived from Taylor series expansions (D'Souza and Garg, 1984) and the 4th order method is used here in order to obtain good accuracy.

In this regard, firstly, Equation (6.6) can be rearranged as

$$\begin{aligned}\dot{\omega}_x &= \frac{\sum M_x+\left(I_y-I_z\right)\omega_y\omega_z}{I_x}\\ \dot{\omega}_y &= \frac{\sum M_y+\left(I_z-I_x\right)\omega_z\omega_x}{I_y}\\ \dot{\omega}_z &= \frac{\sum M_z+\left(I_x-I_y\right)\omega_x\omega_y}{I_z}\end{aligned} \tag{6.21}$$

and the angular velocities for the next time step can be obtained from

$$\omega_x^{t+1} = \omega_x^t + \frac{\Delta t}{6}\left(f_{1x} + 2 f_{2x} + 2 f_{3x} + f_{4x} \right)$$
$$\omega_y^{t+1} = \omega_y^t + \frac{\Delta t}{6}\left(f_{1y} + 2 f_{2y} + 2 f_{3y} + f_{4y} \right) \tag{6.22}$$
$$\omega_z^{t+1} = \omega_z^t + \frac{\Delta t}{6}\left(f_{1z} + 2 f_{2z} + 2 f_{3z} + f_{4z} \right)$$

where f_{1i}, f_{2i}, f_{3i} and f_{4i} are the constants of Runge Kutta method with $i = x, y, z$. These constants can be expressed as

$$\begin{aligned}
f_{1i} &= \dot{\omega}_i\left(\omega_x^t, \omega_y^t, \omega_z^t, t\right) \\
f_{2i} &= \dot{\omega}_i\left(\omega_x^t + f_{1x}\frac{\Delta t}{2}, \omega_y^t + f_{1y}\frac{\Delta t}{2}, \omega_z^t + f_{1z}\frac{\Delta t}{2}, t + \frac{\Delta t}{2}\right) \\
f_{3i} &= \dot{\omega}_i\left(\omega_x^t + f_{2x}\frac{\Delta t}{2}, \omega_y^t + f_{2y}\frac{\Delta t}{2}, \omega_z^t + f_{2z}\frac{\Delta t}{2}, t + \frac{\Delta t}{2}\right) \\
f_{4i} &= \dot{\omega}_i\left(\omega_x^t + f_{3x}\Delta t, \omega_y^t + f_{3y}\Delta t, \omega_z^t + f_{3z}\Delta t, t + \Delta t\right)
\end{aligned} \quad \text{with} \quad i = x, y, z \tag{6.23}$$

Furthermore, Euler angles for the next time step can be obtained from

$$\phi^{t+1} = \phi^t + \frac{\Delta t}{6}\left(g_{1\phi} + 2 g_{2\phi} + 2 g_{3\phi} + g_{4\phi} \right)$$
$$\theta^{t+1} = \theta^t + \frac{\Delta t}{6}\left(g_{1\theta} + 2 g_{2\theta} + 2 g_{3\theta} + g_{4\theta} \right) \tag{6.24}$$
$$\psi^{t+1} = \psi^t + \frac{\Delta t}{6}\left(g_{1\psi} + 2 g_{2\psi} + 2 g_{3\psi} + g_{4\psi} \right)$$

where g_{1k}, g_{2k}, g_{3k} and g_{4k} are the constants of Runge Kutta method with $k = \phi,\ \theta,\ \psi$. Keeping in mind that Euler angles are also the functions of angular velocities, ω_i, the constants of Equation (6.24) can be expressed as

$$\begin{aligned}
g_{1k} &= \dot{k}\left(\omega_x^t, \omega_y^t, \omega_z^t, \phi^t, \theta^t, \psi^t, t\right) \\
g_{2k} &= \dot{k}\left(\omega_x^t + f_{1x}\frac{\Delta t}{2}, \omega_y^t + f_{1y}\frac{\Delta t}{2}, \omega_z^t + f_{1z}\frac{\Delta t}{2}, \phi^t + g_{1\phi}\frac{\Delta t}{2}, \theta^t + g_{1\theta}\frac{\Delta t}{2}, \psi^t + g_{1\psi}\frac{\Delta t}{2}, t + \frac{\Delta t}{2}\right) \\
g_{3k} &= \dot{k}\left(\omega_x^t + f_{2x}\frac{\Delta t}{2}, \omega_y^t + f_{2y}\frac{\Delta t}{2}, \omega_z^t + f_{2z}\frac{\Delta t}{2}, \phi^t + g_{2\phi}\frac{\Delta t}{2}, \theta^t + g_{2\theta}\frac{\Delta t}{2}, \psi^t + g_{2\psi}\frac{\Delta t}{2}, t + \frac{\Delta t}{2}\right) \\
g_{4k} &= \dot{k}\left(\omega_x^t + f_{3x}\Delta t, \omega_y^t + f_{3y}\Delta t, \omega_z^t + f_{3z}\Delta t, \phi^t + g_{3\phi}\Delta t, \theta^t + g_{3\theta}\Delta t, \psi^t + g_{3\psi}\Delta t, t + \Delta t\right)
\end{aligned} \tag{6.25}$$

with $k = \phi,\ \theta,\ \psi$. After obtaining Euler angles for the next time step, they are substituted into Equation (6.15) and the final orientation of the body can be obtained.

Benchmark problem

The impact of 3D cylindrical object to a rectangular plate, shown in Figure 6.41, is studied in order to verify that 3D rotations of rigid body can be represented in PD theory successfully with the above mentioned method. A cylindirical object has a nose with a half spherical shape. This object can be considered as any dropped object on a ship structure or the ship's bow.

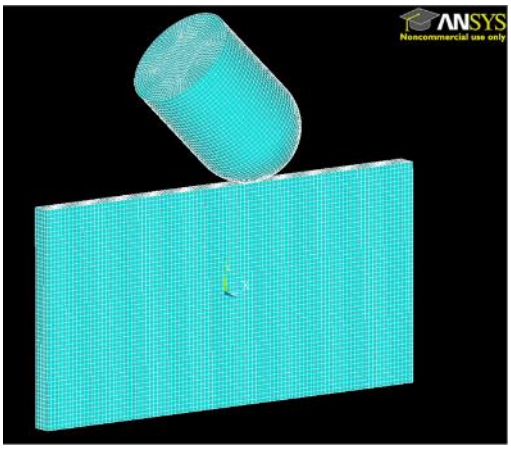

Figure 6.41 Representative model for the impact study

The length, width and thickness dimensions of a plate are, $L = 0.20$ m, $W = 0.10$ m and $H = 0.009$ m, respectively. It has the Young's modulus and the Poisson's ratio of $E = 191$ GPa and $\nu = 1/4$, respectively. A cylindirical object has spherical nose with a diameter of $D = 0.05$ m and the cylinder's length is given as $l = 0.05$ m. The mass densities of the plate and the rigid impactor are the same with $\rho = 8000\ kg/m^3$. The discretization and horizon sizes of the plate for PD model are given as $\Delta x = 0.001$ m and $\delta = 3.015\Delta x$, respectively. Figure 6.41 shows the orientation of a rigid body at the beginning of the analysis. It is inclined 45° with respect to a horizontal edge of the plate and the magnitude of its initial velcocity is assumed as $\boldsymbol{\upsilon}_0 = 32$ m/s which is also directed through 45° with respect to the horizontal edge. The time step size of explicit time integration scheme is chosen as $\Delta t = 8.71\times10^{-8}$ s and the total number of time steps are 2000.

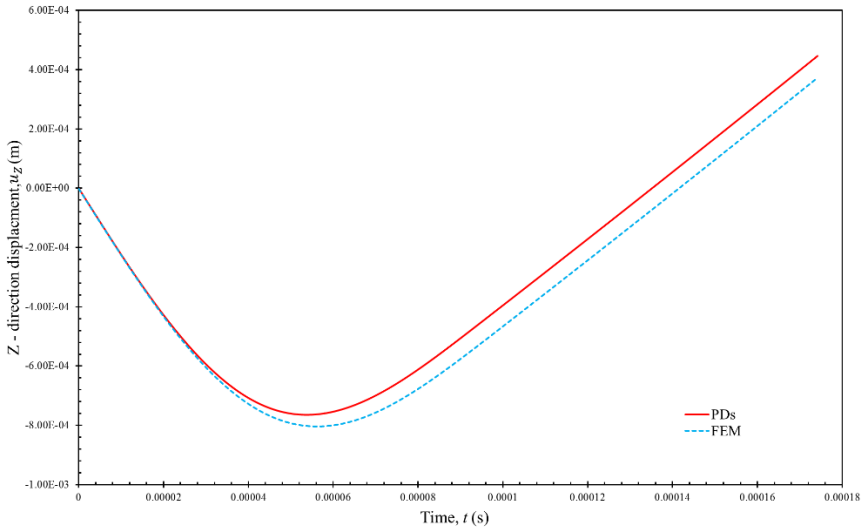

Figure 6.42 The vertical direction displacements of tip of a rigid body

In Figure 6.42, the comparisons of tip point vertical displacements of a rigid body is given as the time progresses. The rigid rotations obtained with PD theory are in good agreement with FE method results. Moreover, the final orientation of the rigid body is found as 48.31° with respect to the horizontal edge of plate and it is 48.24° in FE model results. Thus, it can be concluded that the translational as well as the rotational motions of a rigid body can be represented using the procedure explained in this section along with the procedure defined in Chapter 10 of ref. (Madenci and Oterkus, 2014).

6.3.2.2 Incorporating contact capability of FE software

Up to now, the Peridynamic plate models, given in Sections 6.2 and 6.3.1, are modelled in FE software, ANSYS, using link elements and they are solved using the solver capacity of FE software. As mentioned in Section 6.1.1, the contact capability of FE software can also be utilized to study impact problems in PD theory.

To achieve this, 3D or 2D PD model is created in FE software, ANSYS, as usual using LINK180 and MASS21 elements as explained in Section 3.3.1.2. Then, the node to surface contact elements, i.e. CONTA175, are created on all nodes of the link elements while using ESURF command in ANSYS. Furthermore, the rigid target can also be modelled in any shape using target elements. These elements can be TARGE169 for 2D models and TARGE170 for 3D models.

In solving impact problems, ANSYS uses Augmented Lagrangian method by default. This method is fundamentally based on pure penalty method and it ensures minimum penetration for the target elements while using Lagrange multipliers method for a robust convergence capability. In pure penalty method, the contact capability is achieved by stiffness of a spring element which is assumed to be located inside a contact element, shown in Figure 6.43.

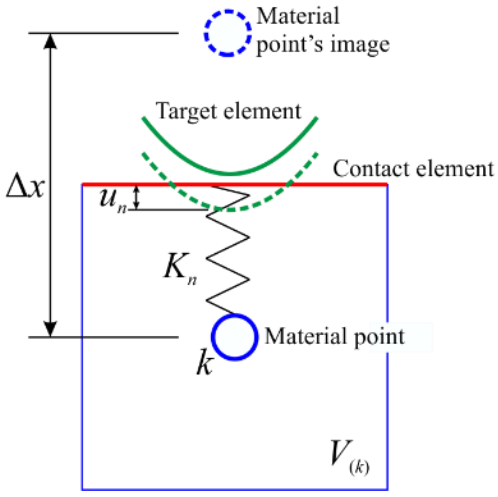

Figure 6.43 Contact and target elements in PD model

Contact spring reacts rigid target with a contact force, F_n, in the normal direction

$$F_n = K_n u_n \tag{6.26}$$

where K_n and u_n represent the contact stiffness and the penetration distance, respectively. In this regard, it is important to define the stiffness of a spring inside a contact element for PD material points. It is proposed as

$$K_n = c_s \frac{V_{(k)}^2}{\Delta x} \tag{6.27}$$

where, c_s denotes the contact force constant and it can be taken as 100 times the value of bond constant, c, of a PD bond. Assuming larger values may result in too stiff contact elements and it may lead to convergence difficulties in FE software. On the other hand, the smaller values may lead to too much penetration of a rigid target element. Moreover, in Equation (6.27), Δx represents the distance between actual material point and its image, which is assumed inside the target element, as shown in

Figure 6.43. The specified normal contact stiffness, K_n, of contact element can be defined in ANSYS using the real constant parameter FKN. Besides, the contact elements can be offsetted towards the target elements using CNOF parameter with a value of $\Delta x/2$. This ensures creating contact elements on the surface of material volume as shown in Figure 6.43.

To conclude, using the above procedure incorporates contact capability in FE software for a current PD model. Note that ANSYS uses implicit time integration scheme in dynamic problems in contrast to a model defined in previous section, i.e. Section 6.3.2.1.

6.3.2.3 Benchmark problem

The contact procedure, explained in Section 6.3.2.2, is now studied for the impact problem defined in Section 6.3. The PD model of an unstiffened panel structure is created in ANSYS and its representative model can be seen from Figure 6.30. As in the figure, it is clamped from its edges whereas the transverse direction forces are removed in this case. The dimensions of the plate are taken as $L = 1200/5$ mm, $W = 720/5$ mm and $H = 5$ mm, respectively. The material properties are chosen according to the provided data in ref. (Alsos and Amdahl, 2009), so that isotropic steel material has the properties of $E = 200$ GPa and $\nu = 1/4$.

The discretized PD plate model can also be seen in Figure 6.31 while keeping in mind that central body loads should be removed in this case. Instead the conical shape indenter is modelled in ANSYS using the target elements, i.e. TARGE170, and the node to surface contact elements, i.e. CONTA175, are created on all nodes of the link elements as can be seen in Figure 6.44. The geometrical parameters of a conical shape indenter can be seen from Figure 6.29 whereas the dimension of its radius is modified considering the dimensions of the plate and it has the value of $r = 200/5$ mm.

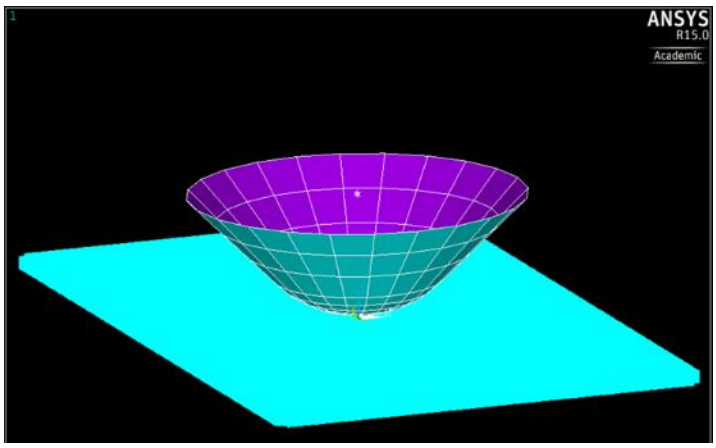

Figure 6.44 The PD model of a plate and a conical shaped rigid target

The PD plate model has the horizon and discretization sizes of $\delta = 1.733\Delta x$ and $\Delta x = H/5$, respectively. A rigid target indenter is moved vertically towards the PD plate model with a velocity of $\upsilon_0 = 10$ mm/min. It is also the same value used in experiments done by Alsos and Amdahl (2009). The loading condition is quasi – static and it is implemeneted in ANSYS using 90 steps in total.

In Figure 6.45, the *x*, *y* and *z* direction displacement results for the material points on the central axes are shown. Moreover, the PD results are compared with the classical theory results obtained by using FE method.

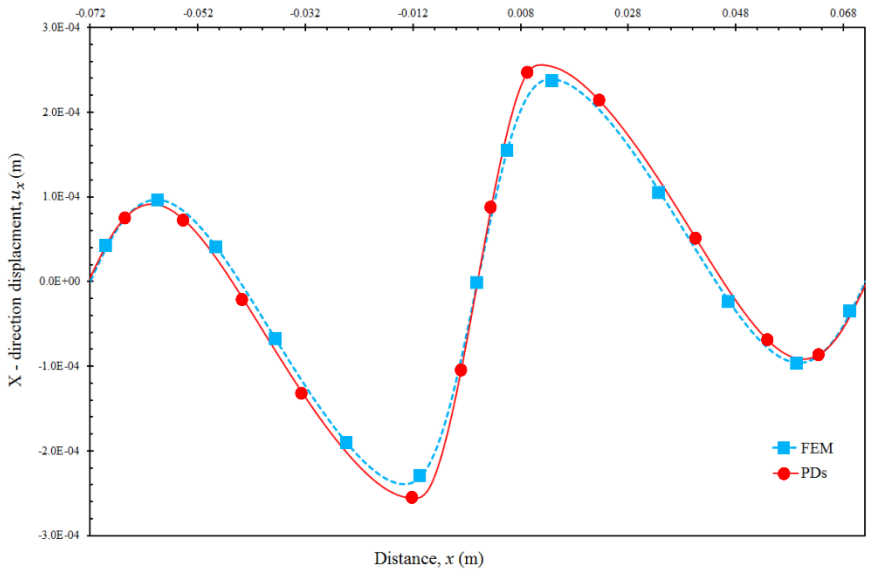

(a) *x* – direction displacement results along the central *x* axis

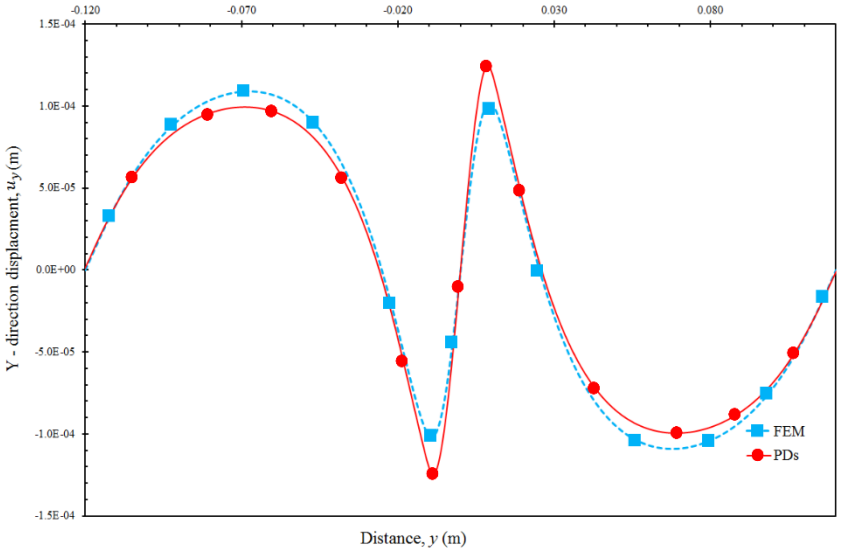

(b) y – direction displacement results along the central y axis

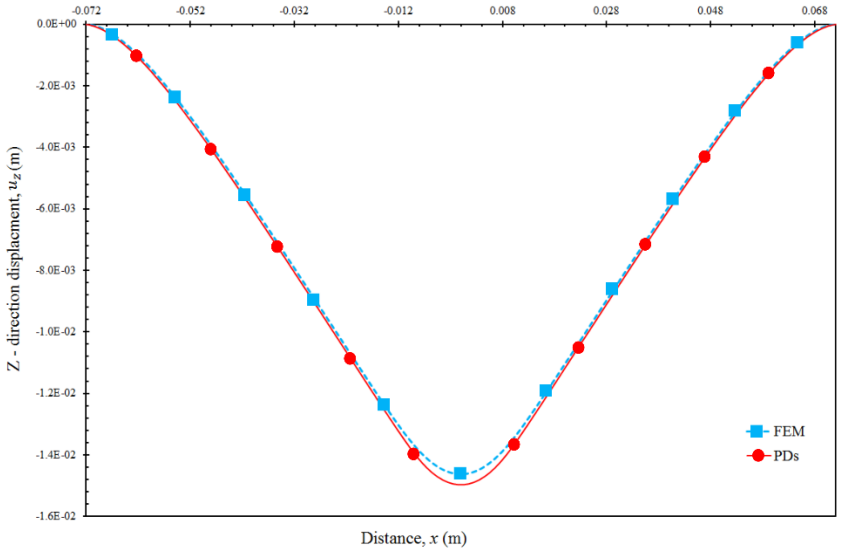

(c) z – direction displacement results along the central x axis

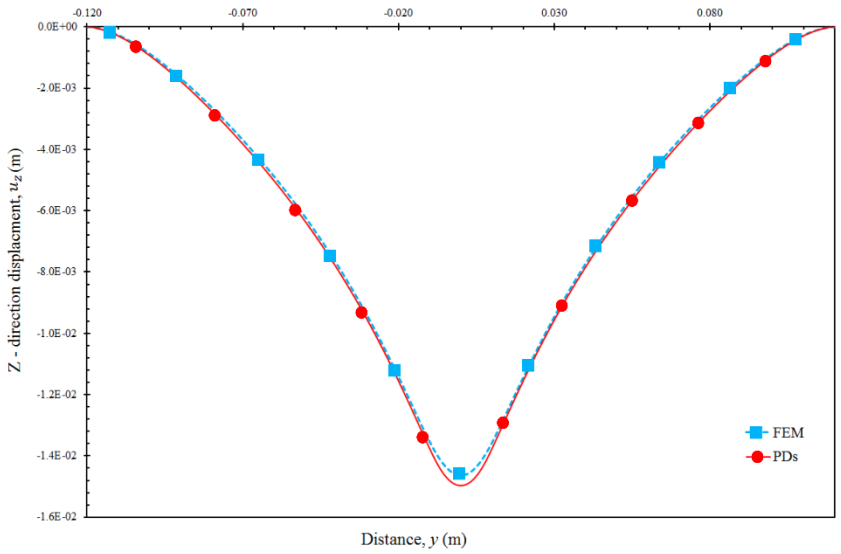

(d) z – direction displacement results along the central y axis

Figure 6.45 Comparison of the displacement results for the impact problem of an unstiffened panel

It can be observed from Figure 6.45a and b that in – plane bending deformations are in agreement with FE model results as well as the out – of – plane bending deformations, which can be seen from Figure 6.45c and d. Furthermore, Figures 6.46 and 6.47 show the deformation plots of the PD and FE models for comparison purposes.

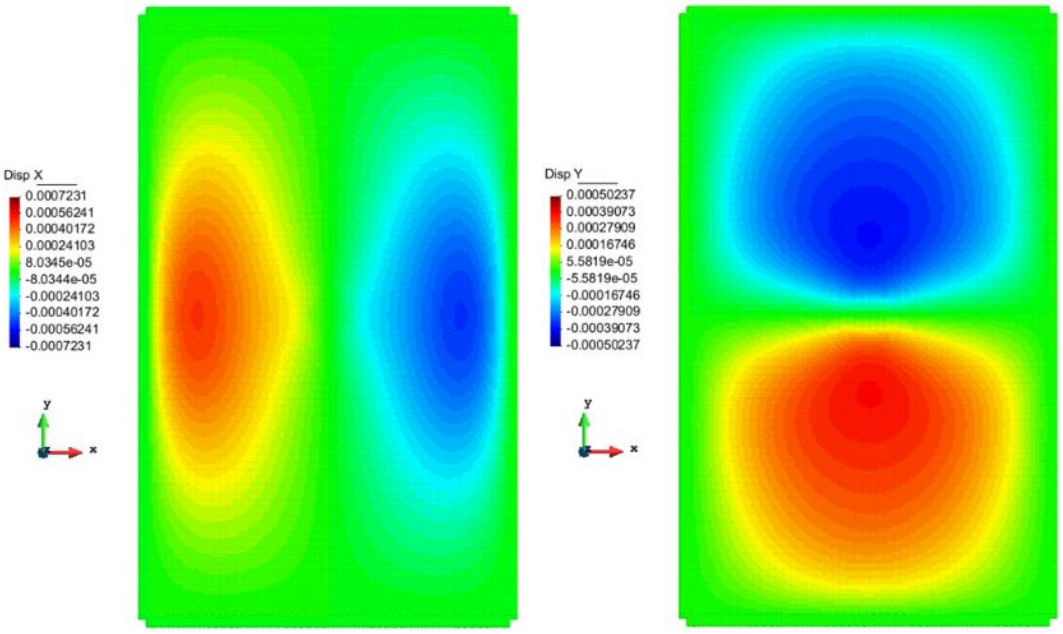

(a) (b)

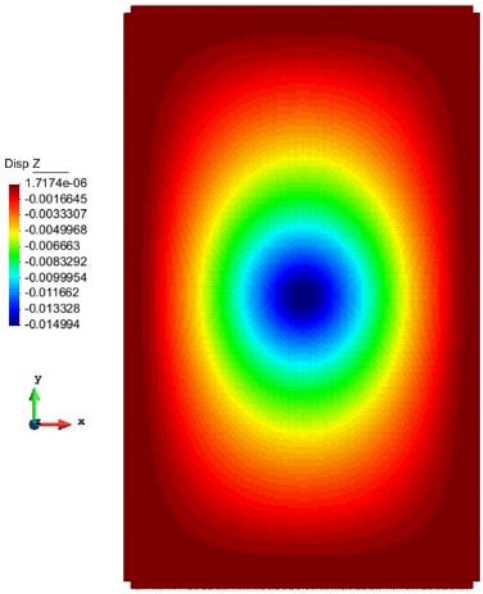

(c)

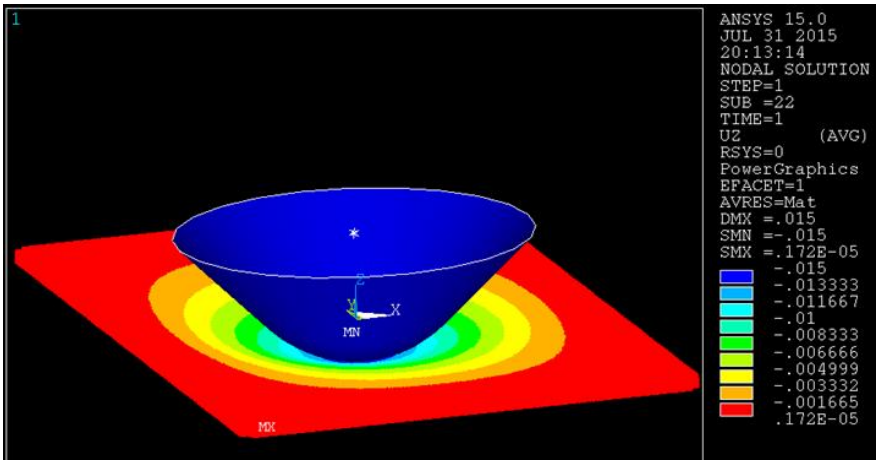

(d)

Figure 6.46 (a) *x*, (b) *y* and (c) *z* direction displacement plots as well as the perspective view of a PD model from ANSYS

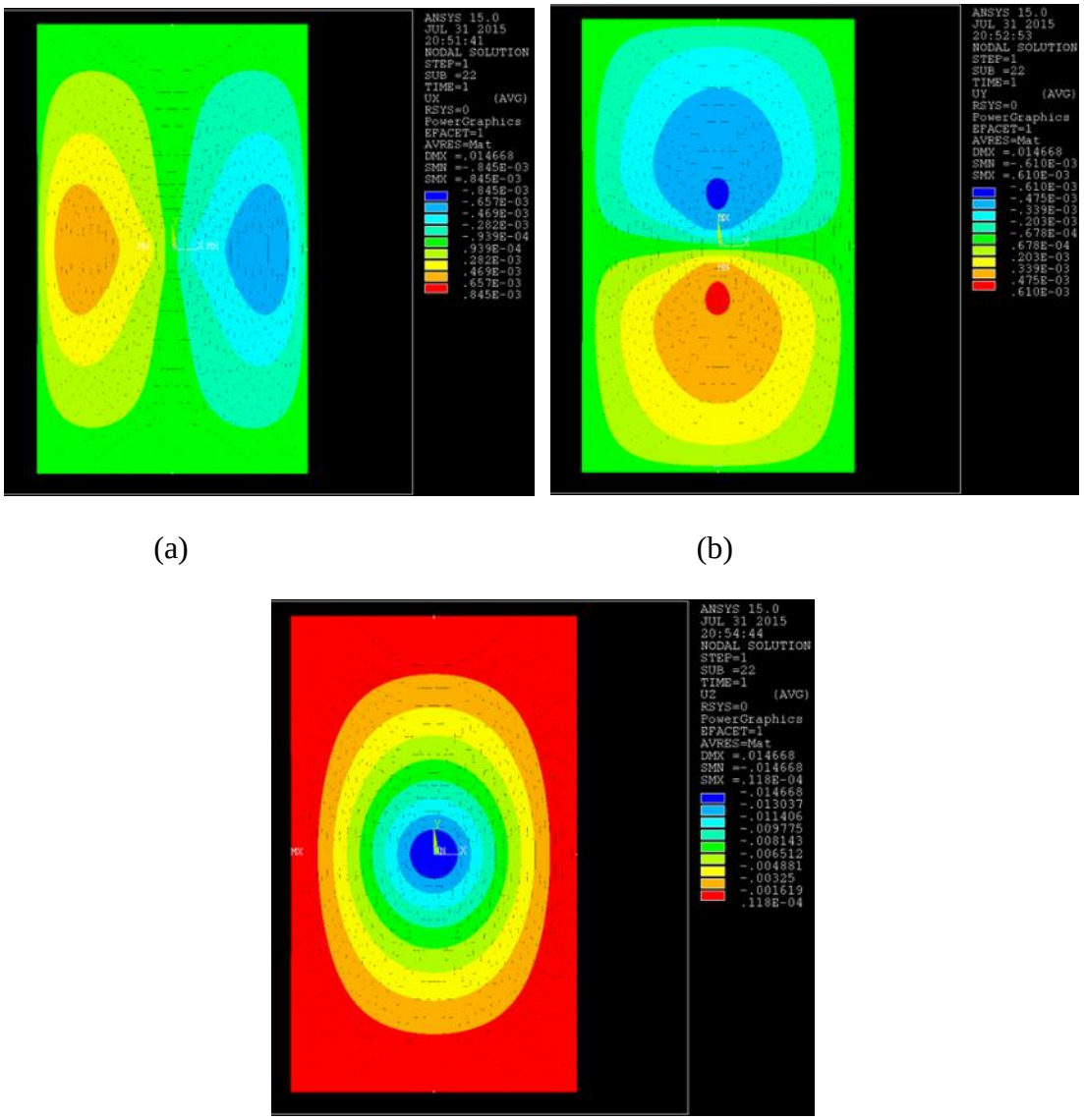

(a) (b)

(c)

Figure 6.47 (a) *x*, (b) *y* and (c) *z* direction displacement plots for a FE model of unstiffened panel

To conclude, the bending deformations of a panel structure are successfully captured in the PD impact study while modelling the rigid target in FE software. Hence, the proposed model, which uses contact and target elements of FE software, is validated. As a result, it is proven that the PD theory can also be an excellent candidate for the collision analyses of ship structures.

6.4 Conclusion

In this section, the plate structures are modelled in PD theory using FE software, ANSYS, and their bending deformations are validated with classical theory results for a particular value of horizon and discretization sizes, i. e. the number of material points in the thickness direction. It is also shown that PD theory can be used to model actual sized ship panel structures for collision and grounding phenomena. Furthermore, incorporating contact capability to current PD codes are studied considering rotational motion of a rigid target. Another option for this can be the use of contact capability of current FE software for PD model. The validity of this method is also demonstrated with a benchmark problem, which represents grounding phenomena of a ship structure.

PD theory can be vital for investigating collision or grounding phenomena in a more detailed sense while including fracture especially for complex ship structures. For this reason, in the next step of this study, the damage capability can be added to current PD model in order to observe fracture characteristics of ship structures. By doing such kind of analyses, more durable ship structures can be manufactured.

The main aim of this section is to bring a new dimension contrary to the existing analytical and numerical modelling tools used for collision and grounding damage analysis of ship structures.

Chapter 7

Conclusions

7.1 The Aim

As it is obvious in the previous chapters of this thesis, Peridynamic (PD) theory has an extensive capability of simulating discontinuities, which may be in the forms of cracks, fracture and the material interfaces of materials. The main advantage of PDs is that the fundamental equations do not include any spatial derivatives of functions. Thus, any supportive or constraint equations do not need to be incorporated while dealing with an intended problem or domain. This intrinsic property of Peridynamics has made it prevalent in every field of solid mechanics but not much in marine structures yet. For the marine sense, the main concern of the researchers, generally, is the computational burden of PD applications. In this regard, the main aim of this study is to pave the way for applications of PD theory in the area of marine structures. In the below paragraphs, the main aims and achievements of each chapter are listed.

In Chapter 2, after an extensive literature survey carried out on structural damage, the fundamental equations of Peridynamics are reviewed in a proper order from its general sense to the most basic form. Moreover, the differences between the proposed forms for its equations are compared.

In Chapter 3, the solution methods for the governing equations of Peridynamic theory are discussed considering the type of problem, which is intended to be solved. In this regard, the implementation of available methods in the literature are covered and their applications for PD models are discussed. The aim of this section is to show how the Peridynamic equations should be handled and correct some misunderstandings on PD theory. One of the biggest miscomprehension is its comparison with FE method. As mentioned in this chapter, finite element (FE) is a numerical method whereas PDs is a theory. Hence, the only realistic comparison can be made between PD theory and the classical theory. As it is shown that it is also possible to do FE implementation for PD theory. The other aspect of this chapter is to show how the big problems can be dealt with, while solving them in a very small time range. In this sense, exploiting the current capacity of computers, which means using the central processing units (CPUs) as well as the graphical processing units (GPUs), is disscussed.

In Chapter 4, the governing equations for simplified structures are derived. The general purpose of this section is to present how the fundamental equations for these structures can be extracted, especially the most relevant ones for marine structures, e.g. beams and plates. It is believed that the derivations for such structures can be a big progress for applications not only for the marine structures but also for every kind of large and complex structures, such as aeroplanes. While doing sophisticated research on these structures, some interesting phenomenon, which is actually the characteristics of real materials observed by experiments, i.e. the dispersion characteristics of simplified structures are also studied. It is shown in later sections that the derived equations of simplified structures can actually capture these phenomenon without any additional effort meaning that without a need of any further modifications on the fundemantal equations. As a result, it is obvious that these simplified theories are also applicable for nano and micro technologies.

Finally, the Chapters 5 and 6 are mostly devoted to the applications of Peridynamic theory for marine structures. In Chapter 5, the damage characteristics of marine structures under shock waves is studied by considering a complex composite structure. Here, it is shown that PD theory is able to capture the damage of such complex structures under extreme loadings. Furthermore, in Chapter 6, the applicability of PD theory for grounding and collision phenomena is demonstrated. The aim of this chapter

is to model three dimensional ship panels and show the behaviours of those under collision or grounding loadings. Besides, the applicability of contact property is discussed and validated with a benchmark problem.

7.2 Future Studies

Whilst doing research in each chapter for the above mentioned purposes, many other subjects are also covered which are not shown in this thesis in order not to ruin its integrity. Some of these studies are presented below along with the future ideas and recommendations.

In Chapter 3, the implementation of PD theory in FE software, ANSYS, is discussed. In addition to those attempts, the damage problems for lamina, which is a single layer composite structure, were also studied for applications in ANSYS and the most fundamental damage chracteristics are captured for such structures. Figure 7.1 shows the crack propagation behaviours for different types of lamina, which is solved by exploting FE software, ANSYS, under simple loading conditions. This study can further be extended to include damage characteristics of composite laminates, which constitute from several layers of lamina on top of each other. To accomplish this task, transverse direction bonds, i.e. shear and normal bonds, of PD theory need to be represented in FE software and it is left for a future study.

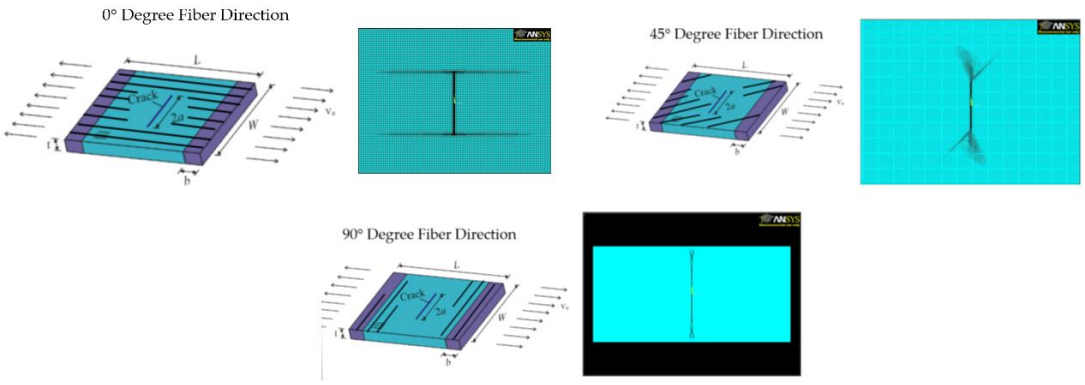

Figure 7.1 Crack propagations for different fiber orientations of lamina

In Chapter 4, simplified theories for beams and plates are presented and these can be extended to ordinary state based PD theory. By doing this, the constraint on the

Poisson's ratio for the proposed plate model can be removed and more general theory of plate can be obtained. Moreover, it is also possible to extend current models considering all degrees of freedom for each axis. For example, the axial and torsional deformations can be added to current PD beam and plate models. By doing this, buckling phenomenon can be captured with PD theory and this is left for a future study.

In Chapter 5, the underwater shock response of marine composites are studied by inducing shock loading directly onto a structure. This study can be extended by modelling fluid, i.e. water, in PDs and coupling the effects of solid and fluid models, i.e. fluid – structure interaction (FSI), in PDs. In this regard, the work done by Demmie and Silling (2007), in which the explosive inside a conctrete shell structure is detonated to a gas form and finally fractures it, was replicated as shown in Figure 7.2.

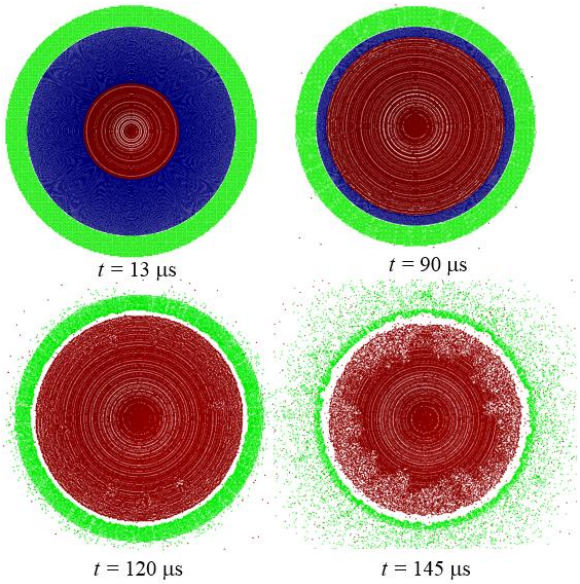

Figure 7.2 Explosion of concrete shell during time

*The red, blue and green colours denote the gas, the TNT explosive and the concrete, respectively.

The gas – solid interaction is able to be captured successfully and the foundings from here can be extended to the fluid – structure interaction case. As a preliminary study, the water shock wave propagation in a tube, shown in Figure 7.3, was carried out in PD theory and the FSI effects are left for a future study.

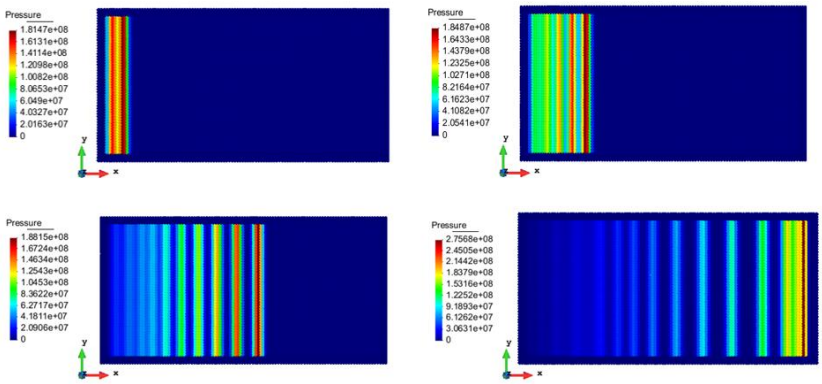

Figure 7.3 Underwater shock wave propagation as the time progresses

In Chapter 6, the collision and grounding phenomena is studied considering the rock or the ship's bow as a rigid striking object. It is also possible to model flexible striking objects for collision phenomenon such as representing the offshore structure's legs. Apart from that, several researches have been carried out to find the effects of impact loadings of ice structures acting on ship and offshore structures. In this sense, the ice load acting on a ship or offshore structure has critical importance and numerical modelling of ice is important. The ice impact problem acting on a rigid target was studied for high impact velocities (Oterkus and Diyaroglu, 2014) and the damage occurred on ice structure was investigated as shown in Figure 7.4. However, the ice cube shown in here is modelled in a brittle sense, which is valid for only high impact velocities, and the complete model of ice is left for a future study. In a complete model, the visco – plastic characteristics should be included as well as the micro –structure of the ice shuld be taken into account.

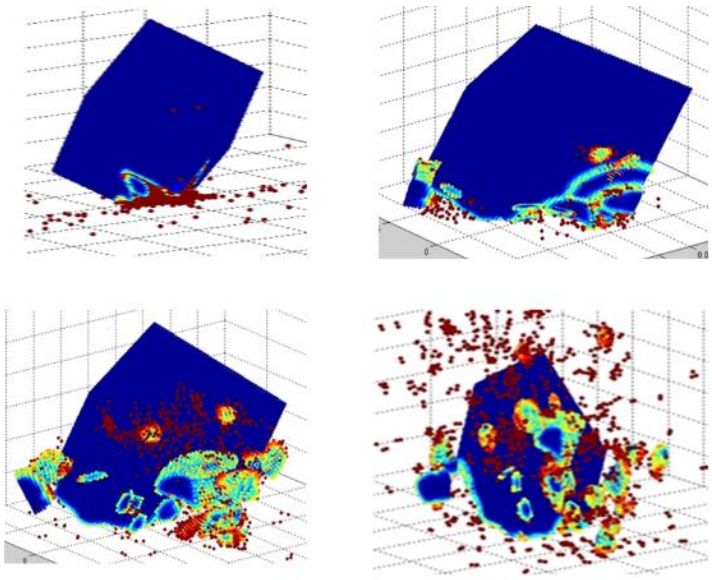

Figure 7.4 Ice cube impact on a rigid target

Finally, different physical fields can be represented in PD theory and some of these are presented with several research papers as mentioned in Section 1.3. In these studies, the advantage of PD theory in material interfaces is utilized and also the coupling of different physical fields is investigated. Each of these can be the subject of a futher study.

References

AbuBakar, A., Dow, R.S., 2013. Simulation of ship grounding damage using the finite element method. Int. J. Solids Struct. 50, 623–636. doi:http://dx.doi.org/10.1016/j.ijsolstr.2012.10.016

Agwai, A., Guven, I., Madenci, E., 2011. Predicting crack propagation with peridynamics: a comparative study. Int. J. Fract. 171, 65–78. doi:10.1007/s10704-011-9628-4

Alsos, H.S., Amdahl, J., 2009. On the resistance to penetration of stiffened plates, Part I – Experiments. Int. J. Impact Eng. 36, 799–807. doi:http://dx.doi.org/10.1016/j.ijimpeng.2008.10.005

Alsos, H.S., Amdahl, J., Hopperstad, O.S., 2009. On the resistance to penetration of stiffened plates, Part II: Numerical analysis. Int. J. Impact Eng. 36, 875–887. doi:10.1016/j.ijimpeng.2008.11.004

Amirkulova, F.A., 2011. Dispersion Relations for Elastic Waves in Plates and Rods. The State University of New Jersey.

An, G.B., Woo, W., Park, J.-U., 2014. Brittle crack-arrest fracture toughness in a high heat-input thick steel weld. Int. J. Fract. 185, 179–185. doi:10.1007/s10704-013-9900-x

APC-2 PEEK Thermoplastic Polymer Technical Data Sheet, 2012. . Cytec Engineering.

Araki, W., Nemoto, K., Adachi, T., Yamaji, A., 2005. Fracture toughness for mixed mode I/II of epoxy resin. Acta Mater. 53, 869–875. doi:http://dx.doi.org/10.1016/j.actamat.2004.10.035

Arora, H., Hooper, P.A., Dear, J.P., 2012. The Effects of Air and Underwater Blast on Composite Sandwich Panels and Tubular Laminate Structures. Exp. Mech. 52, 59–81. doi:10.1007/s11340-011-9506-z

Avachat, S., 2012. Experimental and Numerical Analyses of Dynamic Deformation and Failure in Marine Structures Subjected to Underwater Impulsive Loads. Georgia Institute of Technology.

Avachat, S., Zhou, M., 2013. Experimental Analysis of Dynamic Deformation and Damage in Composite Sandwich Structures Subjected to Underwater Impulsive Loads, in: Chalivendra, V., Song, B., Casem, D. (Eds.), Dynamic Behavior of Materials, Volume 1 SE - 35, Conference Proceedings of the Society for Experimental Mechanics Series. Springer New York, pp. 275–286. doi:10.1007/978-1-4614-4238-7_35

Ayatollahi, M.R., Aliha, M.R.M., 2009. Analysis of a new specimen for mixed mode fracture tests on brittle materials. Eng. Fract. Mech. 76, 1563–1573. doi:10.1016/j.engfracmech.2009.02.016

Bachynski, E.E., Motley, M.R., Young, Y.L., 2011. Dynamic Hydroelastic Scaling of the Underwater Shock Response of Composite Marine Structures. J. Appl. Mech. 79, 14501.

Bathe, K.-J., Baig, M.M.I., 2005. On a composite implicit time integration procedure for nonlinear dynamics. Comput. Struct. 83, 2513–2524. doi:http://dx.doi.org/10.1016/j.compstruc.2005.08.001

Batra, R.C., Hassan, N.M., 2007. Response of fiber reinforced composites to underwater explosive loads. Compos. Part B Eng. 38, 448–468. doi:http://dx.doi.org/10.1016/j.compositesb.2006.09.001

Bayley, C., Aucoin, N., 2013. Fracture testing of welded single edge notch tensile specimens. Eng. Fract. Mech. 102, 257–270. doi:http://dx.doi.org/10.1016/j.engfracmech.2013.02.020

Benzeggagh, M.L., Kenane, M., 1996. Measurement of mixed-mode delamination fracture toughness of unidirectional glass/epoxy composites with mixed-mode bending apparatus. Compos. Sci. Technol. 56, 439–449. doi:http://dx.doi.org/10.1016/0266-3538(96)00005-X

Bobaru, F., Duangpanya, M., 2010. The peridynamic formulation for transient heat conduction. Int. J. Heat Mass Transf. 53, 4047–4059. doi:http://dx.doi.org/10.1016/j.ijheatmasstransfer.2010.05.024

Bobaru, F., Yang, M., Alves, L.F., Silling, S.A., Askari, E., Xu, J., 2009. Convergence, adaptive refinement, and scaling in 1D peridynamics. Int. J. Numer. Methods Eng. 77, 852–877.

Charalambides, M., Kinloch, A.J., Wang, Y., Williams, J.G., 1992. On the analysis of mixed-mode failure. Int. J. Fract. 54, 269–291. doi:10.1007/BF00035361

Chen, X., Gunzburger, M., 2011. Continuous and discontinuous finite element methods for a peridynamics model of mechanics. Comput. Methods Appl. Mech. Eng. 200, 1237–1250. doi:http://dx.doi.org/10.1016/j.cma.2010.10.014

Comtois, J.L.R., Edwards, M.R., Oakes, M.C., 1999. The effect of explosives on polymer matrix composite laminates. Compos. Part A Appl. Sci. Manuf. 30, 181–190. doi:http://dx.doi.org/10.1016/S1359-835X(98)00172-9

Cyply 1002 Reinforced Plastic, 2002. . Cytec Engineered Materials.

D'Souza, A.F., Garg, V.K., 1984. Lagrangian Dynamics, in: Advanced Dynamics Modelling and Analysis. Prentice-Hall.

Demmie, P., Silling, S., 2007. An approach to modeling extreme loading of structures using peridynamics. J. Mech. Mater. Struct. doi:10.2140/jomms.2007.2.1921

Diyaroglu, C., De Meo, D., Oterkus, E., 2015. A Computational Framework for Underwater Shock Response of Marine Structures, in: Soares, C.G., Shenoi, R.A. (Eds.), 5th International Conference on Marine Structures MARSTRUCT. Southampton, UK.

Diyaroglu, C., Oterkus, E., De Meo, D., Madenci, E., 2015a. Peridynamic Modelling of Underwater Shock Response of Marine Composite Structures, in: USNCCM Conference. San Diego, CA, USA.

Diyaroglu, C., Oterkus, E., Oterkus, S., Madenci, E., 2015b. Peridynamics for bending of beams and plates with transverse shear deformation. Int. J. Solids Struct. 69–70, 152–168. doi:http://dx.doi.org/10.1016/j.ijsolstr.2015.04.040

Diyaroglu, C., Oterkus, E., Oterkus, S., Madenci, E., 2014. A Non-local Mindlin Plate Formulation in Peridynamics, in: ASME 2014 International Mechanical Engineering Congress & Exposition. Montreal, Canada.

Du, Q., Ju, L., Tian, L., Zhou, K., 2013a. A Posteriori Error Analysis of Finite Element Method for Linear Nonlocal Diffusion and Peridynamic Models. Math. Comp. 82, 1889–1922.

Du, Q., Tian, L., Zhao, X., 2013b. A Convergent Adaptive Finite Element Algorithm for Nonlocal Diffusion and Peridynamic Models. SIAM J. Numer. Anal. 51, 1211–1234. doi:10.1137/120871638

Ehler, S., Romanoff, J., 2010. 5th International Conference on Collision and Grounding of Ships. Aalto University.

Emmrich, E., Lehoucq, R., Puhst, D., 2013. Peridynamics: A Nonlocal Continuum Theory, in: Griebel, M., Schweitzer, M.A. (Eds.), Meshfree Methods for Partial Differential Equations, Lecture Notes in Computational Science and Engineering. Springer Berlin Heidelberg, pp. 45–65. doi:10.1007/978-3-642-32979-1_3

Emmrich, E., Weckner, O., 2007. The peridynamic equation and its spatial discretisation. Math. Model. Anal. 12, 17–27. doi:10.3846/1392-6292.2007.12.17-27

Emmrich, E., Weckner, O., 2006. The peridynamic equation of motion in non-local elasticity theory, in: Et.al., M.S. (Ed.), Proceeding of III European Conference on Computational Mechanics: Solids, Structures and Coupled Problems in Engineering. Lisbon, Portugal.

Eringen, A.C., 1972. Linear theory of nonlocal elasticity and dispersion of plane waves. Int. J. Eng. Sci. doi:10.1016/0020-7225(72)90050-X

Espinosa, H.D., Lee, S., Moldovan, N., 2006. A Novel Fluid Structure Interaction Experiment to Investigate Deformation of Structural Elements Subjected to Impulsive Loading. Exp. Mech. 46, 805–824. doi:10.1007/s11340-006-0296-7

Farshad, M., Flüeler, P., 1998. Investigation of mode III fracture toughness using an anti-clastic plate bending method. Eng. Fract. Mech. 60, 597–603. doi:http://dx.doi.org/10.1016/S0013-7944(98)00020-4

Fossen, T.I., 1987. Nonlinear Modelling and Control of Underwater Vehicles. Norwegian Institute of Technology.

Fricke, W., von Lilienfeld-Toal, A., Paetzold, H., 2012. Fatigue strength investigations of welded details of stiffened plate structures in steel ships. Int. J. Fatigue 34, 17–26. doi:http://dx.doi.org/10.1016/j.ijfatigue.2011.01.021

Gauch, E., LeBlanc, J., Shukla, A., 2012. Response of preloaded thin composite panels subjected to underwater explosive loading. Comput. Struct. 112–113, 342–353. doi:http://dx.doi.org/10.1016/j.compstruc.2012.08.001

Gerstle, W., Sau, N., Silling, S., 2005. Peridynamic Modelling of Plain and Reinforced Concrete Structures. pp. 1–15.

Gerstle, W., Silling, S., Read, D., Tewary, V., Lehoucq, R., 2008. Peridynamic Simulation of Electromigration. Comput. Mater. Contin. 8, 75–92. doi:10.3970/cmc.2008.008.075

Gong, S.W., Lam, K.Y., 1998. Transient response of stiffened composite submersible hull subjected to underwater explosive shock. Compos. Struct. 41, 27–37. doi:http://dx.doi.org/10.1016/S0263-8223(98)00016-6

Greenwood, D.T., 1988. Basic Concepts and Kinematics of Rigid Body Motion, in: Principles of Dynamics. Prentice-Hall, p. 354.

Griffith, A.A., 1921. The Phenomena of Rupture and Flow in Solids. Philos. Trans. R. Soc. London A Math. Phys. Eng. Sci. 221, 163–198.

Ha, Y.D., Bobaru, F., 2010. Studies of dynamic crack propagation and crack branching with peridynamics. Int. J. Fract. 162, 229–244. doi:10.1007/s10704-010-9442-4

Han, S., Lim, S., Bae, J., Hwang, Y., Lee, S., Oterkus, S., Madenci, E., Diyaroglu, C., Oterkus, E., 2015. Equivalent Acceleration Assessment of JEDEC Moisture Sensitivity Levels Using Peridynamics, in: 65th Electronic Components & Technology Conference. San Diego, CA, USA.

Hashemi, S., Kinloch, A.J., Williams, J.G., 1990. The Analysis of Interlaminar Fracture in Uniaxial Fibre-Polymer Composites. Proc. R. Soc. London A Math. Phys. Eng. Sci. 427, 173–199.

Hassan, N.M., 2005. Damage Development in Static and Dynamic Deformations of Fiber-Reinforced Composite Plates. Virginia Polytechnic Institute and State University.

Hibbeler, R.C., 2007. Three-Dimensional Kinetics of a Rigid Body, in: Engineering Mechanics DYNAMICS. Pearson Prentice Hall, pp. 588–592.

International Association of Classification Societies, 2013. Requirements for Use of Extremely Thick Steel Plates, International Association of Classification Societies (IACS).

Kalavalapally, R., Penmetsa, R., Grandhi, R., 2006. Multidisciplinary optimization of a lightweight torpedo structure subjected to an underwater explosion. Finite Elem. Anal. Des. 43, 103–111. doi:http://dx.doi.org/10.1016/j.finel.2006.07.005

Katiyar, A., Foster, J.T., Ouchi, H., Sharma, M.M., 2014. A peridynamic formulation of pressure driven convective fluid transport in porous media. J. Comput. Phys. 261, 209–229. doi:http://dx.doi.org/10.1016/j.jcp.2013.12.039

Kaw, A.K., 2006. Mechanics of Composite Materials, Second Ed. ed. Taylor & Francis.

Kilic, B., 2008. Peridynamic Theory For Progressive Failure Prediction In Homogeneous And Heterogeneous Materials. The University of Arizona.

Kim, J.G., Hwang, Y.J., Yoon, S.H., Lee, D.G., 2012. Improvement of the fracture toughness of adhesively bonded stainless steel joints with aramid fibers at cryogenic temperatures. Compos. Struct. 94, 2982–2989. doi:http://dx.doi.org/10.1016/j.compstruct.2012.03.023

Klanac, A., Duletic, T., Ehlers, S., Goerlandt, F., Frank, D., 2010. Environmental Risk of Collision for Enclosed Seas: Gulf of Finland, Adriatic, and Implications for Tanker Design, in: Ehlers, S., Romanoff, J. (Eds.), 5th International Conference on Collision and Grounding of Ships, Espoo. Aalto University, Finland.

Kozak, J., 2010. Damage Tests of the Single Shell Ship Fuel Tank with Additional Elastic Protective Coating, in: Ehlers, S., Romanoff, J. (Eds.), 5th International Conference on Collision and Grounding of Ships, Espoo. Finland.

Lam, K.Y., Zong, Z., Wang, Q.X., 2003. Dynamic response of a laminated pipeline on the seabed subjected to underwater shock. Compos. Part B Eng. 34, 59–66. doi:http://dx.doi.org/10.1016/S1359-8368(02)00072-0

Langdon, G.S., Yuen, S.C.K., Nurick, G.N., 2005. Experimental and numerical studies on the response of quadrangular stiffened plates. Part II: localised blast loading. Int. J. Impact Eng. 31, 85–111. doi:http://dx.doi.org/10.1016/j.ijimpeng.2003.09.050

Latourte, F., Grégoire, D., Zenkert, D., Wei, X., Espinosa, H.D., 2011. Failure mechanisms in composite panels subjected to underwater impulsive loads. J. Mech. Phys. Solids 59, 1623–1646. doi:http://dx.doi.org/10.1016/j.jmps.2011.04.013

LeBlanc, J., 2011. Dynamic Response and Damage Evolution of Composite Materials Subjected to Underwater Explosive Loading: An Experimental and Computational Study. University of Rhode Island.

Lee, S., 1997. Mode II delamination failure mechanisms of polymer matrix composites. J. Mater. Sci. 32, 1287–1295. doi:10.1023/A:1018552506085

Leng, S.W., Miao, Z.M., Qiu, F.X., Niu, L.N., Miao, T., 2012. Analysis of the Relationship between CTOD Toughness and Micromechanism of Marine Steel Weld Joints. Appl. Mech. Mater. 117-119, 1867–1873. doi:10.4028/www.scientific.net/AMM.117-119.1867

Li, Q., Manolidis, M., Young, Y.L., 2013. Analytical Modeling of the Underwater Shock Response of Rigid and Elastic Plates Near a Solid Boundary. J. Appl. Mech. 80, 21017.

Liang, C.-C., Tai, Y.-S., 2006. Shock responses of a surface ship subjected to noncontact underwater explosions. Ocean Eng. 33, 748–772. doi:http://dx.doi.org/10.1016/j.oceaneng.2005.03.011

Librescu, L., Oh, S.-Y., Hohe, J., 2006. Dynamic response of anisotropic sandwich flat panels to underwater and in-air explosions. Int. J. Solids Struct. 43, 3794–3816. doi:http://dx.doi.org/10.1016/j.ijsolstr.2005.03.052

Librescu, L., Oh, S.-Y., Hohe, J., 2004. Linear and non-linear dynamic response of sandwich panels to blast loading. Compos. Part B Eng. 35, 673–683. doi:http://dx.doi.org/10.1016/j.compositesb.2003.07.003

Macek, R.W., Silling, S.A., 2007. Peridynamics via finite element analysis. Finite Elem. Anal. Des. 43, 1169–1178. doi:10.1016/j.finel.2007.08.012

Madenci, E., Oterkus, E., 2014. Peridynamic Theory and Its Applications, Peridynamic Theory and Its Applications SE - 2. Springer New York, New York, NY. doi:10.1007/978-1-4614-8465-3

McCoy, R.W., Sun, C.T., 1997. Fluid-structure interaction analysis of a thick-section composite cylinder subjected to underwater blast loading. Compos. Struct. 37, 45–55. doi:http://dx.doi.org/10.1016/S0263-8223(97)00081-0

Melin, S., 1991. Which is the most unfavourable crack orientation? Int. J. Fract. 51, 255–263. doi:10.1007/BF00045811

Minorsky, V.U., 1959. An Analysis of Ship Collisions with Reference to Protection of Nuclear Power Plants. J. Sh. Res. 3, 1–4.

Moon, D.H., Lee, J.S., Lee, J.M., Kim, M.H., 2013. Estimation of Constraint Factor on the Relationship Between J Integral and CTOD for Offshore Structural Steel Weldments, in: Volume 3: Materials Technology; Ocean Space Utilization. ASME, p. V003T03A023. doi:10.1115/OMAE2013-10641

Motley, M.R., Young, Y.L., Liu, Z., 2011. Three-Dimensional Underwater Shock Response of Composite Marine Structures. J. Appl. Mech. 78, 61013.

Mouritz, A.P., 2001. Ballistic impact and explosive blast resistance of stitched composites. Compos. Part B Eng. 32, 431–439. doi:http://dx.doi.org/10.1016/S1359-8368(01)00015-4

Nuismer, R.J., 1975. An energy release rate criterion for mixed mode fracture. Int. J. Fract. 11, 245–250. doi:10.1007/BF00038891

Nurick, G.N., Gelman, M.E., Marshall, N.S., 1996. Tearing of blast loaded plates with clamped boundary conditions. Int. J. Impact Eng. 18, 803–827. doi:http://dx.doi.org/10.1016/S0734-743X(96)00026-7

Nurick, G.N., Shave, G.C., 1996. The deformation and tearing of thin square plates subjected to impulsive loads—An experimental study. Int. J. Impact Eng. 18, 99–116. doi:http://dx.doi.org/10.1016/0734-743X(95)00018-2

O'Brein, T.K., 1997. Composite Interlaminar Shear Fracture Toughness, G2c: Shear Measurement of Sheer Myth? Hampton, USA.

O'Grady, J., Foster, J., 2014a. Peridynamic beams: A non-ordinary, state-based model. Int. J. Solids Struct. 51, 3177–3183. doi:http://dx.doi.org/10.1016/j.ijsolstr.2014.05.014

O'Grady, J., Foster, J., 2014b. Peridynamic plates and flat shells: A non-ordinary, state-based model. Int. J. Solids Struct. 51, 4572–4579. doi:http://dx.doi.org/10.1016/j.ijsolstr.2014.09.003

Oterkus, E., 2010. Peridynamic Theory for Modelling Three-Dimensional Damage Growth in Metallic and Composite Structures. The University of Arizona.

Oterkus, E., De Meo, D., Zhu, N., Diyaroglu, C., 2015. Stress Corrosion Cracking Modelling by Using Peridynamics, in: ASME 2015 International Mechanical Engineering Congress & Exposition. Houston, Texas, USA.

Oterkus, E., Diyaroglu, C., 2014. Multiscale Modelling of Ice-Structure Interactions by Using Peridynamics, in: Offshore Marintec Russia International Specialized Offshore Exhibition and Conference. St. Petersburg, Russia.

Oterkus, E., Diyaroglu, C., De Meo, D., Allegri, G., 2016. Fracture Modes, Damage Tolerance and Failure Mitigation in Marine Composites, in: Graham Jones, J., Summerscales, J. (Eds.), Marine Applications of Advanced Composite Materials. Woodhead, pp. 79–102.

Oterkus, E., Diyaroglu, C., Oterkus, S., Madenci, E., 2013. Peridynamic Formulation for Beam and Shell Type Structures, in: USNCCM Conference. NC, USA.

Oterkus, E., Diyaroglu, C., Zhu, N., Oterkus, S., Madenci, E., 2015. Utilization of Peridynamic Theory for Modeling at the Nano-Scale, in: Baillin, X., Joachim, C., Poupon, G. (Eds.), Nanopackaging: From Nanomaterials to the Atomic Scale SE - 1, Advances in Atom and Single Molecule Machines. Springer International Publishing, pp. 1–16. doi:10.1007/978-3-319-21194-7_1

Oterkus, E., Madenci, E., 2012. Peridynamic analysis of fiber-reinforced composite materials. J. Mech. Mater. Struct. doi:10.2140/jomms.2012.7.45

Oterkus, E., Madenci, E., Weckner, O., Silling, S., Bogert, P., Tessler, A., 2012. Combined finite element and peridynamic analyses for predicting failure in a stiffened composite curved panel with a central slot. Compos. Struct. 94, 839–850. doi:10.1016/j.compstruct.2011.07.019

Oterkus, S., Fox, J., Madenci, E., 2013. Simulation of electro-migration through peridynamics, in: Electronic Components and Technology Conference (ECTC), IEEE 63rd. IEEE, Las Vegas, NV, pp. 1488–1493.

Oterkus, S., Madenci, E., Agwai, A., 2014. Peridynamic thermal diffusion. J. Comput. Phys. 265, 71–96. doi:http://dx.doi.org/10.1016/j.jcp.2014.01.027

Panciroli, R., Abrate, S., 2012. Dynamic response of sandwich shells to underwater blasts. Cent. Eur. J. Eng. 2, 509–522. doi:10.2478/s13531-012-0024-2

Poche, L.B., Zalesak, J.F., 1992. Development of a Water-Filled Conical Shock Tube for Shock Testing of Small Sonar Transducers by Simulation of the Test Conditions for the Heavyweight Test of MIL-S-901D (NAVY). Orlando, Florida.

Quéméner, Y., Huang, C.-H., Lee, C.-F., 2013. Fracture Resistance of Ship Longitudinal Members Including Fatigue Crack, in: Volume 2A: Structures, Safety and Reliability. ASME, p. V02AT02A026. doi:10.1115/OMAE2013-10302

Raimondo, L., Iannucci, L., Robinson, P., Curtis, P.T., 2012. A progressive failure model for mesh-size-independent FE analysis of composite laminates subject to low-velocity impact damage. Compos. Sci. Technol. 72, 624–632. doi:http://dx.doi.org/10.1016/j.compscitech.2012.01.007

Ramesh, T., Chandra, V.S., 2012. Damage and Failure of Composite Materials. Cambridge University Press.

Reis, M. de A. e S., 1978. Wave Propagation in Elastic Beams and Rods. Massachusetts Institute of Technology.

Ritchie, R.O., 2011. The conflicts between strength and toughness. Nat. Mater. 10, 817–822.

Rubio-González, C., Felix-Martinez, C., Gomez-Rosas, G., Ocaña, J.L., Morales, M., Porro, J.A., 2011. Effect of laser shock processing on fatigue crack growth of duplex stainless steel. Mater. Sci. Eng. A 528, 914–919. doi:http://dx.doi.org/10.1016/j.msea.2010.10.020

Schiffer, A., Tagarielli, V.L., 2014. The dynamic response of composite plates to underwater blast: Theoretical and numerical modelling. Int. J. Impact Eng. 70, 1–13. doi:http://dx.doi.org/10.1016/j.ijimpeng.2014.03.002

Schiffer, A., Tagarielli, V.L., Cocks, A.C.F., Petrinic, N., 2012. The Response of Composite Plates to Underwater Blast, in: ASME 2012 International Mechanical Engineering Congress and Exposition Volume 8: Mechanics of Solids, Structures and Fluids. ASME, Houston, Texas, USA, p. 749. doi:10.1115/IMECE2012-85717

Silling, S. A., 2010. Linearized Theory of Peridynamic States. J. Elast. 99, 85–111. doi:10.1007/s10659-009-9234-0

Silling, S.A., 2000. Reformulation of elasticity theory for discontinuities and long-range forces. J. Mech. Phys. Solids 48, 175–209. doi:10.1016/S0022-5096(99)00029-0

Silling, S.A., Askari, E., 2005. A meshfree method based on the peridynamic model of solid mechanics. Comput. Struct. 83, 1526–1535. doi:10.1016/j.compstruc.2004.11.026

Silling, S.A., Epton, M., Weckner, O., Xu, J., Askari, E., 2007. Peridynamic states and constitutive modeling. J. Elast. 88, 151–184. doi:10.1007/s10659-007-9125-1

Soedel, W., 2004. Vibrations of Shells and Plates, 3rd ed. New York : Marcel Dekker.

Stephen, N., 1997. Mindlin Plate Theory: Best Shear Coefficient and Higher Spectra Validity. J. Sound Vib. 202, 539–553.

Sumi, Y., 2014a. Fatigue crack propagation in marine structures under seaway loading. Int. J. Fatigue 58, 218–224. doi:http://dx.doi.org/10.1016/j.ijfatigue.2013.03.002

Sumi, Y., 2014b. Fatigue crack propagation in marine structures under seaway loading. Int. J. Fatigue 58, 218–224. doi:http://dx.doi.org/10.1016/j.ijfatigue.2013.03.002

Sumi, Y., Yajima, H., Toyosada, M., Yoshikawa, T., Aihara, S., Gotoh, K., Ogawa, Y., Matsumoto, T., Hirota, K., Hirasawa, H., Toyoda, M., Morikage, Y., 2013. Fracture control of extremely thick welded steel plates applied to the deck structure of large container ships. J. Mar. Sci. Technol. 18, 497–514. doi:10.1007/s00773-013-0222-5

Taylor, M., Steigmann, D.J., 2015. A Two-Dimensional Peridynamic Model for Thin Plates. Math. Mech. Solids 20, 998–1010.

Teeling-Smith, R.G., Nurick, G.N., 1991. The deformation and tearing of thin circular plates subjected to impulsive loads. Int. J. Impact Eng. 11, 77–91. doi:http://dx.doi.org/10.1016/0734-743X(91)90032-B

Terndrup Pedersen, P., Zhang, S., 1998. On Impact mechanics in ship collisions. Mar. Struct. 11, 429–449. doi:http://dx.doi.org/10.1016/S0951-8339(99)00002-7

Thornton, S.T., Marion, J.B., 2004. Classical Dynamics of Particles and Systems, 5th ed, Classical Dynamics of Particles and Systems. Thomson Brooks/Cole.

Toyosada, M., Gotoh, K., Niwa, T., 2004. Fatigue crack propagation for a through thickness crack: a crack propagation law considering cyclic plasticity near the crack tip. Int. J. Fatigue 26, 983–992. doi:http://dx.doi.org/10.1016/j.ijfatigue.2003.12.006

Turkmen, H.S., Mecitoglu, Z., 1999. Dynamic Response of a Stiffened Laminated Composite Plate Subjected to Blast Load. J. Sound Vib. 221, 371–389. doi:http://dx.doi.org/10.1006/jsvi.1998.1976

Underwood, P., 1983. Dynamic Relaxation, in: Belytschko, T., Hughes, T.J.R. (Eds.), Computational Methods for Transient Analysis. Elsevier, Palo Alto, USA, pp. 245–265.

Wang, Z., Liang, X., Fallah, A.S., Liu, G., Louca, L.A., Wang, L., 2013. A novel efficient method to evaluate the dynamic response of laminated plates subjected to underwater shock. J. Sound Vib. 332, 5618–5634. doi:http://dx.doi.org/10.1016/j.jsv.2013.05.028

Wei, X., de Vaucorbeil, A., Tran, P., Espinosa, H.D., 2013a. A new rate-dependent unidirectional composite model – Application to panels subjected to underwater blast. J. Mech. Phys. Solids 61, 1305–1318. doi:http://dx.doi.org/10.1016/j.jmps.2013.02.006

Wei, X., Tran, P., de Vaucorbeil, A., Ramaswamy, R.B., Latourte, F., Espinosa, H.D., 2013b. Three-dimensional numerical modeling of composite panels subjected to underwater blast. J. Mech. Phys. Solids 61, 1319–1336. doi:http://dx.doi.org/10.1016/j.jmps.2013.02.007

Wengang, M., Jonas, R., 2013. Analysis of Fatigue Crack Initiation and Propagation in Ship Structures, in: Proceedings of the Thirteenth International Conference on Fracture (ICF13). Beijing, China, p. 10.

Wierzbicki, T., Nurick, G.N., 1996. Large deformation of thin plates under localised impulsive loading. Int. J. Impact Eng. 18, 899–918. doi:http://dx.doi.org/10.1016/S0734-743X(96)00027-9

Williams, J.G., 1988. On the calculation of energy release rates for cracked laminates. Int. J. Fract. 36, 101–119. doi:10.1007/BF00017790

Yajima, H., Watanabe, E., Jia, Z., Yoshimoto, K., Ishikawa, T., Funatsu, Y., 2011. Study on Fracture Toughness Evaluation by centre-notched small size specimen for heavy-thick steel plates. Weld. World 55, 78–83. doi:10.1007/BF03321297

Young, Y.L., Liu, Z., Xie, W., 2009. Fluid-Structure and Shock-Bubble Interaction Effects During Underwater Explosions Near Composite Structures. J. Appl. Mech. 76, 51303.

Yu, Y.H., Kim, B.G., Lee, D.G., 2013. Cryogenic reliability of the sandwich insulation board for LNG ship. Compos. Struct. 95, 547–556. doi:http://dx.doi.org/10.1016/j.compstruct.2012.07.007

Yuen, S.C.K., Nurick, G.N., 2005. Experimental and numerical studies on the response of quadrangular stiffened plates. Part I: Subjected to uniform blast load. Int. J. Impact Eng. 31, 55–83. doi:10.1016/j.ijimpeng.2003.09.048

Zhou, K., Du, Q., 2010. Mathematical and Numerical Analysis of Linear Peridynamic Models with Nonlocal Boundary Conditions. SIAM J. Numer. Anal. 48, 1759–1780. doi:10.1137/090781267

Zhu, X.-K., Joyce, J.A., 2012. Review of fracture toughness (G, K, J, CTOD, CTOA) testing and standardization. Eng. Fract. Mech. 85, 1–46. doi:http://dx.doi.org/10.1016/j.engfracmech.2012.02.001